
Shear Viscosity for QCD at High Chemical Potentials

Scher-Viskosität für QCD bei hohen chemischen Potentialen

Zur Erlangung des Grades eines Doktors der Naturwissenschaften (Dr. rer. nat.)

Genehmigte Dissertation von Isabella Danhoni aus Sao Bernardo do Campo

Tag der Einreichung: 17.06.2024 , Tag der Prüfung: 17.07.2024

1. Gutachten: Prof. PhD. Guy D. Moore

2. Gutachten: Prof. Dr. phil. nat. Dirk H. Rischke

Darmstadt, Technische Universität Darmstadt

Veröffentlichungsjahr der Dissertation auf TUpriints: 2024



TECHNISCHE
UNIVERSITÄT
DARMSTADT

Physics Department
Institut für Kernphysik

Shear Viscosity for QCD at High Chemical Potentials
Scher-Viskosität für QCD bei hohen chemischen Potentialen

Accepted doctoral thesis by Isabella Danhoni

Date of submission: 17.06.2024

Date of thesis defense: 17.07.2024

Darmstadt, Technische Universität Darmstadt
Veröffentlichungsjahr der Dissertation auf TUPrints: 2024

Bitte zitieren Sie dieses Dokument als:

URN: urn:nbn:de:tuda-tuprints-278595

URL: <https://tuprints.ulb.tu-darmstadt.de/27859>

Jahr der Veröffentlichung auf TUPrints: 2024

Dieses Dokument wird bereitgestellt von tuprints,
E-Publishing-Service der TU Darmstadt
<https://tuprints.ulb.tu-darmstadt.de>
tuprints@ulb.tu-darmstadt.de

Die Veröffentlichung steht unter folgender Creative Commons Lizenz:

Namensnennung 4.0 International

<https://creativecommons.org/licenses/by/4.0/>

This work is licensed under a Creative Commons License:

Attribution 4.0 International

<https://creativecommons.org/licenses/by/4.0/>

For my sister, Bianca

Erklärungen laut Promotionsordnung

S 8 Abs. 1 lit. c PromO

Ich versichere hiermit, dass die elektronische Version meiner Dissertation mit der schriftlichen Version übereinstimmt.

S 8 Abs. 1 lit. d PromO

Ich versichere hiermit, dass zu einem vorherigen Zeitpunkt noch keine Promotion versucht wurde. In diesem Fall sind nähere Angaben über Zeitpunkt, Hochschule, Dissertationsthema und Ergebnis dieses Versuchs mitzuteilen.

S 9 Abs. 1 PromO

Ich versichere hiermit, dass die vorliegende Dissertation selbstständig und nur unter Verwendung der angegebenen Quellen verfasst wurde.

S 9 Abs. 2 PromO

Die Arbeit hat bisher noch nicht zu Prüfungszwecken gedient.

Darmstadt, 17.06.2024

I. Danhoni

Zusammenfassung

Quark-Gluon-Plasma (QGP) wird in Kollisionen mit niedriger Energie und einer hohen Netobaryonenzahl erzeugt. Folglich ist das baryochemische Potential μ_B mehrere Male höher als die Temperatur T . Dieses Regime kann nicht direkt auf dem Gitter untersucht werden, daher ist die Hochdichteregion des QCD-Phasendiagramms nicht so gut verstanden wie die ($\mu_B = 0$)-Achse. Bei hohen Temperaturen kann man behaupten, dass die Störungsreihe bei einem hohen chemischen Potential, also $\mu_B > T > T_c$, besser funktionieren sollte, als im Fall von $\mu_B = 0$ [41]. Aufgrund der stark gekoppelten Beschaffenheit von weichen Gluonen versagt die Störungstheorie in heißer QCD, bevor die Kopplung groß wird [62]. Bei hohem chemischen Potential wird jedoch die Streuung von Quarks um einen Faktor von μ_B^2/T^2 verstärkt, und man erwartet, dass sich die Störungsreihe besser verhält. Mit dieser Motivation untersuchen wir in dieser Arbeit den Einfluss chemischer Potentiale auf die QCD-Scherviskosität. Insbesondere erweitern wir die Arnold-Moore-Yaffe (AMY) Berechnungen für Scherviskosität bei führendem Logarithmus [13] in schwach gekoppelter, heißer und dichter QCD [41]. Anschließend führen wir auch eine Untersuchung der Scherviskosität mit mehreren erhaltenen Ladungen, nämlich Baryonenzahl (B), Strangeness (S) und elektrischer Ladung (C), unter Verwendung der führenden Logarithmusbehandlung durch. Danach erweitern wir die Hochdichteberechnungen auf die führende Störungsordnung, erstmals berechnet in [9] für verschwindende chemische Potentiale, und auf "fast" nächste führende Ordnung, basierend auf der Arbeit von Ghiglieri et al. [62]. Mit diesen Ergebnissen testen wir die Konvergenz der Störungsreihe. Schließlich untersuchen wir in einer ergänzenden Arbeit die lineare Antwortfunktion der Scherspannung und untersuchen das Vorhandensein eines Verzweigungsschnitts, der den Ursprung in einem System von selbstwechselwirkenden Skalarpartikeln mit quartischen Wechselwirkungen berührt.

Abstract

Quark-gluon plasma (QGP) is generated in lower-energy collisions with a high net baryon number. Consequently, the baryon chemical potential μ_B is several times higher than the temperature T . This regime cannot be directly studied on the lattice; therefore, the high-density region of the QCD phase diagram is not as well understood as the $\mu_B = 0$ axis. At high temperatures, one can claim that the perturbative series should work better at a high chemical potential, such that $\mu_B > T > T_c$, than in the case of $\mu_B = 0$ [41]. Due to the strongly coupled nature of soft gluons, perturbation theory fails in hot QCD before the coupling becomes large [62]. However, at high chemical potential, the scattering from quarks is enhanced by a factor of μ_B^2/T^2 , and one expects the perturbative series to behave better. With this motivation, we study the influence of chemical potentials on the QCD shear viscosity in this thesis. Namely, we extend the Arnold-Moore-Yaffe (AMY) calculations for shear viscosity at leading log [13] in weakly coupled high-temperature and dense QCD[41]. Following this, we also perform a study of shear viscosity with multiple conserved charges, baryonic (B), strangeness (S), and electric (C), using the leading log treatment. After that, we extend the high-density calculations to leading perturbative order, first calculated in [9] for vanishing chemical potentials, and to "almost" next to the leading order, based on the work from Ghiglieri et al. [62]. With these results, we test the convergence of the perturbative series. Finally, in a complementary work, we study the shear-stress linear response function and investigate the existence of a branch cut touching the origin in a system of scalar self-interacting particles with quartic interactions.

Contents

Introduction	3
1 Shear viscosity in heavy-ion collisions	5
2 Scope and Outline of this thesis	8
Hydrodynamics and Heavy-Ion Collisions	11
1 Relativistic hydrodynamics	12
2 Hydrodynamic description of heavy-ion collisions	15
3 Shear viscosity in QCD	17
Kinetic theory	21
1 The Schwinger–Keldysh Contour	22
2 Boltzmann equation for scalar theories	24
3 Boltzmann equation for gauge theories	29
4 Theoretical Framework	32
4.1 Variational solution	35
Shear viscosity at leading logarithmic order	39
1 Collision Integrals at Finite Chemical Potentials	39
1.1 Diagrams (A), (B) and (C)	42
1.2 Diagrams (D) and (E)	45
2 One-function ansatz calculations	48
3 The basis set	53
4 Results	54
Shear response function for a quartic self-interacting theory	59
1 Kinetic Theory and Hydrodynamics	60
2 Linear response theory for the shear-stress tensor	61
3 Numerical analysis	64
Phenomenological shear viscosity across the QCD phase diagram	69
1 Shear viscosity at leading logarithmic order for multiple conserved charges	70

2	Hadron resonance gas model and switching temperature	73
3	The phenomenological model	79
4	$\eta T/w$ for 3 conserved charges	83
Collision operator at leading order		89
1	Contributions from $2 \leftrightarrow 2$ scatterings	90
1.1	Fermion self-energy corrections	92
1.2	Gauge boson self-energy corrections	92
1.3	The parametrizations for s, t and u channels	94
2	Gluon emission in QGP	97
2.1	Gluon emission rate	97
2.2	Solving the integral equation for γ_{bc}^a	102
3	The high-density regime	105
4	Results	106
Next-to-Leading Order corrections		109
1	Soft gluon exchange	110
2	Collinear contributions	113
3	Semi-collinear contributions	116
4	The counterterms	118
5	Summary	122
6	Results	122
Discussion and Conclusions		127
1	Final results and conclusions	127
2	Summary and future prospects	133
Appendix		135
1	HTL at high chemical potential	135
2	Photon emission rate	136
3	Coupling prescription	142

Introduction

For the past decades, ultrarelativistic heavy-ion collisions have investigated the properties of the deconfined phase of hot and dense Quantum Chromodynamics (QCD), the quark-gluon plasma (QGP). Evidence shows that this phase was present in the early universe and has been recreated at microscopic scales in heavy ion collision experiments[69]. These results have sparked considerable interest in this subject for the past few decades, and experiments indicate that the QGP in such collisions is a strongly coupled fluid[7, 6, 1] and behaves closely to a perfect fluid[75, 102, 52]. The current theoretical modeling [57, 128, 134] of the early universe matter produced in heavy-ion collisions is broadly consistent with this picture, a nearly frictionless, strongly coupled quantum liquid over distance scales not much larger than the proton radius, which makes the QGP formed in colliders the hottest, smallest, densest, most perfect fluid known [114].

These ultrarelativistic heavy ion collisions aim, among other things, to recreate droplets of Big Bang matter in the laboratory. In such conditions, one can learn about the properties of QGP as well as about the QCD phase diagram in ways that would not be possible via observations made with telescopes or satellites. Figure 1 illustrates our current understanding of the features of the phase diagram of QCD as a function of temperature and baryon doping, which is the excess of quarks over antiquarks, parametrized by the baryonic chemical potential, μ_B [37]. A general framework for studying heavy-ion collisions typically involves initial state modeling, followed by a pre-equilibrium phase and subsequent hydrodynamic evolution, which is eventually integrated into hadronic transport [114]. This framework constitutes the core of the standard model of heavy-ion collisions [114, 135, 113]. Originally characterized by qualitative success, this theoretical framework has developed impressive predictive power and quantitative accuracy; this is usually demonstrated through applying Bayesian inference techniques[118].

However, many fundamental questions remain in our quest to understand heavy-ion collisions and the QGP. This is a consequence of the impossibility of performing ab initio real-time calculations in quantum chromodynamics beyond weak coupling. In that context, the investigation of small systems, such as proton-proton ($p+p$) and proton-nucleus ($p+A$) collisions have been significantly illuminating. This is because they require pushing the boundaries of our understanding of the bulk collective properties of the quark-gluon

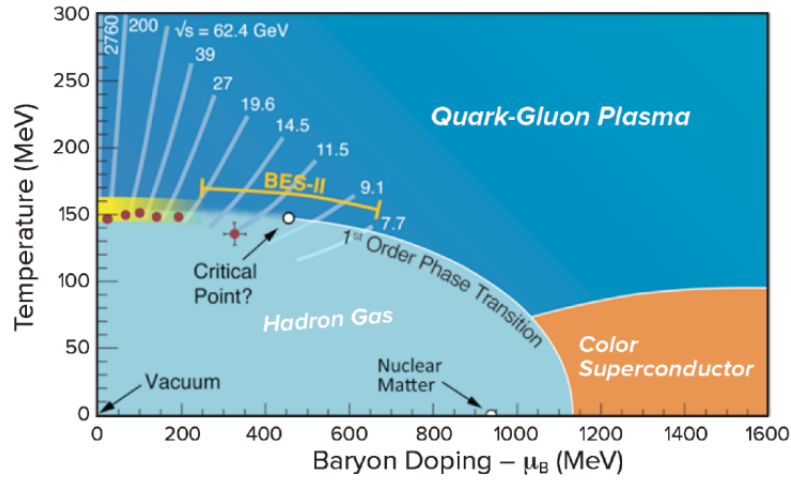


Figure 1: The QCD phase diagram. Here, the red circles mark the location of freeze-out points that were determined experimentally. The white lines indicate the trajectories followed by hydrodynamically expanding matter in the fireball. These trajectories are labeled by the initial collision energies $\sqrt{s_{NN}}$ in GeV. Image from ref. [50].

plasma[114].

Now, we shall present a qualitative picture of these collisions. For clarity, let us focus our description on a system in the center of mass frame (the "lab frame" at a collider). Each incident nucleus is a Lorentz-contracted disc. For large nuclei such as *Pb* or *Au*, the diameter of the disc is about 14 fm (femtometer, or Fermi) and its thickness is about $14/\gamma$ fm, where, at the highest beam energies attainable at RHIC and LHC, the relativistic γ factors are approximately 100 and 2500, respectively, corresponding to beam rapidities of $y = 5.3$ and 8.5 [114, 37].

Each nucleus is characterized by a density of quarks, antiquarks, and gluons, with $q\bar{q}$ pairs emerging from quantum fluctuations in the initial state. These fluctuations manifest as wave functions that become almost real due to the time dilation happening in the accelerated nucleus. These quarks and antiquarks serve as sources for strong, predominantly transverse color fields, giving rise to corresponding field quanta known as gluons, which also carry a color charge. The density of quarks, antiquarks, and gluons escalates with the velocity of the nuclei and exhibits non-uniformity across the nucleus surface, varying from one nucleus to another. The spatial distribution of partons primarily

mirrors the instantaneous distribution of nucleons within the nuclei and of partons within those nucleons. In essence, the incident nuclei represent intricate assemblies of partons with a longitudinal momentum distribution, often referred to as a structure-function. This momentum distribution closely resembles a superposition of those found within individual nucleons, with minor adjustments due to the proximity and motion of nucleons within the nuclei[37, 50].

As the two discs collide, most of the partons will lose some energy. However, most of these interactions are "soft", meaning that they involve little transverse momentum exchange. These strong interactions can be described in terms of interacting fields or layers of energy. Some color charge exchange occurs between the discs, and longitudinal color fields are produced, which fill the space between the two discs. Consequently, the energy in the discs is reduced, and these fields gradually decay into $q\bar{q}$ pairs and gluons[37, 50].

Upon closer examination of experimental observables, such as transverse momentum spectra, collective flows of charged hadrons, or electromagnetic probes, it becomes evident that their accurate estimation relies heavily on the transport parameters of the system. This serves as a strong motivation for the quantitative study of the transport coefficients of this medium, which is created while colliding two heavy ions ultra relativistically [37]. The transport coefficient under investigation in this thesis is shear viscosity, η .

1 Shear viscosity in heavy-ion collisions

Let us begin by defining shear viscosity in a simple system: a gas trapped between two plates. The plate at the top moves with a constant velocity u , and the lower plate is at rest. The distance between the two plates will be named L .

As the gas molecules are free, they will fly a typical distance λ before scattering with another molecule. This distance λ is called the mean free path of the molecule. In the center of the gas, molecules moving downward originated from higher levels, while those moving upward came from lower levels. Since molecules above this point tend to move forward, the downward-moving molecules also tend to move forward. However, the upward-moving molecules originate from a region with a slower forward velocity since the lower plate is not moving, making them less likely to move forward. Therefore, there is a correlation between transverse and vertical velocity in the medium[37, 109]. The particles that hit the bottom plate tend to move in the x direction, and therefore impart a force on that plate, as shown in fig.2. At the top, the opposite happens, upward-going particles are moving at a smaller velocity than the boundary plate, and this generates a net backward force. This force is proportional to the plate area A and to the velocity

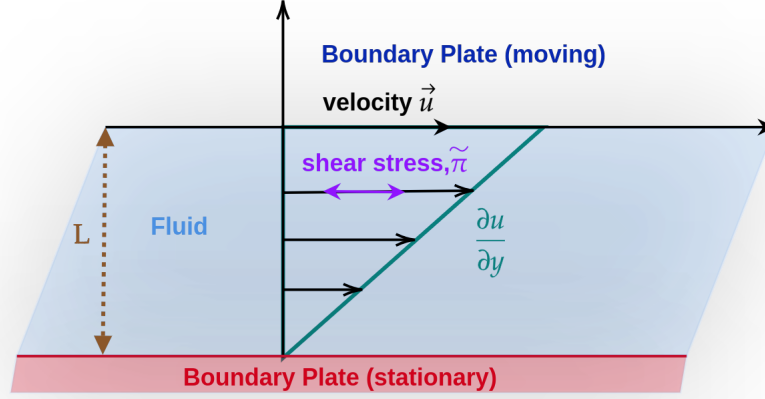


Figure 2: Schematically view of the fluid trapped between two plates.

gradient, given by u/L . The force can be written as

$$F = \eta \frac{Au}{L} \quad (1)$$

alternatively, one can define shear viscosity using the energy-stress tensor as,

$$T_{zx} = -\eta \partial_z u_x \quad (2)$$

In both expressions, η is a material-dependent coefficient. In heavy ion collisions, η is used to quantify the liquidness of the ultrarelativistic constituents. This is done by calculating the ratio η/s , where s is the entropy density. This ratio plays a central role in the equations of hydrodynamics, which governs the amount of entropy produced within the fluid as a sound wave propagates through it.

The nature of this state of matter is determined by two crucial features of QCD [37]. One is related to asymptotic freedom, and the high energies probed at RHIC and the LHC. The interactions between the quarks and gluons could be so weak that an equilibrium thermal state of matter would never be reached. On the other hand, QCD is strongly coupled at energy scales within an order of magnitude of the confinement/deconfinement energy scale. Consequently, in these high temperatures, QCD describes a relativistic fluid consisting of quarks and gluons so strongly coupled to their neighbors that the resulting

liquid cannot even be described using a quasiparticle formalism. The weak coupling picture is more likely to happen at early times in collisions with exceedingly high energy, and the strong coupling picture would become applicable after a hydrodynamic fluid is formed [37, 10].

In this thesis, we focus on the weakly coupled picture. Qualitatively, this picture can be understood using the same tools as in the case of weakly interacting gas of particles. As discussed at the beginning of this section, in this scenario, scatterings are rare, and the directions of the momenta of the gas particles are random. This means that the initial spatial anisotropy in the collision zone is washed out by random motion. Additionally, the azimuthal distribution of particles in the final state is isotropic [37]. In this scenario, a good description of the system can be done using kinetic theory, which consists of treating QGP as an interacting system of quasiparticles. This allows one to calculate transport coefficients purely theoretically[10].

Before hadronization, only full hydrodynamic simulations of the system can generate the sizable anisotropies found[37]. Hydrodynamics is a gradient expansion, assuming a fluid is everywhere close to thermal equilibrium but allowing for small gradients in both temperature and velocity. In ideal (0th order) hydrodynamics, these gradients are ignored, giving an isotropic plasma in the plasma's local rest frame by assumption. For viscous (first order) hydrodynamics, the gradients lead to an anisotropic stress tensor $T_{\mu\nu}$ according to [37],

$$T_{\mu\nu} = \epsilon u_\mu u_\nu + p[\epsilon]\Delta_{\mu\nu} - \eta[\epsilon]\sigma_{\mu\nu} - \zeta[\epsilon]\Delta_{\mu\nu}\nabla_\mu u^\mu + \mathcal{O}(\partial^2), \quad (3)$$

$$\sigma_{\mu\nu} = \Delta_{\mu\alpha}\Delta_{\nu\beta}(\nabla^\alpha u^\beta + \nabla^\beta u^\alpha) - \frac{2}{3}\Delta_{\mu\nu}\Delta_{\alpha\beta}\nabla^\alpha u^\beta, \quad (4)$$

$$\Delta_{\mu\nu} = g_{\mu\nu} + u_\mu u_\nu, \quad (5)$$

Here, ϵ is the energy density, and u_μ is the fluid velocity, which is given by $u_\mu = (1, 0, 0, 0)$ in the local fluid rest frame. The projector is given by $\Delta_{\mu\nu} = \text{diag}(0, 1, 1, 1)$. The first two terms in this equation represent ideal hydrodynamics, while the remaining terms are dissipative corrections. We will review hydrodynamics in more detail in Chapter 2.

Hydrodynamic evolution follows from the conservation of the stress-energy tensor, aligned with the equation of state, the transport coefficients, and the energy and velocity profiles at an initial time [37]. For a hot QCD, determining transport coefficients requires the system to be modeled away from equilibrium. Their determination can be done within two equivalent approaches, the correlator technique in QCD using the Green-Kubo formula and the semiclassical transport theory, e.g., Chapman-Enskog [109, 106]. In the hydrodynamic evolution equations, $\nabla_\mu T_{\mu\nu}$, the kinematic shear viscosity, given by the ratio $\eta/(\epsilon + P) = \eta/(Ts)$, is proportional to the length scale over which momentum can

be transported and describes the relaxation of this fluid. At weak coupling, when the hydrodynamic fluid is made up of quasiparticles with a well-defined mean free path λ_{mfp} , it can be shown that $\eta/(\epsilon + P) \propto \lambda_{mfp}$ [37]. Whether the fluid is weakly or strongly coupled, η/s controls how rapidly sound waves, shear stress, or gradients introduced in the initial conditions are dissipated into heat. Therefore, this quantity is constrained by comparing the hydrodynamic calculations of transport coefficients to data.

2 Scope and Outline of this thesis

In lower-energy collisions, quark-gluon plasma is generated with a significant net baryon number, such that the baryon chemical potential μ_B is several times higher than the temperature. This regime cannot be directly studied on the lattice due to the sign problem (or complex action problem). For a chemical potential $\mu_B \neq 0$, the fermion determinant (or Monte Carlo action) becomes complex, which ruins the probabilistic interpretation of this quantity used in lattice QCD calculations[67]. For this reason, the high-density region of the QCD phase diagram is much less well understood than the $\mu_B = 0$ axis. As experimental efforts focus on bringing clarity to this region, such as RHIC-BES [5], HADES[4] and FAIR[55], the need for parallel theoretical development becomes clear.

At high temperatures, we claim that the perturbative series should work better at a high chemical potential, such that $\mu_B > T > T_c$, than in the case of $\mu_B = 0$ [41]. This is a consequence of the fact that scattering from quarks is enhanced by a factor of μ_B^2/T^2 . Due to the strongly coupled nature of soft gluons, perturbation theory fails in hot QCD before the coupling becomes large. These play a central role in the breakdown of the perturbative expansion for the shear viscosity [62]. However, when quarks play a more significant role at high chemical potential, one expects the perturbative series to behave better. This motivates using a kinetic theory treatment to study transport coefficients in a regime of high density and high temperature.

Previously, Arnold, Moore, and Yaffe have computed the shear viscosity at leading perturbative order in the absence of a chemical potential [9], and Ghiglieri et al have extended this calculation to “almost” next-to-leading order [62]. Separately, we have presented the shear viscosity at finite chemical potential at leading-log order [41]. Finally, we have extended these calculations to “almost” next-to-leading order [62]. This thesis will focus on shear viscosity in QCD, particularly in high-temperature and high-density scenarios.

This thesis is organized as follows. In Chapter 2, we start with a review of relativistic hydrodynamics and an exposition on the dynamics of heavy-ion collisions. We delve into the interplay between relativistic hydrodynamics and the dynamics of heavy-ion collisions,

laying the groundwork for subsequent discussions along this thesis. By the end of this chapter, we discuss shear viscosity in the context of QCD and heavy-ion collisions.

Chapter 3 delves into kinetic theory within the context of QGP. Here, we derive the Boltzmann equation for both abelian and non-abelian theories, which will be extensively used in the following chapters. Additionally, we present an exposition of the theoretical framework employed for the calculations conducted in this thesis and introduce the variational method used to solve the Boltzmann equation in the calculations performed in this work.

Finally, Chapter 4.1 introduces the collision operator and computes shear viscosity at leading logarithmic order on the coupling for high densities. We also discuss a basis set to be used for solving the Boltzmann equation. The results from this chapter were published in 2023 [41]. In Chapter 4, using an analytical result for the eigensystem of the linearized collision term for a classical system of massless scalar particles with quartic self-interactions, we show that the shear-stress linear response function possesses a branch-cut singularity that covers the whole positive imaginary semi-axis. This is demonstrated by truncating the exact, infinite linear system of linear equations for the rank-two tensor modes, which reveals the cut touching the origin. This work results from my collaboration with G. Rocha, K. Ingles, G. Denicol, and J. Noronha [125].

Then, in Chapter 3, we extend our analyses to accommodate multiple conserved charges. We compute shear viscosity for a QGP with three conserved charges: baryonic, strangeness, and electric. Our aim in this chapter will be to map shear viscosity along the QCD phase diagram. For that, we introduce a hadron resonance gas (HRG) description used in the region below the phase transition and a simple interpolation method for connecting the two regions. This work was done in collaboration with J. Noronha-Hostler and J. Salinas San Martin [39].

Chapter 4 describes the computation of shear viscosity at leading order on the coupling. We begin by elucidating the relevant scattering diagrams and detailing the methodology for computing the splitting contribution. Chapter 4 addresses the crucial corrections required to compute shear viscosity at (almost) the next-to-leading order. Here, we present the necessary adjustments and comment on the high-density regime. In the end, we present our results and a comparison with leading order calculations, which allows us to check the convergence of the perturbative series. Finally, in Chapter 9, we provide a comprehensive analysis and synthesize our findings. This chapter discusses the implications of our results and identifies potential avenues for future research.

Hydrodynamics and Heavy-Ion Collisions

In this chapter, we will discuss the evolution of a system with time, which can be addressed as transport phenomena. This evolution can be encoded using the so-called transport coefficients, such as shear viscosity, bulk viscosity, and diffusion. The most general approach to studying transport phenomena in strongly coupled fluids is hydrodynamics [141, 132]. This approach is based on the observation that the evolution of conserved charges governs correlation functions at low energy and small momentum. Additionally, the conservation laws imply that the densities of conserved charges cannot relax locally; instead, they must propagate or diffuse over significant distances. This phenomenon is reflected in hydrodynamic excitations characterized by dispersion relations such as $\omega \sim q$ (sound) or $\omega \sim iq^2$ (diffusion)[132]. Namely, in the surrounding area of each point in space, we define an infinitesimal volume, which is called a fluid element, in which the matter is taken to be homogeneous, i.e., any spatial gradients can be neglected and are described by a finite set of thermodynamic variables and currents [106].

The application of hydrodynamics requires a system to be describable as a fluid. This means that it is a continuous system in which every infinitesimal volume element is assumed to be close to thermodynamic equilibrium throughout its evolution. Therefore, each fluid element must be large enough, in comparison to the microscopic length scales, to guarantee that the system is close to thermodynamic equilibrium and, at the same time, be small enough, relative to the macroscopic length scales, to ensure the continuum limit[43]. One way to quantify the frequency of interactions, which in this case are just collisions, is by comparing the mean-free path, λ , the average distance a particle travels between collisions to the size, L , of the medium. The mean free path is defined as[132, 143]

$$\lambda = \frac{1}{\rho\sigma} \tag{1}$$

where ρ is the density of the medium and σ is the interaction cross section.

The leading order theory of hydrodynamics, called ideal hydrodynamics, only depends on the equation of state and is exactly time-reversible. The next-order theory, (first order) viscous hydrodynamics, involves a new set of parameters called transport coefficients and describes dissipative, time-irreversible phenomena[143]. Determining transport coeffi-

icients involves experimental measurements or computations derived from an underlying field theory. The connection between transport coefficients and correlation functions in a (quantum) field theory is provided by linear response theory. Using linear response theory, one can link transport coefficients to the limit of zero energy and zero momentum of a retarded correlation function, known as the Kubo relations[132]. Calculations based on the Kubo formula are difficult, particularly if the interaction is not weak. The situation simplifies if the system allows a microscopic description in terms of quasi-particles. In such cases, an intermediate effective theory called kinetic theory can be employed to relate the microscopic Lagrangian to the hydrodynamic description. Additionally, kinetic theory offers a more detailed criterion for assessing the applicability of hydrodynamics at a microscopic level[132]. A detailed description of Kinetic Theory will be provided in Chapter 3.

1 Relativistic hydrodynamics

In this section, we explore the fundamentals of relativistic hydrodynamics, a critical framework for understanding the behavior of matter under extreme conditions. We present important definitions of relativistic hydrodynamics and review the concepts necessary for the understanding of this thesis. In a relativistic fluid, the equations of energy and momentum conservation can be written as a single equation[141, 132, 43, 143]

$$\partial_\mu T^{\mu\nu} = 0, \quad (2)$$

Here, $T^{\mu\nu}$ is the energy-momentum tensor. In ideal fluid dynamics, the structure of $T_{\mu\nu}$ is entirely determined by Lorentz invariance,

$$T^{\mu\nu} = (\epsilon + P)u^\mu u^\nu + P\eta^{\mu\nu}, \quad (3)$$

where u^μ is the fluid velocity ($u^2 = -1$) and $\eta^{\mu\nu} = \text{diag}(-1, 1, 1, 1)$ is the metric tensor. A second hydrodynamic equation then gives the conservation of particle number,

$$\partial_\mu (n u^\mu) = 0, \quad (4)$$

where n is the particle density. The hydrodynamic equations must be supplemented by an equation of state $P = P(\epsilon)$ or $P = P(\epsilon, n)$. The four equations given in equ. (2) can be split into two sets using the longitudinal and transverse projectors

$$\Delta_{\mu\nu}^{\parallel} = -u_\mu u_\nu, \quad \Delta_{\mu\nu} = g_{\mu\nu} + u_\mu u_\nu. \quad (5)$$

With the help of thermodynamic relations,

$$d\epsilon = T ds \quad (6)$$

and

$$\epsilon + P = sT, \quad (7)$$

the longitudinal equation can be identified as equivalent to entropy conservation,

$$\partial_\mu (su^\mu) = 0, \quad (8)$$

while the transverse equation can be identified as the relativistic Euler equation

$$Du_\mu = -\frac{1}{\epsilon + P} \nabla_\mu^\perp P, \quad (9)$$

where $D = u \cdot \partial$ and $\nabla_\mu^\perp = \Delta_{\mu\nu} \partial^\nu$. From this relation, one can conclude that the inertia of a relativistic fluid is governed by $\epsilon + P$, the enthalpy of the fluid, also named as ω .

The form of the dissipative terms depends on the precise definition of the fluid velocity [132]. The most usual choice of frame is the Landau frame [132, 99], which simply means defining u^μ by the requirement that in the local rest frame $T^{00} = \epsilon$ and $T^{0i} = 0$. In this frame, the dissipative correction to the energy-momentum tensor in the rest frame has the same form as in the non-relativistic case, given by,

$$\delta\Pi_{ij} = -\eta \left(\nabla_i v_j - \nabla_j v_i - \frac{2}{3} \delta_{ij} \nabla \cdot \mathbf{v} \right) - \zeta \delta_{ij} (\nabla \cdot \mathbf{v}). \quad (10)$$

Here, we write the stress tensor as

$$T^{\mu\nu} = T_0^{\mu\nu} + \delta^{(1)}T^{\mu\nu} + \delta^{(2)}T^{\mu\nu} + \dots, \quad (11)$$

where $T_0^{\mu\nu}$ is the stress tensor of the ideal fluid given by,

$$T^{\mu\nu} = (\epsilon + P)u^\mu u^\nu + P g^{\mu\nu}, \quad (12)$$

$\delta^{(1)}T^{\mu\nu}$ is the first-order viscous correction, and $\delta^{(2)}T^{\mu\nu}$ is the second, and so on. A covariant expression for $\delta^{(1)}T^{\mu\nu}$ is

$$\delta^{(1)}T^{\mu\nu} = -\eta \sigma^{\mu\nu} - \zeta \Delta^{\mu\nu} \partial \cdot u \quad (13)$$

where we have defined

$$\sigma^{\mu\nu} = \Delta^{\mu\alpha} \Delta^{\nu\beta} \left(\partial_\alpha u_\beta + \partial_\beta u_\alpha - \frac{2}{3} \eta_{\alpha\beta} \partial \cdot u \right). \quad (14)$$

The dissipative correction to the conserved particle current is $j_\mu = nu_\mu + \delta j_\mu$ with

$$\delta^{(1)}j_\mu = -\kappa \left(\frac{nT}{\epsilon + P} \right)^2 \Delta_\mu^\perp \left(\frac{\mu}{T} \right), \quad (15)$$

where κ is the thermal conductivity and μ is the chemical potential, associated with the conserved density n . Alternatively, one can define the velocity via the conserved particle current, called the Eckart frame. In that case, there is no dissipative contribution to j_μ , and the thermal conductivity appears in the stress tensor [132].

As is well known, in viscous relativistic hydrodynamics, there is a problem with causality in the equations of motion. This issue is evident in the linearized equation for the diffusive shear mode, where discontinuities in initial conditions can propagate infinitely fast. While these modes are beyond the scope of hydrodynamics, their acausal nature makes numerical implementations more complicated. To overcome these issues, one can include second-order gradient corrections in the stress tensor, which results in the so-called second-order viscous hydrodynamics. One can show that for physically reasonable ranges of the second-order coefficients, the theory is causal [127]. In general, there are a large number of second-order terms [20]. Conformal symmetry implies that $\zeta = 0$ and $\delta^{(1)}T_{\mu\nu} = -\eta\sigma_{\mu\nu}$. The second order correction is

$$\begin{aligned} \delta^{(2)}T^{\mu\nu} = & \eta\tau_{II} \left[\langle D\sigma^{\mu\nu} \rangle + \frac{1}{3}\sigma^{\mu\nu}(\partial \cdot u) \right] \\ & + \lambda_1\sigma^{\langle\mu}{}_\lambda\sigma^{\nu\rangle\lambda} + \lambda_2\sigma^{\langle\mu}{}_\lambda\Omega^{\nu\rangle\lambda} + \lambda_3\Omega^{\langle\mu}{}_\lambda\Omega^{\nu\rangle\lambda}, \end{aligned} \quad (16)$$

where $\sigma^{\mu\nu}$ is the first order shear tensor defined above,

$$A^{\langle\mu\nu\rangle} = \frac{1}{2}\Delta^{\mu\alpha}\Delta^{\nu\beta} \left(A_{\alpha\beta} + A_{\beta\alpha} - \frac{2}{3}\Delta^{\mu\nu}\Delta^{\alpha\beta}A_{\alpha\beta} \right) \quad (17)$$

denotes the transverse traceless part of $A^{\alpha\beta}$ and

$$\Omega^{\mu\nu} = \frac{1}{2}\Delta^{\mu\alpha}\Delta^{\nu\beta} (\partial_\alpha u_\beta - \partial_\beta u_\alpha) \quad (18)$$

is the vorticity. The coefficients τ_{II} and $\lambda_{1,2,3}$ can be determined using kinetic theory [148] or the AdS/CFT correspondence [20, 29].

Equation (16) is a constitutive relation that determines the stress tensor in terms of thermodynamic variables. To obtain the equations of motion, one can use the Israel and Stewart approach [81]. This approach works by promoting $\pi^{\mu\nu} = \delta T^{\mu\nu}$ to a hydrodynamic

variable. The equation of motion for $\pi^{\mu\nu}$ is then given by

$$\begin{aligned} \pi^{\mu\nu} = & -\eta\sigma^{\mu\nu} - \tau_{II} \left[\langle D\pi^{\mu\nu} \rangle + \frac{4}{3} \pi^{\mu\nu} (\partial \cdot u) \right] \\ & + \frac{\lambda_1}{\eta^2} \pi^{\langle\mu}{}_{\lambda} \pi^{\nu\rangle\lambda} - \frac{\lambda_2}{\eta} \pi^{\langle\mu}{}_{\lambda} \Omega^{\nu\rangle\lambda} + \lambda_3 \Omega^{\langle\mu}{}_{\lambda} \Omega^{\nu\rangle\lambda}, \end{aligned} \quad (19)$$

This equation describes the relaxation of $\pi^{\mu\nu}$ to the Navier-Stokes form $-\eta\sigma^{\mu\nu}$. Several more phenomenological approaches include some subset of higher order terms, for example, the already mentioned Israel-Stewart formalism [81] or the equations of Lindblom and Geroch [59]. We note that whatever formalism is used, a necessary condition for the applicability of second-order hydrodynamics is that higher order corrections are small, $\delta^{(2)}T^{\mu\nu} \ll \delta^{(1)}T^{\mu\nu} \ll T^{\mu\nu}$ [141, 132]. Next, we apply the hydrodynamic equations to the context of heavy-ion collisions.

2 Hydrodynamic description of heavy-ion collisions

Relativistic fluid dynamics has successfully explained the various collective phenomena observed in astrophysics, cosmology, and the physics of high-energy heavy-ion collisions. The collective behavior of the hot and dense quark-gluon plasma created in ultra-relativistic heavy-ion collisions has been studied extensively within the relativistic fluid dynamics framework. However, all fluids are dissipative due to the quantum mechanical uncertainty principle [34]. Unfortunately, the relativistic dissipative fluid dynamics theory is not yet conclusively established [84]. Therefore, here we describe a generic implementation of viscous hydrodynamics applied to heavy-ion physics based in [141].

The implementation depends on several steps. The energy and flow velocities are specified at initial times, which we name as τ_o . There is some arbitrariness in initializing the hydrodynamic fields at a time $\tau_o \approx 1 fm/c$. Fortunately, in kinetic theory and hydrodynamics, the final results are not particularly sensitive to this value [83, 103]. One commonly used model for initial conditions is the Glauber model, which gives for the energy density,

$$e(\tau_o, \mathbf{x}_{\perp}) \propto \frac{dN_{\text{coll}}}{dx dy} \quad (20)$$

where the overall constant in this expression is adjusted to reproduce the multiplicity of particles in the event. Here, x and y are the coordinates in space, and \mathbf{x}_{\perp} is the transverse vector of coordinates. The simulations assume Bjorken boost invariance with the ansatz [141]

$$e(\tau, \mathbf{x}_{\perp}, \eta) \equiv e(\tau, \mathbf{x}_{\perp}) \quad (21)$$

$$u^\mu(\tau, \mathbf{x}_\perp, \eta) = (u^\tau, u^x, u^y, u^\eta) = (u^\tau(\tau, \mathbf{x}_\perp), u^x(\tau, \mathbf{x}_\perp), u^y(\tau, \mathbf{x}_\perp), 0) \quad (22)$$

These calculations typically assume that at initial time τ_o the transverse flow velocity is zero, which translates to,

$$u^x(\tau_o, \mathbf{x}_\perp) = u^y(\tau_o, \mathbf{x}_\perp) = 0, u^\tau(\tau_o, \mathbf{x}_\perp) = 1 \quad (23)$$

The strains are taken from the Navier-Stokes theory, and reflect the traceless character of shear stress [141]. This is exemplified by the expression below,

$$\pi^{\mu\nu}(\tau_o, \mathbf{x}_\perp) = \text{diag}(\pi^{\tau\tau}, \pi^{xx}, \pi^{yy}, \tau^2 \pi^{\eta\eta}) = \left(0, \frac{2\eta}{3\tau}, \frac{2\eta}{3\tau}, -\frac{4\eta}{3\tau}\right). \quad (24)$$

With these initial conditions, one can solve the equations of motion. In these equations, shear viscosity affects the hydrodynamic variables, modifying T and u^μ , and the off-diagonal components of the stress tensor through the viscous corrections $\pi^{\mu\nu}$. The magnitude of the viscous corrections depends on the size of the system and the shear viscosity.

Later, the colliding ions start to cool down. At this point, a "freezeout" condition can be imposed. This is done by specifying a freezeout temperature or a kinetic condition, depending on the freezeout model used. During the time evolution, a freezeout surface is constructed. For instance, the freezeout surface can be the space-time three volume Σ where $T_{fo} \simeq 150 \text{ MeV}$ [51].

Finally, particle spectra are computed by matching the hydrodynamic theory onto kinetic theory to compare with experimental data. Specifically, on the freezeout surface final particle spectra are computed using [141]

$$E \frac{dN^a}{d^3\mathbf{p}} = \frac{d_a}{(2\pi)^3} \int_\Sigma d\Sigma_\mu P^\mu f^a(-P \cdot u/T) \quad (25)$$

where a labels the particle species, the distribution function is,

$$f^a(-P \cdot u) = f^a(-P \cdot u/T) + \delta f^a(-P \cdot u/T) \quad (26)$$

Moreover, d_a labels the spin-isospin degeneracy factor for each particle included. The "freezeout" procedure is taken to be equivalent to running the hydro up to a particular proper time τ_f or temperature T_f and declaring that the thermal spectrum of particles at that moment are the measured particle spectrum [141].

In the hydrodynamic regime, the only properties that determine the evolution of the system is the equation of state, which can be characterized by $P(e)$, and the shear viscosity and bulk viscosities, $\eta(e)$ and $\zeta(e)$. In the sense that kinetic theory provides a reasonable guess as to how the surface-to-volume ratio influences the forward evolution; these models can be used to estimate the shear viscosity, which might be more reliable than the hydrodynamic models.

3 Shear viscosity in QCD

Viscosity significantly influences the evolution of real systems. In the context of the Quark-Gluon Plasma (QGP), particularly in heavy ion collisions, viscosity plays a crucial role in shaping the hydrodynamic evolution of the system [132, 141]. It might also be important in neutron star mergers [2]. This section reviews concepts related to shear viscosity in the hadronic and the QGP cases.

The shear viscosity, η , is defined as a linearization about equilibrium. First, we assume that the gradients of velocity, $\partial_i v_j$, are small; typically, this implies that the resulting stress tensor T_{ij} is significantly smaller than the pressure[109]. Also, we assume a hierarchy in which $\lambda \partial_i v_j \ll \lambda^2 \partial_i \partial_j v_k$, which means that the gradients do not change rapidly. The fluid flow, $\partial_i u_j$, is itself related to the stress tensor T_{ij} . For instance, in a system in perfect equilibrium, nonvanishing $\partial_i u_j$ can be generated by distorting the metric, represented by $g_{\mu\nu} = \eta_{\mu\nu} + h_{\mu\nu}$. In the path integral framework, this distortion arises from an interaction Hamiltonian $H_I = h_{\mu\nu} T^{\mu\nu}$ [109]. Following this idea, as discussed in [112], one can derive a Kubo relation for the shear viscosity in terms of equilibrium, unequal time, retarded correlation functions[112, 109]:

$$\eta = i \partial_\omega \int d^3x \int_0^\infty dt e^{i\omega t} \left\langle \left[T^{xy}(x, t), T^{xy}(0, 0) \right] \right\rangle \Big|_{\omega=0}, \quad (27)$$

where $T^{xy}(x, t)$ denotes the traceless part of the stress tensor. In the QGP phase, well above the first-order transition, the QCD medium can be described as a phase of massless quarks and gluons. The energy density is approximately described by the Stefan-Boltzmann equation of state [132]

$$e_{glue} = d_{glue} \int \frac{d^3\mathbf{p}}{(2\pi)^3} \frac{E_{\mathbf{p}}}{e^{E_{\mathbf{p}}/T} - 1} \quad e_{quark} = d_{quark} \int \frac{d^3\mathbf{p}}{(2\pi)^3} \frac{E_{\mathbf{p}}}{e^{E_{\mathbf{p}}/T} + 1} \quad (28)$$

where $d_{glue} = 2 \times 8$ counts spin and color, and $d_{quark} = 2 \times 2 \times 3 \times 3$ counts spin, anti-quarks, flavor, and color. Here $E_{\mathbf{p}}$ is the energy of each particle.

In contrast, well below the phase transition, the correct description is a gas of hadrons. This gas is very dilute, and the measured particle spectrum dominates the thermodynamics. For instance, the number of pions in this low-temperature regime is[132]

$$n_\pi = d_\pi \int \frac{d^3\mathbf{p}}{(2\pi)^3} \frac{1}{e^{E_{\mathbf{p}}/T} - 1} \quad (29)$$

where $E_{\mathbf{p}} = \sqrt{p^2 + m_\pi^2}$ and $d_\pi = 3$ counts the three-fold isospin degeneracy, π^+ , π^- , π^0 , in the spectrum. If all known particles are included up to a mass $m_{res} < 2.5 \text{ GeV}$,

the resulting Hadron Resonance Gas (HRG) equation of state does a reasonable job of reproducing the thermodynamics up to about $T \simeq 180 \text{ MeV}$. However, the validity of the quasi-particle description is unclear above a temperature of $T \simeq 140 \text{ MeV}$ [82, 115]. As the temperature increases, the hadron wave functions overlap until the medium reorganizes into quark and gluon degrees of freedom [141]. While lattice QCD simulations have provided a thorough understanding of the equation of state near the phase transition, determining the transport coefficients is equally essential since shear and bulk viscosities govern energy and momentum transport.

An interesting way to understand the influence of shear viscosity in a system is to write a shear viscosity to entropy ratio, η/s , which is the ratio between the medium relaxation time and the quantum time scale, as discussed earlier. For now, we use kinetic theory in a simplified way to calculate this ratio by considering a simple classical massless gas with particle density n and a constant hard sphere cross-section σ_o [141]. The equation of state of this gas is $e = 3\mathcal{P} = 3nT$ and the shear viscosity is [147, 141]

$$\eta \simeq 1.2 \frac{T}{\sigma_o} \quad (30)$$

Here, N_c is the color number. The entropy is $s = (e + \mathcal{P})/T$ and the resulting shear to entropy ratio is

$$\frac{\eta}{s} \simeq 0.3 \frac{T}{n\sigma_o} \quad (31)$$

This expression estimates the transport time in “natural units”, as the ratio is dimensionless.

At asymptotically high temperatures, the coupling constant α_s becomes weak, allowing for the computation of shear viscosity using perturbation theory. Initially, these calculations considered contributions from only $2 \rightarrow 2$ elastic scattering, and the shear viscosity was computed at leading logarithmic order with self-consistent screening [21]. Later, it was recognized [18, 17] that collinear Bremsstrahlung processes are also relevant for the calculation of shear viscosity at leading order on the coupling, which resulted in a complete, leading order calculation [9]. The ratio of shear viscosity to entropy density, η/s , can be estimated in the perturbative plasma context using Eq. (30), where $s \propto T^3$ and $\sigma \propto \alpha_s^2/T^2$ [141],

$$\frac{\eta}{s} \sim \frac{1}{\alpha_s^2} \quad (32)$$

The final result can be written as

$$\frac{\eta}{s} = \frac{1}{\alpha_s^2} F(m_D/T) \quad (33)$$

where $F(m_D/T)$ is a function of the Debye mass, which was first computed for small values of m_D/T and then extrapolated to more realistic values[9] and is related to the screening effects. Determining the appropriate values for the Debye mass and the coupling constant presents a challenge due to the multiple scales in the problem. At the lowest order in the coupling, the Debye mass is given by[24]

$$m_D^2 = \left(\frac{N_c}{3} + \frac{N_f}{6} \right) g^2 T^2 \quad (34)$$

All calculations around the phase transition region have a great deal of uncertainty. On the hadronic side, there is a relevant contribution from inelastic processes. On the other hand, in the quark-gluon plasma regime, the strong dependence on the Debye scale and the constant coupling is troubling. Hence, it is essential to have a strongly coupled theory where the shear viscosity to entropy ratio can be computed exactly. In the context of strongly coupled $\mathbf{N} = 4$ SYM theory with a large number of colors, η/s can be computed using gauge gravity duality and yields the result[122, 94]

$$\frac{\eta}{s} = \frac{1}{4\pi} \quad (35)$$

From the perspective of heavy ion physics, this result holds significant importance as it demonstrates the existence of field theories where η/s can be surprisingly low. In the next chapter, we shall review kinetic theory in the context of QCD and show how to derive shear viscosity purely theoretically using perturbative QCD to compute the contributing scatterings.

Kinetic theory

The scope of hot, weakly coupled, ultra-relativistic gauge theories includes various spatial and temporal scales. Depending on the regime considered, several methods are available for capturing the physics across these different scales. These methods include but are not limited to, perturbation theory, hard thermal loops, dimensional reduction, kinetic theory, and hydrodynamics. For static properties of the deconfined phase of QCD, the hierarchy of effective theories relevant to different distance scales is well-established [15, 33, 53]. However, when it comes to real-time properties and the study of non-equilibrium responses, deriving an appropriate sequence of effective theories to disentangle the dynamics across distance or time scales is challenging [15, 14]. This challenge can be exemplified by the confusion surrounding the time scale for non-perturbatively large fluctuations in gauge fields, such as those involved in baryon number violation in electroweak theory. Understanding the hierarchy of effective theories for different time scales is important to unravel the real-time dynamics of hot gauge theories.

In the context of kinetic theory, the significance of the effect of interactions becomes relevant, particularly at late times when simple perturbation theory becomes ineffective. There are essentially two ways of understanding this matter. First, let us consider a diagrammatic approach. For extended periods, contributions comparable in magnitude to the lowest-order diagram can emerge from an infinite series of ladder-like diagrams containing nearly on-shell singularities [15]. Summing these diagrams yields the same outcome from an effective kinetic theory description. Next, we discuss currents induced by the fluctuations in plasma. Consider a region in space significantly larger than the inter-particle separation at time zero; if a few more positively charged particles happen to move leftward rather than rightward, and vice versa for negatively charged particles, a net current $j(0)$ forms towards the left. As time elapses, collisions gradually randomize the particle directions, leading to the decay of the net current and the correlation $\langle j(t)j(0) \rangle$ approaching zero. To study the impact of these interactions, shifting focus from quantum field theory to kinetic theory for times significantly larger than $1/T$ [15] is significantly more interesting.

Kinetic theory applies to time scales and distances that are much larger than particle energies and momenta. Moreover, its validity relies on the de Broglie wavelengths and

scattering time scale being significantly smaller than the mean free path and mean free time between collisions. This condition ensures that particles can be treated as propagating classically, with on-shell energies, between collisions, regarded as independent and uncorrelated events[15]. In this chapter, we present the derivation of the Boltzmann equation, which will be sufficient to describe the quasi-particle system we are interested in and correctly compute transport coefficients as shear viscosity. For that, we begin with the essential tools necessary for this derivation, building up from scalar theories to abelian gauge theories and, finally, non-abelian gauge theories, like QCD. Later, we describe the theoretical framework to be used to obtain shear viscosity for QCD at vanishing and nonvanishing chemical potential. Finally, we present a variational method to solve the Boltzmann equation.

1 The Schwinger–Keldysh Contour

This section briefly introduces the Schwinger–Keldysh (SK) formalism, which is instrumental in the kinetic theory description of a hot-dense plasma. The SK formalism is very similar to ordinary equilibrium theory, except that all time-dependent functions are defined for time-arguments on a contour[100], known as the Schwinger–Keldysh contour (illustrated in Fig. 1). This contour is designed with a forward branch (upper part) that goes from $t = -\infty$ all the way to $t = +\infty$, and a backward branch (lower part) that goes from $t = +\infty$ to $t = -\infty$.

This formalism offers a framework to characterize nonequilibrium dynamics based only on the initial equilibrium state and is convenient in the study of time-dependent phenomena with an initial density matrix other than the vacuum. This is because, given a known density matrix of the full system at some finite time t_0 , it can be treated as initial conditions for the evolution. Besides, details of how the system evolves in time with all operator insertions are not necessary for finite-time computations[70].

Let us assume that we are interested in a system isolated for $t < 0$, which means that the Hamiltonian does not depend on time, and we can write $H_0(t < 0) = H_0$. Later in time, this system is disturbed by an external time-dependent field at $t > 0$ [100]. Using the SK-evolution operator, we can obtain the interesting Green’s Functions without assuming the system’s final state at late times; we simply revert to the initial state following the influence of interactions on the system [70]. The SK-evolution operator guides the system’s evolution along the complex time contour C explained here. A well-defined time ordering is necessary since we are interested in time-dependent phenomena. Consequently, it is often advantageous to work with fields and operators labeled by the segment of the contour they occupy. To illustrate, let us consider a complex (bosonic) operator \hat{O} . The

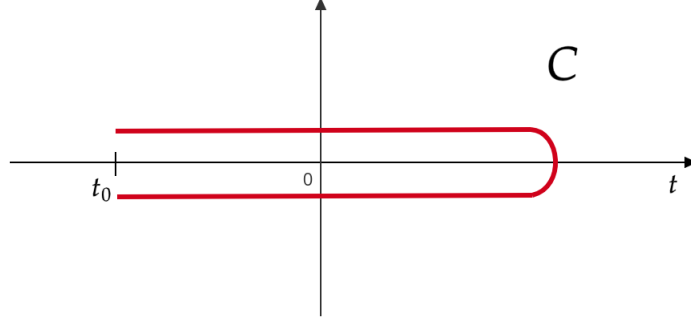


Figure 1: Schwinger-Keldysh closed-time-path contour.

Green's function for this operator on the SK contour is expressed as[70]:

$$G_C(x, y) = -i\langle\Omega|\mathcal{T}_c(\hat{\mathcal{O}}(x)\hat{\mathcal{O}}^\dagger(y))|\Omega\rangle = -i\langle 0|\mathcal{T}_c(U_C\hat{\mathcal{O}}(x)\hat{\mathcal{O}}^\dagger(y))|0\rangle \quad (1)$$

where U_C is the evolution operator in the contour, written as,

$$U_C \equiv \mathcal{T}_C \exp\left(-i \int_C dt' \hat{H}_{int}(t')\right), \quad (2)$$

where \mathcal{T}_C is the time-ordering operator that rearranges the operators in chronological order. Here, there is no need for a normalizing denominator since $U_C|0\rangle = |0\rangle$, and the operator does not acquire a phase. This contour approach is sufficient for deriving the Green's function for such a system. Considering x and y can reside on either the upper or lower part of the contour, so it becomes evident that we should have a 2×2 matrix of real-time Green's functions, corresponding to the choice of operator insertions on either segment. Thus, we define:

$$G_C(x, y) = \begin{pmatrix} G_F(x, y) & G_<(x, y) \\ G_>(x, y) & G_{\bar{F}}(x, y) \end{pmatrix} \quad (3)$$

where the Green's functions in this matrix are defined based on the contour positions. Here, $G_F(x, y)$ represents the Feynman propagator, and $G_{\bar{F}}(x, y)$ the anti-time-ordering

Feynman propagator. These functions are defined as follows[70],

$$iG_F(x, y) = \langle \Omega | \mathcal{T}_C(\hat{O}(x)\hat{O}^\dagger(y)) | \Omega \rangle \quad (4)$$

$$iG_{\bar{F}}(x, y) = \langle \Omega | \tilde{\mathcal{T}}_C(\hat{O}(x)\hat{O}^\dagger(y)) | \Omega \rangle \quad (5)$$

$$iG_>(x, y) = \langle \Omega | \hat{O}(x)\hat{O}^\dagger(y) | \Omega \rangle \quad (6)$$

$$iG_<(x, y) = \langle \Omega | \hat{O}(y)\hat{O}^\dagger(x) | \Omega \rangle \quad (7)$$

$$(8)$$

where $\tilde{\mathcal{T}}$ is anti-time-ordering. With these definitions, one can start working on the Boltzmann equation.

In the upcoming section, we use the SK contour to derive the Boltzmann equation within the framework of scalar theories. Although QCD is not a scalar theory, we leverage this result to subsequently derive the Boltzmann equation for non-abelian theories. We build upon the methodology outlined in multi-component scalar theories and QED.

2 Boltzmann equation for scalar theories

In this section, we delve into the derivation of the Boltzmann equation within the framework of scalar theories. Although our ultimate goal is to apply this equation to QCD, we initiate by focusing on scalar theories. This approach allows us to establish fundamental concepts and a derivation method that we can extend to more complex theories later. We will follow the derivation carried out in [14].

We start by considering a single-component scalar ϕ^4 theory. We write the Green's function for this theory, using the definitions from SK formalism from the last section, $iG_C(x, y) = \langle \mathcal{T}_C(\phi(x)\phi(y)) \rangle$. Here, we are no longer writing the states Ω to make the notation more concise. The four different components from the last section are then given by:

$$\begin{aligned} iG_{11}(x, y) &= \langle \mathcal{T}_C(\phi(x)\phi(y)) \rangle, & iG_{12}(x, y) &= \langle \phi(y)\phi(x) \rangle \\ iG_{21}(x, y) &= \langle \phi(x)\phi(y) \rangle, & iG_{22}(x, y) &= \langle \tilde{\mathcal{T}}_C(\phi(x)\phi(y)) \rangle \end{aligned} \quad (9)$$

We name the four components using the matrix indices to make the next steps easy to follow. These definitions allow us to verify the time-ordering prescriptions, revealing that G_C must adhere to:

$$G_{11} + G_{22} = G_{12} + G_{21} \quad (10)$$

Now, by manipulating linear combinations of the above expressions, we can derive the well-known advanced and retarded propagators, which can be expressed as functions of the components of G_C defined in eq. (9),

$$\begin{aligned} G_R &= G_{11} - G_{12} = G_{21} - G_{22}, \\ G_A &= G_{12} - G_{22} = G_{11} - G_{21} \end{aligned} \quad (11)$$

More explicitly,

$$\begin{aligned} iG_R(x, y) &= \theta(x_0 - y_0) \langle [\phi(x), \phi(y)] \rangle \\ iG_A(x, y) &= -\theta(y_0 - x_0) \langle [\phi(x), \phi(y)] \rangle \end{aligned} \quad (12)$$

As one goes from Minkowski space to Euclidean space, which means,

$$t^2 - \vec{x}^2 \rightarrow -(\tau^2 + \vec{x}^2) \quad (13)$$

the advanced and retarded propagators represent the boundary values as the imaginary (Matsubara) frequency $i\omega_n = 2\pi n/\beta$ is continued below or above the real frequency axis [24].

To derive the Boltzmann equation, we commence by examining a free scalar field theory governed by the Lagrangian:

$$\mathcal{L} = \frac{1}{2}(\partial_\mu \phi)^2 - \frac{1}{2}m^2 \phi^2 \quad (14)$$

The Fourier transforms of the propagator components are as follows:

$$\tilde{G}_{11}(p) = \frac{1}{p_0^2 - \omega_{\mathbf{p}}^2 + i\epsilon} - \frac{i\pi}{\omega_{\mathbf{p}}} [n_{\mathbf{p}} \delta(p_0 - \omega_{\mathbf{p}} + n_{-\mathbf{p}} \delta(p_0 + \omega_{\mathbf{p}})] \quad (15)$$

$$\tilde{G}_{22}(p) = \frac{-1}{p_0^2 - \omega_{\mathbf{p}}^2 + i\epsilon} - \frac{i\pi}{\omega_{\mathbf{p}}} [n_{\mathbf{p}} \delta(p_0 - \omega_{\mathbf{p}} + n_{-\mathbf{p}} \delta(p_0 + \omega_{\mathbf{p}})] \quad (16)$$

$$\tilde{G}_{12}(p) = -\frac{i\pi}{\omega_{\mathbf{p}}} [n_{\mathbf{p}} \delta(p_0 - \omega_{\mathbf{p}} + (1 + n_{-\mathbf{p}}) \delta(p_0 + \omega_{\mathbf{p}})] \quad (17)$$

$$\tilde{G}_{21}(p) = -\frac{i\pi}{\omega_{\mathbf{p}}} [(1 + n_{\mathbf{p}}) \delta(p_0 - \omega_{\mathbf{p}} + n_{-\mathbf{p}} \delta(p_0 + \omega_{\mathbf{p}})] \quad (18)$$

where $n_{\mathbf{p}}$ represents the occupation number. By substituting these expressions back into Eq. (12), we obtain the advanced and retarded propagators:

$$\tilde{G}_R(p) = \frac{1}{(p_0 + i\epsilon)^2 - \omega_{\mathbf{p}}^2}, \quad \tilde{G}_A(p) = \frac{1}{(p_0 - i\epsilon)^2 - \omega_{\mathbf{p}}^2} \quad (19)$$

We introduce the self-energy $\Sigma(x, y)$ to compute this theory's propagator properly. This means that $\Sigma(x, y)$ can be related to the propagator by the following equations:

$$(-\partial_x^2 - m^2)G_C(x, y) = \eta_x \delta(x - y) + \int_C dz \Sigma_C(x, z) G_C(z, y), \quad (20)$$

$$(-\partial_y^2 - m^2)G_C(x, y) = \eta_y \delta(x - y) + \int_C dz \Sigma_C(x, z) G_C(z, y) \quad (21)$$

where η_x varies along the contour, it is +1 if x is on the upper part, and -1 if x is in the lower part. Analogously to the procedure applied to the propagator, the self-energy can also be decomposed into four components, allowing it to be expressed as 2×2 matrix:

$$\Sigma(x, y) \equiv \begin{pmatrix} \Sigma_{11}(x, y) & \Sigma_{12}(x, y) \\ \Sigma_{21}(x, y) & \Sigma_{22}(x, y) \end{pmatrix} \quad (22)$$

One can use this decomposition to obtain a more general form, substituting it in eq. (21):

$$(-\partial_x^2 - m^2)G(x, y) = \sigma_3 \delta(x - y) + \int dz \Sigma(x, z) \sigma_3 G(z, y), \quad (23)$$

$$(-\partial_y^2 - m^2)G(x, y) = \sigma_3 \delta(x - y) + \int dz \Sigma(x, z) \sigma_3 G(z, y), \quad (24)$$

where the integral over z is just an ordinary spacetime integration, and σ_3 is the usual Pauli matrix. With these tools in place, deriving the Boltzmann equation becomes straightforward. First, subtract Eq. (23) from Eq. (24):

$$(\partial_x^2 - \partial_y^2)G_C(x, y) = \int_C dz [G_C(x, z) \Sigma_C(z, y) - \Sigma_C(x, z) G_C(z, y)] \quad (25)$$

Continuing from this point, we assume that the timescale for the system's overall evolution is much larger than the typical wavelength of a particle[14]. Consequently, the variation of the propagator is significantly slower with respect to the average position, given by $(x + y)/2$, compared to the separation, given as $x - y$. For that reason, we write:

$$x = X + \frac{s}{2}, \quad y = X - \frac{s}{2}, \quad x = X + \frac{s}{2} - s' \quad (26)$$

which, when inserted into Eq. (25) gives,

$$2 \frac{\partial}{\partial X^\mu} \frac{\partial}{\partial s_\mu} G_C(X, s) = \int_C ds' \left[G_C \left(X + \frac{s - s'}{2}, s' \right) \Sigma_C \left(X - \frac{s'}{2}, s - s' \right) - \Sigma_C \left(X + \frac{s - s'}{2}, s' \right) G_C \left(X - \frac{s'}{2}, s - s' \right) \right] \quad (27)$$

This variable change also implies that G and Σ will have a slow variation in terms of the new variable X . This is rather convenient for this derivation, as it means that we can simplify this expression by replacing the first argument in the propagator and self-energy (G and Σ) on the right-hand side of eq.(27) by X . This gives, for example, for G_{12} ,

$$2 \frac{\partial}{\partial X^\mu} \frac{\partial}{\partial s_\mu} G_{12}(X, s) = \int ds' \left[G_{11}(X, s') \Sigma_{12}(X, s - s') - G_{12}(X, s') \Sigma_{22}(X, s - s') - \Sigma_{11}(X, s') G_{12}(X, s - s') + \Sigma_{12}(X, s') G_{22}(X, s - s') \right] \quad (28)$$

Next, we Fourier transform this expression with respect to the relative separation s using,

$$\tilde{G}(X, p) \equiv \int ds e^{-ips} G(X, s), \quad (29)$$

which leads to (simplifying the notation)

$$-2ip^\mu \partial_\mu \tilde{G}_{12} = \tilde{\Sigma}_{12}(\tilde{G}_{11} + \tilde{G}_{22}) - \tilde{G}_{12}(\tilde{\Sigma}_{11} + \tilde{\Sigma}_{22}) \quad (30)$$

Rearranging the terms gives:

$$-2ip^\mu \partial_\mu \tilde{G}_{12} = \tilde{\Sigma}_{12} \tilde{G}_{21} - \tilde{G}_{12} \tilde{\Sigma}_{21} \quad (31)$$

Finally, to obtain the Boltzmann equation, one has to assume that the excitations of the nonequilibrium system are viewed as single fundamental particles. One can make the ansatz:

$$\tilde{G}_{12}(X, p) = -\frac{i\pi}{\omega_{\mathbf{p}}} [\delta(p_0 - \omega_{\mathbf{p}}) n_{\mathbf{p}}(X) + \delta(p_0 + \omega_{\mathbf{p}}) (1 + n_{\mathbf{p}}(X))] \quad (32)$$

$$\tilde{G}_{21}(X, p) = -\frac{i\pi}{\omega_{\mathbf{p}}} [\delta(p_0 - \omega_{\mathbf{p}}) (1 + n_{\mathbf{p}}(X)) + \delta(p_0 + \omega_{\mathbf{p}}) n_{\mathbf{p}}(X)] \quad (33)$$

Substituting this ansatz in Eq. (30), one can rearrange the terms to get:

$$(\partial_t + \mathbf{v} \cdot \partial_{\mathbf{x}}) n_{\mathbf{p}} = \frac{i}{2\omega_{\mathbf{p}}} [\tilde{\Sigma}_{12}(\omega_{\mathbf{p}}, \mathbf{p})(1 + n_{\mathbf{p}}) - \tilde{\Sigma}_{21}(\omega_{\mathbf{p}}, \mathbf{p}) n_{\mathbf{p}}] \quad (34)$$

Which looks a lot like a Boltzmann equation. What is left to do is to substitute the explicit propagators, given by:

$$\tilde{\Sigma}_{12}(\omega_{\mathbf{p}}, \mathbf{p}) = -\frac{i\lambda^2}{2} \int \frac{d\mathbf{p}' d\mathbf{k}'}{(2\pi)^6 2\omega_{\mathbf{p}'} 2\omega_{\mathbf{k}} 2\omega_{\mathbf{k}'}} n_{\mathbf{p}'} n_{\mathbf{k}} (1 + n_{\mathbf{k}'}) 2\pi \delta(\omega_{\mathbf{p}} + \omega_{\mathbf{p}'} - \omega_{\mathbf{k}} - \omega_{\mathbf{k}'}), \quad (35)$$

$$\tilde{\Sigma}_{21}(\omega_{\mathbf{p}}, \mathbf{p}) = -\frac{i\lambda^2}{2} \int \frac{d\mathbf{p}' d\mathbf{k}'}{(2\pi)^6 2\omega_{\mathbf{p}'} 2\omega_{\mathbf{k}} 2\omega_{\mathbf{k}'}} (1 + n_{\mathbf{p}'}) (1 + n_{\mathbf{k}}) n_{\mathbf{k}'} 2\pi \delta(\omega_{\mathbf{p}} + \omega_{\mathbf{p}'} - \omega_{\mathbf{k}} - \omega_{\mathbf{k}'}) \quad (36)$$

where $\mathbf{k}' \equiv \mathbf{p} + \mathbf{p}' - \mathbf{k}$. Finally, one can now write the Boltzmann equation for a single component scalar field:

$$(\partial_t + \mathbf{v} \cdot \partial_{\mathbf{x}})n_{\mathbf{p}} = \frac{i\lambda^2}{2} \int \frac{d\mathbf{p}' d\mathbf{k}'}{(2\pi)^6 \omega_{\mathbf{p}} \omega_{\mathbf{p}'} \omega_{\mathbf{k}} \omega_{\mathbf{k}'}} 2\pi \delta(\omega_{\mathbf{p}} + \omega_{\mathbf{p}'} - \omega_{\mathbf{k}} - \omega_{\mathbf{k}'}) \times [n_{\mathbf{p}} n_{\mathbf{k}} (1 + n_{\mathbf{p}'}) (1 + n_{\mathbf{k}'}) - n_{\mathbf{p}'} n_{\mathbf{k}'} (1 + n_{\mathbf{p}}) (1 + n_{\mathbf{k}})] \quad (37)$$

To derive the Boltzmann equation for QCD, one must first extend this derivation into a multi-component case. We assume a field ϕ^a , where a represents the isospin. Due to the increased degrees of freedom, the propagator and self-energy components become matrices. This will bring some problems in our past derivation because the components of G and Σ no longer commute. The new starting point is:

$$(\partial_x^2 - \partial_y^2)G_{12}(x, y) = \frac{1}{2} \left(\{G_{11} + G_{22}, \Sigma_{12}\} - [G_{11} - G_{22}, \Sigma_{12}] - \{\Sigma_{11} + \Sigma_{22}, G_{12}\} - [\Sigma_{11} - \Sigma_{22}, G_{12}] \right) \quad (38)$$

For a multi-component scalar field, the choice of ansatz has to be:

$$\tilde{G}_{12}^{ab}(X, p) = -\frac{i\pi}{\omega_{\mathbf{p}}} [\delta(p_0 - \omega_{\mathbf{p}}) n_{\mathbf{p}}^{ab}(X) + \delta(p_0 + \omega_{\mathbf{p}}) (\delta^{ab} + n_{-\mathbf{p}}^{ba}(X))] \quad (39)$$

$$\tilde{G}_{21}^{ab}(X, p) = -\frac{i\pi}{\omega_{\mathbf{p}}} [\delta(p_0 - \omega_{\mathbf{p}}) (\delta^{ab} + n_{\mathbf{p}}^{ab}(X)) + \delta(p_0 + \omega_{\mathbf{p}}) n_{-\mathbf{p}}^{ba}(X)] \quad (40)$$

Here, $n_{\mathbf{p}}^{ab}(X)$ is the density matrix. The choice of ansatz leads to some simplifications in our expression, and the kinetic equation becomes:

$$(\partial_t + \mathbf{v} \cdot \partial_{\mathbf{x}})n_{\mathbf{p}} = \frac{i}{4\omega_{\mathbf{p}}} \left(\{\Sigma_{12}(\omega_{\mathbf{p}}, \mathbf{p})(1 + n_{\mathbf{p}})\} - \{\tilde{\Sigma}_{21}(\omega_{\mathbf{p}}, \mathbf{p})n_{\mathbf{p}}\} \right) \quad (41)$$

$$- [\Sigma_{11}(\omega_{\mathbf{p}}, \mathbf{p}) - \Sigma_{22}(\omega_{\mathbf{p}}, \mathbf{p}), n_{\mathbf{p}}] \quad (42)$$

This equation can be expressed in terms of loss and gain terms \mathcal{I}_- and \mathcal{I}_+ . For that, we define:

$$\mathcal{I}_- = \frac{i}{2\omega_{\mathbf{p}}} \Sigma_{12}(\omega_{\mathbf{p}}, \mathbf{p}), \quad \mathcal{I}_+ = \frac{i}{2\omega_{\mathbf{p}}} \Sigma_{21}(\omega_{\mathbf{p}}, \mathbf{p}) \quad (43)$$

and

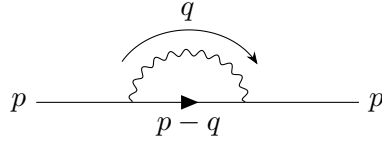
$$\text{Re}\bar{\Sigma} = \frac{1}{4\omega_{\mathbf{p}}} (\Sigma_{11} - \Sigma_{22}) = \frac{1}{4\omega_{\mathbf{p}}} (\Sigma_R - \Sigma_A) = \frac{1}{2\omega_{\mathbf{p}}} \text{Re}\Sigma_R(\omega_{\mathbf{p}}, \mathbf{p}) \quad (44)$$

where $\bar{\Sigma}$ is the correction to the energy of excitation \mathbf{p} . These simple definitions allow us to write the right-hand side of the Boltzmann equation as:

$$C[n] = \frac{1}{2}\{n_{\mathbf{p}}, \mathcal{I}_-\} - \frac{1}{2}\{1 \pm n_{\mathbf{p}}, \mathcal{I}_+\} - i[\text{Re}\bar{\Sigma}, n_{\mathbf{p}}] \quad (45)$$

3 Boltzmann equation for gauge theories

We will now extend our approach from the previous section to gauge theories. First, we will focus on scalar QED and illustrate how the Boltzmann equation can be derived with some adjustments. These adjustments are necessary due to the increased complexity of the self-energy Σ compared to scalar ϕ^4 theory. The leading order contribution for Σ comes from the one-loop diagram as



and can be written as:

$$\tilde{\Sigma}_{12}(p) = -ie^2 \int \frac{d^4q}{(2\pi)^4} (2p-q)_\mu (2p-q)_\nu D_{12}^{\mu\nu}(q) \tilde{G}_{12}(p-q) \quad (46)$$

Where $D^{\mu\nu}$ is the photon propagator, which can be obtained using the photon self-energy Π , using the equations:

$$q^2 D_{12} = \Pi_{11} D_{12} - \Pi_{12} D_{22}, \quad (47)$$

$$q^2 D_{22} = \Pi_{21} D_{12} - \Pi_{22} D_{22} - 1. \quad (48)$$

These relations are simply Eq. (23), if one makes $\Sigma \rightarrow \Pi$ and $m = 0$. Solving for D_{12} results in:

$$D_{12}(q) = \frac{\Pi_{12}}{(q^2 - \Pi_{11})(q^2 + \Pi_{22}) + \Pi_{12}\Pi_{21}} \quad (49)$$

Similar to the scalar case, the advanced and retarded propagators are obtained using the relation:

$$(q^2 - \Pi_{11})(q^2 + \Pi_{22}) + \Pi_{12}\Pi_{21} = (q^2 - \Pi_R)(q^2 - \Pi_A) \quad (50)$$

Therefore,

$$D_{12}(q) = \frac{\Pi_{12}}{(q^2 - \Pi_R)(q^2 - \Pi_A)} = D_R \Pi_{12} D_A = |D_R|^2 \Pi_{12} \quad (51)$$

The photon self-energy will be defined by the one-loop diagram shown at the beginning of this section and given as

$$\Pi_{12}^{\mu\nu}(q) = ie^2 \int \frac{d^4 p'}{(2\pi)^4} (2p' + q)^\mu (2p' + q)^\nu G_{12}(p') G_{21}(p' + q) \quad (52)$$

Analogously to the scalar field case, we use the ansatz:

$$\tilde{G}_{12}(p) = -\frac{i\pi}{\omega_{\mathbf{p}}} [f_{\mathbf{p}} \delta(p_0 - \omega_{\mathbf{p}}) + (1 + \bar{f}_{-\mathbf{p}}) \delta(p_0 + \omega_{\mathbf{p}})] \quad (53)$$

Here, we will use the notation that $f_{\mathbf{p}}$ and $\bar{f}_{-\mathbf{p}}$ are the equilibrium distributions for particles and antiparticles. Substituting it into the photon self-energy, given by Eq. (52), yields:

$$\Pi_{12}^{\mu\nu}(q) = ie^2 \int \frac{d^4 p'}{(2\pi)^3} (2p' + q)^\mu (2p' + q)^\nu [f_{\mathbf{p}'+\mathbf{q}}(1 + f_{\mathbf{p}'}) + \bar{f}_{\mathbf{p}'+\mathbf{q}}(1 + \bar{f}_{\mathbf{p}'})] \quad (54)$$

Now that we have all the ingredients necessary to express $D^{\mu\nu}$, we can write the scalar self-energy explicitly as:

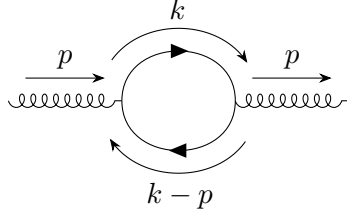
$$\begin{aligned} \Sigma_{12}(\omega_{\mathbf{p}}, \mathbf{p}) &= -ie^2 \int \frac{d^4 p' d^4 q}{(2\pi)^6 2\omega_{\mathbf{p}'} 2\omega_{\mathbf{p}-\mathbf{q}} 2\omega_{\mathbf{p}'+\mathbf{q}}} (2\pi) \delta(\omega_{\mathbf{p}} + \omega_{\mathbf{p}'} - \omega_{\mathbf{p}-\mathbf{q}} - \omega_{\mathbf{p}'+\mathbf{q}}) \\ &\quad \times |(2p - q)_\mu (2p' + q)_\nu D_R^{\mu\nu}(q)|^2 [(1 + f_{\mathbf{p}'}) f_{\mathbf{p}-\mathbf{q}} f_{\mathbf{p}'+\mathbf{q}} + (1 + \bar{f}_{\mathbf{p}'}) \bar{f}_{\mathbf{p}-\mathbf{q}} \bar{f}_{\mathbf{p}'+\mathbf{q}}] \end{aligned} \quad (55)$$

So far, we've only computed one off-diagonal scalar self-energy component Σ_{12} . However, it is quite direct to compute Σ_{21} using the same prescription. With these two expressions in hand, one can finally write the Boltzmann equation for QED as,

$$\begin{aligned} (\partial_t + \mathbf{v} \cdot \partial_{\mathbf{x}}) n_{\mathbf{p}} &= \int \frac{d^4 p' d^4 k}{(2\pi)^6 2\omega_{\mathbf{p}'} 2\omega_{\mathbf{p}'} 2\omega_{\mathbf{k}} 2\omega_{\mathbf{k}'}} |\mathcal{M}_{\mathbf{p}\mathbf{p}' \rightarrow \mathbf{k}\mathbf{k}'}|^2 (2\pi) \delta(\omega_{\mathbf{p}} + \omega_{\mathbf{p}'} - \omega_{\mathbf{k}} - \omega_{\mathbf{k}'}) \\ &\quad \times \left\{ (1 + f_{\mathbf{p}}) f_{\mathbf{k}} [(1 + f_{\mathbf{p}'}) f_{\mathbf{k}'} + (1 + \bar{f}_{\mathbf{p}'}) \bar{f}_{\mathbf{k}'}] \right. \\ &\quad \left. - (1 + f_{\mathbf{k}}) f_{\mathbf{p}} [(1 + f_{\mathbf{k}'}) f_{\mathbf{p}'} + (1 + \bar{f}_{\mathbf{k}'}) \bar{f}_{\mathbf{p}'}] \right\} \end{aligned} \quad (56)$$

Since our objective in this chapter is to derive a Boltzmann equation for QCD, we must now turn to non-abelian gauge theory derivations. As most of the equipment necessary

for this derivation has already been covered in this chapter, what remains is to combine the treatment for multi-component scalar theory with QED. One can begin by computing the gain and loss terms, which come from one-loop contributions to the self-energy. In QCD, the self-energy is computed with a soft resummed gauge boson propagator,



and given as,

$$\Sigma_{12}^{a\bar{a}}(\omega_{\mathbf{p}}, \mathbf{p}) = -ig^2 \int \frac{d\mathbf{p}' d\mathbf{q}}{(2\pi)^6 2\omega_{\mathbf{p}'} 2\omega_{\mathbf{p}-\mathbf{q}} 2\omega_{\mathbf{p}'+\mathbf{q}}} (2\pi) \delta(\omega_{\mathbf{p}} + \omega_{\mathbf{p}'} - \omega_{\mathbf{p}-\mathbf{q}} - \omega_{\mathbf{p}'+\mathbf{q}}) \times |(2p-q)_\mu (2p'+q)_\nu D_R^{\mu\nu}(q)|^2 \left[f_{\mathbf{p}'}^{\bar{b}b} (1 \pm f_{\mathbf{p}-\mathbf{q}})^{c\bar{c}} (1 \pm f_{\mathbf{p}'+\mathbf{q}'})^{d\bar{d}} \right] \quad (57)$$

Here, there is an implied summation over the types and spins of the particles. Analogously, we write the gain and loss terms, as done in the last section,

$$\mathcal{I}_-^{a\bar{a}} = \int_{\mathbf{p}' \mathbf{k}' \mathbf{k}} \mathcal{M}_{\bar{a}\bar{b}\bar{c}\bar{d}}^* \mathcal{M}_{abcd} f_{\mathbf{p}'}^{\bar{b}b} (1 \pm f_{\mathbf{k}})^{c\bar{c}} (1 \pm f_{\mathbf{k}'})^{d\bar{d}} \quad (58)$$

$$\mathcal{I}_+^{a\bar{a}} = \int_{\mathbf{p}' \mathbf{k}' \mathbf{k}} \mathcal{M}_{\bar{a}\bar{b}\bar{c}\bar{d}}^* \mathcal{M}_{abcd} n_{\mathbf{k}}^{\bar{c}c} n_{\mathbf{k}'}^{d\bar{d}} (1 \pm n_{\mathbf{k}'})^{\bar{b}b} \quad (59)$$

$$(60)$$

Finally, at this point, one can follow the same procedure and write the Boltzmann equation for QCD:

$$(\partial_t + \mathbf{v} \cdot \partial_{\mathbf{x}}) f_{\mathbf{p}}^a = \sum_{bcd} \int \frac{d\mathbf{p}' d\mathbf{k} d\mathbf{k}'}{(2\pi)^6 2\omega_{\mathbf{p}} 2\omega_{\mathbf{p}'} 2\omega_{\mathbf{k}} 2\omega_{\mathbf{k}'}} \left| \mathcal{M}_{cd}^{ab}(\mathbf{p}, \mathbf{k}; \mathbf{p}', \mathbf{k}') \right|^2 \delta^{(4)}(P + K - P' - K') \left\{ f_{\mathbf{p}}^a f_{\mathbf{k}}^b [1 \pm f_{\mathbf{p}'}^c] [1 \pm f_{\mathbf{k}'}^d] - f_{\mathbf{p}'}^c f_{\mathbf{k}'}^d [1 \pm f_{\mathbf{p}}^a] [1 \pm f_{\mathbf{k}}^b] \right\} \quad (61)$$

Where capital letters refer to 4-momentum, and $a, b, c,$ and d represent different species of particles, either bosons, quarks, or anti-quarks. From this point, Eq. (61) will be the starting point for our transport coefficient calculations throughout this thesis.

4 Theoretical Framework

Next, we introduce the setup necessary for the description of the QGP and the calculations of shear viscosity. This formalism was first developed by Arnold, Moore, and Yaffe for the leading log order in [13] and later expanded by us to the high-density regime in [41]. Therefore, this section will be based on the latter. We begin by outlining the essential setup required to derive shear viscosity. In this context, it will be sufficient to solve the Boltzmann equation linearized in small deviations away from an equilibrium state, which has a given temperature T and chemical potential μ . Shear viscosity is a property of systems featuring non-uniform flow velocities across space. This entails that the local equilibrium form of the statistical function is:

$$f_0^a(\vec{p}, \vec{x}, t) = \frac{1}{\exp(\gamma\beta(p^0 - u_i p^i - \mu_a)) \mp 1} = \frac{1}{\exp(\beta(-u_\mu P^\mu - \mu_a)) \mp 1}. \quad (62)$$

We use a mostly-positive metric tensor $g_{\mu\nu} = \text{Diag}[-1, +1, +1, +1]$, and natural units, $c = 1$, $\hbar = 1$. Capital letters P, K are 4-vectors, lower case letters \vec{p}, \vec{k} or p_i, k_i are the space components, p^0 and k^0 are the time components, and p, k are the magnitudes of the space components.

Throughout these calculations, $u^\mu = (\gamma, \gamma\vec{v})$ is the local velocity 4-vector, γ is the associated relativistic gamma-factor, and $\beta = \beta(\vec{x}, t) = 1/T$ is the local temperature. The sign ∓ 1 corresponds to $-$ for bosons and $+$ for fermions (with the upper typically assigned to bosons). Additionally, μ_a represents the baryonic chemical potential for species a , which will be nonzero for quark species and have opposite signs for a particle and its antiparticle. Later, we will introduce an effective chemical potential incorporating strangeness and electric charge. However, for simplicity, we now concentrate on an $SU(3)$ gauge theory with n_f vectorlike quark species characterized by identical baryonic chemical potential.

We will ignore the cases where f_0^a is time-dependent, which come from β variations in space, and concentrate on the case where the flow velocity has a traceless-symmetric spatial derivative. Our choice of frame will be the one that has $u_i(\vec{x} = 0) = 0$, giving a shear tensor σ_{ij} that is:

$$\sigma_{ij} \equiv \partial_i u_j + \partial_j u_i - \frac{2}{3} \delta_{ij} \partial_k u_k \neq 0. \quad (63)$$

Under these conditions, the system won't stay in equilibrium. The nonequilibrium distribution can be written by decomposing f^a into an equilibrium and nonequilibrium correlator according to the Landau-Lifshitz conventions; this gives:

$$f^a(\vec{p}, \vec{x}) = f_0^a(\vec{p}, \vec{x}) + f_0(1 \pm f_0) f_1^a(\vec{p}, \vec{x}), \quad (64)$$

This choice of normalization for f_1 with a factor of $f_0(1 \pm f_0)$ is convenient for the computational methods employed in this chapter. It is well known that the term $f_0(1 \pm f_0)f_1$ does not contribute to the energy density T^{00} or momentum density T^{0i} . However, it is expected to contribute to the stress tensor. For instance, this dependence is expected to be linear in a system with small and slowly varying σ_{ij} . As such, one defines:

$$T_{ij} = \mathcal{P}g_{ij} - \eta \sigma_{ij} \quad (65)$$

In the above expression, \mathcal{P} is the pressure and η represents the shear viscosity, characterized as the coefficient governing the linear response of T_{ij} to nonvanishing σ_{ij} , discussed before in Chapter 2.

The stress tensor can be determined from $f^a(\vec{p}, \vec{x})$. Here, our focus lies solely on the leading-order description, wherein particle masses are neglected, yielding an expression given by:

$$T_{ij}(\vec{x}) = \sum_a^{\text{ffhc}} \int \frac{d^3p}{(2\pi)^3} \frac{p_i p_j}{p} f^a(\vec{p}, \vec{x}) \quad (66)$$

where the sum runs over all colors c , helicities h , flavors/particle types f , and particle/antiparticle \bar{f} . Therefore, the sum has 16 terms due to gluons (2 helicities \times 8 colors) and $12n_f$ terms (2 helicities \times 3 colors \times particle + antiparticle) due to n_f flavors of quarks.

The next step is determining f_1^a from σ_{ij} . To accomplish this, we refer to the Boltzmann equation for non-abelian theories derived in the previous Chapter. In a weakly coupled system, the dynamics of f^a are governed by a Boltzmann equation:

$$\left[\frac{\partial}{\partial t} + \vec{v}_p \cdot \frac{\partial}{\partial \vec{x}} \right] f^a(\vec{p}, \vec{x}, t) = -\mathcal{C}^a[f]. \quad (67)$$

We leave out the terms, including the time derivative and the external force, as they won't be relevant to viscosity calculations. Furthermore, we neglect thermal and Lagrangian masses; hence, the velocity vector is the unit vector in the direction of the momentum, $\vec{v}_p = \hat{p} = \vec{p}/p$. Since the focus of this chapter is to derive the theoretical framework, it will be sufficient to consider $2 \leftrightarrow 2$ collisions and save more details of the collision operator for the following chapters. For now, let us express the collision operator as:

$$\begin{aligned} \mathcal{C}^a[f](\vec{p}) &= \frac{1}{2} \sum_{bcd} \int_{\vec{k}, \vec{p}, \vec{k}'} \frac{|\mathcal{M}_{abcd}(P, K, P', K')|^2}{2p^0 2k^0 2p'^0 2k'^0} (2\pi)^4 \delta^4(P + K - P' - K') \\ &\quad \times \left\{ f^a(\vec{p}) f^b(\vec{k}) [1 \pm f^c(\vec{p}')] [1 \pm f^d(\vec{k}')] \right. \\ &\quad \left. - f^c(\vec{p}') f^d(\vec{k}') [1 \pm f^a(\vec{p})] [1 \pm f^b(\vec{k})] \right\} \end{aligned} \quad (68)$$

here, the incoming/outgoing momenta \vec{p}, \vec{k} and \vec{p}', \vec{k}' are all on shell, $p^0 = p$. We use the simplified notation $\int_{\vec{k}} = \int \frac{d^3\vec{k}}{(2\pi)^3}$. The factor $1/2$ is included to prevent double counting in the external state sum when $c \neq d$ and represents the relevant symmetry factor when $c = d$. Finally, \mathcal{M} represents the scattering process to be calculated using perturbation theory at the order relevant for the calculation.

So far, we have introduced all the necessary tools to describe the system. We will proceed by presenting a few additional definitions that will aid in setting up the problem. We begin by introducing a more convenient rescaling of σ_{ij} ,

$$X_{ij} \equiv \frac{1}{\sqrt{6}} \sigma_{ij} \quad (69)$$

Adding to that, one can rewrite the LHS of Eq. (67) in a more convenient way:

$$\hat{p} \cdot \partial_x f_0^a(\vec{p}, \vec{x}) = \beta p^0 f_0^a (1 \pm f_0^a) X_{ij}(x) I_{ij}(\vec{p}) \equiv \beta^2 X_{ij}(x) S_{ij}^a(\vec{p}), \quad (70)$$

$$I_{ij}(\vec{p}) \equiv \sqrt{\frac{3}{2}} \left(\hat{p}_i \hat{p}_j - \frac{1}{3} \delta_{ij} \right), \quad (71)$$

$$S_{ij}^a(\vec{p}) \equiv p^0 T f_0^a (1 \pm f_0^a) I_{ij}(\vec{p}). \quad (72)$$

Here, I_{ij} represents the angular dependence and is normalized as $I_{ij} I_{ij} = 1$. Given that this expression is linear in X_{ij} for the equilibrium distribution, the insertion of the departure from equilibrium f_1 will lead to an expression that is either quadratic in X_{ij} or involves derivatives of this quantity. We will neglect these terms, making use of the results from Ref. [148].

Since the collision operator does not contribute to $f \rightarrow f_0$, it follows that it will be linear in $f_1(\vec{p})$, namely, $f_1(\vec{p}) \propto X_{ij}(\vec{p})$. The distribution f_1 is a scalar quantity; hence, it must also be proportional to the contraction $f_1(\vec{p}, \vec{x}) \propto X_{ij}(\vec{x}) I_{ij}(\vec{p})$. Consequently, without loss of generality, we can express the departure from equilibrium as:

$$f_1^a(\vec{p}, \vec{x}) = \beta^2 X_{ij}(\vec{x}) \chi_{ij}^a(\vec{p}) = \beta^2 X_{ij}(\vec{x}) I_{ij}(\vec{p}) \chi^a(p). \quad (73)$$

Here, $\chi^a(p)$ represents a purely scalar function of p . It characterizes the departure from equilibrium in the presence of shear stress and can be referred to as the relaxation function of each species a . As a consequence of the fact that both sides of Eq. (67) are proportional to X_{ij} , we can reformulate it as

$$S_{ij}^a(\vec{p}) = \mathcal{C} \chi_{ij}^a(\vec{p}). \quad (74)$$

Here $\mathcal{C} \chi_{ij}^a(\vec{p})$ refers to the collision operator of Eq. (68) with $f_1^a \rightarrow \chi_{ij}^a(\vec{p})$ inserted as the departure from equilibrium. In other words, the collision operator is assured to be proportional to X_{ij} , and $\mathcal{C} \chi_{ij}^a(p)$ is the collision operator with this factor of $\beta^2 X_{ij}$ stripped off.

4.1 Variational solution

When confronted with coupled integral equations of this type, a systematic approach involves reducing them to a set of scalar equations, discretizing the permissible values of $|p|$, computing the matrix elements $C^{ab}(|p|, |q|)$ of the collision operator's kernel using quadrature methods. This procedure would then render (74) into a finite-dimensional linear matrix equation. However, it has been argued in [13] that this is not the best strategy due to the integrable singularities present in $C^{ab}(|p|, |q|)$, which would require a large discretization to be overcome. Therefore, we turn to the variational method approach used in [9, 13] in leading log and leading order calculations. It converts Eq. (74) into an equivalent variational problem. We begin by defining the inner product:

$$(f, g) = \beta^3 \sum_a^{\text{ffhc}} \int_{\vec{p}} f^a(\vec{p}) g^a(\vec{p}). \quad (75)$$

The collision operator is Hermitian with respect to this inner product. This implies that one can define a functional $\mathcal{Q}[\chi]$, over the space of $\chi^a(p)$, this can be defined as:

$$\mathcal{Q}[\chi] = (\chi_{ij}, S_{ij}) - \frac{1}{2} (\chi_{ij}, \mathcal{C}\chi_{ij}), \quad (76)$$

Setting the variation with respect to $\chi^a(p)$ equal to zero to find the extremum (maximum) of this functional returns Eq. (74). That is, the functional \mathcal{Q} takes its maximum value when the Boltzmann equation is satisfied. Furthermore, its value at this maximum,

$$Q_{max} = \frac{1}{2} (\chi_{ij}, S_{ij}) = \frac{1}{2} (\chi_{ij}, \mathcal{C}\chi_{ij}) = \frac{1}{2} (S_{ij}, \mathcal{C}^{-1}S_{ij}), \quad (77)$$

determines the viscosity:

$$\eta = \frac{2}{15} Q_{max}. \quad (78)$$

The terms in this functional can be identified as the source:

$$\begin{aligned} (\chi_{ij}, S_{ij}) &= \beta^2 \sum_a^{\text{ffhc}} \int_{\vec{p}} f_0(\vec{p}) [1 \pm f_0(\vec{p})] |\vec{p}| \chi^a I_{ij}(\hat{p}) I_{ij}(\hat{p}) \\ &= \beta^2 \sum_a^{\text{ffhc}} \int_{\vec{p}} f_0(\vec{p}) [1 \pm f_0(\vec{p})] |\vec{p}| \chi^a \end{aligned} \quad (79)$$

and the collision integral:

$$\begin{aligned}
(\chi_{ij}, \mathcal{C}\chi_{ij}) &= \frac{\beta^3}{8} \sum_{abcd}^{\text{ffhc}} \int_{\vec{p}, \vec{k}, \vec{p}', \vec{k}'} \frac{|\mathcal{M}_{abcd}(P, K, P', K')|^2}{2p^0 2k^0 2p'^0 2k'^0} (2\pi)^4 \delta^4(P + K - P' - K') \\
&\quad \times f_0^a(p) f_0^b(k) [1 \pm f_0^c(p')] [1 \pm f_0^d(k')] \\
&\quad \times \left[\chi_{ij}^a(\vec{p}) + \chi_{ij}^b(\vec{k}) - \chi_{ij}^c(\vec{p}') - \chi_{ij}^d(\vec{k}') \right]^2. \tag{80}
\end{aligned}$$

The sum is over all scattering processes taking species a and b into species c and d . The overall factor of $1/8$ compensates for the eight times a given process is taken into account: $a \leftrightarrow b$, $c \leftrightarrow d$, and $(a, b) \leftrightarrow (c, d)$.

To maximize the functional Q_{max} exactly, it is usually necessary to work in the infinite-dimensional space of arbitrary functions $\chi(p)$. However, as established in other variational problems, highly accurate approximate outcomes can be attained by conducting a restricted extremization within a carefully selected finite-dimensional subspace. Therefore, we expand the $\chi(p)$ functions into a finite basis set:

$$\chi^g(p) = \sum_{m=1}^N a_m \phi^{(m)}(p), \quad \chi^q(p) = \sum_{m=1}^N a_{m+N} \phi^{(m)}(p), \quad \chi^{\bar{q}}(p) = \sum_{m=1}^N a_{m+2N} \phi^{(m)}(p). \tag{81}$$

Inserting the $\chi(p)$ functions back into the source and collision integrals, we get the source vector and the truncated scattering matrix:

$$(S_{ij}, \chi_{ij}) = \sum_m a_m \tilde{S}_m, \quad (\chi_{ij}, \mathcal{C}\chi_{ij}) = \sum_{m,n} a_m \tilde{\mathcal{C}}_{mn} a_n, \tag{82}$$

where \tilde{S}_m , $\tilde{\mathcal{C}}_{mn}$ are Eq. (79) and Eq. (80) with χ^a replaced by individual basis functions $\phi^{(m)}$, $\phi^{(n)}$, which gives

$$\begin{aligned}
\tilde{S}_m &= (\phi^{(m)} I_{ij}, S_{ij}) \\
\tilde{\mathcal{C}}_{mn} &= (\phi^{(m)} I_{ij}, \mathcal{C}\phi^{(n)} I_{ij}). \tag{83}
\end{aligned}$$

Within the subspace defined by this basis, one estimates that:

$$\mathcal{Q}[\chi] = a_m \tilde{S}_m - \frac{1}{2} a_m \tilde{\mathcal{C}}_{mn} a_n \tag{84}$$

where \tilde{C}_{mn}^{-1} is to be understood as the matrix inverse of \tilde{C}_{mn} , explicitly, $\tilde{C}_{mn}^{-1}\tilde{C}_{no} = \delta_{mo}$. And shear viscosity is determined by substituting the correct distribution in $T^{\mu\nu}$ and comparing it with the constitutive relation:

$$\begin{aligned}
T^{\mu\nu}(x) &= \int_{\vec{p}} \beta^2 \frac{p^i p^j}{|\vec{p}|} f_0 [1 \pm f_0] \frac{1}{\sqrt{6}} (\nabla_i u_j + \nabla_j u_i - \delta_{ij} \nabla \cdot \vec{u}) \\
&\times \sqrt{\frac{3}{2}} (\hat{p}_i \hat{p}_j - \frac{1}{3} \delta_{ij}) \chi^a \\
&= \frac{\beta^2}{2} \int_{\vec{p}} f_0 [1 \pm f_0] \frac{p^i p^j}{|\vec{p}|} (\hat{p}_i \hat{p}_j - \frac{1}{3} \delta_{ij}) (\nabla_i u_j + \nabla_j u_i \\
&- \delta_{ij} \nabla \cdot \vec{u}) \chi^a \\
&= \frac{\beta^2}{2} \int_{\vec{p}} f_0 [1 \pm f_0] \frac{2}{3} |\vec{p}| (\nabla_i u_j + \nabla_j u_i - \delta_{ij} \nabla \cdot \vec{u}) \chi^a \tag{85}
\end{aligned}$$

and we have to add a factor of $\frac{1}{10}$ that comes from the symmetry of the tensor: $[\delta^{li} \delta^{nj} + \delta^{lj} \delta^{ni} - \frac{2}{3} (\delta^{ln} \delta^{ij})]$. Comparing the functional form with the constitutive relation, we can see that:

$$\eta = \frac{1}{15} \tilde{S}_m \tilde{C}_{mn}^{-1} \tilde{S}_n, \tag{86}$$

Therefore, shear viscosity can be obtained by simply inverting the scattering matrix and multiplying it by the source vector. This procedure will be used for calculations in the following chapters.

Shear viscosity at leading logarithmic order

This chapter describes the first step toward studying chemical potentials in the QCD shear viscosity. For that, we make use of the kinetic theory description of the system detailed in Chapter 3. This kind of investigation of transport coefficients using kinetic theory was first carried out correctly by Arnold, Moore, and Yaffe in [13], where they obtained shear viscosity at leading logarithmic order in the coupling for a system with zero net baryon density in weakly coupled high-temperature QCD. In this regime, the temperature is taken to be much larger than the zero-temperature masses of elementary particles [13, 9], *i.e.*, we require that $T \gg \Lambda_{QCD}$ and $T \gg m_q$. Since we are interested in the chemical potential dependence, dense QCD means that $\mu \geq T$. This chapter is largely derived from my published work [41].

In the previous chapter, we elucidated the principles of kinetic theory and the derivation of the Boltzmann equation for abelian and non-abelian theories. We have also derived the theoretical framework necessary to compute transport coefficients for QGP. Here, we apply these principles and obtain shear viscosity as a function of the chemical potential, considering only contributions at leading logarithmic order on the coupling, g . For that, we present the relevant scattering processes and compute each contribution in detail. Later, we study a good basis set for these calculations. We then can extract the dependence of shear viscosity to the baryonic chemical potential. Here, we perform calculations as a function of μ , which represents the chemical potential from each quark, $\mu = \mu_B/3$. We will use this notation for all kinetic theory calculations performed in this thesis.

1 Collision Integrals at Finite Chemical Potentials

In this section, our objective is to determine the magnitude of the contribution from each diagram to $(\chi_{ij}, \mathcal{C}\chi_{ij})$. To achieve this, we adopt a method similar to that employed by Arnold, Moore, and Yaffe, where we transform the integration over \vec{p}' into an integration over $\vec{q} = \vec{p}' - \vec{p}$. In the weak coupling regime, the diagrams are predominantly influenced by small values of q . The frame choice here will be the plasma frame, in spherical coordinates

chosen with \vec{q} as the z -axis and \vec{p} lying in the $x - z$ plane:

$$\begin{aligned}
(\chi_{ij}, \mathcal{C}\chi_{ij}) &= \frac{\beta^3}{(4\pi)^6} \sum_{abcd}^{\text{ffhc}} \int_0^\infty q^2 dq p^2 dp k^2 dk \int_{-1}^1 d(\cos \theta_{pq}) d(\cos \theta_{kq}) \int_0^{2\pi} d\phi \\
&\times \frac{|\mathcal{M}_{cd}^{ab}|^2}{pkp'k'} \delta^4(P + K - P' - K') f_0^a(p) f_0^b(k) [1 \pm f_0^a(p)] [1 \pm f_0^b(k)] \\
&\times \left[\chi_{ij}^a(\vec{p}) + \chi_{ij}^b(\vec{k}) - \chi_{ij}^c(\vec{p}') - \chi_{ij}^d(\vec{k}') \right]^2
\end{aligned} \tag{1}$$

The azimuthal angle of \vec{k} is ϕ , and θ_{pq} is the plasma frame angle between \vec{p} and \vec{q} .

Following Baym et al. [22], we introduce $\omega = p' - p$, which, along with the energy-momentum delta functions, facilitates further simplification of the integrals:

$$\begin{aligned}
(\chi_{ij}, \mathcal{C}\chi_{ij}) &= \frac{\beta^3}{(4\pi)^6} \sum_{abcd}^{\text{ffhc}} \int_0^\infty dq \int_{-q}^q d\omega \int_{\frac{q-\omega}{2}}^\infty dp \int_{\frac{q+\omega}{2}}^\infty dk \int_0^{2\pi} d\phi \\
&\times \frac{|\mathcal{M}_{cd}^{ab}|^2}{pkp'k'} f f_0^a(p) f_0^b(k) [1 \pm f_0^c(p')] [1 \pm f_0^d(k')] \\
&\times \left[\chi_{ij}^a(\vec{p}) + \chi_{ij}^b(\vec{k}) - \chi_{ij}^c(\vec{p}') - \chi_{ij}^d(\vec{k}') \right]^2.
\end{aligned} \tag{2}$$

In general, the product between different species is given by:

$$\chi_{ij}^a(p) \chi_{ij}^b(k) = \chi^a(p) \chi^b(k) P_2(\cos \theta_{pk}) = \chi^a(p) \chi^b(k) \left(\frac{3}{2} \cos^2 \theta_{pk} - \frac{1}{2} \right) \tag{3}$$

which depends on $\cos \theta_{pk}$ through the Legendre polynomial $P_2(\cos \theta_{pk})$.

At weak coupling, the scattering processes involving t -channel gluon exchange exhibit a screened infrared divergence, resulting in significant contributions at small momentum transfer q . This behavior is well-documented in the literature; see, for instance, [22]. Similarly, the exchange of t -channel quarks leads to logarithmically large cross-sections, contributing to the interchange of particle types $g \leftrightarrow q$ or \bar{q} . The significance of each process is thus magnified by a logarithm of the ratio $\pi T/m_D$, where πT represents the typical particle energy and m_D denotes a screening scale typically small in the weak-coupling regime. In the leading-log approximation, we focus solely on these processes and the region of the scattering integrals where $m_D < q < \pi T$. This approximation simplifies our calculations, providing a qualitative description of how the viscosity evolves as μ/T increases.

The approximation $q \ll \pi T$ first allows us to continue the p, k integrals in Eq. (2) down to 0. Additionally, it simplifies the evaluation of matrix elements, allowing us to employ the following approximations for the Mandelstam variables:

$$\frac{-s}{t} \simeq \frac{u}{t} \simeq \frac{2pk}{q^2}(1 - \cos \phi). \quad (4)$$

One can also use that since $p \simeq p'$, in evaluating f_0 we neglect the difference between p and p' and between k' and k . Finally, for processes with a virtual quark in the t -channel we can approximate $\chi_{ij}^a(p) = \chi_{ij}^a(p')$. For processes with a virtual gluon, the species labels a and b are the same and this approximation gives zero. As the matrix element is strongly divergent, the best approach here is to expand the last line of Eq. (2) to linear order in q :

$$\chi_{ij}^a(\vec{p}) - \chi_{ij}^a(\vec{p}') = -\vec{q} \cdot \nabla \chi_{ij}^a(\vec{p}) + \mathcal{O}(q^2). \quad (5)$$

The collision operator requires the square of this quantity. Explicitly, the first term of Eq. (5) can be written as,

$$\vec{q} \cdot I_{i\dots j}(\hat{p}) \nabla(\chi^a(|\vec{p}|)) = w I_{i\dots j}(\hat{p}) \chi^a(|\vec{p}|)' \quad (6)$$

and the second term,

$$\begin{aligned} \vec{q} \cdot \nabla(I_{i\dots j}(\hat{p})) \chi^a(|\vec{p}|) &= \vec{q} \cdot \left[\sqrt{\frac{3}{2}}(\hat{p}_i \nabla \hat{p}_j + \hat{p}_j \nabla \hat{p}_i) \right] \chi^a(|\vec{p}|) \\ &= \sqrt{\frac{3}{2}} \left(\frac{q_i \hat{p}_j}{p} + \frac{q_j \hat{p}_i}{p} - 2 \frac{\hat{p}_i \hat{p}_j q_i \hat{p}_i}{p} \right) \chi^a(|\vec{p}|) \end{aligned} \quad (7)$$

Hence, the evaluation of this product gives:

$$[\chi_{ij}^a(\vec{p}) - \chi_{ij}^a(\vec{p}')]^2 = \omega^2 [\chi^a(|\vec{p}|)']^2 + 3 \frac{q^2 - \omega^2}{p^2} [\chi^a(p)]^2. \quad (8)$$

The term proportional to ω^2 describes the change in energy, while the term proportional to $q^2 - \omega^2 = q_\perp^2$ describes the change in direction. For the cross-contributions that arise in Eq. (2), one can use the approximations:

$$\cos \theta_{pq} \simeq \cos \theta_{kq} \simeq \cos \theta_{p'q} \simeq \cos \theta_{k'q} \simeq \frac{\omega}{q} \quad (9)$$

$$\cos \theta_{pk} \simeq \cos \theta_{p'k} \simeq \cos \theta_{pk'} \simeq \cos \theta_{p'k'} \simeq \frac{\omega^2}{q^2} + \frac{q^2 - \omega^2}{q^2} \cos \phi. \quad (10)$$

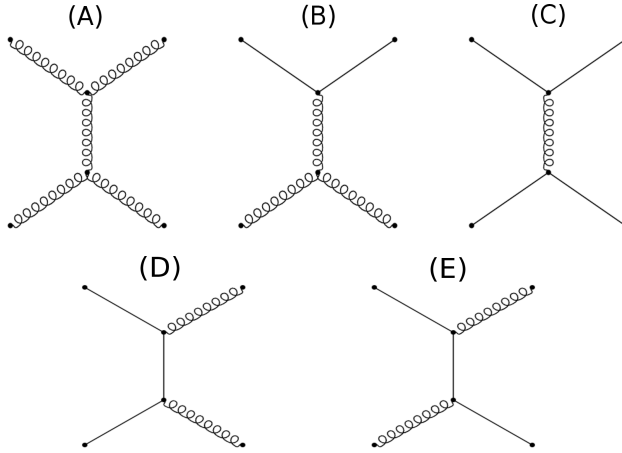


Figure 1: Leading log diagrams for the scattering processes in a gauge theory with fermions. Solid lines as fermions and the helices represent gluons. Time may be regarded as running horizontally.

For the leading log order calculations, we focus on infrared divergent scattering processes, shown in figure 1. Indeed, the inclusion of self-energies is enough to regulate these divergencies; however, in this chapter, we are only interested in obtaining the coefficient of the divergence, which translates to the size of each contribution to shear viscosity. The next subsections will be dedicated to computing each diagram in detail and discussing the large μ region.

1.1 Diagrams (A), (B) and (C)

For diagrams (A), (B), and (C), we will make use of some common approximations, as suggested in [13]. Despite describing different scatterings, in the soft particle exchange ($q \rightarrow 0$) limit, the vertices in diagrams (A)-(C) have a universal form that depends only on the color charge of the particle that is scattering. This simplification can be used for all three diagrams, and it has the form:

$$2p^\mu g t^a \delta_{hh'} \quad (11)$$

Where t^a is the color generator, and h and h' represent the helicities of the scattering particles. This approximation allows one to compute these diagrams easily:

$$|\mathcal{M}_{cd}^{ab}|_{\text{lead-log}}^2 = A_{ab} \frac{4p^2 k^2}{q^4} (1 - \cos \phi)^2 \quad (12)$$

where $A_{ab} = 4d_A T_{Ra} T_{Rb} g^4$, and we have only summed over the outgoing particles' helicity. Here $d_A = N_c^2 - 1 = 8$ is the dimension of the adjoint representation, and T_R is the trace normalization, $1/2$ for quarks, and $N_c = 3$ for gluons. After reinstating this matrix element into the integral and leveraging the relation (8), the integrals over ϕ and ω become straightforward. $\nabla_q \chi(p) \nabla_q \chi(k)$ cross-terms vanish upon integrating over ω and ϕ , leaving behind only those terms where the statistical function appears twice on one side of the diagram. The remaining ones are:

$$\begin{aligned} (\chi_{ij}, \mathcal{C}\chi_{ij})^{(A)-(C)} &= \sum_{ab}^{\text{fh}} \frac{2A_{ab} \beta^3 8\pi}{(4\pi)^6} \int_0^\infty dq \int_0^\infty dp \int_0^\infty dk \frac{k^2}{q} \\ &\quad \times f_0^a(p) f_0^b(k) [1 \pm f_0^a(p)] [1 \pm f_0^b(k)] \\ &\quad \times [p^2 [\chi^a(|\vec{p}|)']^2 + 6[\chi^a(p)]^2] \end{aligned} \quad (13)$$

The Bose-Einstein distributions are not dependent on the chemical potential, and the integral over k for diagram (A) is well known to give:

$$\int_0^\infty dk k^2 f_0^b(k) [1 \pm f_0^b(k)] = \lambda_b T^3 \frac{\pi^2}{6} \quad (14)$$

Where λ_b is 2 for bosons and 1 for fermions.

On the other hand, for diagram (B), there are two distinct contributions: The first is given when both χ factors correspond to the fermion line and the second when both χ factors correspond to the gluon line. In both cases, the integration over energy is feasible. From now on, we name the integrals after the departure from equilibrium we are left with; for example, B_f will result from integrating over the gluon momentum when quark χ -factors are present. Evaluating the contribution where both χ represent quarks, we find:

$$\begin{aligned} (\chi_{ij}, \mathcal{C}\chi_{ij})^{(B_f)} &= \sum_{ab}^{\text{fh}} \frac{4d_A T_{Ra} T_{Rb} \lambda_b}{2^9 3 \pi^3} \int_0^\infty dp f_0^f(p) [1 - f_0^f(p)] \\ &\quad \left\{ p^2 [\chi^f(|\vec{p}|)']^2 + 6 [\chi^f(p)]^2 \right\}. \end{aligned} \quad (15)$$

Here \sum^{fh} means that the sum runs over flavor and helicity but not over particle-antiparticle (which is explicit) or color (which is included in the color factors). Similarly, there is a contribution when the line represents an antiquark:

$$(\chi_{ij}, \mathcal{C}\chi_{ij})^{(B_{\bar{f}})} = \sum^{\text{fh}} \frac{4d_A T_{Ra} T_{Rb} \lambda_b}{2^9 3 \pi^3} \int_0^\infty dp f_0^{\bar{f}}(p) \left[1 - f_0^{\bar{f}}(p) \right] \left\{ p^2 \left[\chi^{\bar{f}}(|\vec{p}|)' \right]^2 + 6 \left[\chi^{\bar{f}}(p) \right]^2 \right\}. \quad (16)$$

These integrals depend on χ^f and must be performed numerically for each combination of basis functions, except for the case of $N = 1$, which can be computed analytically.

On the other hand, the bosons' departure from equilibrium is given after the integration over the fermion vertex is performed. The integral to be computed this time is:

$$\begin{aligned} & \sum_{\pm} \int_0^\infty dk k^2 \frac{1}{e^{\beta(k \pm \mu)} + 1} \left[1 - \frac{1}{e^{\beta(k \pm \mu)} + 1} \right] \\ &= \sum_{\pm} \int_0^\infty dk 2kT \frac{1}{e^{\beta(k \pm \mu)} + 1} \\ &= \frac{\pi^2 T^3}{3} + \mu^2 T. \end{aligned} \quad (17)$$

Once we put the results back in Eq. (2), we are left with:

$$(\chi_{ij}, \mathcal{C}\chi_{ij})^{(B_g)} = \sum_{ab}^{\text{h}} \frac{4A_{ab} \beta^3 8\pi}{(4\pi)^6} \left(\frac{T^3 \pi^2}{6} + \frac{T \mu^2}{2} \right) \times \int_0^\infty dp f_0^g(p) [1 + f_0^g(p)] \left\{ p^2 [\chi^g(p)]'^2 + 6 \chi^g(p)^2 \right\}. \quad (18)$$

We observe here that the gluonic contribution to diagram (B) surpasses the contribution to diagram (A) in regimes where the μ^2 term mentioned above significantly outweighs the T^2 term. Consequently, at high chemical potentials, diagram (B) will outweigh diagram (A) in significance.

Using the approximations described for diagrams (A) and (B), it is straightforward to compute diagram (C). This time, only fermionic departures from equilibrium are relevant, and the scatterer is always a fermion, leading to a $\mu^2 T + \pi^2 T^3/3$ type contribution similarly

to what was observed for diagram (B). Explicitly, one finds:

$$\begin{aligned}
(\chi_{ij}, \mathcal{C}\chi_{ij})^{(C_f)} &= \sum_{ab}^{\text{fh}} \frac{4A_{ab}\beta^3 8\pi}{(4\pi)^6} \left(\frac{T^3\pi^2}{6} + \frac{T\mu^2}{2} \right) \times \\
&\quad \int_0^\infty dp \left\{ f_0^f(p)[1 - f_0^f(p)] \left[p^2[\chi^f(p)]^2 + 6[\chi^f(p)]^2 \right] \right\} \\
(\chi_{ij}, \mathcal{C}\chi_{ij})^{(C_{\bar{f}})} &= \sum_{ab}^{\bar{\text{f}}h} \frac{4A_{ab}\beta^3 8\pi}{(4\pi)^6} \left(\frac{T^3\pi^2}{6} + \frac{T\mu^2}{2} \right) \times \\
&\quad \int_0^\infty dp \left\{ f_0^{\bar{f}}(p)[1 - f_0^{\bar{f}}(p)] \left[p^2[\chi^{\bar{f}}(p)]^2 + 6[\chi^{\bar{f}}(p)]^2 \right] \right\}
\end{aligned} \tag{19}$$

Compared to the χ^f -dependent term originated from the integration in diagram (B), this contribution is amplified by μ^2/T^2 and will prevail in the high chemical potential regime. Consequently, in this regime, the fermionic contributions to shear viscosity outweigh those from gluons, given that fermions dominate the stress tensor by a factor of μ^4/T^4 . Hence, diagram (C) is the most crucial process under these conditions.

1.2 Diagrams (D) and (E)

At leading logarithmic order on the coupling, diagrams (D) and (E) can be treated using the same approximations. Not only are these diagrams similar, but they are also highly suppressed in the high-density region. We will dedicate this section to carefully applying these approximations. We begin with diagram (D), which can take the following possibilities: $f\bar{f} \rightarrow gg$, $\bar{f}f \rightarrow gg$, $gg \rightarrow f\bar{f}$ and $gg \rightarrow \bar{f}f$. As the chemical potential increases, the number of anti-fermions decreases, and the rate for this process becomes small.

Using well-known results from QED, one should be able to compute diagram (D) and get:

$$|\mathcal{M}_{gg}^{f\bar{f}}|_{\text{lead-log}}^2 = A_f \left(\frac{u}{t} + \frac{t}{u} \right) \tag{20}$$

where $A_f = 4d_A T_{Rf} C_{Rf} g^4$. Interchanging the outgoing legs makes $t/u \rightarrow u/t$, so one can keep only u/t and multiply the result by 2. Diagrams (D) and (E) present an infrared log divergence, which allows one to make use of all possible small q approximations. In that sense, we write the equilibrium distributions as,

$$f_0(w+p) = f_0(p), \quad f_0(k-w) = f_0(k) \tag{21}$$

and the angles

$$\cos \theta_{pp'} \simeq \cos \theta_{kk'} \simeq 1 \quad (22)$$

That includes the fact that at small q the matrix element can be rewritten as:

$$\frac{u}{t} \simeq \frac{2kp}{q^2}(1 - \cos \phi). \quad (23)$$

Plugging these back into Eq. (2) gives:

$$\begin{aligned} (\chi_{ij}, \mathcal{C}\chi_{ij})^{(D)} &= \sum^{\text{fh}} \frac{4A_f \beta^3}{(4\pi)^6} \int_0^\infty dq \int_{-q}^q d\omega \int_0^\infty dk \int_0^{2\pi} d\phi (1 - \cos \phi) \frac{2pk}{q^2} \\ &\times f_0^f(p) f_0^{\bar{f}}(k) [1 \pm f_0^g(p)] [1 \pm f_0^g(k)] \left\{ [\chi^f(p) - \chi^g(k)]^2 \right. \\ &+ [\chi^{\bar{f}}(k) - \chi^g(k)]^2 + 2P_2(\cos \theta_{pk}) [\chi^f(p) - \chi^g(k)] \\ &\left. [\chi^{\bar{f}}(k) - \chi^g(k)] \right\}. \end{aligned} \quad (24)$$

The crossing terms vanish for $l > 0$ as a consequence of the orthogonality of the Legendre Polynomials, using Eq. (9):

$$\int_{-q}^q d\omega \int_0^{2\pi} d\phi P_2 \left(\frac{q^2 - \omega^2}{q^2} \cos \phi \right) (1 - \cos \phi) = 0 \quad (25)$$

For the remaining terms, the integrals over ω and ϕ are trivial. One is left with two possible integrals, one over fermions and one over anti-fermions. For the term involving the fermions, one must compute:

$$\int dk k \frac{1}{e^{\beta(k-\mu)} + 1} \left(1 + \frac{1}{e^{\beta k} - 1} \right) \quad (26)$$

Which gives:

$$\begin{aligned} (\chi_{ij}, \mathcal{C}\chi_{ij})^{(D_f)} &= \sum^{\text{fh}} \frac{4A_f \beta 8\pi}{(4\pi)^6} \int_0^\infty dp p f_0^f(p) [1 \pm f_0^g(p)] [\chi^f(p) - \chi^g(k)]^2 \\ &\times \left[\frac{2\pi^2}{6} + \frac{\mu^2}{2T^2} - \text{Li}_2 \left(\frac{e^{\mu/T}}{1 + e^{\mu/T}} \right) - \frac{1}{2} \ln^2 \left(1 + e^{\mu/T} \right) \right] \\ &\times \frac{1}{e^{\mu/T} + 1} \end{aligned} \quad (27)$$

And for the term involving anti-fermions:

$$\int dk k \frac{1}{e^{\beta(k+\mu)} + 1} \left(1 + \frac{1}{e^{\beta k} - 1} \right) \quad (28)$$

The result is:

$$\begin{aligned} (\chi_{ij}, \mathcal{C}\chi_{ij})^{(D_{\bar{f}})} &= \sum_{\bar{f}h} \frac{4A_f \beta 8\pi}{(4\pi)^6} \int_0^\infty dp p f_0^{\bar{f}}(p) [1 \pm f_0^g(p)] [\chi^{\bar{f}}(k) - \chi^g(k)]^2 \\ &\times \frac{e^{\mu/T}}{e^{\mu/T} + 1} \left(\frac{\pi^2}{6} - \text{Li}_2(-e^{\mu/T}) \right) \end{aligned} \quad (29)$$

The involvement of an incoming antiquark in this diagram causes these results to be suppressed by $e^{-\mu/T}$ in the large μ/T regime, as antiquarks become exponentially rare with a fugacity of $e^{-\mu/T}$.

Finally, the Compton scattering diagram (E) differs slightly from the annihilation diagram (D) in leading log order. As discussed in [13] for Compton scattering, the matrix element is given by $(-s/t)$, but at leading order in small q one can consider $-s/t = u/t$. The computation is straightforward and gives:

$$\begin{aligned} (\chi_{i\dots j}, \mathcal{C}\chi_{i\dots j})^{(E_f)} &= \sum_{fh} \frac{4A_f \beta 8\pi}{(4\pi)^6} \int_0^\infty dp p f_0^f(p) [1 \pm f_0^g(p)] [\chi^f(p) - \chi^g(p)]^2 \\ &\times e^{-\mu/T} \frac{e^{\mu/T}}{e^{\mu/T} + 1} \left(\frac{\pi^2}{6} - \text{Li}_2(-e^{\mu/T}) \right) \end{aligned} \quad (30)$$

$$\begin{aligned} (\chi_{ij}, \mathcal{C}\chi_{ij})^{(E_{\bar{f}})} &= \sum_{\bar{f}h} \frac{4A_f \beta 8\pi}{(4\pi)^6} \int_0^\infty dp p f_0^{\bar{f}}(p) [1 \pm f_0^g(p)] [\chi^{\bar{f}}(p) - \chi^g(p)]^2 \\ &\times \frac{e^{\mu/T}}{e^{\mu/T} + 1} \left[\frac{2\pi^2}{6} + \frac{\mu^2}{2T^2} - \text{Li}_2\left(\frac{e^{\mu/T}}{1 + e^{\mu/T}}\right) \right. \\ &\left. - \frac{1}{2} \ln^2(1 + e^{\mu/T}) \right]. \end{aligned} \quad (31)$$

As previously mentioned, diagram (E) is also highly suppressed in dense regions. At leading-log order, this phenomenon results from the fact that the final-state quark's energy matches the initial-state gluon's energy. To overcome a considerable Pauli blocking factor, the final-state quark must have an energy $E \geq \mu$. At the same time, a sufficiently energetic gluon has a Boltzmann suppression factor of $e^{-\mu/T}$, which makes it considerably difficult

to have a highly energetic final-state quark. Consequently, the process is again suppressed by $e^{-\mu/T}$. The Compton scattering of an antiquark is similarly suppressed because the incoming antiquark statistical function has the same $e^{-\mu/T}$ suppression factor. Therefore, processes (D) and (E) not only become less important in comparison with process (C), but their reduced importance is exponential and not just polynomial[41].

2 One-function ansatz calculations

As a warm-up, one can perform some of these integrals analytically. In this section, we obtain the scattering matrix for a one-function ansatz given by $\phi = p^2/T$. First, we compute the integrals for each possibility of our 5 diagrams, leaving a dependence on the chemical potential, and then we put these results in a scattering matrix.

We begin with diagram (A), which only considers contributions from boson scattering. Hence, at leading log order, the chemical potential won't play any part in this calculation, and the integrals can be easily computed as:

$$\begin{aligned}
(\chi_{i\dots j}, \mathcal{C}\chi_{i\dots j})^{(A)} &= \sum_{ab}^h \frac{4d_A T_{Ra} T_{Rb} \lambda_b}{2^8 3\pi^3} \int_0^\infty dp f_0^g(p) [1 + f_0^g(p)] \{p^2 [\chi^g(p)]^2 \\
&\quad + 6\chi^g(p)^2\} \\
&= \frac{d_A T_A T_A}{24\pi^3} \int_0^\infty dp \left[\frac{1}{e^{\frac{p^2}{T}} - 1} \left(1 + \frac{1}{e^{\frac{p^2}{T}} - 1} \right) \right] \left(\frac{4p^2}{T^2} + \frac{6p^4}{T^2} \right) \\
&= \frac{10d_A T_A T_A T^3}{24\pi^3} 4! \zeta(4) \\
&= \frac{\pi T^3 d_A T_A T_A}{9}
\end{aligned} \tag{32}$$

On the other hand, diagram (B) has one vertice with external gluons states and another with external quark states. Using the same definitions from the last section, we can write:

$$\begin{aligned}
(\chi_{i\dots j}, \mathcal{C}\chi_{i\dots j})^{(B_q)} &= \sum^{fh} \frac{4d_A T_{Ra} T_{Rb} \lambda_b}{2^9 3\pi^3} \int_0^\infty dp f_0^f(p) [1 - f_0^f(p)] \\
&\quad \left\{ p^2 [\chi^f(|\vec{p}|)]^2 + 6[\chi^f(p)]^2 \right\}
\end{aligned} \tag{33}$$

$$= \frac{16d_A T_A N_f T_F}{2^9 3\pi^3} \int_0^\infty dp \frac{p^4 e^{p-\mu}}{(e^{p-\mu} + 1)^2} \tag{34}$$

To perform the integral, one can use the relation:

$$F_s(x) = \frac{1}{\Gamma(s+1)} \int_0^\infty \frac{t^s}{e^{t-x} + 1} dt = -\text{Li}_{s+1}(-e^x) \quad (35)$$

and that gives us:

$$(\chi_{i\dots j}, \mathcal{C}\chi_{i\dots j})^{(B_q)} = -\frac{10d_A T_A N_f T_F T^3}{\pi^3} \text{Li}_4(-e^{\mu/T})$$

Analogously for anti-fermions:

$$\begin{aligned} (\chi_{i\dots j}, \mathcal{C}\chi_{i\dots j})^{(B_{\bar{q}})} &= \sum^{fh} \frac{4d_A T_{Ra} T_{Rb} \lambda_b}{2^9 3 \pi^3} \int_0^\infty dp f_0^f(p) [1 - f_0^f(p)] \\ &\quad \left\{ p^2 [\chi^{\bar{f}}(|\vec{p}|)]^2 + 6 [\chi^{\bar{f}}(p)]^2 \right\} \end{aligned} \quad (36)$$

$$\begin{aligned} &= \frac{16d_A T_A N_f T_F T^3}{2^9 3 \pi^3} \int_0^\infty dp \frac{p^4 e^{p+\mu}}{(e^{p+\mu} + 1)^2} \\ &= -\frac{10d_A T_A N_f T_F T^3}{\pi^3} \text{Li}_4(-e^{-\mu/T}) \end{aligned} \quad (37)$$

$$(38)$$

There is also the possibility of starting the integration by the fermionic vertex, which allows us to work on the departure from equilibrium from bosons:

$$\begin{aligned} (\chi_{i\dots j}, \mathcal{C}\chi_{i\dots j})^{(B_g)} &= \sum_{ab}^{\bar{f}hc} \frac{4A_{ab} \beta^3 8\pi}{(4\pi)^6} \left(\frac{T^3 \pi^2}{6} + \frac{T\mu^2}{2} \right) \int_0^\infty dp \\ &\quad f_0^g(p) [1 + f_0^g(p)] \left\{ p^2 [\chi^g(p)]^2 + 6 \chi^g(p)^2 \right\} \\ &= \frac{N_f T_F d_A T_A}{12\pi^3} \left(\frac{T^3 \pi^2}{6} + \frac{T\mu^2}{2} \right) \int_0^\infty dp \frac{p^4 e^p}{(e^p - 1)^2} \\ &= \frac{2N_f T_F d_A T_A T^3}{3\pi} \left(\frac{\pi^2}{6} + \frac{\mu^2}{2T^2} \right) \end{aligned} \quad (39)$$

Diagram (C) has only fermionic vertexes. The collision integrals can be computed again

using relation Eq. (35), which gives:

$$\begin{aligned}
(\chi_{i\dots j}, \mathcal{C}\chi_{i\dots j})^{(C_q)} &= \sum_{ab}^{fhc} \frac{4A_{ab}\beta^3 8\pi}{(4\pi)^6} \left(\frac{T^3\pi^2}{6} + \frac{T\mu^2}{2} \right) \int_0^\infty dp \\
&\quad \left\{ f_0^f(p)[1 - f_0^f(p)] \left[p^2[\chi^f(p)]'^2 + 6[\chi^f(p)]^2 \right] \right\} \\
&= \frac{d_A N_f T_F N_f T_F T^3}{32\pi^5} \left(\frac{\pi^2}{6} + \frac{\mu^2}{2T^2} \right) \int_0^\infty dp \frac{p^4 e^{p-\mu}}{(e^{p-\mu} + 1)^2} \\
&= -\frac{60d_A N_f T_F N_f T_F T^3}{\pi^5} \left(\frac{\pi^2}{6} + \frac{\mu^2}{2T^2} \right) \text{Li}_4(-e^{\mu/T}) \quad (40)
\end{aligned}$$

Repeat these steps for anti-fermionic external states ($C_{\bar{q}}$),

$$\begin{aligned}
(\chi_{i\dots j}, \mathcal{C}\chi_{i\dots j})^{(C_{\bar{q}})} &= \sum_{ab}^{\bar{f}hc} \frac{4A_{ab}\beta^3 8\pi}{(4\pi)^6} \left(\frac{T^3\pi^2}{6} + \frac{T\mu^2}{2} \right) \int_0^\infty dp \\
&\quad \left\{ f_0^{\bar{f}}(p)[1 - f_0^{\bar{f}}(p)] \left[p^2[\chi^{\bar{f}}(p)]'^2 + 6[\chi^{\bar{f}}(p)]^2 \right] \right\} \\
&= \frac{d_A N_f T_F N_f T_F T^3}{32\pi^5} \left(\frac{\pi^2}{6} + \frac{\mu^2}{2T^2} \right) \int_0^\infty dp \frac{p^4 e^{p+\mu}}{(e^{p+\mu} + 1)^2} \\
&= -\frac{60d_A N_f T_F N_f T_F T^3}{\pi^5} \left(\frac{\pi^2}{6} + \frac{\mu^2}{2T^2} \right) \text{Li}_4(-e^{-\mu/T}) \quad (41)
\end{aligned}$$

Finally, diagram (D) has contributions that are not diagonal; this means contributions of the type $\chi^f \chi^g$ and $\chi^{\bar{f}} \chi^g$, so we divide it into 3 integrals:

$$\int_0^\infty dp p f_0^f(p)[1 \pm f_0^g(p)] \left[\chi^f(p) \right]^2 \quad (42)$$

$$\int_0^\infty dp p f_0^f(p)[1 \pm f_0^g(p)] \left[\chi^g(p) \right]^2 \quad (43)$$

$$-\int_0^\infty dp p f_0^f(p)[1 \pm f_0^g(p)] \left[\chi^f(p) \chi^g(p) \right] \quad (44)$$

Because of the basis choice, for the one parameter ansatz, the three integrals will look the

same:

$$\begin{aligned}
(\chi_{i\dots j}, \mathcal{C}\chi_{i\dots j})^{(D_q)} &= \sum_f^{\bar{f}h} \frac{4A_f\beta 8\pi}{(4\pi)^6} \int_0^\infty dp p f_0^f(p) [1 \pm f_0^g(p)] [\chi(p)]^2 \frac{1}{e^\mu + 1} \\
&\times \left[\frac{2\pi^2}{6} + \frac{\mu^2}{2} - \text{Li}_2\left(\frac{e^\mu}{1+e^\mu}\right) - \frac{1}{2} \ln^2(1+e^\mu) \right] \quad (45)
\end{aligned}$$

The integral we must compute is:

$$\int p^5 dp \frac{1}{e^{p-\mu} + 1} \left(1 + \frac{1}{e^p - 1} \right) \quad (46)$$

where $p/T \rightarrow p$ and $\mu/T \rightarrow \mu$. We rewrite it as:

$$e^\mu \int dp \frac{p^5 e^p}{(e^p - 1)(e^p + e^\mu)} \quad (47)$$

Now we make the same change of variables $v = e^p - 1$, $p = \ln(v + 1)$ and $dp = e^{-p} dv$:

$$e^\mu \int dv \frac{\ln^5(v + 1)}{v(v + e^\mu + 1)}$$

And integrate this by parts. This gives:

$$\begin{aligned}
(\chi_{i\dots j}, \mathcal{C}\chi_{i\dots j})^{(D_q)} &= \frac{N_f d_A T_F C_F T^3}{8\pi^5} \left[\frac{8e^{\mu/T} (\pi^6 - 945 \text{Li}_6(-e^{\mu/T}))}{63(e^{\mu/T} + 1)} \right] \frac{1}{e^\mu + 1} \\
&\times \left[\frac{2\pi^2}{6} + \frac{\mu^2}{2} - \text{Li}_2\left(\frac{e^\mu}{1+e^\mu}\right) - \frac{1}{2} \ln^2(1+e^\mu) \right]
\end{aligned}$$

This result is also the contribution for $\chi^f \chi^g$ and $\chi^g \chi^g$. We repeat the process for the anti-fermions.

$$\begin{aligned}
(\chi_{i\dots j}, \mathcal{C}\chi_{i\dots j})^{(D_{\bar{q}})} &= \sum_f^{\bar{f}h} \frac{4A_f\beta 8\pi}{(4\pi)^6} \int_0^\infty dp p f_0^{\bar{f}}(p) [1 \pm f_0^g(p)] [\chi^{\bar{f}}(p) - \chi^g(p)]^2 \\
&\times \frac{e^\mu}{e^\mu + 1} \left(\frac{\pi^2}{6} - \text{Li}_2(-e^\mu) \right)
\end{aligned}$$

Again, we only need to perform one of the integrals, and we can use the same change of variables we did before and integrate by parts a few times.

$$\begin{aligned}
(\chi_{i\dots j}, \mathcal{C}\chi_{i\dots j})^{(D\bar{q})} &= \frac{N_f d_A T_F C_F T^3}{8\pi^5} \left[\frac{8e^{\mu/T} (\pi^6 - 945\text{Li}_6(-e^{-\mu/T}))}{63(e^{\mu/T} + 1)} \right] \\
&\times \frac{e^\mu}{e^\mu + 1} \left(\frac{\pi^2}{6} - \text{Li}_2(-e^\mu) \right)
\end{aligned}$$

This result is also the contribution for $\chi^{\bar{f}}\chi^g$ and $\chi^g\chi^g$. So this diagram contributes for the scattering matrix with the terms $\chi^g\chi^g$, $\chi^{\bar{f}}\chi^g$ and $\chi^{\bar{f}}\chi^{\bar{f}}$. At last, the remaining integrals for diagram (E) will be exactly the same as computed for diagram (D),

$$\begin{aligned}
(\chi_{i\dots j}, \mathcal{C}\chi_{i\dots j})^{(E_q)} &= \frac{N_f d_A T_F C_F T^3}{8\pi^5} \left[\frac{8e^{\mu/T} (\pi^6 - 945\text{Li}_6(-e^{-\mu/T}))}{63(e^{\mu/T} + 1)} \right] \\
&\times \frac{1}{e^\mu + 1} \left(\frac{\pi^2}{6} - \text{Li}_2(-e^\mu) \right)
\end{aligned} \tag{48}$$

$$\begin{aligned}
(\chi_{i\dots j}, \mathcal{C}\chi_{i\dots j})^{(E\bar{q})} &= \frac{N_f d_A T_F C_F T^3}{8\pi^5} \left[\frac{8e^{\mu/T} (\pi^6 - 945\text{Li}_6(-e^{-\mu/T}))}{63(e^{\mu/T} + 1)} \right] \\
&\times \frac{e^\mu}{e^\mu + 1} \left[\frac{2\pi^2}{6} + \frac{\mu^2}{2} - \text{Li}_2\left(\frac{e^\mu}{1 + e^\mu}\right) \right. \\
&\left. - \frac{1}{2} \ln^2(1 + e^\mu) \right]
\end{aligned} \tag{49}$$

These integrals can now be evaluated for each chemical potential of interest and will be the input for the scattering matrix, which is organized as follows,

$$\tilde{C} = \begin{bmatrix} \chi^g\chi^g & -\chi^g\chi^q & -\chi^g\chi^{\bar{q}} \\ -\chi^q\chi^g & \chi^q\chi^q & 0 \\ -\chi^{\bar{q}}\chi^g & 0 & \chi^{\bar{q}}\chi^{\bar{q}} \end{bmatrix} \tag{50}$$

So, for example, the first coordinate of this matrix, represented by $\chi^g\chi^g$, is the result of the sum of all integrals that have contributions for external gluon states. Hence, all diagrams but diagram (C). The zeros are a consequence of Eq. (25).

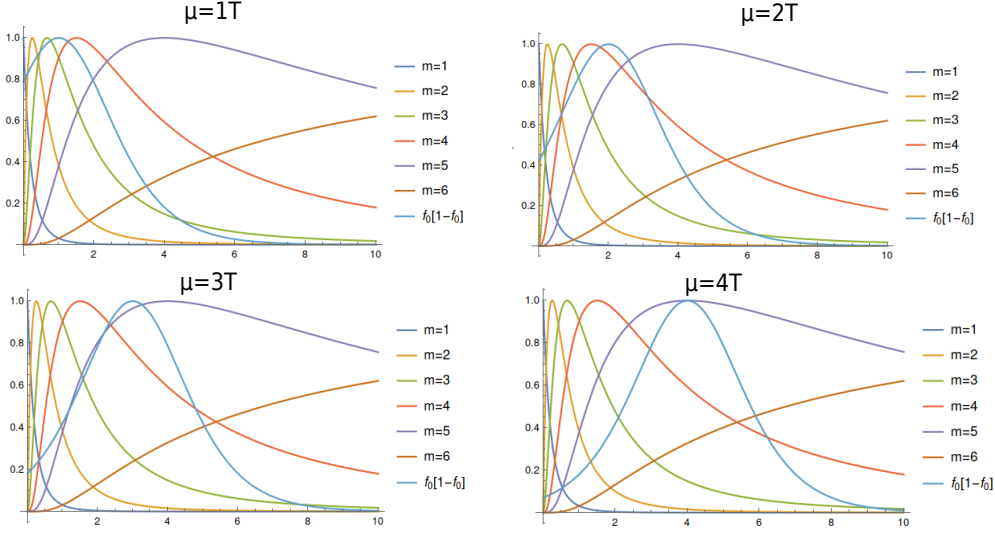


Figure 2: Basis set as a function of the momentum for $N = 6$ normalized by the one-function ansatz p^2/T , plotted along with the statistical function for $\mu = 0$

3 The basis set

In this section, we check the convergence of our results as the basis size is expanded. The procedure implemented in this work is based on an extremization technique that uses a finite-sized functional basis, as discussed around Eq. (81). For this work, we have used the basis set proposed in Ref. [13]:

$$\phi^{(m)} = \frac{p(p/T)^m}{(1 + p/T)^{N-1}}, \quad m = 1, \dots, N. \quad (51)$$

In figure (2), we display the basis set for $N = 6$ as a function of momentum for different values of μ . Each curve represents $\phi^{(m)}$ as m goes from 1 to N normalized by the 1-parameter ansatz, $\phi = p^2/T$. Along with that, we also plot the statistical distribution $f_0[1 - f_0]$ as functions of momentum for chemical potential varying between $1T$ and $4T$.

The subspace defined by this basis strictly increases as N is increased. However, we check that there is rapid convergence as we increase N . Therefore, we vary N in Eq. (51) and examine how the resulting shear viscosity changes. This is illustrated in figure 4, which shows the difference of the N -basis answer from the 6-basis answer for $N = 1, 2, 3, 4, 5$. We observe a rapid convergence with basis size, although the single-function basis works

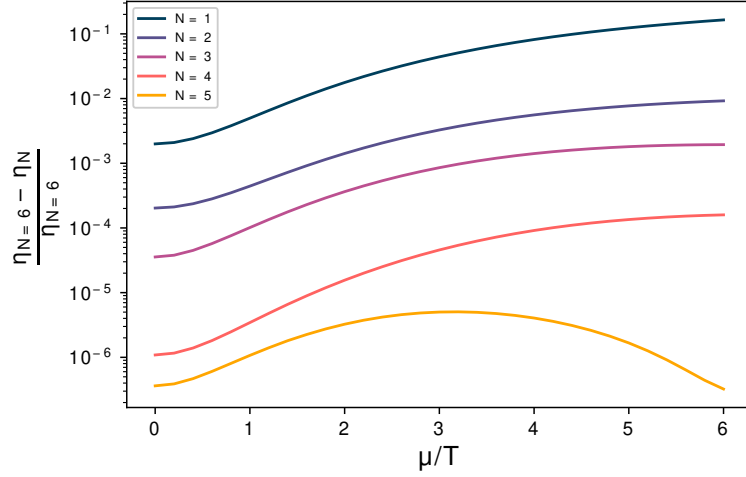


Figure 3: Basis-size dependence of the extracted shear viscosity. The curves show the relative error for the different basis set sizes compared to $N = 6$.

much less well than in the $\mu = 0$ case. In what follows, we will use $N = 6$, which the figure indicates is more than sufficient to eliminate issues associated with finite basis size.

4 Results

In the previous sections, we have derived all the computational apparatus necessary to obtain shear viscosity as a function of the chemical potential. We have also demonstrated the importance of each diagram for the different regimes of interest and tested the convergence of our results with the basis choice presented. Now, we display the result for shear viscosity calculated with a 6-function basis in figure 4.

The figure shows that the shear viscosity depends strongly on μ when expressed in units of the temperature T . Physically, this phenomenon is a consequence of the rapid increase in the number of quarks as μ/T escalates at fixed T . Therefore, it makes sense to normalize the shear viscosity in terms of something that gives a more physically relevant result. For that, we write the thermodynamical quantities of interest for a free gas of u , d , s flavors, using the partition function[143],

$$T \ln Z_{QGP} = \frac{g_g V}{90\pi^2} T^4 + \frac{g_f V}{12} \left(\frac{7\pi^2}{30} T^4 + \mu^2 T^2 + \frac{1}{2\pi^2} \mu^4 \right) \quad (52)$$

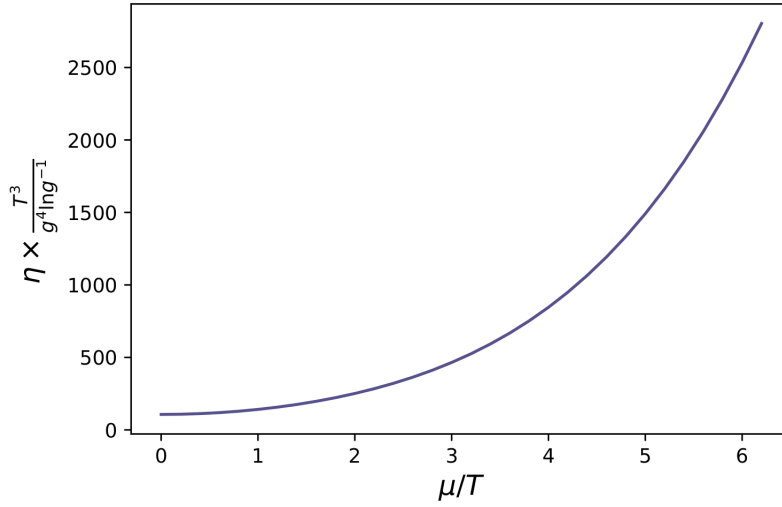


Figure 4: Shear viscosity, normalized to the temperature, for a 6-function basis, 3 flavors of quarks and $N_c = 3$, as a function of chemical potential. For $\mu = 0$, we recover the value obtained in Ref. [13].

Here, $g_g = 16$ accounts for the gluon degrees of freedom since the gluon has 8 colors and two helicities. The factor $g_f = 18$ accounts for 2 helicities, 3 flavors, and 3 colors for the quarks. Therefore, the leading-order entropy density s , pressure \mathcal{P} , and energy density e , as functions of (T, μ) , are:

$$s = \frac{19\pi^2}{9}T^3 + 3\mu^2T \quad (53)$$

$$3\mathcal{P} = e = \frac{19\pi^2 T^4}{12} + \frac{9}{2}\mu^2 T^2 + \frac{9\mu^4}{4\pi^2}$$

In figure 5, we show the shear-viscosity to entropy density ratio η/s , and in figure 6, we plot the ratio of the shear viscosity to the enthalpy density, $\eta T/(e + P)$, also referred in the hydrodynamics community as the kinematic shear viscosity. The advantage of η/s is that the ratio is directly dimensionless, and it is also a combination that has been speculated to satisfy a conjectured lower bound [94]. In both plots, a factor of $g^4 \ln(g)$ is extracted such that the result is a single dimensionless curve valid at all coupling strengths in the leading-log approximation. On top of that, all results shown here were computed using a 6-function basis set and considering the 3-color, 3-flavor case, which is of the most physical interest.

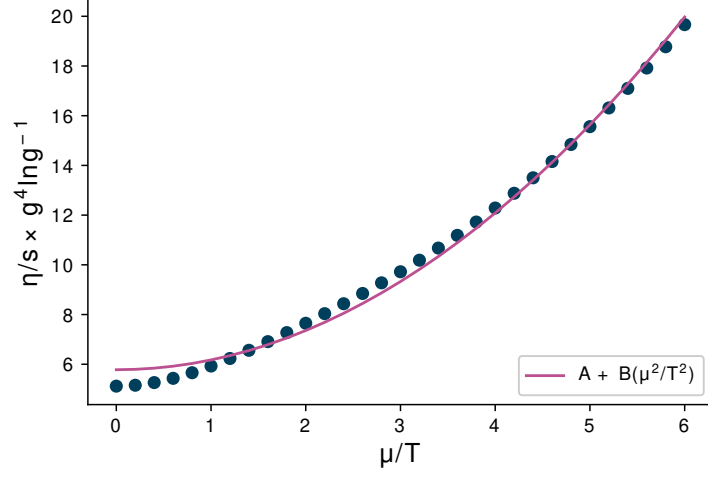


Figure 5: Shear viscosity divided by the entropy density as a function of μ . The points represent our leading-log calculation. The pink line is a quadratic fit, which gives a fair but imperfect representation of our result.

Figure 5 clearly shows that this ratio follows a parabola in the high-density region. That can be interpreted as follows. The dominant scattering mechanism for particles to change their direction is the $\ell(\ell + 1)\chi^2$ term in the collision operator in Eq. (8). For soft scattering, this is well described in terms of momentum diffusion with a momentum-diffusion coefficient \hat{q} :

$$\hat{q} \equiv \int \frac{d^2 q_{\perp}}{(2\pi)^2} q_{\perp}^2 C(q_{\perp}) \quad (54)$$

where $C(q_{\perp})$ is the differential rate to exchange transverse momentum q_{\perp} . In a thermal system without chemical potential, this is given by:

$$C(q_{\perp}) = g^2 C_F T \frac{m_D^2}{(q_{\perp}^2)(q_{\perp}^2 + m_D^2)} \quad (55)$$

In a high-density regime, the expression for \hat{q} remains the same, but the Debye screening mass is now dependent on the chemical potential, that is, it takes the value of $m_D^2 \sim g^2 \mu^2$. This causes an increase in the value of the form $\hat{q} \sim g^4 \mu^2 T$. At the same time, the amount by which a particle must change momentum for the system to equilibrate also increases and is directly dependent on the chemical potential, $(\Delta p)^2 \sim \mu^2$ rather than T^2 . The time

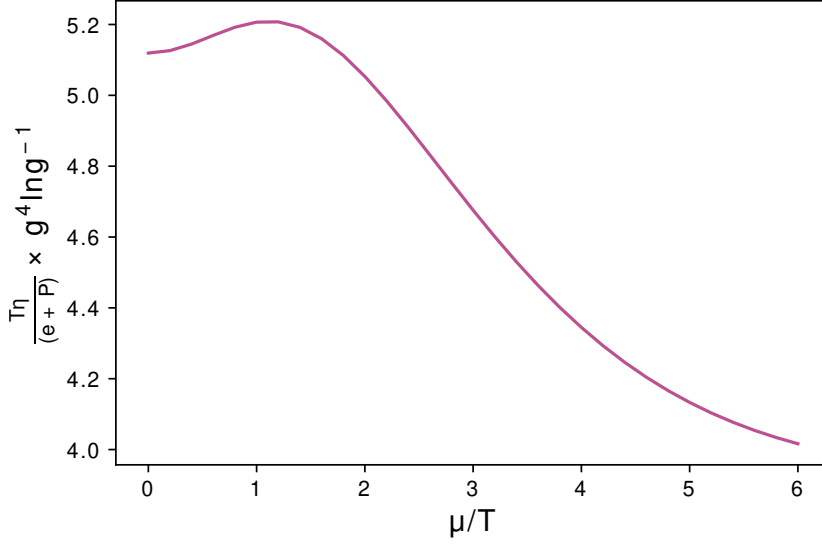


Figure 6: Kinematic shear viscosity $\eta T/(e + \mathcal{P})$ as a function of μ .

scale necessary for the system to equilibrate can then be estimated as:

$$t \sim \frac{(\Delta p)^2}{\hat{q}} \sim \frac{1}{g^4 T} \quad (56)$$

Hence, shear viscosity can be estimated as:

$$\eta \sim \frac{P}{t} \sim \frac{\mu^4}{g^4 T}. \quad (57)$$

As Eq. (53) shows, at large μ/T , the entropy scales as $s \propto \mu^2 T$. Therefore, one would expect that η/s behaves as:

$$g^4 \log(g^{-1}) \eta/s = A + B \mu^2/T^2. \quad (58)$$

Naturally, the true curve does not follow this form precisely since there is a transition, as μ/T is increased, from a system where gluons carry much of the energy and cause much of the scattering to a system where both are dominated by quarks[41]. However, the expectation for parabolic behavior at large μ/T is certainly justified in this calculation.

In contrast with η/s , which is of theoretical interest, the kinematic viscosity $\eta T/(e + P)$ holds more physical relevance, directly controlling the time scale on which the system approaches equilibrium. This significance arises from the enthalpy density's role in hydrodynamic equations alongside shear viscosity. Since both η and $e + P$ scale as μ^4 in the large- μ regime, we expect the ratio $T\eta/(e + P)$ to depend weakly on μ/T and to approach a constant at large μ/T [41]. This is observed in our results. Interestingly, this constant value is smaller than the value we obtain at $\mu = 0$, indicating that, in terms of the time scale $1/T$, a high-density fluid will relax somewhat more quickly than one at vanishing chemical potential[41]. The same behavior is also present in $\eta T/(e + P)$ calculations using holography for strongly coupled fluids[69], as mentioned earlier in this thesis.

Shear response function for a quartic self-interacting theory

So far in this thesis, we have computed shear viscosity for QGP in leading log order using kinetic theory to describe our system. Here, we use a similar description in terms of relativistic dissipative hydrodynamic models [45, 44, 133, 129, 119, 130] to study the shear response on a scalar theory. As explained in Chapter 2, hydrodynamics describes the long-time, long-wavelength behavior of the conserved quantities of a given system. Information on the dynamics is then encoded in the conserved currents of the system, such as the energy-momentum tensor and particle currents. When the system is in local equilibrium, the evolution of these currents is dictated by thermodynamic parameters such as temperature, chemical potential, and the four-velocity of the fluid [126].

The most widely used viscous hydrodynamic formulation in heavy-ion collisions was first proposed by Israel and Stewart [80, 81]. The interpretation of Israel-Stewart-like theories is subject to ongoing debate, as they involve various transport coefficients beyond the shear and bulk viscosities [110, 144]. Here, we are interested in the perspective that posits that Israel-Stewart-like equations of motion and their transport coefficients should reflect the underlying microscopic interactions, extending the regime of validity of Navier-Stokes theory to the transient non-equilibrium regime [126, 47, 45, 43, 108]. In this view, the relaxation time of a dissipative current is associated with a pole of the retarded Green's function governing the underlying dynamics in the linearized regime [47]. However, evidence suggests that the shear-stress retarded Green's function may possess a branch-cut singularity that touches the origin in frequency space [110, 117, 58].

In this Chapter, we study the shear-stress linear response function and investigate the existence of a branch cut touching the origin in a system of scalar self-interacting particles, even when Boltzmann statistics are used. This is done using recent developments [46], where the spectrum and eigenfunctions of the linearized collision term were computed exactly for this system. Therefore, the presence of the branch cut in this system is not attributed to Bose statistics effects but likely arises from the interaction characteristics of the particles, such as a vanishing cross-section at high energy, observed in both quantum and classical regimes. This chapter is based on the work from [125] done with collaborators.

Here, we include the numerical calculations I carried out with the help of K. Ingles and cross-checked with G. Rocha's version.

1 Kinetic Theory and Hydrodynamics

In Chapter 3, we have carefully derived the Boltzmann equation for scalar theories as a first step to achieve the derivation of this equation for gauge theories. In this chapter, we make use of Eq. (41) in a slightly different notation. If quantum statistics effects are neglected and only two-to-two processes are considered, it reads [42],

$$p^\mu \partial_\mu f_{\mathbf{p}} = \int dK dK' dP' W_{pp' \leftrightarrow kk'} (f_{\mathbf{p}} f_{\mathbf{k}'} - f_{\mathbf{p}'} f_{\mathbf{k}}), \quad (1)$$

where we introduced the Lorentz-invariant integral measure for on-shell massless particles, given by $dP \equiv d^3p/[(2\pi)^3 p^0]$, similarly to Chapter 3. Here, we define W as the transition rate, given by

$$W_{pp' \leftrightarrow kk'} = (2\pi)^6 s \sigma(s, \Theta) \delta^{(4)}(p + p' - k - k'), \quad (2)$$

and $\sigma(s, \Theta)$ is the differential cross section, which depends on the Mandelstam Variable s . For the calculations performed here, we use the most minus $(+, -, -, -)$ metric signature, contrasting with the previous Chapters, but we keep natural units so that $\hbar = c = k_B = 1$.

As mentioned above, in this study, we consider a system composed of massless scalar particles whose dynamics are given by the Lagrangian density,

$$\mathcal{L} = \frac{1}{2} \partial_\mu \varphi \partial^\mu \varphi - \frac{\lambda \varphi^4}{4!}. \quad (3)$$

In this case, the corresponding total cross section at leading order in the coupling constant is given simply by[121],

$$\sigma_T(s) = \frac{1}{2} \int d\Phi d\Theta \sin \Theta \sigma(s, \Theta) = \frac{\lambda^2}{32\pi s} \equiv \frac{g}{s}, \quad (4)$$

where Φ is the azimuthal angle in the momentum rest frame and $g \equiv \lambda^2/(32\pi)$.

The energy-momentum tensor for this system will be given by Eq. (12), with the correction terms from Eq. (13), using the convention that $\pi^{\mu\nu} = -\eta\sigma^{\mu\nu}$ is the shear-stress tensor we can write,

$$T^{\mu\nu} = \varepsilon u^\mu u^\nu - P \Delta^{\mu\nu} + \pi^{\mu\nu}, \quad (5)$$

and the particle four-current is written as

$$N^\mu = n u^\mu + \nu^\mu, \quad (6)$$

where n is the total particle density, and ν^μ is the particle diffusion 4-current. In what follows, we shall consider linear perturbations around a local equilibrium state. Then, assuming Landau's prescription for the definition of this state gives

$$n \equiv n_0(\mu, T), \quad \varepsilon \equiv \varepsilon_0(\mu, T) \quad P \equiv P_0(\mu, T) + \Pi, \quad (7)$$

which define μ and T , so the total particle and energy density coincides with the local equilibrium. In the above equation, Π is the bulk viscous pressure. In Kinetic Theory, the components related to the local equilibrium state, appearing in Eq. (6), can be computed by performing integrals in momentum space, as shown in Chapter 4.1. Using Eq. (66) and Eq. (53), we can also write the constitutive relation for the pressure as,

$$P_0 \equiv -\frac{1}{3}\Delta_{\mu\nu}T^{\mu\nu} = \frac{1}{3}\int dP (-\Delta_{\mu\nu}p^\mu p^\nu) f_{0\mathbf{p}}, \quad (8)$$

where $\Delta^{\mu\nu}$ was defined in Eq. (5), and the equilibrium distribution is the usual one, as presented in Eq. (62). Using this, we can write the remaining dissipative currents

$$\begin{aligned} \Pi &\equiv \frac{1}{3}\int dP (-\Delta_{\mu\nu}p^\mu p^\nu) (f_{\mathbf{p}} - f_{0\mathbf{p}}), \\ \nu^\mu &\equiv \Delta_\nu^\mu N^\nu = \int dP p^{\langle\mu} f_{\mathbf{p}}, \\ \pi^{\mu\nu} &\equiv \Delta_{\alpha\beta}^{\mu\nu}T^{\alpha\beta} = \int dP p^{\langle\mu} p^{\nu\rangle} f_{\mathbf{p}}, \end{aligned} \quad (9)$$

where we introduced the double symmetric, traceless projection tensor,

$$\Delta^{\mu\nu\alpha\beta} \equiv \frac{1}{2}\left(\Delta^{\mu\alpha}\Delta^{\nu\beta} + \Delta^{\nu\alpha}\Delta^{\mu\beta}\right) - \frac{1}{3}\Delta^{\mu\nu}\Delta^{\alpha\beta}. \quad (10)$$

We also note that, for massless particles and Landau matching conditions, the bulk viscous pressure is $\Pi = 0$.

2 Linear response theory for the shear-stress tensor

In this section, we investigate the linear response theory for a system of self-interacting scalar particles based on the Boltzmann equation. We focus on the shear tensor's contribution and consider it the only relevant one. Additionally, this section presents the results for the eigensystem of the linearized collision term. Understanding the basis formed

by the eigenfunctions of this operator is crucial for our analysis. We begin by writing cross-section given by Eq. (4) for a ϕ^4 theory and Boltzmann statistics as

$$\begin{aligned} p^\mu \partial_\mu f_{0\mathbf{p}} + p^\mu \partial_\mu \delta f_{\mathbf{p}} &= \frac{g}{2} \int dK dK' dP' (2\pi)^5 \delta^{(4)}(p + p' - q - q') \\ &\times f_{0\mathbf{p}} f_{0\mathbf{p}'} (\phi_{\mathbf{k}} + \phi_{\mathbf{k}'} - \phi_{\mathbf{p}} - \phi_{\mathbf{p}'}) \\ &\equiv f_{0\mathbf{p}} \hat{L} \phi_{\mathbf{p}}, \end{aligned} \quad (11)$$

where $\phi_{\mathbf{p}}$ is the relative deviation from local equilibrium, defined similarly to Chapter 4 (Eq. (64)), but without the Bose stimulation factor. In general, $p^\mu \partial_\mu f_{0\mathbf{p}}$ is expressed in terms of gradients of perturbations in temperature, chemical potential, and fluid four-velocity. Next, we consider that only gradients related to the shear stress are relevant,

$$p^\mu \partial_\mu f_{0\mathbf{p}} \simeq -f_{0\mathbf{p}} \beta p^{\langle \mu} p^{\nu \rangle} \sigma_{\mu\nu}, \quad (12)$$

where $\sigma_{\mu\nu}$ is given in Eq. (14). Here, we define δu_μ as the 4-velocity perturbations and the velocity of the unperturbed system as u_μ . It is important to note that in the linear regime, $u_\mu \delta u^\mu = 0$. Additionally, all projections are now taken with respect to u_μ .

At this point, we perform some simplifications analogously to Chapter 3. We assume that non-equilibrium perturbations are spatially homogeneous. This implies that space-like gradients of $\delta f_{\mathbf{p}}$ in the local rest frame are negligible, and therefore the Boltzmann equation can be written as

$$p^\mu \partial_\mu \delta f_{\mathbf{p}} = E_{\mathbf{p}} u^\mu \partial_\mu \delta f_{\mathbf{p}} + p^\mu \nabla_\mu \delta f_{\mathbf{p}} \simeq E_{\mathbf{p}} u^\mu \partial_\mu \delta f_{\mathbf{p}}, \quad (13)$$

where $E_{\mathbf{p}} \equiv u_\mu p^\mu$ and $\nabla_\mu = \Delta_\mu^\nu \partial_\nu$ reduces to spatial gradients in the local rest frame of the fluid. Given the simplifications represented by Eqs. (12) and (13), the Fourier-space evolution of the perturbations around local equilibrium is given by

$$f_{0\mathbf{p}} E_{\mathbf{p}} i\Omega \tilde{\phi}_{\mathbf{p}} - f_{0\mathbf{p}} \hat{L} \tilde{\phi}_{\mathbf{p}} = f_{0\mathbf{p}} \beta p^{\langle \mu} p^{\nu \rangle} \tilde{\sigma}_{\mu\nu}, \quad (14)$$

which is an inhomogeneous linear integral equation for $\tilde{\phi}_{\mathbf{p}}$. In most cases, the Boltzmann equation cannot be solved analytically, making it necessary to employ numerical methods as in [117]. However, in [46], the authors were able to find the eigenfunctions of the linearized collision term for the system described by the Lagrangian in Eq. (3) (at leading order in λ). The eigenfunctions and eigenvalues are given as,

$$\begin{aligned} \hat{L} \left[L_{n\mathbf{p}}^{(2\ell+1)} p^{\langle \mu_1} \dots p^{\mu_\ell \rangle} \right] &= \chi_n^{(\ell)} L_{n\mathbf{p}}^{(2\ell+1)} p^{\langle \mu_1} \dots p^{\mu_\ell \rangle}, \\ \chi_{n\ell} &= -\frac{g}{2} \mathcal{M} \left(\frac{n + \ell - 1}{n + \ell + 1} + \delta_{n0} \delta_{\ell 0} \right), \end{aligned} \quad (15)$$

where $L_{n\mathbf{p}}^{(2\ell+1)} = L_{n\mathbf{p}}^{(2\ell+1)}(\beta E_{\mathbf{p}})$ represents associated Laguerre polynomials, which form a complete set of orthogonal polynomials. Here, $\mathcal{M} = (n_0\beta)/2$ is the matrix element of interest, and $p^{\langle\mu_1 \dots \mu_\ell\rangle} \equiv \Delta^{\mu_1 \dots \mu_\ell} \nu_1 \dots \nu_\ell p^{\nu_1} \dots p^{\nu_\ell}$ denote irreducible tensors constructed from products of the four-momentum. These tensors are symmetric, orthogonal to u^μ , and traceless for each pair of indices[42, 43].

The 2ℓ -rank tensor $\Delta_{\nu_1 \dots \nu_\ell}^{\mu_1 \dots \mu_\ell}$ is built using combinations of the projection operator $\Delta^{\mu\nu} = g^{\mu\nu} - u^\mu u^\nu$. It is important to note that this tensor is designed in a way that ensures symmetry concerning permutations in any of the indices $\mu_1 \dots \mu_\ell$ and $\nu_1 \dots \nu_\ell$, separately, and also to make it traceless within each subset of indices [42, 43]. These irreducible tensors satisfy the orthogonality relation given by

$$\int dP p^{\langle\mu_1 \dots \mu_\ell\rangle} p_{\langle\nu_1 \dots \nu_\ell\rangle} H(E_{\mathbf{p}}) = \frac{\ell!}{(2\ell+1)!!} \Delta_{\nu_1 \dots \nu_\ell}^{\mu_1 \dots \mu_\ell} \delta_{\ell m} \int \frac{d^3 p}{(2\pi)^3 p^0} (\Delta^{\mu\nu} p_\mu p_\nu)^\ell H(E_p), \quad (16)$$

where $H(E_p)$ represents an arbitrary weight function that is sufficiently regular to ensure convergence of the integral[126], the set of eigenfunctions satisfies the following orthogonality relation:

$$\int dP (\Delta^{\mu\nu} p_\mu p_\nu)^\ell L_{n\mathbf{p}}^{(2\ell+1)} L_{m\mathbf{p}}^{(2\ell+1)} f_{0\mathbf{p}} = A_n^{(\ell)} \delta_{nm} \equiv (-1)^\ell \frac{n_0}{2\beta^{2\ell-1}} \frac{(n+2\ell+1)!}{n!} \delta_{nm}, \quad (17)$$

where n_0 is the local particle density. Even with the eigenfunctions of the collision operator, there are still some subtleties to be taken into account while solving equation (14). This is a consequence of the non-commutativity of the operator \hat{L} and $E_{\mathbf{p}}$ when considered as operators acting on momentum-space functions [126]. Specifically for this problem, the action of $E_{\mathbf{p}}$ on the eigenfunctions \hat{L} can be determined using basic properties of associated Laguerre polynomials [49, 68]. To make this complication more clear, let us consider the case $\ell = 2$ and write the operators acting on our eigenfunctions,

$$\beta E_{\mathbf{p}} L_{n,\mathbf{p}}^{(5)} = -(n+1)L_{n+1,\mathbf{p}}^{(5)} + 2(n+3)L_{n,\mathbf{p}}^{(5)} - (n+5)L_{n-1,\mathbf{p}}^{(5)}, \quad (18)$$

which is a linear combination of eigenfunctions of \hat{L} with different eigenvalues. In contrast, we know from Eq. (15) that

$$\hat{L} \left[L_{n\mathbf{p}}^5 p^{\langle\mu_1 \dots \mu_\ell\rangle} \right] = \chi_n^5 L_{n\mathbf{p}}^5 p^{\langle\mu_1 \dots \mu_\ell\rangle} \quad (19)$$

Then, acting on an eigenfunction with \hat{L} and $E_{\mathbf{p}}$ leads to different results when these operators are interchanged. Unfortunately, this complication implies that one can perform a numerical analysis or use techniques like trotterization to study this system. In this thesis, we focus on the numerical analysis, which will be described in detail in the following section.

3 Numerical analysis

In this section, we provide a numerical method to solve Eq. (14). For that, we make use of the knowledge of the eigenfunctions of the linearized collision term. We analyze the system of equations formed by the moments of $f_{\mathbf{p}}$ constructed with respect to eigenfunctions of the linearized collision term. Using the discussion from the previous section, we focus on calculating the shear-stress response function numerically. For that, we perform an integration with the corresponding tensor rank-2 eigenfunctions of the linearized collision term $\int dP(\dots)L_n^{(5)}p^{(\alpha}p^{\beta)}$ on both sides of Eq. (14),

$$\begin{aligned} i\frac{\Omega}{\beta} \left[-\Phi_1^{\alpha\beta} + 6\Phi_0^{\alpha\beta} \right] - \chi_{02}\Phi_0^{\alpha\beta} &= \frac{8n_0}{\beta^2}\tilde{\sigma}^{\alpha\beta}, \quad n = 0, \\ i\frac{\Omega}{\beta} \left[-(n+1)\Phi_{n+1}^{\alpha\beta} + 2(n+3)\Phi_n^{\alpha\beta} - (n+5)\Phi_{n-1}^{\alpha\beta} \right] - \chi_{n,2}\Phi_n^{\alpha\beta} &= 0, \quad n = 1, 2, 3, \dots \end{aligned} \quad (20)$$

Where we defined the eigenmodes

$$\Phi_n^{\mu\nu} \equiv \int dP L_n^{(5)} p^{(\mu} p^{\nu)} \delta f_{\mathbf{p}}. \quad (21)$$

We also have employed the fact that the linearized collision term is self-adjoint, which means that given two arbitrary functions of momentum $A_{\mathbf{p}}$ and $B_{\mathbf{p}}$, we have

$$\int dP f_{0\mathbf{p}} A_{\mathbf{p}} \hat{L} B_{\mathbf{p}} = \int dP f_{0\mathbf{p}} B_{\mathbf{p}} \hat{L} A_{\mathbf{p}} \quad (22)$$

Next, we make use of the eigenfunction equation (15), and the identity

$$\beta E_{\mathbf{p}} L_{n,\mathbf{p}}^{(2\ell+1)} = -(n+1)L_{n+1,\mathbf{p}}^{(2\ell+1)} + 2(n+\ell+1)L_{n,\mathbf{p}}^{(2\ell+1)} - (n+2\ell+1)L_{n-1,\mathbf{p}}^{(2\ell+1)}, \quad (23)$$

which is a consequence of the basic properties of the Laguerre polynomials.

From definition (21), it is clear that $\Phi_0^{\alpha\beta} = \pi^{\alpha\beta}$ is the shear-stress tensor. Therefore, its linear response is completely determined by solving Eq. (20) for $\Phi_0^{\alpha\beta}$. That equation can be written as

$$\begin{aligned} \sum_m \mathcal{M}_{nm} \Phi_m^{\alpha\beta} &= B_n \\ \mathcal{M}_{nm} &= -i\hat{\Omega}(n+1)\delta_{n+1,m} + [2(n+3)i\hat{\Omega} - \hat{\chi}_n^{(2)}]\delta_{n,m} - i\hat{\Omega}(n+5)\delta_{n-1,m} \\ \mathcal{B}_n &= \frac{8}{\beta^2} I_{1,0} \sigma^{\alpha\beta} \delta_{n,0}, \end{aligned} \quad (24)$$

where we have employed the normalized variables for simplification

$$\widehat{\Omega} = \frac{\Omega}{g\beta I_{00}}, \quad \widehat{\chi}_n^{(2)} = \frac{\chi_n^{(2)}}{gI_{00}} = -\frac{1}{2} \frac{n+1}{n+3}. \quad (25)$$

The shear-stress linear response problem is then formally solved by

$$\begin{aligned} \pi^{\alpha\beta} &= \Phi_0^{\alpha\beta} = \sum_j (\mathcal{S}^{-1})_{0j} \mathcal{B}_j^{\alpha\beta} \equiv 2\eta(\widehat{\Omega}) \widetilde{\sigma}^{\alpha\beta}, \\ \eta(\widehat{\Omega}) &= \frac{8}{g\beta^3} (\mathcal{S}^{-1})_{00}. \end{aligned} \quad (26)$$

Thus the linear response problem can be solved by $\Phi_0^{\alpha\beta} = (\mathcal{M}^{-1})_{00} \mathcal{B}_0$. We observe that \mathcal{M} forms an infinite tridiagonal matrix. For a finite-dimensional truncation of this matrix, a closed form of the elements of its inverse can be derived [126],

$$\begin{aligned} (\mathcal{S}_N)_{nm} &= b_n \delta_{n+1,m} + a_n \delta_{n,m} + c_n \delta_{n-1,m}, \quad n, m = 0, 1, 2, \dots, N-1, \\ a_n &= 2(n+3)i\widehat{\Omega} + \frac{1}{2} \frac{n+1}{n+3}, \quad b_n = -i\widehat{\Omega}(n+1), \quad c_n = -i\widehat{\Omega}(n+5), \end{aligned} \quad (27)$$

Particularly for this problem, we have:

$$(\mathcal{S}_N^{-1})_{00} = \frac{\varphi_2(\widehat{\Omega})}{\theta_N(\widehat{\Omega})}, \quad (28)$$

where φ_2 and θ_N are obtained, respectively, by the following recursion relations

$$\begin{aligned} \varphi_j &= a_{j-1} \varphi_{j+1} - b_{j-1} c_j \varphi_{j+2}, \quad j = N-1, N-2, \dots, 2, 1, \\ \theta_{j+1} &= a_{j-1} \theta_{j-1} - b_{j-2} c_{j-1} \theta_{j-2}, \quad j = 2, 3, \dots, N, \end{aligned} \quad (29)$$

With the initial conditions:

$$\varphi_{N+1} = 1, \quad \varphi_N = a_{N-1}, \quad \theta_0 = 1, \quad \theta_1 = a_0, \quad (30)$$

Where a_n, b_n , and c_n for $(\mathcal{M}^{-1})_{00}$ are given as a function of the eigenvalues and eigenvectors of the linearized collision operator:

$$a_n = 2(n+3)i\widehat{\Omega} + \frac{1}{2} \frac{n+1}{n+3}, \quad b_n = -i\widehat{\Omega}(n+1), \quad c_n = -i\widehat{\Omega}(n+5), \quad (31)$$

Here, N represents the rank of the matrix truncation. Thus, examining the linear response simplifies to analyzing the ratio's analytical properties φ_2/θ_N as $N \rightarrow \infty$. Specifically, as

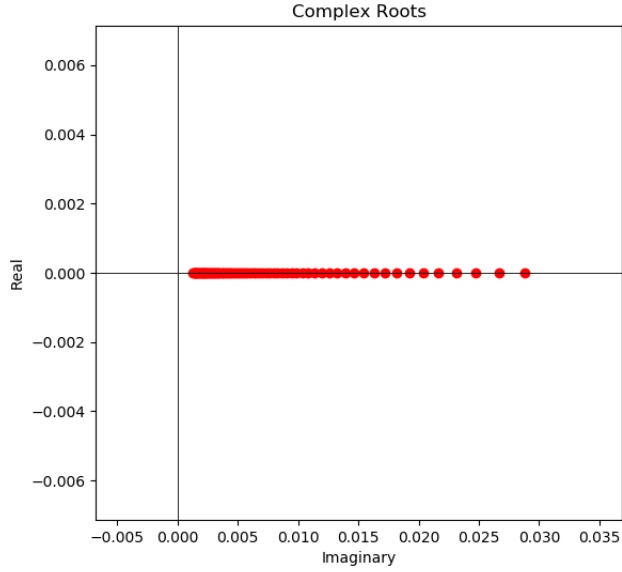


Figure 1: Poles of the response function for $N = 100$

the roots of $\varphi_2(\widehat{\Omega})$ and $\theta_N(\widehat{\Omega})$ are distinct, the poles of the homogeneous Green function correspond to the zeros of θ_N . In Fig. 1, we display the poles found for a basis of size $N = 100$. The poles lie on the $\text{Re } z = 0$ axis due to our choice of sign in the Fourier transform,

$$f(x, p) = \int \frac{d^4 q}{(2\pi)^4} e^{iqx} \hat{f}(q, p), \quad (32)$$

The plot indicates the existence of a branch cut as N approaches infinity, as evidenced by the decreasing separation of the poles with each increase in N . In Fig. 3, we illustrate the pole nearest to the origin as N increases, up to $N = 700$. Once again, we observe that the poles become closer to zero with increasing the basis size. Additionally, the plot shows that the minimum pole decreases significantly as a function of N , with a relation approximately given by $\text{min pole} \sim 1/N^{0.996}$. To assess whether the poles converge to a continuous line or a set of discrete points, in Fig. 3, we show the average relative distance between the 15 poles closest to the origin,

$$\langle \Delta\Omega \rangle_{15} = \sum_{k=1}^{14} \frac{|\omega_{k+1} - \omega_k|}{|\omega_k|}, \quad (33)$$

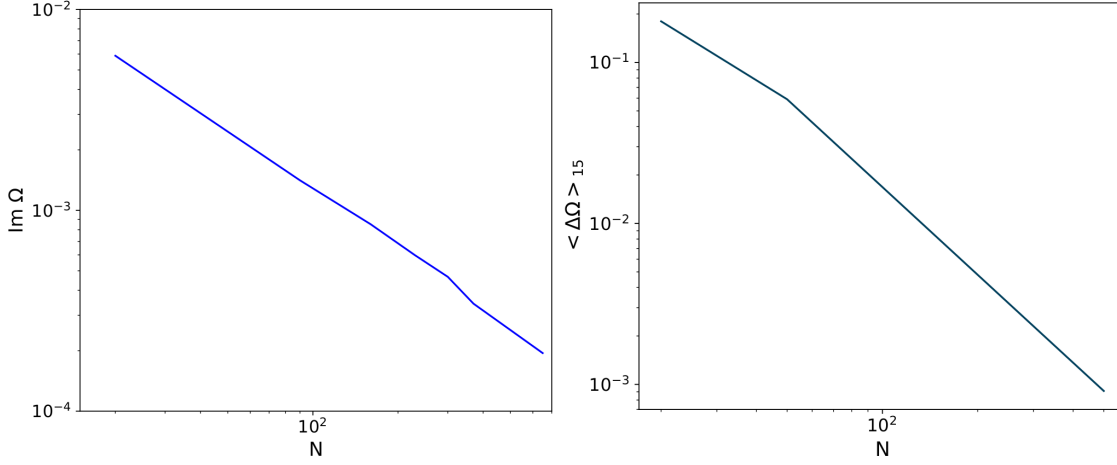


Figure 2: Left: Pole nearest to the origin for N up to $N = 700$. Right: Average relative distance between the 15 poles closest to the origin $\langle \Delta \Omega \rangle_{15}$

as a function of N , ω_k represents the k -th pole closest to the origin. Since all poles lie on the real axis with $\text{Re } z = 0$, we have $|\omega_{k+1} - \omega_k| = |\omega_{k+1}| - |\omega_k|$. The fitting results indicate that $\langle \Delta \Omega \rangle_{15} \sim 1/N^{1.794}$. This means that the average relative distance between the poles closest to $\hat{\Omega} = 0$ will converge to zero faster than the pole nearest to the origin converges to $\hat{\Omega} = 0$.

These findings indicate the shear response function for the $\lambda\phi^4$ possesses a branch cut along the imaginary axis, $i0^+ < \Omega < i\infty$ as $N \rightarrow \infty$ [125]. Additionally, they imply that this behavior for the non-hydrodynamic modes is not associated with quantum statistics or quantum effects but is associated with long-lived hydrodynamic modes present in the ϕ^4 theory. Since the cross-section is negligible for large (center-of-momentum) energies, high-energy modes overpopulate evolution at late times and give rise to infinitely many long-lived modes. We note that the value of $\text{Im}\hat{\Omega}$ for a singularity is related to the relaxation time of the mode. Hence, its extension to the origin means that obtaining the relaxation time for this system is not possible using the usual method [43].

Phenomenological shear viscosity across the QCD phase diagram

In this chapter, we extend the calculations of shear viscosity from Chapter 4.1 to a system with multiple conserved charges. In this case, shear viscosity will depend on an effective chemical potential that is a function of baryonic (μ_B), strangeness (μ_S), and electric charge (μ_Q) chemical potentials. Additionally, we conduct a phenomenological study of shear viscosity across the QCD phase diagram, incorporating a Hadron Resonance Gas (HRG) model for the temperature regime below the first-order transition. As mentioned in Chapter 2, HRG can reproduce the thermodynamics of the system for lower temperatures.

Usually, perturbative Quantum Chromodynamics (pQCD) calculations are useful at very high temperatures, where the QGP tends to transition from a strongly coupled to a weakly coupled state. However, the exact temperature at which pQCD calculations apply still needs to be determined. On the other end of the temperature spectrum, when temperatures are low, it becomes feasible to compute the shear viscosity employing kinetic theory and the well-known characteristics of the Hadron Resonance Gas (HRG) [39]. For example, one can incorporate an HRG model featuring an excluded volume [66, 115, 104], which diminishes as the temperature rises (a trend anticipated if a minimum value of η/s exists at the cross-over phase transition). This observed behavior of η/s in the HRG is explained by the increasing degrees of freedom at higher temperatures, thereby increasing the entropy and consequently reducing η/s [116]. In this work, we use data from the Particle Data Group (PDG) as of 2021, encompassing over 700 hadrons, to obtain values of $\eta T/\omega$ below the first-order phase transition.

However, neither of these techniques describes the intermediate region well. Therefore, in this work, we employ an interpolation function to connect these two regimes and carefully explain the procedure necessary to obtain a sensible shear viscosity compared to what we know from experimental data and Bayesian analysis. This chapter is based on work from [39]. Here, my collaborator J. Salinas San Martin performed enthalpy calculations using excluded volume HRG for the region below the phase transition and provided me the data from Particle Data Group (PDG) as of 2021.

1 Shear viscosity at leading logarithmic order for multiple conserved charges

As a detailed description of how to compute shear viscosity was already given in Chapter 4.1, we will focus on the necessary changes to include strangeness and electric charges in this calculation. The procedure can be repeated for the case of multiple chemical potentials with some minor differences. As a consequence of having multiple charges, different flavors of quarks and antiquarks must have different relaxation functions:

$$\begin{aligned}
 \chi^g(p) &= \sum_{m=1}^N a_m \phi^{(m)}(k), & \chi^u(p) &= \sum_{m=1}^N a_{m+N} \phi^{(m)}(k), & \chi^d(k) &= \sum_{m=1}^N a_{m+2N} \phi^{(m)}(k) \\
 \chi^s(k) &= \sum_{m=1}^N a_{m+3N} \phi^{(m)}(k), & \chi^{\bar{u}}(k) &= \sum_{m=1}^N a_{m+4N} \phi^{(m)}(k), & \chi^{\bar{d}}(k) &= \sum_{m=1}^N a_{m+5N} \phi^{(m)}(k) \\
 \chi^{\bar{s}}(k) &= \sum_{m=1}^N a_{m+6N} \phi^{(m)}(k)
 \end{aligned} \tag{1}$$

and the basis set used for it was the same as used in [41]:

$$\phi^{(m)} = \frac{k(k/T)^m}{(1+k/T)^{N-1}} \quad m = 1, \dots, N \tag{2}$$

This change implies that the contribution from each quark in all diagrams has to be counted separately, and therefore, the scattering matrix will evolve differently as a function of each chemical potential. As discussed previously, at finite densities, the shear viscosity is normalized by $\eta T/w$ such that we require knowledge of the enthalpy or $\varepsilon + P$. To do that, we used a free gas of BSQ charges with three active flavors, analogously to the description used in Chapter 4.1 [143],

$$T \ln Z_{QGP} = \frac{g_g V}{90\pi^2} T^4 + \sum_i \frac{g_f V}{12} \left(\frac{7\pi^2}{30} T^4 + \tilde{\mu}_i^2 T^2 + \frac{1}{2\pi^2} \tilde{\mu}_i^4 \right) \tag{3}$$

Here, $g_g = 16$ accounts for the gluon degrees of freedom since the gluon has eight colors and two helicities. The factor $g_f = 6$ accounts for two helicities and three colors for the quarks, and the sum is over quarks flavors. The contribution from antiquarks is already included in the partition function and doesn't require extra counting. These calculations were performed for QGP with three flavors: u, d, s . And $\tilde{\mu}$ is the effective chemical potential for each particle, i , defined as:

$$\tilde{\mu}_i = B_i \frac{\mu_B}{T} + S_i \frac{\mu_S}{T} + Q_i \frac{\mu_Q}{T} \tag{4}$$

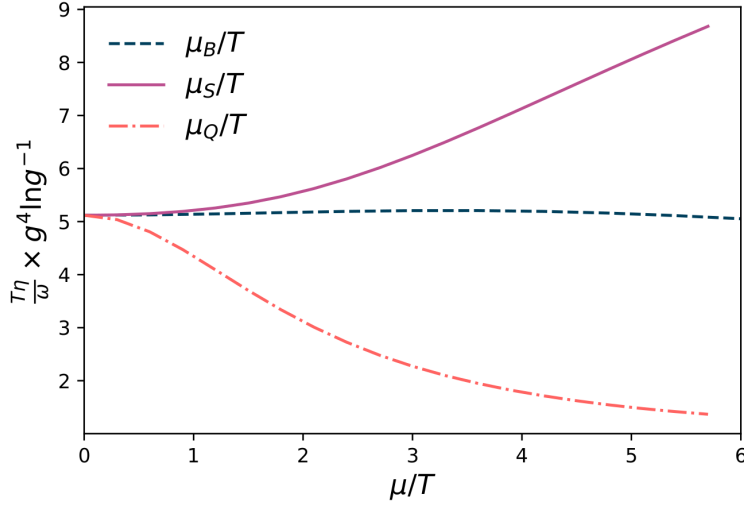


Figure 1: $\eta T/\omega$ as a function of μ_S/T , μ_B/T and μ_Q/T .

and B_i is the baryon number, S_i is strangeness, and Q_i is the electric charge. Additionally, μ_B , μ_S , and μ_Q are the corresponding chemical potentials for each conserved charge.

Figure 1 shows a curve for $\eta T/w$ as a function of μ_S/T , μ_Q/T , and μ_B/T while having the other chemical potentials set to zero. We observe that the curves have entirely different behaviors, suggesting that shear viscosity is strongly dependent on which chemical potential is present in the system. We find that $\eta T/w$ increases with increasing μ_S/T whereas $\eta T/w$ decreases with increasing μ_Q/T . In Chapter 4.1, we showed that $\eta T/w$ increased slightly before generally decreasing at $\mu_B/T \gtrsim 1$. Therefore, all 3 chemical potentials lead to strikingly different shear dependencies. This can be explained by the fact that ρ_Q , the net density associated with the conserved electric charge, grows slower as a function of μ_Q than the equivalent for ρ_B and ρ_S . This increase affects the enthalpy, which will change significantly less than for the same value of μ_B or μ_S . We also note that the values of μ_S and μ_Q were chosen to be positive for these calculations, even though the symmetry $\eta T/w(\mu) = \eta T/w(-\mu)$ should be observed.

To understand the interplay between chemical potentials, we first set $\mu_Q = 0$ and vary μ_B and μ_S (corresponding to isospin symmetric matter). In Fig. 2 we plot μ_B/T on the x-axis while varying μ_S/T using different colors on the left and on the right, we analogously vary μ_S/T on the x-axis and μ_B/T in different colors. The plots show that even small values of μ_S/T significantly influence the curves, leading to an overall increase,

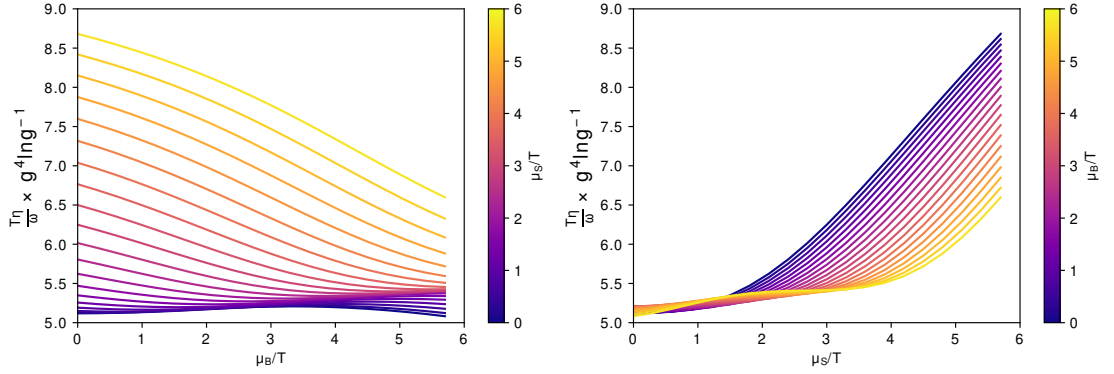


Figure 2: $\eta T / (e + P)$ as a function of μ_S for each μ_B . The color code indicates the value of the chemical potential over the temperature

especially for smaller values of μ_B/T . It is also clear that while μ_B/T seems to change the overall magnitude of $\eta T / \omega$, leading to quicker relaxation of the fluid, while μ_S/T causes $\eta T / \omega$ to increase, corresponding to a slower relaxation.

Typically, heavy-ion collisions do not exclusively explore finite μ_B , but instead, they investigate the "strangeness neutral" (SN) scenario, characterized by the enforcement of two key conditions:

$$\langle n_Q \rangle = \frac{Z}{A} \langle n_B \rangle \quad (5)$$

$$\langle n_S \rangle = 0 \quad (6)$$

Here, Z is the charge number, and A is the number of nucleons of the heavy-ion. The first condition implies the conservation of electric charges. On the other hand, the second condition is a consequence of the initial conditions of the heavy-ion collisions. Since the incident nuclei do not carry strangeness, the net strangeness $\langle n_S \rangle = 0$ is fixed [56].

In principle, in this work, we have 4 degrees of freedom $\{T, \mu_B, \mu_S, \mu_Q\}$. Still, for the strangeness neutral trajectories through the QCD phase diagram, $\mu_S(T, \mu_B)$ and $\mu_Q(T, \mu_B)$ are constrained to be single values for a specific temperature and baryon chemical potential, therefore in this case, we have only 2 degrees of freedom. In Fig. 3, we compare $\eta T / \omega$ for the case of only finite μ_B (pink) to the strangeness neutral trajectory (shown in blue) where we set $Z/A = 0.4$. For just finite μ_B , there is a non-monotonic behavior in $\eta T / \omega$, which was first observed in [41]. In contrast, once we enforce the strangeness neutrality conditions, the non-monotonicity disappears, and $\eta T / \omega$ only decreases with increasing μ_B , which agrees with the curves obtained in Fig. 2, since for strangeness neutrality μ_Q

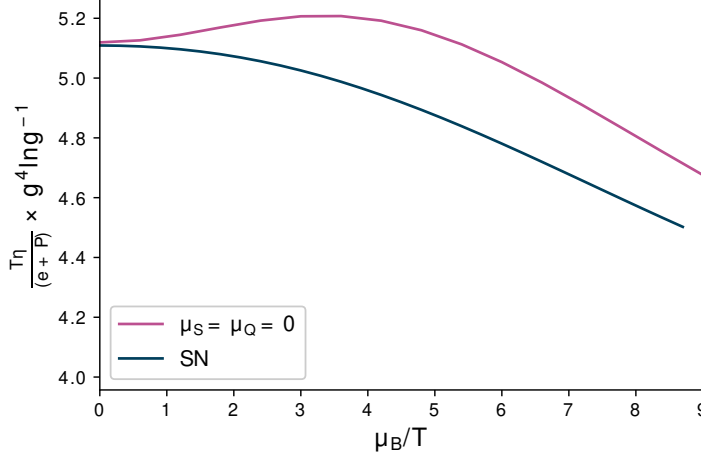


Figure 3: Shear viscosity as a function of $\mu_S(\mu_B, T)$ and $\mu_Q(\mu_B, T)$ for the strangeness neutral case that has the conditions shown in Eq. (5-6) compared with the case of $\mu_S = \mu_Q = 0$.

is small compared to μ_S and μ_B , and will have a small influence. In the next section, we explore the confined phase of QCD, the hadronic phase, and define the switching temperature, where one expects the system to go from the confined to the deconfined phase.

2 Hadron resonance gas model and switching temperature

At low temperatures within heavy-ion collisions, the quark-gluon plasma undergoes a phase transition; it suffers a freeze-out into a gas comprised of interacting hadrons. To describe this phase, we begin with the ideal hadron resonance gas model, where the equation of state is described using a gas of free hadrons. With this model, one can obtain thermodynamical quantities and transport coefficients, assuming that hadrons are point-like particles. The total density of particles for species i can be calculated as follows:

$$\frac{n_i^{id}(T, \mu_B, \mu_S, \mu_Q)}{T^3} = \frac{g_i}{2\pi^2} \int_0^\infty dk k^2 \left[\exp\left(\frac{\sqrt{k^2 + m_i^2}}{T} - \tilde{\mu}_i\right) + (-1)^{B_i-1} \right]^{-1} \quad (7)$$

where B_i is the baryon number of the particle, p is the momentum, m_i is the mass of the particle, and the degeneracy $g_i = 2J_i + 1$ comes from spin J_i . The effective chemical potential for species i is defined in the same way as in Eq. (4).

It is well known that hadrons interact with each other in several different channels. Some of these channels represent repulsive interactions, while others represent attractive interactions. As hadronic species are included, the treatment used in [142] is not guaranteed to be applicable. This is because the standard assumption behind hadron resonance models is that the interacting hadronic system can be described by a free gas of the original hadrons and resonances [115]. In general, the inclusion of resonances represents the contribution from the attractive channels, while repulsive interactions are usually modeled using excluded volume corrections to the thermodynamics, for instance [71, 91, 124, 115]. Given that, we incorporate repulsive interactions via an excluded volume approach, where the hard-core volume is typically specified as [115, 104]:

$$V = 4 \cdot \frac{4}{3}\pi r^3 \quad (8)$$

where r is the radius of an individual hadron. The factor of 4 arises from considering that the excluded volume for a sphere is 8 times its volume. However, this volume is shared between two interacting particles, resulting in a factor of 4. We assume that all hadrons have the same volume for the calculations performed in this Chapter. The radius for the excluded volume has been tuned to reproduce the lattice QCD entropy in [104] using the PDG16+ particle list. Here, we use the PDG2021+ particle list, which includes more particles. However, these are predominately heavier particles, so their influence does not play a strong role in the entropy calculation, as shown in [131].

In kinetic theory, the shear viscosity is related to,

$$\eta \propto n \sum_i \lambda_i \langle |k| \rangle_i \quad (9)$$

where the total particle number density is

$$n_{tot} = \sum_i n_i \quad (10)$$

Here, the total particle density describes the amount of total matter summed with the anti-matter in the system, not the net amount of matter. And, λ_i is the mean free path, related to the inverse of the space occupied by the density of hadrons as,

$$\lambda \propto 1/(n_i r^2) \quad (11)$$

and $\langle |k| \rangle_i$ is the average thermal momentum of particle i , given by,

$$\langle |k| \rangle_i = \frac{\int_0^\infty k^3 \exp \left[-\sqrt{k^2 + m_i^2/T} + \tilde{\mu}_i \right] dk}{\int_0^\infty k^2 \exp \left[-\sqrt{k^2 + m_i^2/T} + \tilde{\mu}_i \right] dk} \quad (12)$$

which is the integral weighted by momentum. We note that the $\tilde{\mu}_i$ term is independent of the momentum, which allows us to pull it out of the integral, and Eq. (13) is rewritten as,

$$\langle |k| \rangle_i = \frac{\int_0^\infty k^3 \exp \left[-\sqrt{k^2 + m_i^2/T} \right] dk}{\int_0^\infty k^2 \exp \left[-\sqrt{k^2 + m_i^2/T} \right] dk} \quad (13)$$

even at finite chemical potentials. Substituting this into Eq. (9), we can write

$$\eta \propto \frac{1}{r^2} \sum_i \frac{n_i}{n} \frac{\int_0^\infty k^3 \exp \left[-\sqrt{k^2 + m_i^2/T} \right] dk}{\int_0^\infty k^2 \exp \left[-\sqrt{k^2 + m_i^2/T} \right] dk} \quad (14)$$

where we assume a single hard-core radius for all hadrons considered here. When including the excluded volume effects, the particle number density n_i can be written as,

$$n_i^{ex} = \frac{e^{-vp/T} n_i^{id}}{1 + v e^{-vp/T} n_{tot}^{id}} \quad (15)$$

where the total excluded volume particle number density is given by the sum of the number densities as,

$$\begin{aligned} n_{tot}^{ex} &= \sum_i n_i^{ex} \\ &= \sum_i \frac{e^{-vp/T} n_i^{id}}{1 + v e^{-vp/T} n_{tot}^{id}} \end{aligned} \quad (16)$$

and, since the excluded volume v is the same for all particle species, we pull out the n_i^{id} term from the summation, simplifying this to,

$$n_{tot}^{ex} = n_{tot}^{id} \frac{e^{-vp/T}}{1 + v e^{-vp/T} n_{tot}^{id}}. \quad (17)$$

Therefore, the density ratios

$$\frac{n_i^{ex}}{n_{tot}^{ex}} = \frac{n_i^{id}}{n_{tot}^{id}} \quad (18)$$

are remain the same.

Now, we can finally write the shear viscosity at finite $\tilde{\mu}$ using an excluded volume description for a hadron resonance gas:

$$\eta^{HRG} = \frac{5}{64\sqrt{8}} \frac{1}{r^2} \frac{1}{n_{tot}^{id}} \sum_i n_i^{id} \frac{\int_0^\infty k^3 \exp\left(\frac{-\sqrt{k^2+m_i^2}}{T} + \tilde{\mu}_i\right) dk}{\int_0^\infty k^2 \exp\left(\frac{-\sqrt{k^2+m_i^2}}{T} + \tilde{\mu}_i\right) dk} \quad (19)$$

where the prefactors were derived in [101, 66]. Then the normalization for η^{HRG} requires an excluded volume calculation for the energy density ε^{ex} , given by,

$$\varepsilon^{ex}(T, \mu) = \frac{\varepsilon^{id}(T, \mu)}{\exp[v p^{ex}(T, \mu)/T] + v n_{tot}^{id}(T, \mu)}, \quad (20)$$

where the excluded volume pressure p^{ex} is given by:

$$\frac{p^{ex}(T, \mu_B, \mu_S, \mu_Q)}{T} = n^{id}(T, \mu_B, \mu_S, \mu_Q) \exp\left(\frac{-v p^{ex}(T, \mu_B, \mu_S, \mu_Q)}{T}\right), \quad (21)$$

The excluded volume pressure has a self-consistent equation, which can be solved analytically using the Lambert W function if we only have a single v for all hadrons:

$$p^{ex}(T, \mu_B, \mu_S, \mu_Q) = \frac{T}{v} W(v n^{id}(T, \mu_B, \mu_S, \mu_Q)), \quad (22)$$

such that we calculate the kinematic shear as,

$$\frac{\eta^{HRG} T}{(\varepsilon^{ex} + p^{ex})} = \frac{\eta^{HRG} T}{w^{ex}}, \quad (23)$$

which, in the limit of $\tilde{\mu} \rightarrow 0$ can be simply calculated as η^{HRG}/s^{ex} , where the entropy s^{ex} can be obtained from the thermodynamical relation:

$$s^{ex} = \left. \frac{\partial p^{ex}}{\partial T} \right|_{\mu}. \quad (24)$$

Figure 4 compares η/s between two choices of ratio size, 0.1 fm and 0.25 fm , in the temperatures below where one would expect a first-order transition. The plot shows that shear viscosity is highly dependent on the radius. We also note that the difference between the magnitudes of the two radii is observed for the entire temperature range considered in this work.

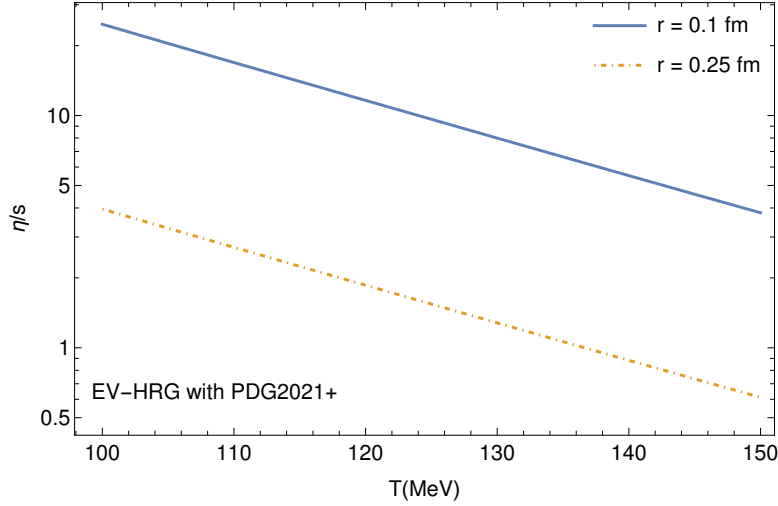


Figure 4: η/s as a function of the temperature. The excluded volume result for the PDG2021+ list for $r = 0.1\text{ fm}$ (blue line) is compared to $r = 0.25\text{ fm}$ (yellow dot-dashed line).

However, the region close to the first-order transition line cannot be described by either the perturbative QCD or HRG model presented in this thesis. Therefore, we use an interpolation function to connect the two models. We first consider the chiral phase transition line with just finite μ_B as it is usually defined using a Taylor expansion over the switching temperature:

$$\frac{T_{sw}(\mu_B)}{T_{sw,0}} = \left[1 - \kappa_2 \left(\frac{\mu_B}{T_{sw,0}} \right)^2 - \kappa_4 \left(\frac{\mu_B}{T_{sw,0}} \right)^4 \right], \quad (25)$$

Where $T_{sw} = T_{sw,0} = 156\text{ MeV}$, with T_{sw} being the chiral transition line temperature, which varies with μ_B , as shown in Fig. 5. Since we intend to work with multiple conserved

charges, we replace that with the extension of Eq. (25), given by,

$$\frac{T_{sw}(\mu_B, \mu_S, \mu_Q)}{T_{sw,0}} = \left\{ 1 - \sum_{i,j,k} \sum_{X,Y,Z=B,S,Q} \left[\kappa_{i+j=2}^{XY} \left(\frac{\mu_X^i \mu_Y^j}{T_{sw,0}^2} \right) + \kappa_{i+j+k=4}^{XYZ} \left(\frac{\mu_X^i \mu_Y^j \mu_Z^k}{T_{sw,0}^2} \right) \right] \right\}, \quad (26)$$

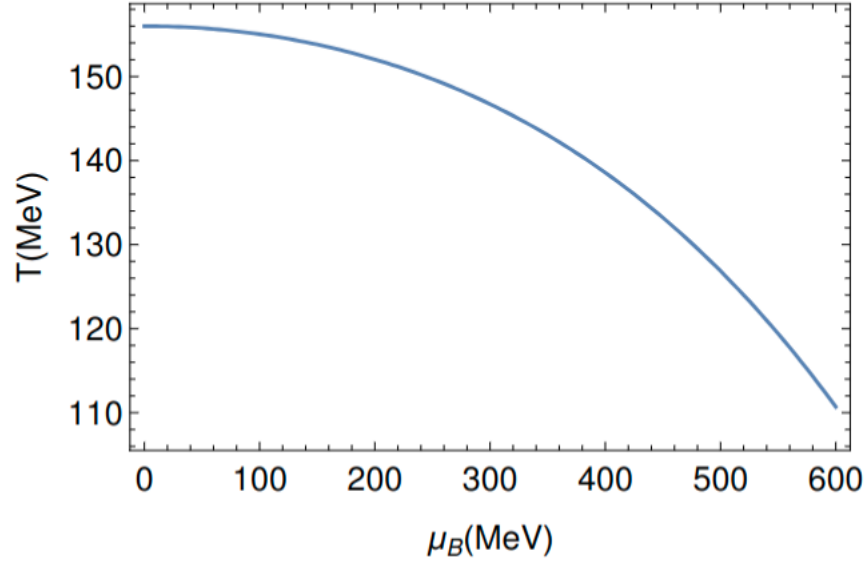


Figure 5: First order transition line between HRG and QGP regimes for $\mu_S = \mu_Q = 0$ and finite μ_B . This is the expected transition between confined and deconfined QCD.

However, current lattice QCD results [23] do not include all non-diagonal terms, therefore, Eq. (26) simplifies to

$$\frac{T_{sw}(\mu_B, \mu_S, \mu_Q)}{T_{sw,0}} = \left\{ 1 - \sum_{X=B,S,Q} \left[\kappa_2^X \left(\frac{\mu_X}{T_{sw,0}} \right)^2 + \kappa_4^X \left(\frac{\mu_X}{T_{sw,0}} \right)^4 \right] - 2\kappa_2^{BS} \frac{\mu_B \mu_S}{T^2} \right\}, \quad (27)$$

Table 1 lists the κ_n^X coefficients used in this work. The actual lattice QCD calculations have statistical error bars on their calculations, but here, we chose to use the central values or an average over collaboration, given the available results.

n	κ_n^B	κ_n^S	κ_n^Q	κ_n^{BS}
2	0.015	0.017	0.029	-0.0050
4	0.0007	0.004	0.008	n/a

Table 1: Values used for the κ_n^X coefficients and single available off-diagonal term κ_2^{BS} that describe the slope of the pseudo-critical temperature for the diagonal terms in Eq. (27). These values are averaged central values from different lattice QCD collaborations [31, 25, 30, 23, 48]

The next section describes the procedure used to connect the shear viscosity values from HRG and pQCD.

3 The phenomenological model

This section builds the phenomenological model for shear viscosity up to the three conserved charges. We connect the HRG and pQCD using an interpolating function for the different temperature regimes studied here, separated as follows. Temperatures below the switching line ($T_{sw} = 156$ MeV for $\mu_B = 0$), i.e., $T < T_{sw}$, are studied using the hadron resonance gas model with excluded volume. For the region above the switching line, i.e., $T > T_{sw}$, pQCD is expected to be the most appropriate description; however, we have set our lower boundary by comparing pQCD results and lattice calculations. In [138, 107, 74], it has been shown that pQCD calculations of thermodynamic observables match lattice calculations at temperatures above $T \gtrsim 300$ MeV for $\mu_B = \mu_S = \mu_Q = 0$. Therefore, we set our intermediate region between $T = 156$ MeV to $T = 300$ MeV, where we implement an interpolating function.

As discussed in section 1, shear viscosity for $T > 300$ MeV was obtained using kinetic theory as a function of the BSQ chemical potentials and the strong coupling $1/(g^4 \log(g^{-1}))$. As a consequence of the logarithmic dependence of the coupling, it is not possible to reach reasonable values of shear viscosity without first performing a rescaling of these results. For that purpose, we used the results for η/s obtained by Ghiglieri, Moore, and Teaney (GMT) for calculations at (almost) NLO[62] as follows. We begin by extracting the values of η/s for NLO for a fixed coupling using the two-loop Electrostatic QCD (EQCD [33, 32, 34, 88, 87]) value with $\mu_{EQCD} = (2.7 \leftrightarrow 4\pi)T$. We use these values to match our results at $\mu_B = \mu_S = \mu_Q = 0$ and set the scale for each temperature for $\tilde{\mu} \geq 0$. Once the pQCD results at vanishing densities have been rescaled, the interpolation function can be calculated by simply matching the pQCD and HRG results as follows.

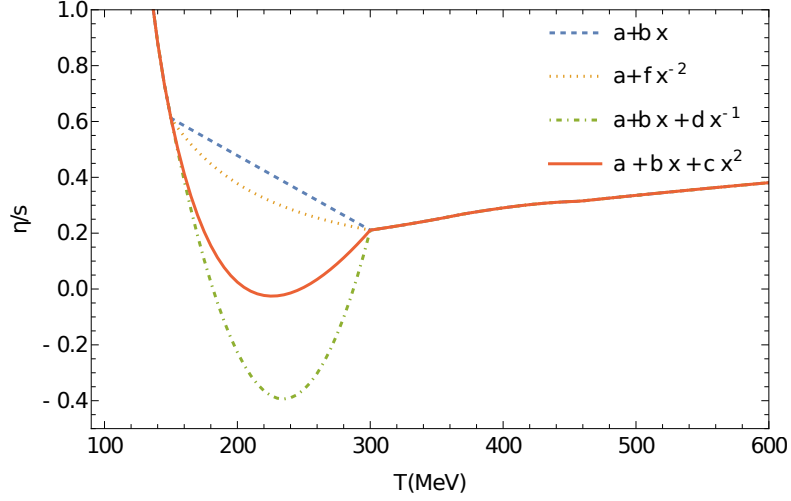


Figure 6: Different functional forms connecting the HRG shear viscosity at low T and $r = 0.25$ fm to rescaled pQCD shear viscosity to GMT [62] at high T

Here, we choose to use a simple polynomial fit defined by:

$$F(x) = a + bx + cx^2 + dx^{-1} + fx^{-2}, \quad (28)$$

where a, b, c, d, f are free parameters that ensure that the shear viscosity matches the HRG and pQCD at their respective transition points. For instance, we make $c = d = f = 0$ for a linear fit, and using $d = f = 0$ leads to a quadratic fit. Additionally, we ensure that $\eta T/w$ is continuous.

To make it more clear, we explain the matching for the linear fitting used here,

$$F(x) = a + bx, \quad (29)$$

which means that we have set $c = d = f = 0$ from Eq. (28). At fixed $\tilde{\mu}$, one takes the transition point, given by the switching line obtained in the previous section, from the HRG calculation to the interpolation function at $T_{sw,HRG}(\mu_B)$. The corresponding shear viscosity is

$$(\eta T/w)_1 \equiv \eta T/w(T_{sw,HRG}(\mu_B), \tilde{\mu}) \quad (30)$$

similarly, we define the transition point from the interpolation function to the pQCD shear viscosity at $T_{sw,pQCD}(\mu_B)$ where the corresponding shear viscosity is

$$(\eta T/w)_2 \equiv \eta T/w(T_{sw,pQCD}(\mu_B), \tilde{\mu}). \quad (31)$$

Then, we can determine a and b from these two points just by enforcing continuity. Since this is a linear function, we know that b is the slope. Therefore, we can substitute our two points at $T_1 = T_{sw,HRG}(\mu_B)$ and $T_2 = T_{sw,pQCD}(\mu_B)$ to calculate b combining Eq. (30) and Eq. (31) as:

$$b = \frac{(\eta T/w)_2 - (\eta T/w)_1}{T_{sw,pQCD} - T_{sw,HRG}}. \quad (32)$$

We can then substitute in b at either point back into Eq. (29), such that a is obtained as,

$$\begin{aligned} (\eta T/w)_1 &= a + \frac{(\eta T/w)_2 - (\eta T/w)_1}{T_{sw,pQCD} - T_{sw,HRG}} T_{sw,HRG} \\ a &= (\eta T/w)_1 - \frac{(\eta T/w)_2 - (\eta T/w)_1}{T_{sw,pQCD} - T_{sw,HRG}} T_{sw,HRG}. \end{aligned} \quad (33)$$

The same procedure applies for all polynomials of the form of Eq. (28), which always determines at least two unknown variables. If there are $N > 3$ coefficients, then $N - 2$ coefficients remain free parameters, which must be determined for each $\tilde{\mu}$ desired value.

In Fig. 6, we plot a comparison between 4 different choices of interpolating functions. We note that the pQCD results in Fig. 6 are already rescaled according to the GMT results from [62], and we use the HRG for $r = 0.25$ fm since the minimum value for this ratio is close enough to the pQCD to make the matching acceptable. As evident from Fig. 6, the location and overall value of the minimum $(\eta/s)_{min}$ is strongly dependent on the functional form of the interpolation function. Some functional forms lead to nonphysical values of $\eta/s < 0$. For this work, we ensure that shear viscosity is always positive, consistently with stability constraints for relativistic viscous fluids [26, 8]. We choose to take $a + bx$ (blue curve in Fig. 6), which only has two coefficients fixed by the transition points. Our a, f coefficients are determined independently along slices of $\tilde{\mu}$.

As a final comment to Fig. 6, the overall magnitude, especially at high and low T , is significantly high when compared to what is expected for $\eta/s(T)$ using Bayesian analyses [52, 113, 28, 120]. Therefore, we implement an overall normalization constant g_{norm} (which can shift the final curve up or downward but does influence the dependence on $\tilde{\mu}$) that will be discussed in detail in the next section. We also note that our choice of overall normalization is justified as we are primarily interested in obtaining models with a finite $\tilde{\mu}$ behavior such that given an η/s at $\tilde{\mu} = 0$, we can then use this approach to extrapolate to finite $\tilde{\mu}$. This allows us to explore the non-trivial behavior presented by HRG and pQCD with 3 conserved charges.

Free Parameters	
Parameter	Default Value
$(\eta/s)_{set}$	0.08
$T_{sw,HRG}$	156
$T_{sw,pQCD}$	300 MeV
r	0.25 fm
Constrained Parameters	
Parameter	Source
g_{norm}	$(\eta/s)_{set}/(\eta/s)_{min}$
g_{GMT}	$(\eta/s)_{T,pQCD}/(\eta/s)_{T,GMT}$
a, b, c, d, f	determined from matching

Table 2: Table with free and constrained parameters in the phenomenological $\eta T/w$ presented here [39].

In summary, our shear viscosity algorithm is [39]

$$\left(\frac{\eta T}{w}\right)_{tot}(T, \tilde{\mu}) = g_{norm} \begin{cases} \left(\frac{\eta T}{w}\right)_{HRG} & T < T_{sw,HRG} \\ \left(\frac{\eta T}{w}\right)_{int} & T_{sw,HRG} < T < T_{sw,pQCD} \\ g_{GMT} \left(\frac{\eta T}{w}\right)_{pQCD} & T > T_{sw,pQCD} \end{cases} \quad (34)$$

where g_{GMT} is the scaling factor to reproduce the pQCD results from NLO calculations [62] at $\tilde{\mu} = 0$ and g_{norm} is the overall normalization constant, constrained at $\tilde{\mu} = 0$.

We summarize all parameters in Tab. 2. The parameter g_{norm} is constrained by $(\eta/s)_{set}$ and the details of the rest of the calculation that leads to a certain minimum of η/s at $\mu_B = 0$; and g_{GMT} is determined from the calculations in [62]. The value of $(\eta/s)_{set}$ is guided by experimental data, $T_{sw,HRG}$ and $T_{sw,pQCD}$ are guided by comparisons of the HRG and pQCD results to lattice QCD, and r is constrained within the given range if one uses PDG2021+ to reproduce lattice QCD thermodynamic results.

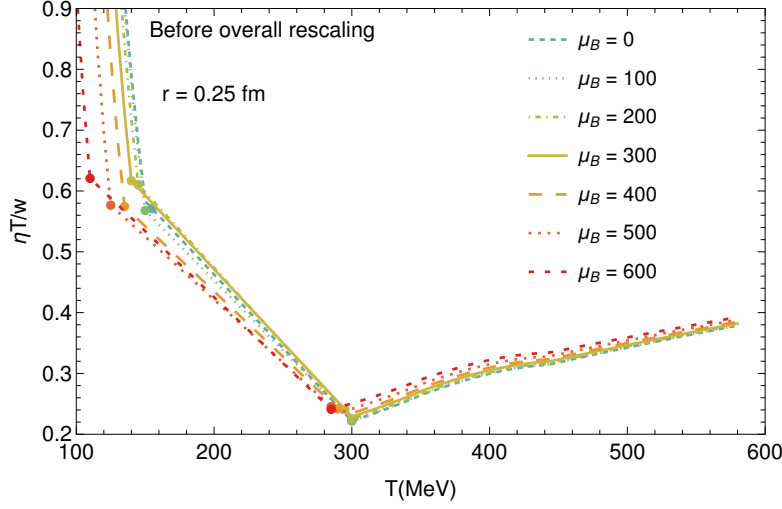


Figure 7: $\eta T/w$ as a function of the temperature for each value of μ_B in MeV for $r = 0.25$ fm. The results are shown before an overall rescaling is applied (i.e., $g_{norm} = 1$), but include the pQCD rescaling.

4 $\eta T/w$ for 3 conserved charges

This section discusses results for the phenomenological $\eta T/w$ built in the last section. Additionally, we motivate and explain our choice of overall rescaling. We begin with results for conserved baryon density and later consider the implications of all 3 conserved charges. In Fig. 7, we show the result of our $\eta T/w$ for $\mu_B = 0$ –600 MeV where in this case, we have not yet included an overall rescaling, i.e., $g_{norm} = 1$. Fig. 7 shows the $r = 0.25$ fm case in the HRG phase. The pQCD sector has the same renormalization to GMT at $\tilde{\mu} = 0$. The region where shear viscosity is calculated with our interpolation function in Eq. (28) is marked on each edge using large dots. We observe that the minimum is always located around $T = 300$ MeV, which is a consequence of the high values found for HRG calculations compared to the values found by GMT for the QGP phase.

However, one issue observed is that the $\eta T/w$ in Fig. 7 are still above the KSS bound [94] and differ in magnitude from what is seen in the Bayesian analyses. Thus, we will use our scaling factor g_{norm} to readjust the magnitude of η/s at $\tilde{\mu} = 0$ to obtain more reasonable values compared to experimental data. Then, g_{norm} remains constant across $\tilde{\mu}$.

Here, we follow the same procedure as in [104]:

- Find the minimum value of $(\eta/s)_{min}$ at $\mu_B = 0$. With that, we identify T_{min} as being the temperature where $(\eta/s)_{min}$ has its minimum value for $\mu_B = 0$.
- Then we can determine g_{norm} from

$$g_{norm} = \frac{(\eta/s)_{set}}{(\eta/s)_{min}} \quad (35)$$

where we have chosen $(\eta/s)_{set} \equiv 0.08$ to be the new minimum of η/s at $\mu_B = 0$ in the following results.

Initially, one could consider employing a data-driven method to establish the values for $(\eta/s)_{set}$ and the other parameters listed in Table 2. However, the main objective of this study is to use these models to obtain a plausible behavior across μ_B, μ_S, μ_Q , as there is scarce theoretical and experimental guidance available on $\eta T/w$ under finite densities.

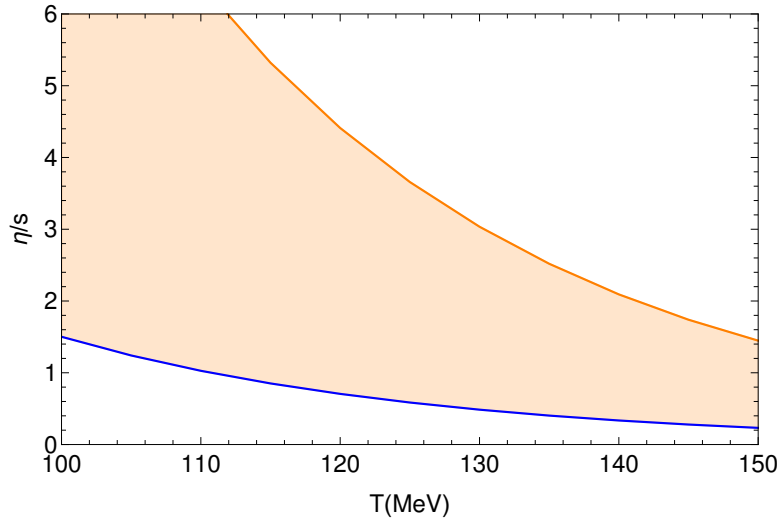


Figure 8: η/s as a function of the temperature in orange for $r = 0.1$ fm and blue for $r = 0.25$ fm. The shaded region corresponds to the uncertainty in our calculations due to the effective core radius choice.

From this point, we will now set $(\eta/s)_{set} = 0.08$ such that $g_{norm} \neq 1$. As mentioned before, the value of g_{norm} only shifts the overall magnitude of $\eta T/w$ but does not change the behavior across T, μ_B . Figure 8 shows the renormalized η/s at $\tilde{\mu} = 0$ for two different

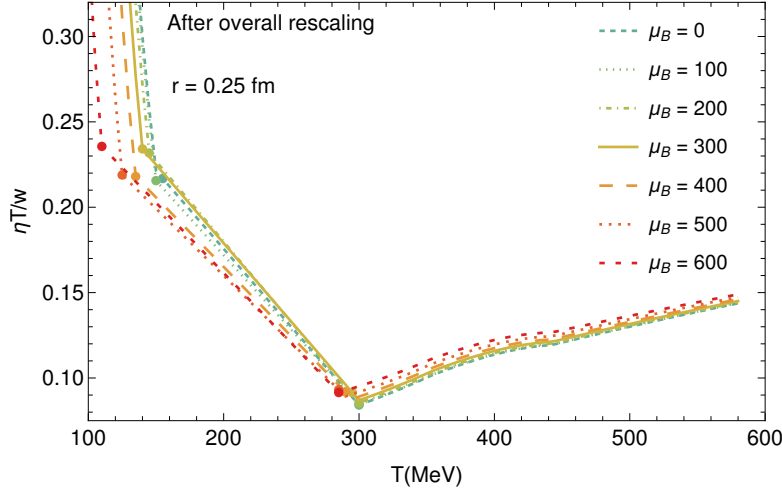


Figure 9: $\eta T/w(T, \mu_B)$ along different slices of μ_B in MeV for $r = 0.25$ fm. Here, we show the curves with the overall rescaling g_{norm} . The large dots show the interpolation region on the plot.

values of $r = 0.1$ fm (orange line) and $r = 0.25$ fm (blue line). Even after the overall rescaling, the values of η/s in the hadronic phase for $r = 0.1$ fm remain significantly higher than those predicted by other hadronic models, such as SMASH [73]. Hence, for the remainder of this Chapter, we focus only on the $r = 0.25$ fm case, which leads to values of shear viscosity that are more reasonable in magnitude and have a relevant finite $\bar{\mu}$ dependence for the pQCD limit.

We now study our shear viscosity at finite μ_B , using the formalism from the last section. As explained earlier, we use the same functional form at finite μ_B . However, the coefficients in the function form depend on μ_B , since they are determined at the matching points at both high and low temperatures to the pQCD and HRG results. In Fig. 9, we plot our results at finite μ_B for $r = 0.25$ fm where we have included the rescaling. The first effect we observe from our final functional is that, since the shear viscosity in the HRG phase at the transition point is generally higher than the shear viscosity at the pQCD transition point, i.e.,

$$\frac{\eta T}{w}(T_{sw,HRG}(\mu_B), \mu_B) > \frac{\eta T}{w}(T_{sw,pQCD}(\mu_B), \mu_B), \quad (36)$$

the minimum in $\eta T/w$ for a fixed μ_B ends up being at $T \sim 300$ MeV. One other effect that we see is that due to the drop in T_{sw} at finite μ_B , the $\eta T/w(T_{sw,HRG}(\mu_B), \mu_B)$ ends up increasing at large μ_B . In contrast, the transition point between pQCD and

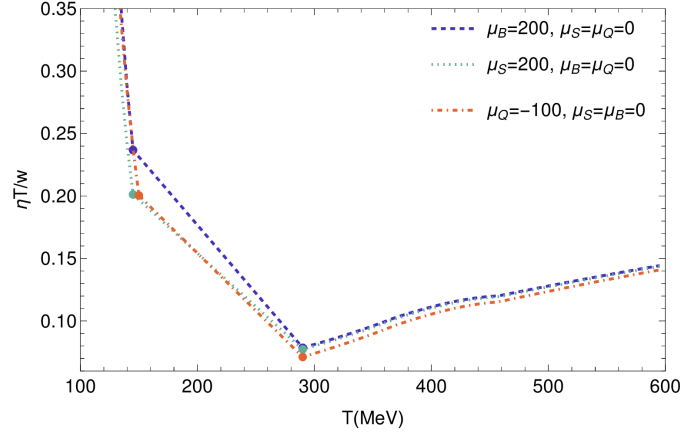


Figure 10: $\eta T/w$ as a function of the temperature for $r = 0.25$ fm comparing the three scenarios of $\mu_B > 0$ with $\mu_S = \mu_Q = 0$, $\mu_S > 0$ with $\mu_B = \mu_Q = 0$, and $\mu_Q > 0$ with $\mu_B = \mu_S = 0$. The large dots mark the edges of the interpolation region on the plot.

the interpolation does not vary nearly as strong with μ_B and therefore remains close to $\eta T/w(T_{sw,pQCD}(\mu_B), \mu_B) \sim (\eta/s)_{set}$.

In Figs. 7-9, we can also study the dependence of the HRG phase on T, μ_B . Generally, the HRG varies much more in T than the pQCD phase. Our setup also shows that the HRG has a stronger μ_B dependence than the pQCD phase. For a fixed T but increasing μ_B , we find that $\eta T/w$ for the HRG regime consistently decreases, and the same behavior is observed for a fixed μ_B but increasing T . Thus, the HRG regime has the opposite behavior compared to the pQCD phase, which increases with increasing T and μ_B . The difference in how $\eta T/w$ behaves in the HRG vs pQCD regime can be understood as follows. In the hadronic phase, we use a geometric cross-section for all the contributing scatterings in the system; as the number of particles increases and the scatterings become more frequent, this system will equilibrate faster. In the deconfined phase, this equilibration is only slightly affected by the density of particles, which tends to a constant.

Next, in Fig. 10, we compare three simple scenarios: $\mu_B > 0$ with $\mu_S = \mu_Q = 0$, $\mu_S > 0$ with $\mu_B = \mu_Q = 0$, and $\mu_Q > 0$ with $\mu_B = \mu_S = 0$. This is similar to what was previously shown for pQCD in Fig. 1, but here, we have matched the HRG calculations and plotted the final functional form obtained. The pQCD results for $\eta T/w$ are nearly identical for μ_B and μ_S finite for the range of chemical potentials we considered here. However, the HRG results find that a finite μ_S leads to a considerable suppression of $\eta T/w$ in the HRG phase.

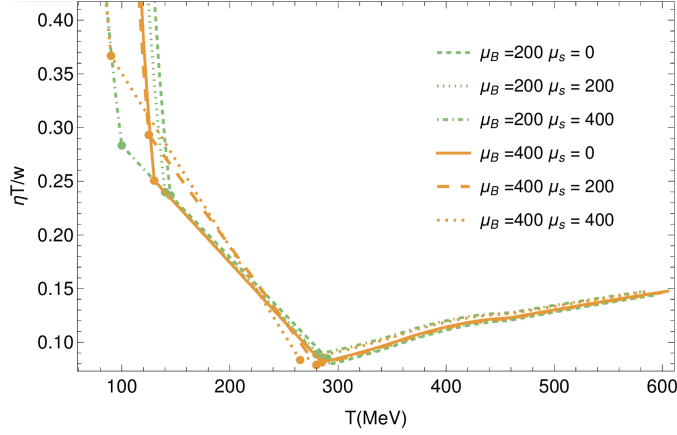


Figure 11: $\eta T/w$ as a function of the temperature for each value of μ_B for $r = 0.25$ fm. The interpolation region is indicated with closed-circle markers.

Using the same procedure described in the last section, we also show $\eta T/w$ for the case of $\mu_Q = 0$, $\mu_B > 0$, and $\mu_S > 0$ in Fig. 11 plotted vs the T . The colors here represent different values of μ_B , while the different line styles are the values of μ_S , as indicated in the figure. For $\mu_B = 200$ [MeV], the effect of μ_S is very small in the $0 - 200$ [MeV] range. However, at $\mu_S = 400$ [MeV], shear viscosity shifts to higher values in the pQCD regime. Additionally, we see a substantial shift in the transition between interpolation and HRG to lower values of T , such that the HRG calculation only appears around $T \sim 100$ [MeV]. We note that the shift in switching temperature is much smaller in the deconfined region than for the first-order phase transition. This happens because the Taylor series in Eq. (27) scales with μ/T_0 where the more significant value of T_0 for pQCD implies that a larger μ is needed to see the same effect (compared to the HRG transition). Finally, Fig. 12 shows the effect of positive and negative μ_Q on a system with $\mu_S = \mu_B > 0$. We observe that for the HRG region, $\mu_Q > 0$, there is a bigger suppression of $\eta T/w$ than for $\mu_Q < 0$. The opposite happens for the deconfined region, where the influence of μ_Q is not as pronounced as in the HRG phase.

Here, we have allowed the calculations of $\eta T/w$ from HRG and pQCD to determine the value of $\eta T/w(T_{sw,HRG}(\mu_B), \mu_B)$ and $\eta T/w(T_{sw,pQCD}(\mu_B), \mu_B)$ at the transition points. The pQCD results' overall magnitude is motivated by NLO calculations, which will be discussed further in this thesis. Although convergence has not yet been shown in the series, there is no clear indication of how to compute NNLO. On the other hand, in the

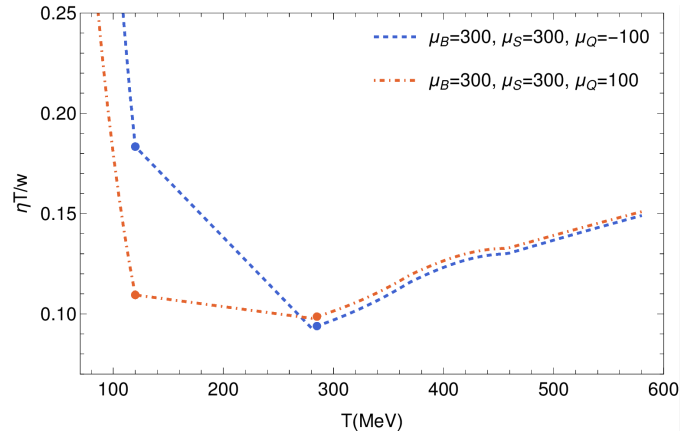


Figure 12: $\eta T/w$ as a function of the temperature for $r = 0.25$ fm when all three chemical potentials are finite. Here we hold $\mu_B = \mu_S = 300$ MeV fixed and vary only μ_Q .

HRG results, the magnitude results from a correlated combination between the number of hadronic states in the system, the masses, and the excluded volume [39]. Additionally, the HRG calculations depend on the assumption of a fixed volume for all hadrons. The overall magnitude may change if one were to measure further hadronic states eventually or include more complicated interactions.

Collision operator at leading order

In Chapter 4.1, we performed leading-log calculations of shear viscosity at high-temperature and high-density gauge theories — neglecting relative corrections suppressed only by powers of the inverse logarithm of the gauge coupling, $1/\log(1/g)$. Leading-log calculations may be regarded as improvements over phenomenological estimates based on relaxation time approximations [140, 139, 123, 27, 93, 92, 76]. However, they cannot be trusted to provide even a factor of two estimate in any real application, because the logarithm of the inverse gauge coupling, is never that large even for electromagnetism. This motivates us to extend these calculations to the leading order in g .

Transport coefficients are dominantly sensitive to the dynamics of excitations (i.e., quarks and gluons) with typical momenta of the order of the temperature T . And, as discussed in [9], it is possible to formulate an effective kinetic theory that correctly describes the leading-order dynamics of such excitations. The leading-order collision operator encodes the contribution of tree-level $2 \leftrightarrow 2$ scattering processes, with Hard-Loop, resummed propagators in the soft-sensitive channels, as well as collinear, effective $1 \leftrightarrow 2$ processes, resumming the effect of an infinite number of soft scatterings. Both processes contribute to order $g^4 T$ to the collision operator; a subset of $C_a^{2 \leftrightarrow 2}[f]$ is logarithmically enhanced, $g^4 T \ln(1/g)$, due to the sensitivity to the soft scale gT . $C_a^{2 \leftrightarrow 2}[f]$ and $C_a^{1 \leftrightarrow 2}[f]$ are described in detail in [10, 9]. Therefore, the collision term has the form:

$$\mathcal{C}_a[f] = \mathcal{C}_a^{2 \leftrightarrow 2}[f] + \mathcal{C}_a^{1 \leftrightarrow 2}[f] \quad (1)$$

In this Chapter, we perform a complete leading-order evaluation of shear viscosity. First, we describe the collision operator at leading order, considering contributions from $2 \leftrightarrow 2$ and $1 \leftrightarrow 2$ processes. Later, we present the results of these calculations and prepare the reader for the next-to-leading order corrections computed in the next chapter. These results, along with NLO results, are part of the work from [40] done in collaboration with my supervisor Guy D. Moore.

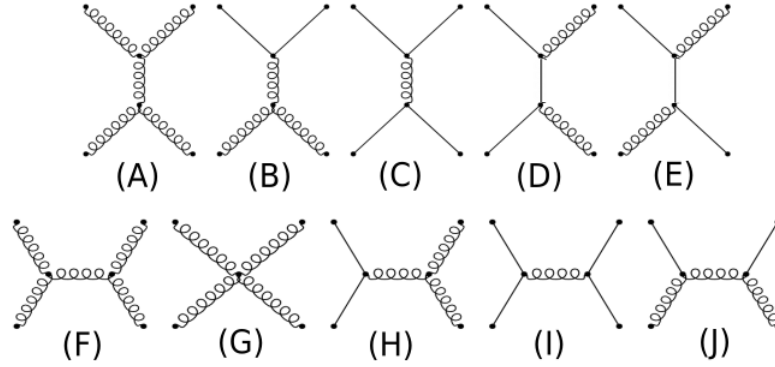


Figure 1: Diagrams contributing to the collision operator at the leading order.

1 Contributions from $2 \leftrightarrow 2$ scatterings

This section introduces the matrix elements contributing to $2 \leftrightarrow 2$ processes at leading order. These contributions come from the diagrams shown in Fig. 1, listed from (A) to (J). Here, diagrams (A) to (E) are the same as those used in Chapter 4.1 for the leading log calculations; the difference is that we do not cut the infrared divergences this time. Instead, we include thermal masses to regularize the collision integrals and obtain the full leading order contribution. The matrix elements generated from these diagrams, \mathcal{M}_{cd}^{ab} , are listed in table 1. The left column indicates the species involved in each scattering, and the right column shows the sum of the contributions from diagrams (A) to (J) to each specific scattering possibility. Here, underlined terms indicate the existence of an infrared divergence and the need for thermal self-energy correction to regulate its contribution. Singly underlined denominators indicate IR-sensitive contributions from soft gauge boson exchange, while double-underlined denominators indicate IR-sensitive contributions from a soft exchanged fermion. In terms of the collision operator, these contributions can be written as:

$$\begin{aligned}
 \mathcal{C}_a^{2 \leftrightarrow 2}[f](\vec{p}) = & \frac{1}{2} \sum_{bcd} \int_{\mathbf{k}\mathbf{p}'\mathbf{k}'} |M_{cd}^{ab}(\mathbf{p}, \mathbf{k}; \mathbf{p}', \mathbf{k}')|^2 (2\pi)^4 \delta^{(4)}(P + K - P' - K') \\
 & \left\{ f^a(\mathbf{p}) f^b(\mathbf{k}) [1 \pm f^c(\mathbf{p}')] [1 \pm f^d(\mathbf{k}')] - f^c(\mathbf{p}') f^d(\mathbf{k}') [1 \pm f^a(\mathbf{p})] [1 \pm f^b(\mathbf{k})] \right\}
 \end{aligned} \tag{2}$$

$ab \leftrightarrow cd$	$ \mathcal{M}_{cd}^{ab} ^2 / g^4$
$q_1 q_2 \leftrightarrow q_1 q_2$, $q_1 \bar{q}_2 \leftrightarrow q_1 \bar{q}_2$, $\bar{q}_1 q_2 \leftrightarrow \bar{q}_1 q_2$, $\bar{q}_1 \bar{q}_2 \leftrightarrow \bar{q}_1 \bar{q}_2$	$8 \frac{d_F^2 C_F^2}{d_A} \left(\frac{s^2 + u^2}{t^2} \right)$
$q_1 q_1 \leftrightarrow q_1 q_1$, $\bar{q}_1 \bar{q}_1 \leftrightarrow \bar{q}_1 \bar{q}_1$	$8 \frac{d_F^2 C_F^2}{d_A} \left(\frac{s^2 + u^2}{t^2} + \frac{s^2 + t^2}{u^2} \right) + 16 d_F C_F \left(C_F - \frac{C_A}{2} \right) \frac{s^2}{tu}$
$q_1 \bar{q}_1 \leftrightarrow q_1 \bar{q}_1$	$8 \frac{d_F^2 C_F^2}{d_A} \left(\frac{s^2 + u^2}{t^2} + \frac{t^2 + u^2}{s^2} \right) + 16 d_F C_F \left(C_F - \frac{C_A}{2} \right) \frac{u^2}{st}$
$q_1 \bar{q}_1 \leftrightarrow q_2 \bar{q}_2$	$8 \frac{d_F^2 C_F^2}{d_A} \left(\frac{t^2 + u^2}{s^2} \right)$
$q_1 \bar{q}_1 \leftrightarrow g g$	$8 d_F C_F^2 \left(\frac{u}{t} + \frac{t}{u} \right) - 8 d_F C_F C_A \left(\frac{t^2 + u^2}{s^2} \right)$
$q_1 g \leftrightarrow q_1 g$, $\bar{q}_1 g \leftrightarrow \bar{q}_1 g$	$-8 d_F C_F^2 \left(\frac{u}{s} + \frac{s}{u} \right) + 8 d_F C_F C_A \left(\frac{s^2 + u^2}{t^2} \right)$
$g g \leftrightarrow g g$	$16 d_A C_A^2 \left(3 - \frac{su}{t^2} - \frac{st}{u^2} - \frac{tu}{s^2} \right)$

Table 1: Expressions for the squares of vacuum matrix elements for $2 \leftrightarrow 2$ particle processes in QCD-like theories, after summing over spins and colors of all four particles. Where q_1 and q_2 represent fermions of distinct flavors, and \bar{q}_1 and \bar{q}_2 are the associated antifermions. Moreover, g represents a gauge boson. Table taken from [9].

where the incoming/outgoing momenta \vec{p}, \vec{k} and \vec{p}', \vec{k}' are all on shell, $p^0 = p$. The matrix squared element $|\mathcal{M}_{cd}^{ab}|$ is summed over all spin polarizations, colors, and hard thermal loop (HTL) resummed. We write $\int_{\vec{k}} = \int \frac{d^3\vec{k}}{(2\pi)^3}$ to simplify the notation. Next, we delve into the self-energy corrections for soft fermion and boson exchange.

1.1 Fermion self-energy corrections

Diagrams (D) and (E) represent $2 \leftrightarrow 2$ particle processes involving t (or u) channel fermion exchange and are displayed in table 1 double-underlined. When these processes are computed using free propagators, the resulting squared matrix elements generate logarithmic infrared divergences in the collision term[13, 9].

To cut off this divergence, one can include the retarded thermal self-energy. This computation can be rather involved, in that one can perform the same cut-off by replacing the matrix element with that computed in the Hard Thermal Loop (HTL) approximation that self-consistently treats the medium interaction correctly to leading order. This was already done for the photon rate by Refs. [90, 19], and for AMY calculations of leading order[9]. It was later shown in Refs. [3, 95] that there is a simpler treatment, which is also correct at this order. This process involves substituting the small angle approximation of the full Hard Thermal Loop (HTL) rate for the infrared divergent small angle approximation in the complete matrix element. Specifically for a soft fermion exchange in the t or u channel, one can use:

$$\frac{u-s}{t} \rightarrow \frac{u-s}{t} \frac{q^2}{q^2 + \xi_q^2 m_q^2} \quad (3)$$

where q is the exchanged momentum, $\xi_q = e/2$, and m_q is given by:

$$m_q^2 = 2g^2 \int_{\mathbf{p}} [2C_F f_g(\mathbf{p}) + C_F(f_q(\mathbf{p}) + f_{\bar{q}}(\mathbf{p}))] \quad (4)$$

Here, m_q the in-medium effective masses of quarks, and $\xi_q = e/2$ is chosen so that the matrix element reproduces the full HTL results at leading order for isotropic distributions [3, 61].

1.2 Gauge boson self-energy corrections

Analogously to diagrams (D) and (E), processes involving t or u-channel gauge boson exchange also have infrared divergencies when computed with free propagators. These diagrams are named as (A)-(C) in fig. 1. To handle this, one has to include the thermal gauge boson self-energy on the internal propagator to cut off the infrared sensitivity of

these processes. The self-energy must be taken to be an $O(1)$ correction, and all momenta must be considered to be in the same order[111, 9]. For that, we use,

$$\frac{(s^2 + u^2)}{t^2} = \frac{1}{2} + \frac{1}{2} \frac{(s - u)^2}{t^2} \quad \frac{su}{t^2} = \frac{1}{4} - \frac{1}{4} \frac{(s - u)^2}{t^2}, \quad (5)$$

Now, the matrix element of interest, $(s - u)^2/t^2$, can be written as:

$$\frac{(s - u)^2}{t^2} \longrightarrow |D^{ret}_{\mu\nu}(P - P')(P - P')^\mu(K - K')^\nu|^2, \quad (6)$$

where $D^{ret}_{\mu\nu}$ is the retarded boson propagator, and P, P', K and K' are the 4-momenta of the initial and final states. Furthermore, this can be understood by writing the square vacuum amplitude for t-channel exchange between massless scalars[10]:

$$|D^{ret}(P - P')_{\mu\alpha}(P - P')^\mu(K - K')^\nu|^2 = \left| \frac{(P - P') \cdot (K - K')}{(P - P')^2} \right|^2 = \frac{(s - u)^2}{t^2} \quad (7)$$

Following the same notation as [111], the plasma frame frequency and momentum carried by the gauge boson propagator are denoted as ω and q . The retarded gauge boson propagator can be conveniently expressed as:

$$D^{ret}_{00}(\omega, \mathbf{q}) = \frac{1}{q^2 - \Pi_{00}(\omega, \mathbf{q})} \quad (8)$$

$$D^{ret}_{ij}(\omega, \mathbf{q}) = \frac{\delta_{ij} - \hat{\mathbf{q}}_i \hat{\mathbf{q}}_j}{q^2 - \omega^2 + \Pi_T(\omega, \mathbf{p})} \quad (9)$$

$$D^{ret}_{0i}(\omega, \mathbf{q}) = D^{ret}_{i0}(\omega, \mathbf{q}) = 0 \quad (10)$$

The sign of D^{ret}_{ij} is opposite to the most common convention due to the metric, but the sign of Π_T^{ret} corresponds to the common usage. The equilibrium transverse and longitudinal gauge boson self-energies in the hard thermal loop approximation are [89, 146]

$$\Pi_T(\omega, \mathbf{q}) = m_D^2 \left\{ \frac{\omega^2}{2q^2} + \frac{\omega(q^2 - \omega^2)}{4q^3} \left[\ln \left(\frac{q + \omega}{q - \omega} \right) - i\pi \right] \right\}, \quad (11)$$

$$\Pi_{00}(\omega, \mathbf{q}) = -m_D^2 \left\{ 1 - \frac{\omega}{2q} \left[\ln \left(\frac{q + \omega}{q - \omega} \right) - i\pi \right] \right\}, \quad (12)$$

where we have assumed $|\omega| < q$, which is the only case of relevance for the calculations performed in this thesis. The expressions for obtaining these HTLs are detailed in the appendix 1, along with a comparison between HTL at $\mu = 0$ and $\mu > 0$. The remaining diagrams and the interference terms are finite and can be computed directly. Therefore, the next section describes the parametrizations used to compute these integrals in each channel.

1.3 The parametrizations for s , t and u channels

Performing the collision integrals at the leading order can be computationally challenging because one needs to perform multi-dimensional numerical integration at high precision. One straightforward method is to use an adaptive Monte Carlo integrator. However, as commented earlier in this thesis, we use one-dimensional adaptive Gaussian integration. In this section, we describe the convenient parametrizations for each channel and perform all possible integrations analytically, leaving only 4 integrals that must be numerically evaluated. The remaining of this section will be based on the work from [9], where the authors have first derived and computed these collision integrals.

t and u channels

For terms containing $t = -(P' - P)^2$ in the denominator, we use the techniques derived in Chapter 3 for the leading log calculations. First, use the spatial delta function to perform the \mathbf{k}' integration, and to shift the \mathbf{p}' integration into an integration over $\mathbf{p}' - \mathbf{p} \equiv \mathbf{q}$. Again, the angular integrals may be written in spherical coordinates defined such that the z axis is in the direction of \mathbf{q} while \mathbf{p} lies in the xz plane,

$$\begin{aligned} \left(\chi_{ij}, \mathcal{C}^{2 \leftrightarrow 2} \chi_{ij} \right) &= \frac{\beta^3}{(4\pi)^6} \sum_{abcd} \int_0^\infty q^2 dq p^2 dp k^2 dk \int_{-1}^1 d \cos \theta_{pq} d \cos \theta_{kq} \int_0^{2\pi} d\phi \frac{1}{p k p' k'} \\ &\quad \times \left| \mathcal{M}_{cd}^{ab} \right|^2 \delta(p+k-p'-k') f_0^a(p) f_0^b(k) [1 \pm f_0^c(p')] [1 \pm f_0^d(k')] \\ &\quad \times \left[\chi_{ij}^a(\mathbf{p}) + \chi_{ij}^b(\mathbf{k}) - \chi_{ij}^c(\mathbf{p}') - \chi_{ij}^d(\mathbf{k}') \right]^2, \end{aligned} \quad (13)$$

Here, we also use the same convention as the leading log calculations, where p , k , and q denote the magnitudes of the corresponding three-momenta, $p' \equiv |\mathbf{q} + \mathbf{p}|$ and $k' \equiv |\mathbf{k} - \mathbf{q}|$ are the magnitudes of the outgoing momenta, ϕ is the angle between the \mathbf{p}, \mathbf{q} plane and the \mathbf{k}, \mathbf{q} plane, and θ_{pq} is the angle between \mathbf{p} and \mathbf{q} .

Next, one may introduce a dummy integration variable ω , defined to equal the energy transfer $p' - p$, so that

$$\delta(p + k - p' - k') = \int_{-\infty}^{\infty} d\omega \delta(\omega + p - p') \delta(\omega - k + k'). \quad (14)$$

Following the same procedure as the leading log calculations, one can compute all angular

integrals except one, and the remaining integrals are

$$\begin{aligned}
(\chi_{ij}, \mathcal{C}^{2\leftrightarrow 2} \chi_{ij}) &= \frac{\beta^3}{(4\pi)^6} \sum_{abcd} \int_0^\infty dq \int_{-q}^q d\omega \int_{\frac{q-\omega}{2}}^\infty dp \int_{\frac{q+\omega}{2}}^\infty dk \int_0^{2\pi} d\phi \\
&\quad \times \left| \mathcal{M}_{cd}^{ab} \right|^2 f_0^a(p) f_0^b(k) [1 \pm f_0^c(p')] [1 \pm f_0^d(k')] \\
&\quad \times \left[\chi_{ij}^a(\mathbf{p}) + \chi_{ij}^b(\mathbf{k}) - \chi_{ij}^c(\mathbf{p}') - \chi_{ij}^d(\mathbf{k}') \right]^2, \quad (15)
\end{aligned}$$

with $p' = p + \omega$ and $k' = k - \omega$. For evaluating the final factor of (15), we use the relationship

$$I_{ij}(\hat{\mathbf{p}}) I_{ij}(\hat{\mathbf{k}}) = P_\ell(\cos \theta_{pk}). \quad (16)$$

One, therefore needs expressions for the angles between all species, as well as the remaining Mandelstam variables s and u , which may appear in \mathcal{M}^2 . They are[13, 9]

$$s = \frac{-t}{2q^2} \left\{ [(p+p')(k+k') + q^2] - \cos \phi \sqrt{(4pp' + t)(4kk' + t)} \right\}, \quad (17a)$$

$$u = -t - s, \quad (17b)$$

and

$$\cos \theta_{pq} = \frac{\omega}{q} + \frac{t}{2pq}, \quad \cos \theta_{p'q} = \frac{\omega}{q} - \frac{t}{2p'q}, \quad (18a)$$

$$\cos \theta_{kq} = \frac{\omega}{q} - \frac{t}{2kq}, \quad \cos \theta_{k'q} = \frac{\omega}{q} + \frac{t}{2k'q}, \quad (18b)$$

$$\cos \theta_{pp'} = 1 + \frac{t}{2pp'}, \quad \cos \theta_{kk'} = 1 + \frac{t}{2kk'}, \quad (18c)$$

$$\cos \theta_{pk'} = 1 + \frac{u}{2pk'}, \quad \cos \theta_{p'k} = 1 + \frac{u}{2p'k}, \quad (18d)$$

$$\cos \theta_{pk} = 1 - \frac{s}{2pk}, \quad \cos \theta_{p'k'} = 1 - \frac{s}{2p'k'}. \quad (18e)$$

where only t appears in the denominator of the matrix element, the ϕ integration can be straightforwardly conducted analytically, while the remaining integrals necessitate numerical evaluation. Analogously, when the denominator contains $u = -(K' - P)^2$, the natural choice of variables is exchanging \mathbf{p}' and \mathbf{k}' in the t channel parameterization.

s channel

On the other hand, for terms in which $s = -(P + K)^2$ appears in the denominator, one may use the spatial delta function to perform the \mathbf{k}' integration. However, the shift this time has to be from \mathbf{k} to $\mathbf{q} = \mathbf{p} + \mathbf{k}$, the total incoming spatial momentum (and the momentum on the internal propagator in s channel exchange processes). Again choosing spherical coordinates so that \mathbf{q} lies on the z axis and \mathbf{p} lies in the xz plane, the $2 \leftrightarrow 2$ contribution (68) becomes

$$\begin{aligned} \left(\chi_{ij}, \mathcal{C}^{2 \leftrightarrow 2} \chi_{ij} \right) &= \frac{\beta^3}{(4\pi)^6} \sum_{abcd} \int_0^\infty q^2 dq p^2 dp p'^2 dp' \int_{-1}^1 d \cos \theta_{pq} d \cos \theta_{p'q} \int_0^{2\pi} d\phi \frac{1}{p k p' k'} \\ &\quad \times \left| \mathcal{M}_{cd}^{ab} \right|^2 \delta(p+k-p'-k') f_0^a(p) f_0^b(k) [1 \pm f_0^c(p')] [1 \pm f_0^d(k')] \\ &\quad \times \left[\chi_{ij}^a(\mathbf{p}) + \chi_{ij}^b(\mathbf{k}) - \chi_{ij}^c(\mathbf{p}') - \chi_{ij}^d(\mathbf{k}') \right]^2, \end{aligned} \quad (19)$$

where now $k = |\mathbf{q} - \mathbf{p}|$, $k' = |\mathbf{q} - \mathbf{p}'|$, and ϕ is the azimuthal angle of \mathbf{k} (and \mathbf{k}'). Analogously to the t channel, we introduce the total energy ω via

$$\delta(p + k - p' - k') = \int_0^\infty d\omega \delta(\omega - p - k) \delta(\omega - p' - k'), \quad (20)$$

and defining $s = \omega^2 - q^2$, one finds

$$\delta(\omega - p - k) = \frac{k}{pq} \delta\left(\cos \theta_{pq} - \frac{\omega}{q} + \frac{s}{2pq}\right) \Theta(\omega - p), \quad (21)$$

$$\delta(\omega - p' - k') = \frac{k'}{p'q} \delta\left(\cos \theta_{p'q} - \frac{\omega}{q} + \frac{s}{2p'q}\right) \Theta(\omega - p'). \quad (22)$$

Integration over $\cos \theta_{pq}$ and $\cos \theta_{p'q}$ yields unity provided $q < \omega$, $|2p - \omega| < q$, and $|2p' - \omega| < q$ (and zero otherwise). Therefore,

$$\begin{aligned} \left(\chi_{ij}, \mathcal{C}^{2 \leftrightarrow 2} \chi_{ij} \right) &= \frac{\beta^3}{(4\pi)^6} \sum_{abcd} \int_0^\infty d\omega \int_0^\omega dq \int_{\frac{\omega-q}{2}}^{\frac{\omega+q}{2}} dp \int_{\frac{\omega-q}{2}}^{\frac{\omega+q}{2}} dp' \int_0^{2\pi} d\phi \\ &\quad \times \left| \mathcal{M}_{cd}^{ab} \right|^2 f_0^a(p) f_0^b(k) [1 \pm f_0^c(p')] [1 \pm f_0^d(k')] \\ &\quad \times \left[\left(\chi_{ij}^a(\mathbf{p}) + \chi_{ij}^b(\mathbf{k}) - \chi_{ij}^c(\mathbf{p}') - \chi_{ij}^d(\mathbf{k}') \right)^2 \right]. \end{aligned} \quad (23)$$

with $k = \omega - p$ and $k' = \omega - p'$. The other Mandelstam variables are

$$t = \frac{s}{2q^2} \left\{ [(p-k)(p'-k') - q^2] + \cos \phi \sqrt{(4pk-s)(4p'k'-s)} \right\}, \quad (24a)$$

$$u = -s - t, \quad (24b)$$

and the angles between \mathbf{q} and the external momenta are

$$\cos \theta_{pq} = \frac{\omega}{q} - \frac{s}{2pq}, \quad \cos \theta_{p'q} = \frac{\omega}{q} - \frac{s}{2p'q}, \quad (25a)$$

$$\cos \theta_{kq} = \frac{\omega}{q} - \frac{s}{2kq}, \quad \cos \theta_{k'q} = \frac{\omega}{q} - \frac{s}{2k'q}. \quad (25b)$$

Eqs. (18c)–(18e) for the angles between external momenta still hold. The angular integration over ϕ can be easily performed analytically, leaving four integrals to do numerically, similarly to the t channel.

2 Gluon emission in QGP

While the soft scatterings described in the last section may not appreciably change the momentum state of the particle, they could bring it slightly off-shell, thereby making it kinematically possible for the particle to decay through nearly collinear splitting [95]. As a consequence of that, effective $1 \leftrightarrow 2$ processes become a leading order effect. Hence, understanding the rate of gluon emission in a hot QCD plasma is essential for computing transport coefficients, such as shear viscosity [11]. The internal time scale associated with these phenomena closely mirrors the mean free time for soft scattering interactions with other particles within the plasma. Consequently, the gluon emission rate is susceptible to multiple scatterings throughout the emission event. This phenomenon is known as the Landau-Pomeranchuk-Migdal (LPM) effect [98, 97, 105]. Particularly in the nearly-collinear scenario, any additional explicit factors, such as g_s , are effectively offset by significant enhancements arising from the internal quark propagators and softly exchanged gluons. In this section, we will focus on the contributions of bremsstrahlung and pair annihilation to the rate of gluon emission, based on the works from [11, 12]. We present the expression for the gluon emission rate, starting from the photon emission rate expression, and a method to evaluate this rate. A detailed derivation for the photon emission rate can be found in the appendix 2.

2.1 Gluon emission rate

Here, we notice that, as pointed out in [11], the main difference between photon and gluon emission [136, 85, 86, 72, 79, 137] is that the gluon also carries color. Thus, a hard

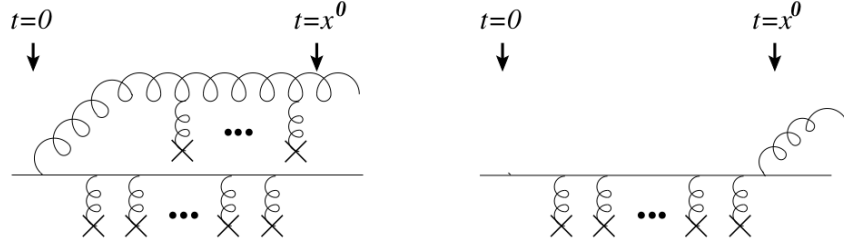


Figure 2: The diagrams show that the interactions are time ordered from left to right, whose interference contributes to the rate of gluon emission. The first diagram represents gluon emission at time zero, the second at time x^0 , and both diagrams show the evolution between these two times. Figure from [11]

gluon emitted can interact with the random colored background field akin to the emitting particle. However, when considering hard gluon emission, it is crucial to discern that the emitted gluon constitutes a distinct (quasi)particle from the soft background[11].

The gluon and quark involved in this emission process must be nearly collinear, leading to interactions that must happen in a definite order; this is illustrated in Fig.2. This ordering is necessary so the entire wave packet is well localized in all three dimensions. Nonetheless, there are a few complications to this description. Firstly, a color matrix T_{ab}^A is incorporated at the vertex of the hard particle. Secondly, correlations emerge between the soft gauge field encountered by the gluon and either emitter line.

Given that the interactions are ordered, it becomes feasible to summarize the diagrams using an integral equation. This equation comprises three components in the collision term, each corresponding to the three distinct types of correlations between lines illustrated in Fig. 3. The group theoretic coefficients can be found using,

$$T_R^b T_R^a T_R^b = \left(C_R - \frac{1}{2} C_A \right) T_R^a, \quad T_R^c T_R^b i f^{abc} = \frac{1}{2} C_A T_R^a. \quad (26)$$

where T_R^a denote representation R color generators. The temporal ordering of the soft gluon correlators allows one to determine the group factor for the whole diagram. This is done simply by including a factor of $(C_R - \frac{1}{2} C_A)$ to each line between emitters and $\frac{1}{2} C_A$ to each line from an emitter to the emitted gluon [11].

As a reflection of the fact that the gluon can scatter during the process time scale, which is $1/g^2 T$, a cross-rung can change either \mathbf{p} , \mathbf{k} , or both. Hence, using the expression for

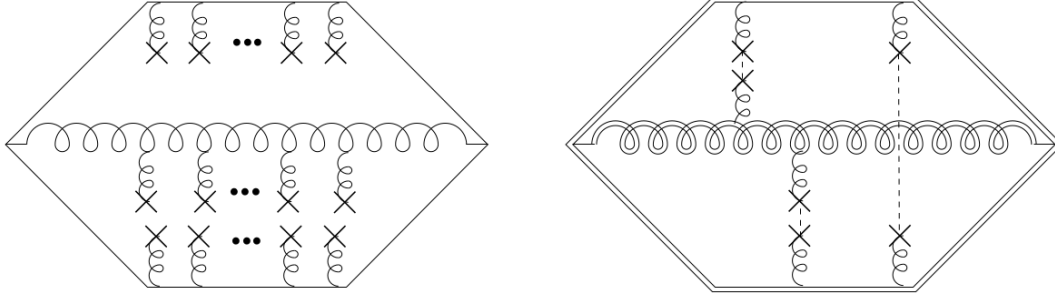


Figure 3: Diagrams showing the interference of the two gluon emission amplitudes of Fig. 2. Left: the product of amplitudes in a given background field. Right: the result after averaging over random background fields. Each line interacts with the soft background. When the background is averaged over, besides same-line correlations, represented by double lines for the sidebars, there are three distinct kinds of correlations between lines. Figure from [11].

photon emission from 2 and adding the differences, we can write:

$$\frac{d\Gamma_g^{\text{LPM}}}{d^3\mathbf{k}} = \frac{\alpha_s}{4\pi^2 k} \sum_s N_s d_s C_s \int_{-\infty}^{+\infty} \frac{dp_{\parallel}}{2\pi} \left\{ \int \frac{d^2\mathbf{p}_{\perp}}{(2\pi)^2} \frac{d^2\mathbf{k}_{\perp}}{(2\pi)^2} f_s(p_{\parallel} + k_{\parallel}) [1 \mp f_s(p_{\parallel})] \right. \\ \left. \times [1 + f_b(k_{\parallel})] \left| \mathcal{J}_{p_{\parallel} \leftarrow p_{\parallel} + k_{\parallel}}^{(s)} \right|^2 2\Delta_{\mathbf{p}\mathbf{k}} \cdot \text{Re} \mathbf{F}_s(\mathbf{p}_{\perp}, \mathbf{k}_{\perp}; p_{\parallel}, k_{\parallel}) \right\} \Big|_{k_{\parallel} \rightarrow k}, \quad (27)$$

Here, $1 + f_b(k)$ is a radiation stimulation factor, $\Delta_{\mathbf{p}\mathbf{k}} \equiv \mathbf{p}_{\perp} - p_{\parallel} \mathbf{k}_{\perp} / k_{\parallel}$ is the component of \mathbf{p} perpendicular to \mathbf{k} , and $|\mathbf{F}_s|$ is defined by the integral equation [11]:

$$2\Delta_{\mathbf{p}\mathbf{k}} (2\pi)^2 \delta^{(2)}(\mathbf{k}_{\perp}) = i \delta E \mathbf{F}_s(\mathbf{p}_{\perp}, \mathbf{k}_{\perp}; p_{\parallel}, k_{\parallel}) + g^2 \int_Q 2\pi \delta(q^0 - q_{\parallel}) \left\langle \left\langle A^+(Q) [A^+(Q)]^* \right\rangle \right\rangle \\ \times \left\{ (C_s - \frac{1}{2} C_A) [\mathbf{F}_s(\mathbf{p}_{\perp}, \mathbf{k}_{\perp}; p_{\parallel}, k_{\parallel}) - \mathbf{F}_s(\mathbf{p}_{\perp} - \mathbf{q}_{\perp}, \mathbf{k}_{\perp}; p_{\parallel}, k_{\parallel})] \right. \\ \left. + \frac{1}{2} C_A [\mathbf{F}_s(\mathbf{p}_{\perp}, \mathbf{k}_{\perp}; p_{\parallel}, k_{\parallel}) - \mathbf{F}_s(\mathbf{p}_{\perp} + \mathbf{q}_{\perp}, \mathbf{k}_{\perp} - \mathbf{q}_{\perp}; p_{\parallel}, k_{\parallel})] \right. \\ \left. + \frac{1}{2} C_A [\mathbf{F}_s(\mathbf{p}_{\perp}, \mathbf{k}_{\perp}; p_{\parallel}, k_{\parallel}) - \mathbf{F}_s(\mathbf{p}_{\perp}, \mathbf{k}_{\perp} + \mathbf{q}_{\perp}; p_{\parallel}, k_{\parallel})] \right\}. \quad (28)$$

Next, we exploit the rotational invariance of the problem, similarly to what is done for the collision operator. Except for $|\mathbf{F}_s|$, the elements of the integrand in the rate formula (27)

are invariant under small angle ($\theta \sim g$) rotations, which predominantly affects \mathbf{p}_\perp and \mathbf{k}_\perp at leading order, while leaving p_\parallel and k_\parallel largely unaffected[11]. Thus, we can decompose the $d^2p_\perp > d^2k_\perp$ into one component involving the relative momentum $\Delta_{\mathbf{p}\mathbf{q}}$ and another integral accounting for small rotations. The integration over small rotations can be merged into \mathbf{F}_s , defining a new function solely dependent on the quantity $\mathbf{h} \equiv k_\parallel \Delta_{\mathbf{p}\mathbf{q}}$, which can be expressed as,

$$\mathbf{h} = k_\parallel \mathbf{p}_\perp - p_\parallel \mathbf{k}_\perp. \quad (29)$$

This may also be written as $\mathbf{h} = (\mathbf{k} \times \mathbf{p}) \times \mathbf{e}_\parallel$, where \mathbf{e}_\parallel is the unit vector in the \parallel direction. The corresponding equations that only track changes in \mathbf{h} are

$$\begin{aligned} \frac{d\Gamma_g}{d^3\mathbf{k}} &= \frac{\alpha_s}{4\pi^2 k^2} \sum_s N_s d_s C_s \int_{-\infty}^{+\infty} \frac{dp}{2\pi} \int \frac{d^2\mathbf{h}}{(2\pi)^2} f_s(p+k) [1 \mp f_s(p)] [1 + f_b(k)] \\ &\quad \times \frac{1}{k^3} |\mathcal{J}_{p \leftarrow p+k}^{(s)}|^2 2\mathbf{h} \cdot \text{Re} \mathbf{F}_s(\mathbf{h}; p, k), \end{aligned} \quad (30)$$

where $\mathbf{F}_s(\mathbf{h}; p, k)$ is the solution to the integral equation

$$\begin{aligned} 2\mathbf{h} &= i \delta E(\mathbf{h}; p, k) \mathbf{F}_s(\mathbf{h}; p, k) + g^2 \int_Q 2\pi \delta(q^0 - q_\parallel) \left\langle \left\langle A^+(Q) [A^+(Q)]^* \right\rangle \right\rangle \\ &\quad \times \left\{ (C_s - \frac{1}{2} C_A) [\mathbf{F}_s(\mathbf{h}; p, k) - \mathbf{F}_s(\mathbf{h} - k \mathbf{q}_\perp; p, k)] \right. \\ &\quad \quad \quad \left. + \frac{1}{2} C_A [\mathbf{F}_s(\mathbf{h}; p, k) - \mathbf{F}_s(\mathbf{h} + (k+p) \mathbf{q}_\perp; p, k)] \right. \\ &\quad \quad \quad \left. + \frac{1}{2} C_A [\mathbf{F}_s(\mathbf{h}; p, k) - \mathbf{F}_s(\mathbf{h} - p \mathbf{q}_\perp; p, k)] \right\}, \end{aligned} \quad (31)$$

Here, $A^+(Q)$ represents the thermal Wightman correlator for the gluonic field, whereas δE is the energy difference between the initial and final collinear particles. It reads

$$\delta E(\mathbf{h}; p, k) = \frac{m_g^2}{2k} + \frac{m_s^2}{2p} + \frac{m_s^2}{2(-p-k)} - \frac{\mathbf{h}^2}{2pk(-p-k)}. \quad (32)$$

where m_s^2 is the asymptotic mass of the particle with momentum p . To simplify the presentation of these and the subsequent equations, we have omitted the \parallel subscripts from p_\parallel and k_\parallel . Additionally, it is worth noting that rotational invariance dictates that $\mathbf{F}_s(\mathbf{h}; p, k)$ should be proportional to \mathbf{h} multiplied by a scalar function of $|\mathbf{h}|$, p , and k . However, the integral equation (31) is more effectively expressed when $\mathbf{F}_s(\mathbf{h}; p, k)$ remains as a vector function.

Since this computation is rather involved, from this point, we will only consider the case $g \leftrightarrow gg$, in eq. (30). The other possibilities, $g \leftrightarrow qg$, $g \leftrightarrow \bar{q}g$ and $g \leftrightarrow \bar{q}q$ can be computed analogously. In the fully gluonic case, the sum over species s is only over gluons, which have $N_s = 2$, $d_s = d_A$, and $C_s = C_A$. The splitting function for gluons is [11, 9]

$$P_{gg \leftarrow g}(z) = \frac{1 + z^4 + (1-z)^4}{z(1-z)} \quad (33)$$

where $P_{gg \leftarrow g}(z)$ is the Altarelli-Parisi (or DGLAP) splitting function. For $z < 1$, which means hard gluons [11], it gives

$$|\mathcal{J}_{p \leftarrow p+k}^{(g)}|^2 = \frac{p^4 + k^4 + (p+k)^4}{8p^3 (p+k)^3}. \quad (34)$$

At this point, we note that one can recover photon emission results from the final gluon emission expressions (30) by substituting $C_A=0$ inside the integral equation, indicating that the emitted particle is colorless rather than in the adjoint representation. Please refer to 2 or consult [11, 9] for more detailed information.

Our aim in this section is to write the second term in the collision operator in Eq. (1). This is done by rewriting the leading-order equilibrium differential rate production for hard gluons, as defined in Eq. (30) in a similar form of (2). First, Eq. (30) is evaluated in equilibrium and then multiplied by $\nu_g/(2\pi)^3$. We begin by noting that further symmetry in this result, whether for quark or gluon emitters, can be revealed by reorganizing group factors such that the expression within curly braces in the integral equation (31) is

$$\left\{ \begin{aligned} & \frac{1}{2}(C_{R_3} + C_{R_1} - C_{R_2}) [\mathbf{F}_s(\mathbf{h}; p, k) - \mathbf{F}_s(\mathbf{h}-p_2 \mathbf{q}_\perp; p, k)] + \\ & \frac{1}{2}(C_{R_1} + C_{R_2} - C_{R_3}) [\mathbf{F}_s(\mathbf{h}; p, k) - \mathbf{F}_s(\mathbf{h}-p_3 \mathbf{q}_\perp; p, k)] + \\ & \frac{1}{2}(C_{R_2} + C_{R_3} - C_{R_1}) [\mathbf{F}_s(\mathbf{h}; p, k) - \mathbf{F}_s(\mathbf{h}-p_1 \mathbf{q}_\perp; p, k)] \end{aligned} \right\}, \quad (35)$$

where (p_1, p_2, p_3) denotes the three momenta $(p, k, -p-k)$ and $(C_{R_1}, C_{R_2}, C_{R_3})$ denote the quadratic Casimirs (C_s, C_A, C_s) of the corresponding color representations.

Next, we define γ_{bc}^a as the splitting rate, using the splitting function $|\mathcal{J}_{p \leftarrow p+k}^{(g)}|$. In the full gluonic case, the splitting rate is given by:

$$\gamma_{gg}^g(p; p-k, k) = \frac{g^2 d_A C_A}{64\pi^4} \left(\frac{p^4 + k^4 + (p+k)^4}{8p^3 (p+k)^3} \right) \int \frac{d\mathbf{h}^2}{(2\pi)^2} 2\mathbf{h} \cdot \text{Re} \mathbf{F}_s(\mathbf{h}) \quad (36)$$

As pointed out in [10], this differential gluon production rate is an infrared divergent quantity. This divergence comes from the part of the integral that represents processes

where a hard gluon with momentum \mathbf{p}' nearly equal to \mathbf{k} undergoes a soft scattering with emission or absorption of a soft gluon to produce a hard gluon with momentum \mathbf{k} . However, it was observed that physical quantities depend on this production rate with the subtraction of the corresponding rate at which gluons are scattered out of mode \mathbf{k} , and the infrared sensitivity cancels in the difference between these rates, therefore causing the collision terms to be infrared safe [11].

Finally, we can express the complete collision operator for $1 \leftrightarrow 2$ processes using the production rate. Here, we use a , b , and c to represent the species and write the collision term in a more general form,

$$\begin{aligned}
\mathcal{C}_a^{1 \leftrightarrow 2}[f](\vec{p}) &= \frac{(2\pi)^3}{2|\vec{p}|^2 \nu_a} \sum_{bc} \int_0^\infty dp' dk \delta(|\mathbf{p}| - p' - k) \gamma_{bc}^a(\mathbf{p}; p' \hat{\mathbf{p}}, k \hat{\mathbf{p}}) \\
&\quad \left\{ f^a(\mathbf{p}) [1 \pm f^b(p' \hat{\mathbf{p}})] [1 \pm f^c(k \hat{\mathbf{p}})] - f^b(p' \hat{\mathbf{p}}) f^c(k \hat{\mathbf{p}}) [1 \pm f^a(\mathbf{p})] \right\} \\
&+ \frac{(2\pi)^3}{2|\vec{p}|^2 \nu_a} \sum_{bc} \int_0^\infty dk dp' \delta(|\mathbf{p}| + k - p') \gamma_{bc}^a(\mathbf{p}; p' \hat{\mathbf{p}}, k \hat{\mathbf{p}}) \\
&\quad \left\{ f^a(\mathbf{p}) f^b(k \hat{\mathbf{p}}) [1 \pm f^c(p' \hat{\mathbf{p}})] - f^c(p' \hat{\mathbf{p}}) [1 \pm f^a(\hat{\mathbf{p}})] [1 \pm f^b(k \hat{\mathbf{p}})] \right\} \quad (37)
\end{aligned}$$

The splitting rate is now determined by solving the integral equation Eq. (31). This integral equation is rather involved, and it was computed in ref. [9] using a variational method similar to the one used to compute shear viscosity. Later, it was shown in [16] that this process is way more straightforward if worked out in the impact parameter space instead of the momentum space. We explore this approach in the following section, describing the method used to build the code for the splitting rate, written by G. Moore and adapted to be used in this work.

2.2 Solving the integral equation for γ_{bc}^a

Here, we show how to compute the splitting rate in the impact parameter space. For the sake of clarity, we begin with some definitions. In the last section, we have presented the splitting rate for the full gluonic case, $\gamma_{gg}^g(p'; p, k)$, here we introduce a more general form, $\gamma_{bc}^a(p'; p, k)$, for particle types $a \leftrightarrow bc$ with momenta $p' \leftrightarrow pk$. For non-Abelian gauge theories such as QCD, the splitting/joining functions of interest are given in equilibrium by [11, 9]

$$\gamma_{qg}^q(p'; p, k) = \gamma_{\bar{q}g}^{\bar{q}}(p'; p, k) = \frac{p'^2 + p^2}{p'^2 p^2 k^3} \mathcal{F}_q(p', p, k), \quad (38a)$$

$$\gamma_{q\bar{q}}^g(p'; p, k) = \frac{p^2 + k^2}{k^2 p^2 p'^3} \mathcal{F}_q(k, -p, p'), \quad (38b)$$

$$\gamma_{gg}^g(p'; p, k) = \frac{p'^4 + p^4 + k^4}{p'^3 p^3 k^3} \mathcal{F}_g(p', p, k), \quad (38c)$$

where

$$\mathcal{F}_s(p', p, k) \equiv \frac{d_s C_s \alpha}{2(2\pi)^3} \int \frac{d^2 h}{(2\pi)^2} 2\mathbf{h} \cdot \text{Re} \mathbf{F}_s(\mathbf{h}; p', p, k) \quad (39)$$

and $\alpha \equiv g^2/(4\pi)$. The function $\mathbf{F}_s(\mathbf{h}; p', p, k)$, is the same as defined in the last section, and for fixed given values of p' , p , and k , depends only on \mathbf{h} . For simplicity we will use the notation $\mathbf{F}_s(\mathbf{h}; p', p, k) = \mathbf{F}(\mathbf{h})$, and rewrite the integral equation Eq. (31) for \mathbf{F} as,

$$\begin{aligned} 2\mathbf{h} = & i\delta E(\mathbf{h}, p, \omega)\mathbf{F}(\mathbf{h}) + \int \frac{d^2 q_\perp}{(2\pi)^2} \mathcal{C}(\mathbf{q}^\perp) \left\{ (C_R - C_A/2)[\mathbf{F}(\mathbf{h}) - \mathbf{F}(\mathbf{h} - \omega\mathbf{q}_\perp)] \right. \\ & \left. + \frac{C_A}{2}[\mathbf{F}(\mathbf{h}) - \mathbf{F}(\mathbf{h} + p\mathbf{q}_\perp)] + \frac{C_A}{2}[\mathbf{F}(\mathbf{h}) - \mathbf{F}(\mathbf{h} - (p - \omega)\mathbf{q}_\perp)] \right\}. \end{aligned} \quad (40)$$

where

$$\mathcal{C}(\mathbf{q}^\perp) \equiv \int \frac{dq^z}{2\pi} \langle A^-(Q)[A^-(Q)]^* \rangle \Big|_{q^0=q^z}. \quad (41)$$

Here $Q = (q^0, \mathbf{q}^\perp, q^z)$, $A^- \equiv A^0 - A^z$, and $\langle A^-(Q)[A^-(Q)]^* \rangle$ is again the thermal Wightman correlator evaluated in the hard-thermal-loop approximation.

To tackle this, we follow [16], and Fourier transform this integral equation into an ordinary differential equation by going to impact parameter space. This process is straightforward if one defines,

$$\mathbf{F}(\mathbf{h}) \equiv \int d^2 \mathbf{b} e^{-i\mathbf{h} \cdot \mathbf{b}} \mathbf{F}(\mathbf{b}). \quad (42)$$

and Eq. (40) becomes

$$\begin{aligned} 0 = & i \left(-\frac{m_p^2}{2p} + \frac{m_k^2}{2k} + \frac{m_{p-k}^2}{2(p-k)} - \frac{p}{k(p-k)} \nabla_b^2 \right) \mathbf{F}(b) \\ & + \frac{1}{2\pi} \left(C_1 K(b) + C_2 K\left(\frac{bk}{p}\right) + C_3 K\left(\frac{b(p-k)}{p}\right) \right) \mathbf{F}(b) \end{aligned} \quad (43)$$

where $C_1, C_2, C_3 = C_{particle} - C_A/2$, and m_{p-k} is still the asymptotic mass but identified with the corresponding momentum since these masses could be either from gluons or quarks. Finally, K is the modified Bessel function of the second kind so that

$$K(b) = K_0(b) + \ln(b/2) + \gamma_E \quad (44)$$

We can now rewrite it as a scalar equation. First, we make $\vec{f} = \vec{b}u(b)$. Then we plug it back into Eq. (43),

$$0 = i \left(-\frac{m_p^2}{2p} + \frac{m_k^2}{2k} + \frac{m_{p-k}^2}{2(p-k)} \right) u - i \frac{p}{k(p-k)} \frac{3}{b} u'(b) - i \frac{p}{k(p-k)} u''(b) + \left(C_1 K(b) + C_2 K\left(\frac{bk}{p}\right) + C_3 K\left(\frac{b(p-k)}{p}\right) \right) u(b) \quad (45)$$

In this form, we analyze the behavior of the imaginary part to decide which solution is the correct one for our problem. For example, if the imaginary part shows a $1/b^2$ behavior, the solution to this problem is given by the real part times $4/\pi$. In the end, we multiply our solution by a factor of $(k(p-k))/pT$ to make up for the rescaling of the equation. Since numerically solving this equation can be a rather involved process, we add conditions to the derivatives of $u(b)$. We define $u(b)u(b) = b^2u(b)$. It obeys

$$uu'' = \frac{uu'}{b} + \frac{\left(-\frac{m_p^2}{2p} + \frac{m_k^2}{2k} + \frac{m_{p-k}^2}{2(p-k)} \right) uu - i \frac{C_1 K(b) + C_2 K\left(\frac{bk}{p}\right) + C_3 K\left(\frac{b(p-k)}{p}\right)}{\frac{p}{k(p-k)}} uu \quad (46)$$

Again, we must select the interesting solution to our problem. When the value at $b = 0$ is purely imaginary and 1, we want the solution where,

$$u(b) = \frac{2}{\pi} \frac{k(p-k)}{pTb} \text{Re}[u_{slope}] \quad (47)$$

For off-shell production, there is an additional scalar longitudinal component equation. However, this is related to the original equation with a missing factor of h on the left-hand side. Consequently, the term $\frac{3}{b}u'$ becomes $\frac{1}{b}u'$, and the boundary condition shifts to requiring $\text{Im}[u] = \text{const}$ when the purely real behavior of u' is $\frac{1}{b}$.

The solution to this problem involves a code that can handle differential equations with exponentially diminishing boundary conditions for large values. The objective is to isolate the finite component orthogonal to the divergent one at the origin. However, we will not be providing more details on the numeric evaluation of this differential equation because this is out of the scope of this thesis. In the next section, we comment on the high-density regime.

3 The high-density regime

In this section, we delve into the differences between the description of QGP at vanishing chemical potential, $\mu = 0$, and at high densities, $\mu > 0$. In leading-order and, consequently, next-to-leading-order calculations, it is necessary to regulate the infrared divergences arising from soft gluon exchanges in diagrams (A) to (E), as discussed in the last section. In [10], the author has tested the efficiency of hard thermal loops for a leading-order computation of transport coefficients at vanishing chemical potential, which we will use in this thesis.

Here, we make use of the results from [35] for hard thermal loops at high densities. In their work, the authors have shown that hard thermal loops are always proportional to the square of the thermal gluon mass, which is given by,

$$m_g = \frac{1}{9}N_g g^2 T + \frac{1}{18}N_f g^2 \left(T^2 + \frac{3}{\pi^2} \mu^2 \right) \quad (48)$$

At high chemical potential, there is an increase in the number of quarks and, therefore, an increase in the screening effect produced in this plasma. Hence, one must shift the screening mass as $m_D^2 \propto T^2 + \mu^2/\pi^2$, where the inclusion of π here is necessary to scale m_D at high densities correctly. Here, we use this result to regularize infrared divergences on the soft gluon exchange. This effect also influences the NLO calculations since the contribution to soft gluon corrections has a linear dependence on m_D . Similarly to the hard thermal loops, the splitting/joining processes will also be affected by the shift in the screening mass. Apart from that, smaller contributions at NLO from collinear and semi-collinear processes also depend on this shift, as we will see in the next Chapter.

Additionally, the physical picture of a dense plasma can be understood analogously to the leading log case from Chapter 4.1. The dominant scattering mechanism for particles to change their direction, for soft scattering, is well described in terms of momentum diffusion with a momentum-diffusion coefficient \hat{q} :

$$\hat{q} \equiv \int \frac{d^2 q_\perp}{(2\pi)^2} q_\perp^2 C(q_\perp) \quad (49)$$

where $C(q_\perp)$ is the differential rate to exchange transverse momentum q_\perp . In a thermal system without chemical potential, this is given by:

$$C(q_\perp) = g^2 C_F T \frac{m_D^2}{(q_\perp^2)(q_\perp^2 + m_D^2)} \quad (50)$$

In a high-density regime, the expression for \hat{q} remains the same; however, due to the shift of the screening mass, the momentum-diffusion coefficient is now directly dependent on

the chemical potential. This affects not only the statistical distributions of the system but also influences the relevance of the contributing scatterings.

4 Results

In the previous sections, we presented the ingredients necessary for the computation of shear viscosity in the leading order, except for the basis set. In the original AMY leading order calculations[9], the authors have presented a convenient basis for calculations at vanishing chemical potentials; however, since we are interested in the behavior of shear viscosity as a function of chemical potential, we will use the basis discussed in Chapter 4.1. This section presents results for the shear viscosity for different chemical potentials using the computational apparatus described in this Chapter. Starting with low temperatures and then going to the region where perturbation theory is expected to be mostly accurate.

Following the same approach used for the leading log analysis, we plot the shear viscosity to entropy density ratio η/s for LO in figure 4. Here, we chose to present η as a function of the temperature, going from lower temperatures, where only three flavors are included, up to high temperatures, where six flavors are expected to contribute. In figure 5, we show the kinematic viscosity, $\eta T/(e + P)$, as a function of the temperature in GeV. For these plots, we have used the EQCD coupling $\mu_{EQCD} = 2.7 T$, following the treatment from [62], more details about the coupling prescription can be found in Appendix 3. Given that our calculations include high chemical potentials, there is no literature indicating which choice of coupling is the most appropriate, so we remark that other couplings could also be reasonable and still give different results. The different colors in these plots represent lines with a fixed chemical potential, $\mu = 0, 3, \text{ and } 6$. The plots show behavior similar to that found for the leading log calculations. As the chemical potential increases, η/s is also increased. On the other hand, $\eta T/(e + P)$ has the opposite behavior and decreases with the chemical potential. The plots show that the qualitative conclusions from Chapter 4.1 remain valid up to the leading order. We observe the ratio $T\eta/(e + P)$ to depend weakly on μ/T [41]. Additionally, we observe again that in terms of the time scale $1/T$, a high-density fluid will relax somewhat more quickly than one at vanishing chemical potential[41].

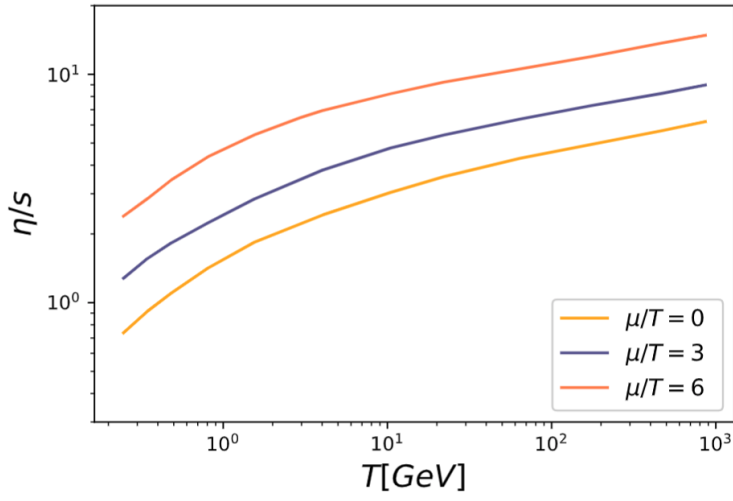


Figure 4: η/s as a function of the temperature for $\mu = 0, 3, 6$, calculated using $\mu_{EQCD} = 2.7 T$.

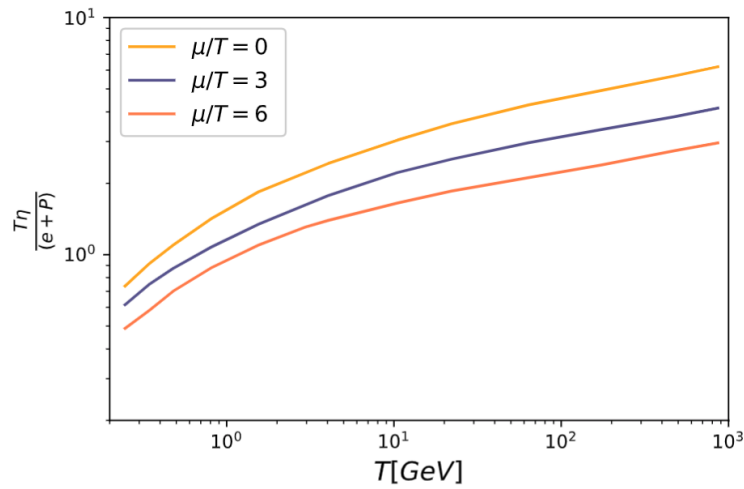


Figure 5: Kinematic shear viscosity as a function of the temperature for $\mu = 0, 3, 6$, calculated using $\mu_{EQCD} = 2.7 T$.

Next-to-Leading Order corrections

In the last Chapter, we described how to reorganize the collision operator to include screening effects and collinear processes. Next, we focus on the next-to-leading order corrections, first computed by Ghiglieri, Moore, and Teaney in [62]. In this work, the authors carefully described how to reorganize the leading-order treatment of Arnold, Moore, and Yaffe [9] into a contribution from generic momenta without screening, cut off at a transverse scale μ_{\perp} , and effective diffusion and identity changing processes. According

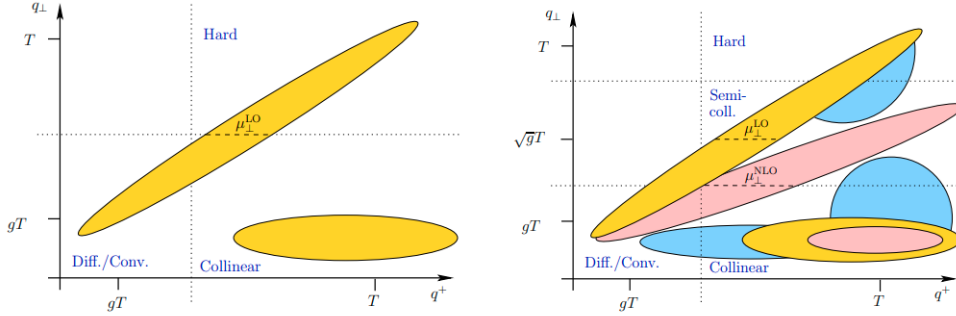


Figure 1: Left: kinematic regions, in terms of exchanged transverse momentum and exchanged light-cone momentum q^+ , which are relevant at leading order. Right: the same regions (yellow) plus regions that are relevant at next-to-leading order (pink) and where subtractions of leading-order effects are needed (blue). Figure taken from [62].

to this characterization, the linearized collision operator C is constructed purely as a g^4 entity multiplied by a logarithm plus a constant, thereby lacking any contributions formally subleading in g content. In this Chapter, we revisit the methodology to incorporate $O(g)$ corrections and describe the extension to the high-density regime.

Corrections of $O(g)$ can only arise if the calculations are sensitive to $q \sim gT$, as shown in Fig. 1. These energy levels are highly occupied, and loop corrections are of order $g^2 f_0(q) \sim g$ when bosons propagate at this energy scale [62]. Furthermore, the HTL

effects, essential at this momentum due to the infrared divergencies, as already described in Chapter 4, receive the first non-HTL corrections at $O(g)$. Additionally, in the $2 \leftrightarrow 2$ processes, the gT scale will only appear when the exchanged momentum is small or when an external particle becomes soft, meaning that $p \sim O(gT)$. In the first case, the process degenerates into a diffusion or identity change process. In the latter case, the states are nearly collinear or semi-collinear processes as referred to in [62]. In the case of $1 \leftrightarrow 2$ processes, the authors observed that the gT scale would appear in the transverse exchange momentum q_\perp and the screening mass m_∞ . Furthermore, the leading order treatment used in the last Chapter (Eq. 16) involved a collinear approximation which breaks down when one of the splitting daughters (final state particles) becomes soft, $k \sim gT$, $p - k \sim gT$, or when the transverse momentum becomes larger, $h \sim \sqrt{g}T^2$. The large- h region is what was called semi-collinear processes in [62]. In this Chapter, we review each correction, except for the soft quark exchange, which, up to this day, can only be estimated and will not have a central part in the high-density region. Later, we present the results of shear viscosity at high densities at the next-to-leading order on the coupling.

1 Soft gluon exchange

Typically, NLO contributions from soft gluon exchange come from diagrams (A), (B), and (C) of Fig (1) when one or both the external gluons are soft. It was shown in [62, 77], that the effect of soft gluon exchange on the evolution of the system can be summarized by a Fokker-Planck equation. To conserve energy and momentum, the Fokker-Planck equation must be supplemented by gain terms that describe how the momentum lost by a parton in the bath is redistributed. This redistribution of energy and momentum is essential in determining the transport coefficients, like shear viscosity and diffusion. The computation of these gain terms is not amenable to an evaluation using light-cone techniques since more than one light-like particle is involved, and therefore, computing the gain terms constitutes a major obstacle to computing transport coefficients at NLO. The Fokker-Planck collision kernel can be written as[62]

$$(C_{\text{diff}}^{2 \leftrightarrow 2} f_1)^a(\mathbf{p}) = -\frac{1}{2} \frac{\partial}{\partial p^i} \hat{q}_a^{ij} f_0^a(p) (1 \pm f_0^a(p)) \frac{\partial f_1^a(\mathbf{p})}{\partial p^j} + \text{gain-terms}, \quad (1)$$

where

$$\hat{q}_a^{ij} = \hat{q}_{a,L} \hat{p}^i \hat{p}^j + \frac{1}{2} \hat{q}_a (\delta^{ij} - \hat{p}^i \hat{p}^j) \quad (2)$$

represents the momentum diffusion parallel and perpendicular to the momentum of a particle through \hat{q}_L and \hat{q} , respectively. The gain terms will take the form:

$$\text{gain-terms} = \frac{1}{2} \frac{\partial}{\partial p^i} \left(f_0^a(p) (1 \pm f_0^a(p)) \sum_b \nu_b \int_{\mathbf{k}} \mathcal{C}_{ab}^{ij}(\hat{\mathbf{p}} \cdot \hat{\mathbf{k}}) f_0^b(k) (1 \pm f_0^b(k)) \frac{\partial f_1^b(\mathbf{k})}{\partial k^j} \right). \quad (3)$$

This gain term describes the redistribution of energy lost by a parton with momentum \mathbf{k} , as mentioned at the beginning of this section. The explicit form of the angular function, $\mathcal{C}_{ab}^{ij}(\hat{\mathbf{p}} \cdot \hat{\mathbf{k}})$, will be given ahead in the text. Since the diagrams of interest here are (A), (B), and (C), our aim here is to describe the t -channel matrix element in the soft approximation, which was done in [10, 9], and in Chapter 4 in the following form,

$$\frac{|\mathcal{M}_{ab}^{soft\,gt}|^2}{(2p)^2(2k)^2} = \frac{\nu_a C_{R_a} \nu_b C_{R_b} g^4}{d_A} |D_{\mu\nu}^{ret}(Q) v_{\mathbf{p}}^\mu v_{\mathbf{k}}^\nu|^2. \quad (4)$$

Here, $D_{\mu\nu}^{ret}$ is again the retarded HTL-resummed propagator as given in [36, 54] in the Coulomb gauge. Furthermore, in the soft expansion used in this section, it is possible to approximate the departures from equilibrium appearing as,

$$\left[f_1^a(\mathbf{p}) + f_1^b(\mathbf{k}) - f_1^a(\mathbf{p}') - f_1^b(\mathbf{k}') \right]^2 = \left[q^i \frac{\partial f_1^a(\mathbf{p})}{\partial p^i} - q^j \frac{\partial f_1^b(\mathbf{k})}{\partial k^j} \right]^2. \quad (5)$$

With the use of these approximations, the $2 \leftrightarrow 2$ collision operator can be rewritten in terms of the derivatives of f_1^a , and separated into a gain term and a loss term as follows,

$$(f_1, C_{diff}^{2 \rightarrow 2} f_1) \equiv (f_1, C_{diff}^{2 \rightarrow 2} f_1)|_{loss} + (f_1, C_{diff}^{2 \rightarrow 2} f_1)|_{gain}, \quad (6)$$

where the loss term is given by,

$$(f_1, C_{diff}^{2 \rightarrow 2} f_1)|_{loss} = \frac{1}{2} \beta^3 \sum_a \nu_a \int_{\mathbf{p}} f_0^a(p) (1 \pm f_0^a(p)) \hat{q}_a^{ij} \frac{\partial f_1^a(\mathbf{p})}{\partial p^i} \frac{\partial f_1^a(\mathbf{p})}{\partial p^j}, \quad (7)$$

and the gain term in the soft approximation can be rewritten as,

$$(f_1, C_{diff}^{2 \rightarrow 2} f_1)|_{gain} = -\frac{\beta^3}{2} \sum_{ab} \nu_a \nu_b \int_{\mathbf{pk}} f_0^a(p) (1 \pm f_0^a(p)) f_0^b(k) (1 \pm f_0^b(k)) \mathcal{C}_{ab}^{ij}(\hat{\mathbf{p}} \cdot \hat{\mathbf{k}}) \frac{\partial f_1^a(\mathbf{p})}{\partial p^i} \frac{\partial f_1^b(\mathbf{k})}{\partial k^j}, \quad (8)$$

and finally, the angular function $\mathcal{C}_{ab}^{ij}(\hat{\mathbf{p}} \cdot \hat{\mathbf{k}})$ is written as,

$$\mathcal{C}_{ab}^{ij}(\hat{\mathbf{p}} \cdot \hat{\mathbf{k}}) = \frac{g^4 C_{R_a} C_{R_b}}{d_A} \int \frac{d^4 Q}{(2\pi)^4} |D_{\mu\nu}^{ret}(Q) v_{\mathbf{p}}^\mu v_{\mathbf{k}}^\nu|^2 2\pi \delta(v_{\mathbf{p}} \cdot Q) 2\pi \delta(v_{\mathbf{k}} \cdot Q) q^i q^j, \quad (9)$$

and \hat{q}_a^{ij} is given by:

$$\hat{q}_a^{ij} = \sum_b \nu_b \int_{\mathbf{k}} f_0^b(k) (1 \pm f_0^b(k)) C_{ab}^{ij}(\hat{\mathbf{p}} \cdot \hat{\mathbf{k}}), \quad (10)$$

The expression for the loss term $(f_1, C_{\text{diff}}^{2\leftrightarrow 2} f_1)|_{\text{loss}}$ was carefully examined in [62], and the authors noticed that it involves a single light-like vector denoted as $v_{\mathbf{p}}$. The properties of light-like correlators were studied by Caron-Huot [38] while he was investigating the bremsstrahlung energy loss of high energy partons moving in the quark-gluon plasma at weak coupling. And made it possible to evaluate these soft contributions to \hat{q} and \hat{q}_L in a closed form [16, 63, 61],

$$\hat{q}^a \Big|_{\text{soft}} = \frac{g^2 C_{R_a} T m_D^2}{2\pi} \ln \frac{\mu_{\perp}}{m_D}, \quad \hat{q}_L^a \Big|_{\text{soft}} = \frac{g^2 C_{R_a} T m_D^2}{4\pi} \ln \frac{\sqrt{2}\mu_{\perp}}{m_D}. \quad (11)$$

Here $gT \ll \mu_{\perp} \ll T$ is a cutoff on the transverse momentum $q_{\perp} \equiv \sqrt{q^2 - \omega^2}$ integration, which is meant to separate the soft from the hard scale. The dependence on this cutoff cancels against the region where $\omega, q \gtrsim T$. This is the region where the bare matrix elements can be employed to evaluate the hard contribution to $C^{2\leftrightarrow 2}$ [62]. We also note that the simple form of \hat{q} and \hat{q}_L is a consequence of the fact that points separated by light-like intervals are causally disconnected concerning the influence of soft gauge fields. Next, we make use of the explicit form of the angular dependence of $f_1^a(\mathbf{p}) = \beta^2 \chi_{ij}(\mathbf{p}) X_{ij}$, presented in Chapter 4.1, inserted in the inner product of Eq. (80). With that, we can simplify the loss term and rewrite it as

$$\left(\chi_{ij}, C_{\text{diff}}^{2\leftrightarrow 2} \chi_{ij} \right) \Big|_{\text{loss}} = \frac{\beta^3}{2} \sum_a \nu_a \int_{\mathbf{p}} f_0^a(p) (1 \pm f_0^a(p)) \times \left[(\chi^a(p)')^2 \hat{q}_L^a \Big|_{\text{soft}} + \frac{\ell(\ell+1) \chi^a(p)^2}{2p^2} \hat{q}^a \Big|_{\text{soft}} \right], \quad (12)$$

which is the form commonly used to evaluate transport coefficients like shear viscosity and diffusion.

So far, we have presented the formalism necessary to treat the soft gluon exchange contributions from diagrams (A)-(C), which are of order $O(g)$. However, in order to compute next-to-leading order corrections from these diagrams, we follow the prescription from [62], and perform a shift in the transverse momentum diffusion coefficient \hat{q}^a as [38]

$$\delta \hat{q}^a = \frac{g^4 C_{R_a} C_A m_D T^2}{32\pi^2} (3\pi^2 + 10 - 4 \ln 2). \quad (13)$$

the shift included in the soft gluon exchange diffusion rate gives,

$$\left(\chi_{ij}, C^{\delta\hat{q}} \chi_{ij}\right) = \frac{\beta^3}{2} \sum_a \nu_a \delta\hat{q}^a \int_{\mathbf{p}} f_0^a(p) [1 \pm f_0^a(p)] \frac{\ell(\ell+1) \chi^a(p)^2}{2p^2}. \quad (14)$$

This contribution is diagonal and has similar behavior to the leading log contributions from Chapter 4.1. The gain terms will not be calculated in this thesis since their contribution can, up to this day, only be estimated, and as suggested in [62], can be set to zero.

2 Collinear contributions

In this section, we present the formalism used to introduce NLO corrections to the $1 \leftrightarrow 2$ collision kernel from Chapter 4. Similarly to the leading order treatment, we approximate these contributions to be collinear. Then, we introduce a shift in the thermal masses to obtain the NLO contribution. For the sake of clarity, we write again the collision operator for $2 \leftrightarrow 1$ processes in a more compact way,

$$\begin{aligned} C_a^{1 \leftrightarrow 2}[f](\vec{p}) &= \frac{(2\pi)^3}{2|\vec{p}|^2 \nu_a} \sum_{bc} \int_0^\infty dp' dk \delta(|\mathbf{p}| - p' - k') \gamma_{bc}^a(\mathbf{p}; p' \hat{\mathbf{p}}, k' \hat{\mathbf{p}}) \\ &\quad \left\{ f^a(\mathbf{p}) [1 \pm f^b(p' \hat{\mathbf{p}})] [1 \pm f^c(k' \hat{\mathbf{p}})] - f^b(p' \hat{\mathbf{p}}) f^c(k' \hat{\mathbf{p}}) [1 \pm f^a(\mathbf{p})] \right\} \\ &+ \frac{(2\pi)^3}{2|\vec{p}|^2 \nu_a} \sum_{bc} \int_0^\infty dk dp' \delta(|\mathbf{p}| + k - p') \gamma_{bc}^a(\mathbf{p}; p' \hat{\mathbf{p}}, k \hat{\mathbf{p}}) \\ &\quad \left\{ f^a(\mathbf{p}) f^b(k \hat{\mathbf{p}}) [1 \pm f^c(p' \hat{\mathbf{p}})] - f^c(p' \hat{\mathbf{p}}) [1 \pm f^a(\hat{\mathbf{p}})] [1 \pm f^b(k \hat{\mathbf{p}})] \right\} \end{aligned} \quad (15)$$

where the $\gamma_{bc}^a(p; p-k, k)$ is defined by the integral,

$$\gamma_{bc}^a(p; p-k, k) = \frac{g^2 d_{R_b} C_{R_b}}{64\pi^4} \begin{cases} \frac{p^4 + k^4 + (p-k)^4}{p^3 k^3 (p-k)^3} & g \leftrightarrow gg \\ \frac{p^2 + (p-k)^2}{p^2 k^3 (p-k)^2} & q \leftrightarrow qg \\ \frac{p^2 + (p-k)^2}{p^3 k^2 (p-k)^2} & g \leftrightarrow q\bar{q} \end{cases} \int \frac{d\mathbf{h}^2}{(2\pi)^2} 2\mathbf{h} \cdot \text{Re}\mathbf{F}(\mathbf{h}) \quad (16)$$

Here we follow the same procedure described in [64], which means we Fourier transform \mathbf{h} and \mathbf{q}_\perp into impact-parameter variables, as proposed in [16] to solve Eq. (31), in the same way as in Chapter 4. This diagonalizes the collision kernel $C(k_\perp)$ and converts an integral equation into a differential equation. Additionally, the source on the left-hand side becomes a boundary condition at $\mathbf{b} = 0$. At the same time, the desired final integral

corresponds to a boundary value of the ordinary differential equation (ODE) solution. Hence, using the definition from Chapter 4,

$$\mathbf{F}(\mathbf{b}) = \int \frac{d^2h}{(2\pi)^2} e^{i\mathbf{b}\cdot\mathbf{h}} \mathbf{F}(\mathbf{h}), \quad (17)$$

we have that

$$\text{Re} \int \frac{d^2h}{(2\pi)^2} 2\mathbf{h} \cdot \mathbf{F}(\mathbf{h}) = \text{Im}(2\nabla_{\mathbf{b}} \cdot \mathbf{F}(0)), \quad (18)$$

and Eq. (31) becomes

$$\begin{aligned} -2i\nabla\delta^2(\mathbf{b}) &= \frac{i}{2p\omega(p-\omega)} (p(p-\omega)m_{\infty\omega}^2 + p\omega m_{\infty p-\omega}^2 - \omega(p-\omega)m_{\infty p}^2 - \nabla_{\mathbf{b}}^2) \mathbf{F}(\mathbf{b}) \\ &+ \left(\mathcal{C}'_R(|\omega|b) - \frac{\mathcal{C}'_A(|\omega|b)}{2} + \frac{\mathcal{C}'_A(|p|b)}{2} + \frac{\mathcal{C}'_A(|p-\omega|b)}{2} \right) \mathbf{F}(\mathbf{b}), \end{aligned} \quad (19)$$

with

$$\mathcal{C}'_R(|\omega|b) \equiv \int \frac{d^2\mathbf{k}_{\perp}}{(2\pi)^2} (1 - e^{i\omega\mathbf{b}\cdot\mathbf{k}_{\perp}}) \mathcal{C}_R(\mathbf{k}_{\perp}). \quad (20)$$

Here, we are interested in the effects of $\mathcal{O}(g)$ that can manifest into our collision operator. These can be cast as:

- the effective thermal masses squared $m_{\infty,p}^2$,
- the collision kernel $\mathcal{C}(\mathbf{k}_{\perp})$ receive $\mathcal{O}(g)$ corrections

These corrections will affect the differential Eq. (19), which now has contributions in the following form[64],

$$m_{\infty p, LO+NLO}^2 = m_{\infty p}^2 + \delta m_{\infty p}^2, \quad (21)$$

$$\mathcal{C}'_{R, LO+NLO}(b) = \mathcal{C}'_R(b) + \delta\mathcal{C}'_R(b). \quad (22)$$

where $\delta m_{\infty p}$ represents the shift in the LO thermal mass that is necessary to make it NLO and is given by

$$\delta m_{\infty}^2 = -gC_F \frac{Tm_D}{2\pi}, \quad (23)$$

This thesis highlights that the NLO collision kernel was first computed in [38] in momentum space. Later, the Fourier transformation into impact parameter space was performed in [64], giving the form we present in this section. Furthermore, in [38], the authors have also explicitly shown that “three-pole” contributions are absent at NLO, so the sum of

two-body (dipole) interactions on the second line of Eq. (19) still hold. Which agrees with the treatment used in this work.

Finally, Eq. (19) can be solved perturbatively, by treating $\mathbf{F}(\mathbf{b})$ formally as an expansion in powers of δm_∞ and $\delta \mathcal{C}$, so that the function $\mathbf{F}(\mathbf{b})$ can be written as,

$$\mathbf{F}(\mathbf{b}) = \mathbf{F}_0(\mathbf{b}) + \mathbf{F}_1(\mathbf{b}) + \dots \quad (24)$$

A first-order expansion is already sufficient to compute the effects of order $O(g)$. The zero-order expression is just Eq. (19), and the linear order the expression reads[64]

$$\begin{aligned} 0 = & \left(\frac{i}{2p\omega(p-\omega)} \left((p(p-\omega)m_{\infty\omega}^2 + p\omega m_{\infty p-\omega}^2 - \omega(p-\omega)m_{\infty p}^2 - \nabla_{\mathbf{b}}^2) \right. \right. \\ & \left. \left. + \mathcal{C}'_R(|\omega|b) - \frac{\mathcal{C}'_A(|\omega|b)}{2} + \frac{\mathcal{C}'_A(|p|b)}{2} + \frac{\mathcal{C}'_A(|p-\omega|b)}{2} \right) \mathbf{F}_1(\mathbf{b}) \right. \\ & \left. + \left(\frac{i}{2p\omega(p-\omega)} \left((p(p-\omega)\delta m_{\infty\omega}^2 + p\omega \delta m_{\infty p-\omega}^2 - \omega(p-\omega)\delta m_{\infty p}^2) \right. \right. \right. \\ & \left. \left. \left. + \delta \mathcal{C}'_R(|\omega|b) - \frac{\delta \mathcal{C}'_A(|\omega|b)}{2} + \frac{\delta \mathcal{C}'_A(|p|b)}{2} + \frac{\delta \mathcal{C}'_A(|p-\omega|b)}{2} \right) \mathbf{F}_0(\mathbf{b}), \right. \end{aligned} \quad (25)$$

where the leading order solution $\mathbf{F}_0(\mathbf{b})$ acts as a source term in the differential equation for $\mathbf{F}_1(\mathbf{b})$. To evaluate Eq. (19), one must deal with mixed boundary conditions. These conditions are: the function $\mathbf{f}(\mathbf{b})$ must decay to zero as $\mathbf{b} \rightarrow \infty$, and it must yield the correct normalization, which, at zero, is given by

$$\nabla_{\mathbf{b}}^2 \mathbf{f}_0(\mathbf{b}) = \frac{4p^+(k+p^+)}{k} \nabla \delta^2(\mathbf{b}) \quad (26)$$

Here, $p^+ = \frac{p_0+p_z}{2}$, is the light-cone coordinate. Hence, the evaluation is done by evolving the differential equation starting at large \mathbf{b} , with initial conditions ensuring that the solution decays as $\mathbf{b} \rightarrow \infty$ but with an arbitrary normalization. Subsequently, one solves the differential equation inward towards the origin. This solution is then scaled by a complex constant so that Eq. (26) is satisfied. Similarly, when solving Eq. (25) for $\mathbf{f}_1(\mathbf{b})$, the boundary condition that $\mathbf{f}_1(\mathbf{b})$ should decay at large \mathbf{b} is insufficient to completely determine the solution[64, 60].

Consequently, one typically obtains a solution that combines the solution to Eq. (25) with the correct boundary condition $\lim_{\mathbf{b} \rightarrow 0} \nabla^2 \mathbf{f}_1(\mathbf{b}) = 0$, along with a multiple of the homogeneous solution with the incorrect boundary condition at zero. However, the homogeneous solution is proportional to \mathbf{f}_0 , which is known, allowing it to be subtracted to obtain the solution with the correct boundary condition. For more details on the boundary conditions and the numerical evaluation of these equations, one should refer to [64, 60, 65]

3 Semi-collinear contributions

Next, we focus on the semi-collinear processes. These contributions lie between elastic scattering, where the particle undergoes a substantial change in energy and transverse momentum, and collinear contributions, where the change in energy is significant but the change in transverse momentum is small[62]. As a result, it requires subtractions from each. Additionally, it requires subtraction of its soft-exchange tail.

To obtain the semi-collinear contributions, we will treat the emission in the Bethe-Heitler limit, which means ignoring LPM corrections. First, we consider the simplifying approximation used in the collinear contributions as \mathbf{h} becomes large, namely $\mathbf{h} \gg gT^2$. As shown in [62] and discussed in the last section, the integral equation, Eq. (18), can be solved iteratively in large δE :

$$\begin{aligned} \mathbf{F}_{b1}(\mathbf{h}) &= 2\mathbf{h}/i\delta E(\mathbf{h}), \\ \mathbf{F}_{b2}(\mathbf{h}) &= \frac{i}{\delta E(\mathbf{h})} \int \frac{d^2q_{\perp}}{(2\pi)^2} \bar{C}(q_{\perp}) \left\{ \left(C_{Rb} - \frac{C_A}{2} \right) [\mathbf{F}_{b1}(\mathbf{h}) - \mathbf{F}_{b1}(\mathbf{h} - k\mathbf{q}_p)] \right. \\ &\quad \left. + \frac{C_A}{2} [\mathbf{F}_{b1}(\mathbf{h}) - \mathbf{F}_{b1}(\mathbf{b} + p\mathbf{q}_p)] + \frac{C_A}{2} [\mathbf{F}_{b1}(\mathbf{b}) - \mathbf{F}_{b1}(\mathbf{h} - (p-k)\mathbf{q}_p)] \right\}. \end{aligned} \quad (27)$$

We can assume that the \mathbf{h}^2 term dominates in the expression for δE , so $\delta E(\mathbf{h}) = \mathbf{h}^2/(2pk(p-k))$. However, this expansion breaks down for high values of h . The reason is that we can no longer neglect q^- relative to q_{\perp} . This discrepancy arises because $q^- = \delta E \sim gT \sim q_{\perp}$, which contrasts with the assumption made in exchange processes where $q_{\parallel} = \omega$ (implying $q^- = 0$), that we have used to compute the collinear processes. Therefore, the kinematics of scattering are changed and $\bar{C}(q_{\perp})$ must be recomputed. A more accurate form for $\bar{C}(q_{\perp})$ in this regime is [64, 61]

$$\bar{C}_{\text{NLO}}(q_{\perp}, \delta E) = \frac{g^2 T m_D^2}{(q_{\perp}^2 + \delta E^2)(q_{\perp}^2 + \delta E^2 + m_D^2)} + \frac{2g^2 T \delta E^2}{q_{\perp}^2 (q_{\perp}^2 + \delta E^2)}. \quad (28)$$

Physically, this arises from two distinct processes: one where the splitting is induced by elastic scattering and another where the absorption of a soft on-shell particle induces it. Consequently, we need to perform two subtractions. The first subtraction accounts for the already-computed leading-order (LO) $1 \leftrightarrow 2$ contribution, corresponding to the small δE limit. The second subtraction adjusts for the already-included LO $2 \leftrightarrow 2$ contribution, as discussed in [62]:

$$\delta \bar{C}(q_{\perp}, \delta E) = \frac{g^2 T m_D^2}{(q_{\perp}^2 + \delta E^2)(q_{\perp}^2 + \delta E^2 + m_D^2)} - \frac{g^2 T m_D^2}{q_{\perp}^2 (q_{\perp}^2 + m_D^2)}. \quad (29)$$

The second term is the LO collinear form for \tilde{C} (the small δE limit of Eq. (28), which will be calculated using the Bethe-Heitler bremsstrahlung emission rate). The other subtraction of the $m_D \rightarrow 0$ limit removed the second term appearing in Eq. (28). Therefore, we can use the full expression for $\delta\tilde{C}$ in Eq. (27), and obtain the manifestly finite result for the semi-collinear rate as,

$$\begin{aligned} \gamma_{bc}^a \Big|_{\text{semi}}(p; p-k, k) &= \frac{g^2}{32\pi^4} \begin{cases} d_A C_A \frac{p^4+k^4+(p-k)^4}{p^3 k^3 (p-k)^3} & g \leftrightarrow gg \\ d_F C_F \frac{p^2+(p-k)^2}{p^2 (p-k)^2 k^3} & q \leftrightarrow qq \\ d_F C_F \frac{(p-k)^2+k^2}{(p-k)^2 k^2 p^3} & g \leftrightarrow q\bar{q} \end{cases} \int \frac{d^2\mathbf{h}}{(2\pi)^2} \int \frac{d^2\mathbf{q}'}{(2\pi)^2} \delta\tilde{C}(\mathbf{q}', \delta E) \\ &\times \left[\left(C_R - \frac{C_A}{2} \right) \left(\frac{\mathbf{h}}{\delta E(\mathbf{h})} - \frac{\mathbf{h} - k\mathbf{q}_\perp}{\delta E(\mathbf{h} - k\mathbf{q}_\perp)} \right)^2 + \frac{C_A}{2} \left(\frac{\mathbf{h}}{\delta E(\mathbf{h})} - \frac{\mathbf{h} + p\mathbf{q}_\perp}{\delta E(\mathbf{h} + p\mathbf{q}_\perp)} \right)^2 \right. \\ &\quad \left. + \frac{C_A}{2} \left(\frac{\mathbf{h}}{\delta E(\mathbf{h})} - \frac{\mathbf{h} - (p-k)\mathbf{q}_\perp}{\delta E(\mathbf{h} - (p-k)\mathbf{q}_\perp)} \right)^2 \right], \end{aligned} \quad (30)$$

To compute this rate, we first write explicitly the integral equation for each term of $\delta\tilde{C}$; the first term gives,

$$\begin{aligned} \gamma_{bc}^a \Big|_{\text{first}}(p; p-k, k) &= \frac{g^2}{32\pi^4} \begin{cases} d_A C_A \frac{p^4+k^4+(p-k)^4}{p^3 k^3 (p-k)^3} & g \leftrightarrow gg \\ d_F C_F \frac{p^2+(p-k)^2}{p^2 (p-k)^2 k^3} & q \leftrightarrow qq \\ d_F C_F \frac{(p-k)^2+k^2}{(p-k)^2 k^2 p^3} & g \leftrightarrow q\bar{q} \end{cases} \int \frac{d^2\mathbf{h}}{(2\pi)^2} \int \frac{d^2\mathbf{q}_\perp}{(2\pi)^2} \\ &\times \frac{g^2 T m_D^2}{(\mathbf{q}_\perp^2 + \delta E(\mathbf{h})^2)(\mathbf{q}_\perp^2 + \delta E(\mathbf{h})^2 + m_D^2)} \left[\left(C_R - \frac{C_A}{2} \right) \left(\frac{\mathbf{h}}{\delta E(\mathbf{h})} - \frac{\mathbf{h} - k\mathbf{q}_\perp}{\delta E(\mathbf{h} - k\mathbf{q}_\perp)} \right)^2 \right. \\ &\quad \left. + \frac{C_A}{2} \left(\frac{\mathbf{h}}{\delta E(\mathbf{h})} - \frac{\mathbf{h} + p\mathbf{q}_\perp}{\delta E(\mathbf{h} + p\mathbf{q}_\perp)} \right)^2 + \frac{C_A}{2} \left(\frac{\mathbf{h}}{\delta E(\mathbf{h})} - \frac{\mathbf{h} - (p-k)\mathbf{q}_\perp}{\delta E(\mathbf{h} - (p-k)\mathbf{q}_\perp)} \right)^2 \right] \end{aligned} \quad (31)$$

with $(C_R - C_A/2)$ appearing on the $\mathbf{h} + p\mathbf{q}_\perp$ term for $g \leftrightarrow q\bar{q}$ processes. The angular integrals for this expression can be performed analytically using,

$$\int_0^{2\pi} \frac{1}{1 + A \cos \phi} = \frac{2\pi}{\sqrt{1 - A^2}} \quad (32)$$

$$\int_0^{2\pi} \frac{1}{(1 + A \cos \phi)^2} = \frac{2\pi}{(1 - A^2)^{3/2}}, \quad (33)$$

leaving only the integrals over the magnitude of \mathbf{h} and the exchanged momentum \mathbf{q}_\perp to be performed numerically. The remaining term of $\delta\tilde{C}$ represents the Bette-Heitler subtraction,

given by,

$$\begin{aligned} \gamma_{bc}^a \Big|_{\text{BH}}(p; p-k, k) &= \frac{g^2}{32\pi^4} \begin{cases} d_A C_A \frac{p^4+k^4+(p-k)^4}{p^3 k^3 (p-k)^3} & g \leftrightarrow gg \\ d_F C_F \frac{p^2+(p-k)^2}{p^2 (p-k)^2 k^3} & q \leftrightarrow qg \\ d_F C_F \frac{(p-k)^2+k^2}{(p-k)^2 k^2 p^3} & g \leftrightarrow q\bar{q} \end{cases} \int \frac{d^2 \mathbf{h}}{(2\pi)^2} \int \frac{d^2 \mathbf{q}_\perp}{(2\pi)^2} \\ &\times \frac{g^2 T m_D^2}{\mathbf{q}_\perp^2 (\mathbf{q}_\perp^2 + m_D^2)} \left[\left(C_R - \frac{C_A}{2} \right) \left(\frac{\mathbf{h}}{\delta E(\mathbf{h})} - \frac{\mathbf{h} - k \mathbf{q}_\perp}{\delta E(\mathbf{h} - k \mathbf{q}_\perp)} \right)^2 \right. \\ &\left. + \frac{C_A}{2} \left(\frac{\mathbf{h}}{\delta E(\mathbf{h})} - \frac{\mathbf{h} + p \mathbf{q}_\perp}{\delta E(\mathbf{h} + p \mathbf{q}_\perp)} \right)^2 + \frac{C_A}{2} \left(\frac{\mathbf{h}}{\delta E(\mathbf{h})} - \frac{\mathbf{h} - (p-k) \mathbf{q}_\perp}{\delta E(\mathbf{h} - (p-k) \mathbf{q}_\perp)} \right)^2 \right]. \end{aligned} \quad (34)$$

This can be calculated using the same numerical approach for the collinear processes in Chapter 4, with some minor modifications to accommodate the Bette-Heitler limit. This part of the calculation was also performed using Guy Moore's code for gluon emission. The final result from these two contributions is then inserted into Eq. (15), resulting in

$$\begin{aligned} \left(f_1, \mathcal{C}^{\text{semi}} f_1 \right) &\equiv \frac{2\pi}{T^3} \sum_{abc} \int_0^\infty dp \int_0^p dk \gamma_{bc}^a \Big|_{\text{semi}}(p; p-k, k) f_0^a(p) [1 \pm f_0^b(k)] [1 \pm f_0^c(p-k)] \\ &\times \left[f_1^a(\mathbf{p}) - f_1^b(k\hat{\mathbf{p}}) - f_1^c((p-k)\hat{\mathbf{p}}) \right]^2. \end{aligned} \quad (35)$$

There are other methods for obtaining the semi-collinear rate, but it was noted in [62] that this is the most practical one. It also leads to a manifestly positive collision operator at NLO, which is important since we rely on a variational method to obtain shear viscosity.

4 The counterterms

As mentioned earlier in this Chapter, the computation of next-to-leading order transport coefficients requires reorganizing the leading order collision operator. Some of the contributions computed in the LO treatment are already of order $\mathcal{O}(g)$ and must be subtracted to avoid double counting. Therefore, in this section, we focus on the counterterms to be subtracted at NLO. First, we name $(f_1, \mathcal{C}_{\mathcal{O}(g)}^{2\leftrightarrow 2} \text{finite} f_1)$ as the $\mathcal{O}(g)$ region of the $2 \leftrightarrow 2$ processes that needs to be subtracted. As argued in [62], both gluon and quark exchange processes contribute to this double counting so that we can rewrite it as a sum of the quark (antiquarks will have the same contribution except for the statistical functions) and gluon contributions

$$\left(\chi_{ij}, \mathcal{C}_{\mathcal{O}(g)}^{2\leftrightarrow 2} \text{finite} \chi_{ij} \right) = \left(\chi_{ij}, \mathcal{C}_{\mathcal{O}(g)}^{2\leftrightarrow 2} \text{finite}_g \chi_{ij} \right) + \left(\chi_{ij}, \mathcal{C}_{\mathcal{O}(g)}^{2\leftrightarrow 2} \text{finite}_q \chi_{ij} \right), \quad (36)$$

where the g and q labels represent gluon and quark (and antiquark) exchange contributions.

Next, we use the same parameterization for the t channel in Chapter 4. Which is given by (suppressing particle-species labels and an overall factor of $1/(2^8\pi^5)$) [9]

$$\begin{aligned} (\chi_{ij}, \mathcal{C}^{2\leftrightarrow 2}\chi_{ij}) &= \int_0^\infty dq \int_{-q}^q d\omega \int_{\frac{q-\omega}{2}}^{\frac{q+\omega}{2}} dp \int_{\frac{q+\omega}{2}}^\infty dk \frac{|\mathcal{M}|^2}{16pkp'k'} f_0(p)f_0(k)[1\pm f_0(p')][1\pm f_0(k')] \\ &\times \left(\chi_{ij}(\mathbf{p}) + \chi_{ij}(\mathbf{k}) - \chi_{ij}(\mathbf{p}') - \chi_{ij}(\mathbf{k}') \right)^2. \end{aligned} \quad (37)$$

We begin with the evaluation of the gluon exchange contribution. For that, we must consider the region where ω and q and an external gluon line (p or k) are soft. Using these assumptions, we are able to simplify Eq. (37), and write it as,

$$\begin{aligned} (\chi_{ij}, \mathcal{C}^{2\leftrightarrow 2}\chi_{ij})_{\text{soft } gk} &= \frac{\beta}{(4\pi)^6} \sum_a \int_{-\infty}^{+\infty} d\omega \int_0^{\mu_\perp} dq_\perp \frac{q_\perp}{q} \int_0^\infty dp \int_{\frac{q+\omega}{2}}^{\mu_k} \frac{dk}{k(k-\omega)} \int_0^{2\pi} d\phi \\ &\times 2(2 - \delta^{ag}) |\mathcal{M}_{\text{soft } gtk}^{ag}|^2 f_0^a(p) [1 \pm f_0^a(p)] \\ &\times \left[\chi_{ij}^a(\mathbf{p}) + \chi_{ij}^g(\mathbf{k}) - \chi_{ij}^a(\mathbf{p}') - \chi_{ij}^g(\mathbf{k}') \right]^2. \end{aligned} \quad (38)$$

Within this context, μ_\perp and μ_k serve as cutoffs, delineating the soft and hard scales. This final line transforms into,

$$\begin{aligned} &\left[\chi_{ij}^a(\mathbf{p}) + \chi_{ij}^g(\mathbf{k}) - \chi_{ij}^a(\mathbf{p}') - \chi_{ij}^g(\mathbf{k}') \right]_{\text{soft } k}^2 = \omega^2 [(\chi^a(p)')^2 + (\chi^g(0)')^2] \\ + \frac{\ell(\ell+1)}{2} q_\perp^2 \left(\frac{\chi^a(p)}{p} \right)^2 - 2k(k-\omega) \left[P_\ell \left(1 - \frac{q_\perp^2}{2k(k-\omega)} \right) - 1 \right] (\chi^g(0)')^2 + \mathcal{O}(g^3), \end{aligned} \quad (39)$$

where the $(\chi^g(0)')^2$ is a consequence of the infrared nature of the $\ell = 2$ departure from equilibrium, as shown in [62]. Furthermore, the matrix element pertinent to this scaling can be extracted from Appendix A of the reference [9]. It is given by,

$$|\mathcal{M}_{\text{soft, } g,t,k}^{ag}|^2 = 16d_A C_A T_{R_a} g^4 p^2 \left| (2k-\omega) G_R^L(Q) + \frac{q_\perp^2}{q^2} \cos(\phi) \sqrt{4k(k-\omega) - q_\perp^2} G_R^T(Q) \right|^2. \quad (40)$$

At this point, symmetry factors must be taken into account. The $gg \leftrightarrow gg$ process receives a factor of 2 due to the identical u -channel contribution and another factor of 2 from the region where $p \sim gT$ and $k \sim T$. Conversely, the $qg \leftrightarrow qg$ process acquires a factor of

4 owing to the symmetries of the initial and final states. Thus, the overall contribution becomes:

$$\begin{aligned}
\left(\chi_{ij}, \mathcal{C}_{\mathcal{O}(g)g}^{2\leftrightarrow 2} \chi_{ij}\right) &= \frac{d_A C_A g^4}{32\pi^5 T} \int_{-\infty}^{+\infty} d\omega \int_0^\infty dq_\perp \frac{q_\perp}{q} \int_0^\infty dp p^2 \int_{\frac{q+\omega}{2}}^{\mu_k} \frac{dk}{k(k-\omega)} \\
&\times \left[(2k-\omega)^2 |G_R^L(Q)|^2 + \frac{q_\perp^4}{2q^4} (4k(k-\omega) - q_\perp^2) |G_R^T(Q)|^2 \right] \\
&\times \sum_a T_{R_a} f_0^a(p) [1 \pm f_0^a(p)] \left[\omega^2 [(\chi^a(p)')^2 + (\chi^g(0)')^2] \right. \\
&\left. + \frac{\ell(\ell+1)}{2} \frac{q_\perp^2}{p^2} [\chi^a(p)]^2 - 2k(k-\omega) \left[P_\ell \left(1 - \frac{q_\perp^2}{2k(k-\omega)} \right) - 1 \right] (\chi^g(0)')^2 \right], \tag{41}
\end{aligned}$$

Next, we must perform the integrals in ω and then subtract the bare, UV-divergent contribution from (41). A comprehensive treatment of this procedure can be found in the Appendix of [62]. In this discussion, we only provide an overview of the essential points of this derivation and apply the results to our calculation. The resulting $d\omega$ integration is then computed numerically and gives,

$$\begin{aligned}
\left(\chi_{ij}, \mathcal{C}_{\mathcal{O}(g)\text{finite } g}^{2\leftrightarrow 2} \chi_{ij}\right) &= \frac{d_A C_A g^4 m_D}{32\pi^5 T} \sum_a T_{R_a} \int_0^\infty dp p^2 f_0^a(p) [1 \pm f_0^a(p)] \\
&\times \left\{ 4.2695 [(\chi^a(p)')^2 + (\chi^g(0)')^2] + 7.1769 \frac{\ell(\ell+1)}{2p^2} [(\chi^a(p))^2 + (p\chi^g(0)')^2] \right. \\
&\left. + 18.0669 \delta_{\ell 2} [\chi^g(0)']^2 \right\}. \tag{42}
\end{aligned}$$

Next, we turn to the fermion exchange processes, i.e., Compton scattering and $q\bar{q}$ annihilation. Let us revisit Eq. (37). This time, we aim to expand it for $\omega, q, p \sim gT$, and $k \sim T$. Additionally, we'll encounter a comparable contribution for $p \sim T$ and $k \sim gT$. Consequently, the departure from equilibrium for Compton processes becomes[62]:

$$\left[\chi_{ij}^q(\mathbf{p}) + \chi_{ij}^g(\mathbf{k}) - \chi_{ij}^g(\mathbf{p}') - \chi_{ij}^q(\mathbf{k}') \right]_{\text{soft } p}^2 = (\chi^g(k) - \chi^q(k))^2 + (\chi^g(0))^2 + \mathcal{O}(g). \tag{43}$$

We can compute the annihilation case analogously. Given the $\hat{\mathbf{p}} \cdot \hat{\mathbf{k}}$ independence of that

expression, we can directly compute the averaged expansion over ϕ , which is

$$\int_0^{2\pi} \frac{d\phi}{2\pi} |\mathcal{M}_{qg}^{gg}|_{\text{soft } q}^2 = -\frac{8d_F C_F^2 g^4 k}{q^2} \left\{ (p+\omega) [(\omega-q)^2 S_R^+(Q) S_A^+(Q) + (\omega+q)^2 S_R^-(Q) S_A^-(Q)] - \frac{1}{2} [(\omega-q)^3 S_R^+(Q) S_A^+(Q) + (\omega+q)^3 S_R^-(Q) S_A^-(Q)] \right\}, \quad (44)$$

so that the $\mathcal{O}(g)$ contribution from soft p becomes,

$$\begin{aligned} \left(\chi_{ij}, \mathcal{C}_{\mathcal{O}(g)\text{ soft } p}^{2\leftrightarrow 2} \chi_{ij} \right) &= -\frac{d_F C_F^2 N_f g^4}{16\pi^5 T^2} \int_0^\infty \frac{dq_\perp q_\perp}{q^3} \int_{-\infty}^\infty d\omega \int_0^\infty dk k \int_{\frac{q-\omega}{2}}^{\mu_p} \frac{dp}{2(p+\omega)} \\ &\times \left\{ (p+\omega) [(\omega-q)^2 S_R^+(Q) S_A^+(Q) + (\omega+q)^2 S_R^-(Q) S_A^-(Q)] \right. \\ &\left. - \frac{1}{2} [(\omega-q)^3 S_R^+(Q) S_A^+(Q) + (\omega+q)^3 S_R^-(Q) S_A^-(Q)] \right\} \\ &\times f_0^q(k) [1 + f_0^g(k)] [(\chi^q(k) - \chi^g(k))^2 + (\chi^q(0))^2], \quad (45) \end{aligned}$$

We included $8N_f$ to accommodate the initial and final state symmetries, accounting for the antiquark contribution in the Compton case and the u -channel contribution in the annihilation case. For the $\ell = 2$ scenario, we utilized the property $\chi^q = \chi^{\bar{q}}$. Proceeding with the integration over dp with a UV cutoff and discarding linearly divergent terms akin to the gluon exchange case, we retain only the terms that are even in ω , resulting in:

$$\begin{aligned} \left(\chi_{ij}, \mathcal{C}_{\mathcal{O}(g)\text{ soft } p}^{2\leftrightarrow 2} \chi_{ij} \right) &= \frac{d_F C_F^2 N_f g^4}{64\pi^5 T^2} \int_0^\infty dk k f_0^q(k) [1 + f_0^g(k)] [(\chi^q(k) - \chi^g(k))^2 + (\chi^q(0))^2] \\ &\times \int_{-\infty}^\infty d\omega \int_0^\infty \frac{dq_\perp q_\perp}{q^3} \left\{ q [(\omega-q)^2 S_R^+(Q) S_A^+(Q) + (\omega+q)^2 S_R^-(Q) S_A^-(Q)] \right. \\ &\left. - \tanh^{-1} \left(\frac{\omega}{q} \right) [(\omega-q)^3 S_R^+(Q) S_A^+(Q) + (\omega+q)^3 S_R^-(Q) S_A^-(Q)] \right\}. \quad (46) \end{aligned}$$

The two-dimensional integration over ω and q_\perp is finite, as the $\mathcal{O}(g)$ correction to the conversion rates is free of linear ultraviolet (UV) divergences in the transverse integrals. The numerical integration gives [62]:

$$\begin{aligned} \left(\chi_{ij}, \mathcal{C}_{\mathcal{O}(g)\text{ soft } p}^{2\leftrightarrow 2} \chi_{ij} \right) &= \frac{d_F C_F^2 N_f g^4 m_\infty}{64\pi^5 T^2} 9.95268 \int_0^\infty dk k f_0^q(k) [1 + f_0^g(k)] \\ &\times [(\chi^q(k) - \chi^g(k))^2 + (\chi^q(0))^2]. \quad (47) \end{aligned}$$

This was just the contribution from having p soft and k hard. Conversely, the opposite scenario yields an equivalent contribution, which is evident from the symmetries of the

integrand. Therefore, the total contribution from double-counting amounts to 2 times Eq. (47)[62],

$$\left(\chi_{ij}, C_{\mathcal{O}(g)}^{2\leftrightarrow 2} \chi_{ij}\right) = \frac{d_F C_F^2 N_f g^4 m_\infty}{32\pi^5 T^2} 9.95268 \int_0^\infty dk k f_0^q(k) [1 + f_0^g(k)] \times [(\chi^q(k) - \chi^g(k))^2 + (\chi^q(0))^2]. \quad (48)$$

5 Summary

In summary, the corrections to be added to the strict leading-order contributions of the previous section produce a collision operator that is fully NLO. The NLO collision term will be given as,

$$(f_1, C_{NLO} f_1) = (f_1, C_{LO} f_1) + (f_1, \delta C f_1), \quad (49)$$

where

$$(f_1, \delta C f_1) \equiv (f_1, C^{\delta\hat{q}} f_1) - (f_1, C_{\mathcal{O}(g)}^{2\leftrightarrow 2} f_1) + (f_1, C^{\text{semi}} f_1) + (f_1, \delta C^{1\leftrightarrow 2} f_1), \quad (50)$$

The first term is the contribution from soft gluon scattering. The second term is the sum of the counter terms from the last section. The third term is the contribution from semi-collinear processes. Finally, the last term is the correction to the splitting rate. In the next section, we present our results.

6 Results

So far in this thesis, we have presented the formalism necessary for the computation of shear viscosity at leading order and discussed the relevant next-leading-order corrections. Our basis for NLO calculations was chosen following the analysis presented in Chapter 4.1. We reproduce this basis again here,

$$\phi^{(m)} = \frac{p(p/T)^m}{(1 + p/T)^{N-1}}, \quad m = 1, \dots, N. \quad (51)$$

We note that this choice differs from the original choice for NLO calculations in [62] but gives compatible results at vanishing chemical potential. Using the formalism presented in this thesis for the leading order collision operator and adding the NLO corrections discussed in the previous sections, we can finally compute shear viscosity at (almost) NLO.

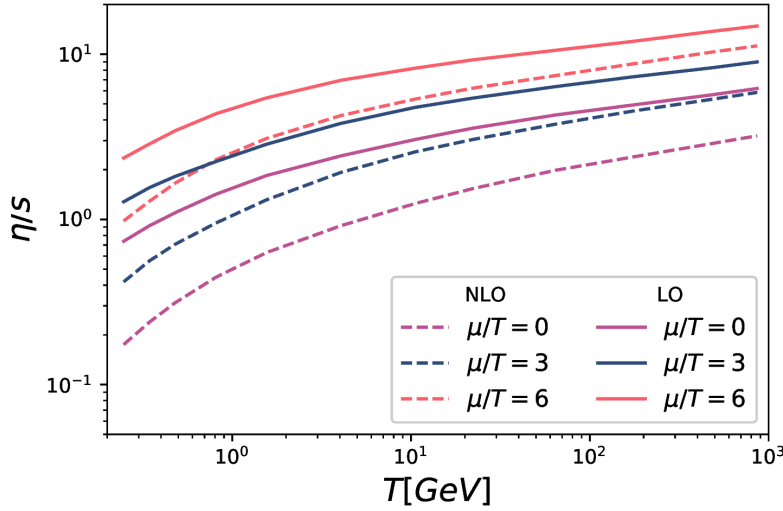


Figure 2: η/s as a function of the temperature for $\mu = 0, 3, 6$. The dashed lines represent NLO order results, while continuous lines are LO results. Both were calculated using $\mu_{EQCD} = 2.7T$

In figure 4, we plot the shear-viscosity to entropy density ratio η/s . The continuous lines represent leading order results, while the dashed lines show NLO calculations. In figure 5, we show the kinematic viscosity, $\eta T/(e + P)$. The plots clearly show that at high chemical potential, NLO calculations work better, especially at high temperatures, with contributions from 6 different flavors and the region where the applicability of perturbation theory is better established. We have used the EQCD coupling $\mu_{EQCD} = 2.7T$ for these plots, following the treatment from [62], details of the coupling prescription are given in Appendix 3.

Since the motivation to study high-density regimes comes from the claim that perturbation theory should have a better convergence at high densities, we present a more detailed comparison between LO and NLO results in Fig. 5. We plot the ratio between LO and NLO calculations as a function of the temperature for each fixed chemical potential. As expected, corrections from NLO contributions are dominant close to $\mu/T = 0$ and dominate the collision operator. Once one goes to higher densities, these soft gluon contributions are less important, and LO effects again dominate the collision operator, especially for a 6-flavor plasma, but still with a significant contribution from NLO.

One can also notice that despite having different values, all orders present the same dependence on the chemical potential; they all follow a parabola at the high-density

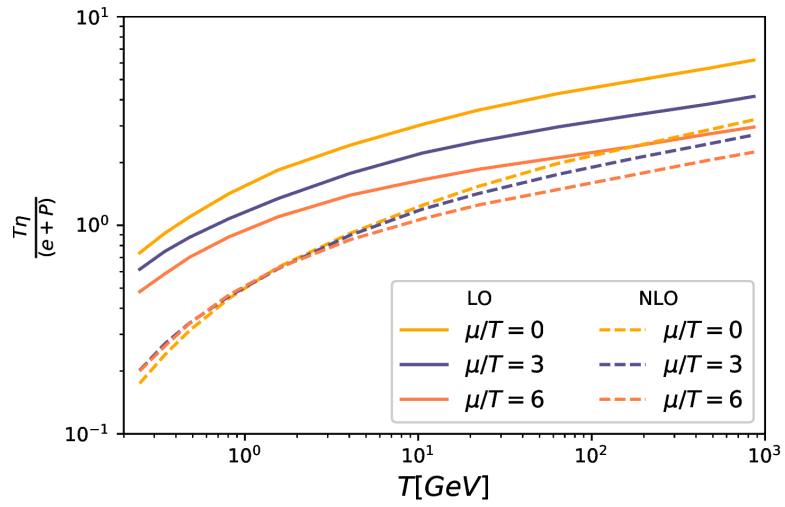


Figure 3: Kinematic shear viscosity as a function of the temperature for $\mu = 0, 3, 6$. The dashed lines represent NLO order results, while continuous lines are LO results.

region, as presented in Fig. 5, and pointed out in Chapter 4.1. Naturally, as observed for lower order calculations, the true curve does not follow this form precisely since there is a transition, as μ/T increases from a system where gluons carry much of the energy and cause much of the scattering to a system where both are dominated by quarks. However, the parabolic behavior is also clearly present at NLO as well.

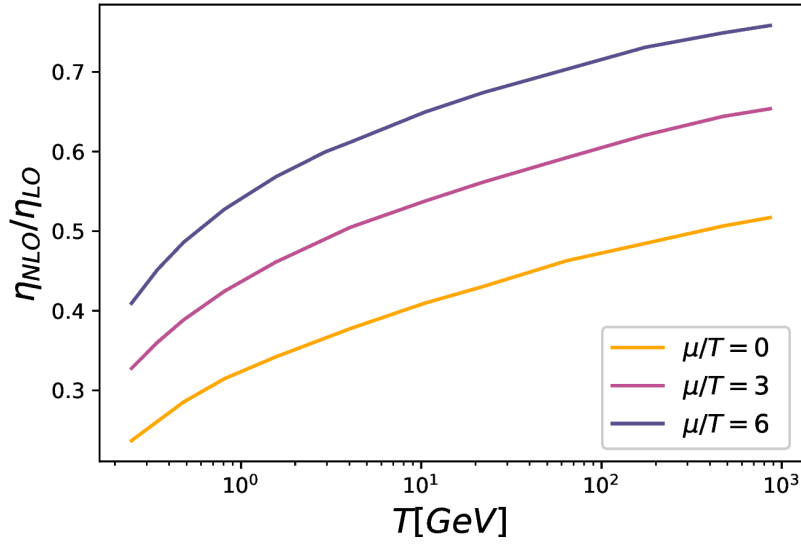


Figure 4: Comparison of LO and NLO calculations as a temperature function for $\mu = 0, 3, 6$. Both were calculated using $\mu_{EQCD} = 2.7T$.

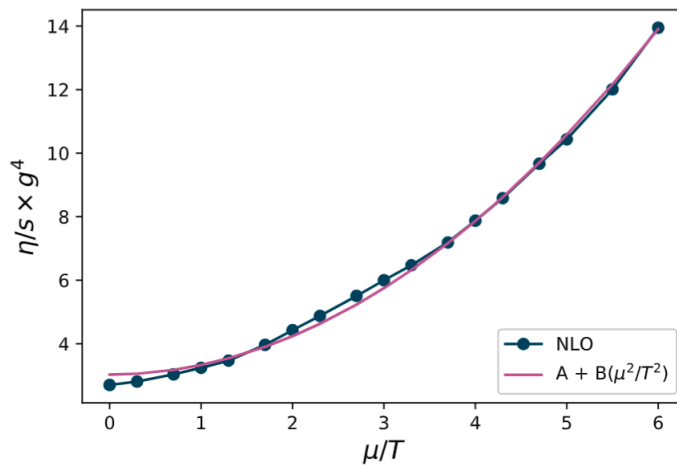


Figure 5: NLO shear viscosity plotted in blue with a quadratic fit of the form $A + B(\mu^2/T^2)$ in pink.

Discussion and Conclusions

In this final chapter, we synthesize the results presented in previous Chapters of this thesis and draw our conclusions. First, we provide a concise overview of studies performed in this work, emphasizing key insights based on our results. Additionally, we endeavor to establish connections between the results shown in this thesis. Finally, we present our final conclusions and delve into the prospects for future research.

1 Final results and conclusions

We will now recover the main results presented in this thesis. Following the sequence laid out here, we begin by recapping the results concerning calculations of shear viscosity as a function of μ/T at leading logarithmic order, shown in figs 5 and 6. In Chapter 4.1, we have successfully extended AMY shear viscosity calculation at leading logarithmic order to high densities, using the computational apparatus described in Chapter 3 and the collision operator presented in Chapter 4.1. For clarity, we reproduce these plots again in fig 1. In both plots, a factor of $g^4 \ln(g)$ is extracted, resulting in a dimensionless curve.

On top of that, we have performed analytical calculations for a one-function ansatz and observed that a one-function basis is not sufficient for the study of transport coefficients at high density, in contrast to what was found for vanishing densities. However, good results were observed for a basis of size six. Therefore, our final results were computed using a 6-function basis set, and on top of that, we considered the most physically relevant scenario, with 3-color and 3-flavor (up, down, and strange). The curves obtained show that η/s has a clear dependence on the chemical potential. The left plot of Figure 1 clearly shows that this ratio follows a parabola in the high-density region. As discussed in Chapter 4.1, this is a consequence of the dependence of the debye mass on the chemical potential since now the Fermi sphere has a ratio of μ instead of T . Additionally, we can point out that the dominant scattering mechanism for particles to change their direction, for soft scattering, is well described in terms of momentum diffusion with a momentum-diffusion coefficient \hat{q} given by:

$$\hat{q} \equiv \int \frac{d^2 q_{\perp}}{(2\pi)^2} q_{\perp}^2 C(q_{\perp}) \quad (1)$$

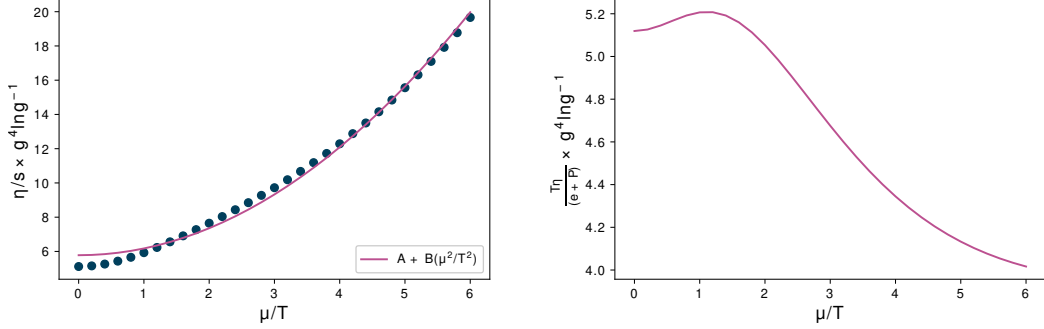


Figure 1: Left: Shear viscosity divided by the entropy density as a function of μ . The points represent our leading-log calculation. The pink line is a quadratic fit, which gives a fair but imperfect representation of our result. Right: Kinematic shear viscosity $\eta T/(e+P)$ as a function of μ .

where $C(q_\perp)$ is the differential rate to exchange transverse momentum q_\perp . In a thermal system without chemical potential, this is given by:

$$C(q_\perp) = g^2 C_F T \frac{m_D^2}{(q_\perp^2)(q_\perp^2 + m_D^2)} \quad (2)$$

As a consequence of the shift of the screening mass, the momentum-diffusion coefficient is now directly dependent on the chemical potential.

On the other hand, the right plot of Fig. 1 shows the kinematic shear viscosity, $\eta T/(e+P)$. As expected, this curve approaches a constant and is not strongly dependent on the chemical potential. Interestingly, this constant value is smaller than the value we obtain at $\mu = 0$, indicating that, in terms of the time scale $1/T$, a high-density fluid will relax somewhat more quickly than one at vanishing chemical potential [41].

Next, we extended this formalism to multiple conserved charges in Chapter 3 and performed a phenomenological study of shear viscosity over the QCD phase diagram. We used a hadron resonance gas description with a state-of-the-art list of resonances for the region below the first-order phase transition. In principle, the region above this transition could be described using pQCD. However, as pointed out in chapter 3, it was observed in [138, 107, 74] that pQCD calculations of thermodynamic observables match lattice calculations at temperatures above $T \gtrsim 300$ MeV for $\mu_B = \mu_S = \mu_Q = 0$. Hence, based on these results, we chose to fix our lower boundary at $T = 300$ MeV and leave the region in between to be interpolated.

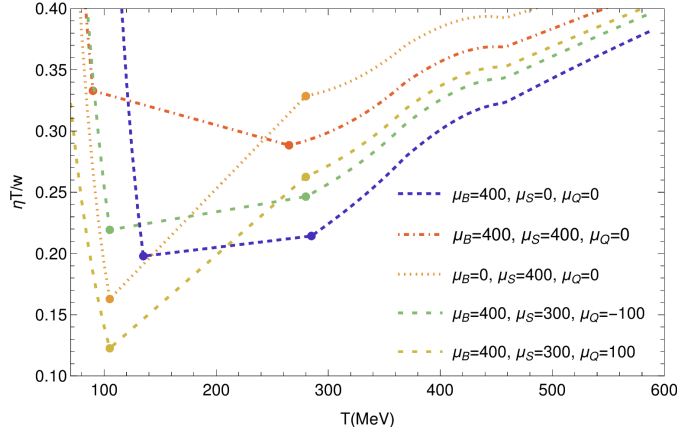


Figure 2: $\eta T/\omega$ as a function of the temperature for each value of μ_B in MeV for $r = 0.25$ fm. Here, we fixed $\eta/s(T_{sw,HRG}(0), 0) = \eta/s(T_{sw,pQCD}(0), 0)$ and rescaled the HRG η/ω for $\tilde{\mu} = 0$ to understand better the finite chemical potential behavior in the deconfined region. The large dots mark the edges of the interpolation region on the plot.

In this work, we have applied a phenomenological approach to produce curves of $\eta T/\omega(T, \mu_B, \mu_S, \mu_Q)$ on the QCD phase diagram, which can be used to feed relativistic viscous hydrodynamic codes simulating collisions at energies covered by the RHIC Beam Energy Scan. In figure 2, we show the variation of shear viscosity when the HRG values are renormalized to match the QGP transition such that $\eta/s(T_{sw,HRG}(0), 0) = \eta/s(T_{sw,pQCD}(0), 0)$. In this plot, we can clearly see the effect of each conserved charge on our kinetic theory calculations. And how sometimes the two regions have different dependencies on each chemical potential. For instance, we can use the blue line ($\mu_B = 400$ MeV) as a baseline since only the baryon chemical potential is considered. Comparing it to the orange dotted line, $\mu_S = 400$ MeV, we observe that $\mu_S > 0$ increases $\eta T/\omega$ in the pQCD regime and decreases $\eta T/\omega$ in the HRG, causing a minimum in the overall $\eta T/\omega$ at $T \sim 100$ MeV, for $\mu_S > 0$, and then grows with T . For the case of $\mu_B = \mu_S = 400$ MeV, the HRG regime increases $\eta T/\omega$. Finally, we compare the scenario where μ_B and μ_S are fixed ($\mu_B = 400$ MeV, $\mu_S = 300$ MeV), and $\mu_Q = \mp 100$ MeV. We observe that $\mu_Q < 0$ flattens $\eta T/\omega$ across T because the HRG and pQCD results have similar values at their respective transition points. However, for $\mu_Q > 0$ we find that a minimum of $\eta T/\omega$ occurs at low T . In this work, we have considered three scenarios, one conserved charge ($\mu_B > 0$ with $\mu_S = \mu_Q = 0$), two conserved charges ($\mu_B > 0$ and $\mu_S > 0$ with $\mu_Q = 0$)

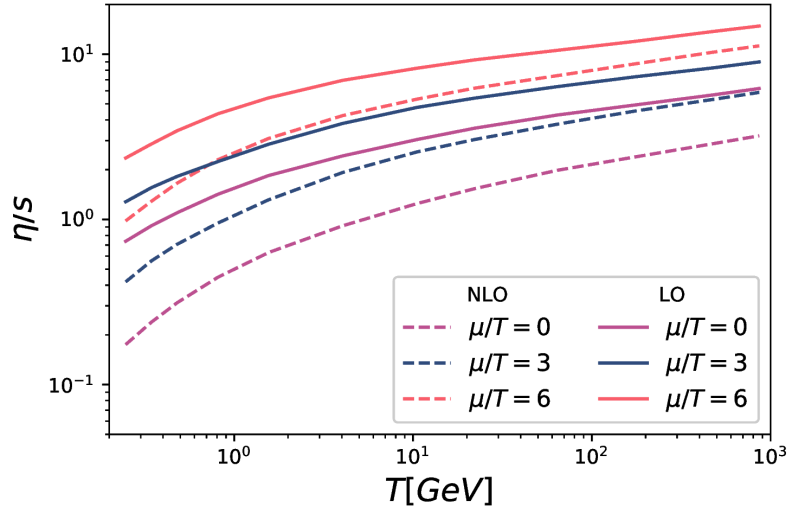


Figure 3: η/s as a function of the temperature for $\mu = 0, 3, 6$. The dashed lines represent NLO order results, while continuous lines are LO results. Both were calculated using the coupling $\mu_{EQCD} = 2.7T$

and three conserved charges. With that, we have presented the first study of $\eta T/w$ with three conserved charges along the QCD phase diagram and used an easily reproducible procedure.

Following that, we computed shear viscosity at leading order on the coupling in Chapter 4. For these calculations, we have used thermal masses to treat the infrared divergences appearing in diagrams (A) to (E) and included contributions from gluon emission and pair annihilation. More details on the HTL approximation can be found in 1. Later, in chapter 4, we computed the (almost) next-to-leading order corrections to the collision operator and extended these calculations to the high-density region. We carefully described the corrections from soft gluon exchange, which present similar behavior to the leading log contributions from Chapter 4.1; the semi-collinear and collinear processes; and finally, the necessary counter terms at $\mathcal{O}(g)$. We observed that the soft gluon exchange remains the most significant contribution, especially at high densities.

Here, we present results from leading order and (almost) next-to-leading order together since they can be directly compared. In figure 3, we plot the shear-viscosity to entropy density ratio η/s for LO and NLO, and in figure 4, we show the kinematic viscosity. The plots clearly show that at high chemical potential, NLO calculations work better, especially at high temperatures, with contributions from 6 different flavors.

In this work, we have used the EQCD coupling $\mu_{EQCD} = 2.7T$, following the treatment from [62]. We note that other choices for μ_{EQCD} could also be reasonable since there is no literature to determine a reasonable choice at such a dense region. Here, we have performed a first NLO determination of the shear viscosity of QCD at high temperature *and* baryon chemical potential. Compared to vanishing- μ QCD, we find that the viscosity is larger when expressed in terms of η/s and smaller in terms of $(e + P)/T$, as observed for the leading log calculations. This indicates that leading log calculations are an interesting method for studying shear viscosity as a function of chemical potential since it is computationally much simpler and is in qualitative agreement with NLO results.

We have also argued that the behavior of Debye vs magnetic screening scales is more favorable at high chemical potentials, implying a wider range of validity for the perturbative analysis. Though we do not expect the perturbative analysis to work quantitatively down to the temperatures and densities obtained in intermediate-energy heavy-ion collisions, we do expect the calculations to work much closer to this regime than proves to be the case in the $\mu = 0$ case. This is because, as we demonstrated, the relevant physics is much more dominated by quarks and less by gluons, and the strong mutual interactions between gluons are the cause of large NLO effects on the $\mu = 0$ axis [62].

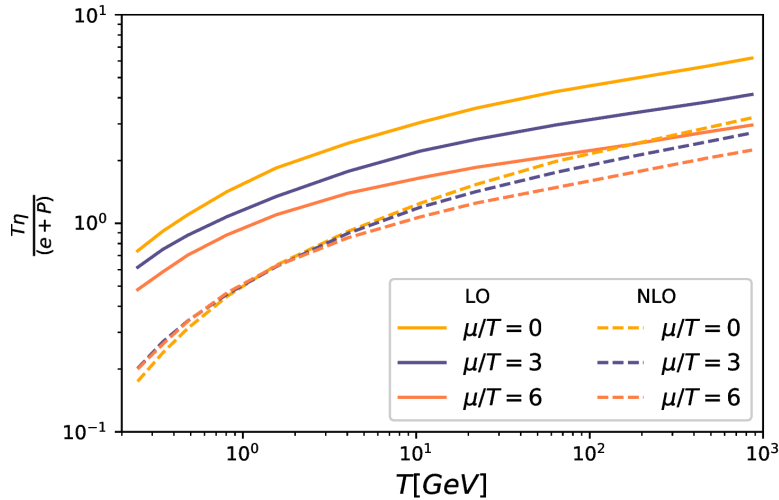


Figure 4: Kinematic shear viscosity as a function of the temperature for $\mu = 0, 3, 6$. The dashed lines represent NLO order results, while continuous lines are LO results. Both were calculated using the coupling $\mu_{EQCD} = 2.7T$

A more detailed comparison between LO and NLO results is shown in Fig. 5. As

described in Chapter 4, corrections from NLO contributions are dominant close to $\mu/T = 0$. However, one expects that perturbation theory should be better behaved at high densities, and this is what we observe in the plot. Once one goes to higher densities, these soft gluon contributions are less important, and LO effects again dominate the collision operator, but still with a big contribution from NLO.

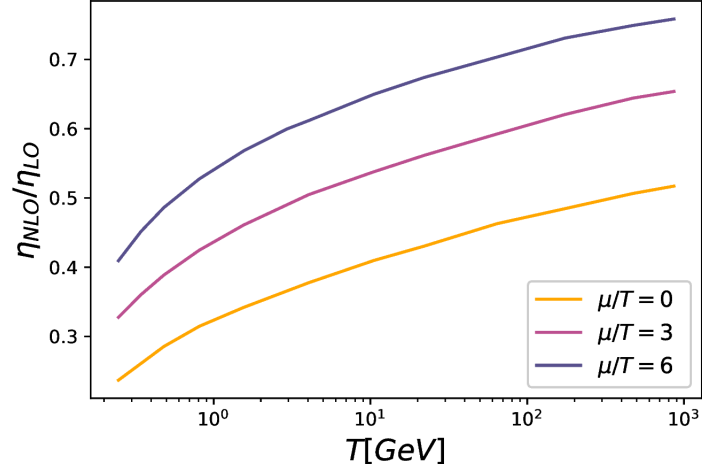


Figure 5: Comparison of LO and NLO calculations as a temperature function for $\mu = 0, 3, 6$. Both were calculated using $\mu_{EQCD} = 2.7T$.

Finally, we have also studied the shear-stress linear response function in chapter 4. In this work, we investigated the existence of a branch cut touching the origin in a system of scalar self-interacting particles with quartic interactions using Boltzmann statistics. What we observed is that the response function for the shear stress, which has the form $\tilde{\pi}^{\mu\nu} = 2\eta(\hat{\Omega})\tilde{\sigma}^{\mu\nu}$, possesses a branch-cut singularity in the Fourier variable $\Omega = q_\mu u^\mu$ for homogeneous perturbations around local equilibrium ($\hat{\Omega} = 2\Omega/(gn_0\beta^2)$). In this thesis, we performed a numerical evaluation of the poles, which indicated the existence of a branch cut even for small values of basis size N [125]. This can be verified by the fact that the average distance between poles decreases with the basis size, and we observe that the poles become closer to zero with the increase in the rank of the matrix truncation, suggesting that the shear response function for the $\lambda\phi^4$ possesses a branch cut along the imaginary axis, $i0^+ < \Omega < i\infty$ as $N \rightarrow \infty$ [125].

These results imply that this behavior for the non-hydrodynamic modes is not associated with quantum effects. The existence of the branch cut is associated with long-lived non-

hydrodynamic modes present in this theory. This is a consequence of the fact that the total cross-section for this system has the functional form $\sigma(s) = g/s$, which is negligible for particles with large energy in the center of the momentum frame [125]. Therefore, we observe that there is a more subtle relation between the hydrodynamic transport properties and non-equilibrium evolution, which is clearly seen when considering more realistic approaches to the collision term. However, we also observe that this high-energy modes do not contribute to the transport properties of the system. This is a consequence of the fact that their interactions are weak.

2 Summary and future prospects

Throughout this thesis, we have performed a study of shear viscosity using both kinetic theory and hydrodynamics. We mainly focused on the high-density region for this analysis since it is a region that is not accessible through lattice calculations and, therefore, is much less well-known than the temperature axis of the QCD phase diagram. We computed shear for a system with three flavors at leading logarithmic order and up to six flavors at (almost) next-to-leading order. These results show that although perturbation theory works better at high μ , NLO effects still contribute with large corrections. Apart from that, we have extended this formalism to multiple conserved charges at leading log order and studied the behavior of shear viscosity as a function of an effective chemical potential. These results were combined with an excluded volume HRG description for the hadronic phase, describing shear along the four-dimensional QCD phase diagram. Finally, we have studied the shear-stress linear response function and observed that, indeed, there is a strong indication of the existence of a branch cut, which is related to the non-hydrodynamic modes of the theory and is not connected to quantum effects.

These results leave several opportunities for future work. For instance, it would be interesting to investigate shear viscosity and diffusion for a system with multiple conserved charges at NLO. These results would be useful input for hydrodynamics simulations since there is very little theoretical guidance for transport coefficients in the high-density region. Apart from that, the formalism used in this thesis could be used in different systems with lower temperatures but higher densities, such as neutron stars. However, the regime with very large chemical potential and low temperature has some subtleties due to the possibility of color superconductivity and the contribution from a different spectrum of resonances. Additionally, in a system with the size of a neutron star, the time scales are much larger than the ones studied in this thesis, causing different processes to contribute to transport coefficients.

Appendix

1 HTL at high chemical potential

In this section, we discuss the HTL approximation for the high-density regime. Before delving into comparisons, we begin with some simple definitions following Eq. (11). For convenience, we define [111]:

$$\tilde{\Pi}_L = -\Pi_{00}, \quad \tilde{\Pi}_T = \frac{q^2}{q^2 - \omega^2} \Pi_T \quad (1)$$

Using these, one can rewrite Eq. (7) as[111]:

$$2 \left(\frac{u^2 + s^2}{t^2} \right) = \frac{1}{|q^2 + \tilde{\Pi}_L|^2} (4pp' + t)(4kk' + t) \quad (2)$$

$$- \frac{2}{|q^2 + \tilde{\Pi}_L^*| |q^2 + \tilde{\Pi}_T|} (p + p')(k + k') \sqrt{(4pp' + t)(4kk' + t)} \cos \phi \quad (3)$$

$$+ \frac{1}{|q^2 + \tilde{\Pi}_T|^2} [(4pp' + t)(4kk' + t) \cos^2 \phi + q^2(2\omega^2 + 4pp' + 4kk')] \quad (4)$$

Here, ϕ is the angle between the \mathbf{q}, \mathbf{p} plane and the \mathbf{q}, \mathbf{k} plane. We note that complete expressions for Π_L and Π_T were obtained by Weldon [145]. The usual expressions for the hard thermal loop limit of the self-energies were extracted as a particular limit. Here, we employ the same procedure as in [111] and substitute all self-energies with just the thermal part of the self-energy in the HTL approximation whenever that treatment is parametrically justified. The thermal parts are given by:

$$\tilde{\Pi}_{L,th} = \frac{g^2 N_f T^2}{3} H(\omega, q), \quad \tilde{\Pi}_{T,th} = \frac{g^2 N_f T^2}{3} \left(-\frac{1}{2} H(\omega, q) + \frac{q^2}{2(q^2 - \omega^2)} G(\omega, q) \right) \quad (5)$$

where $H(\omega, q)$ and $G(\omega, q)$ are, using $2\omega_+ = \omega + q$ and $2\omega_- = \omega - q$ [111]:

$$\begin{aligned}
\text{Re}G(\omega, q) &= \frac{3}{\pi^2 T^2} \int_0^\infty dk f(k) \left(4k + \frac{q^2 - \omega^2}{2q} \ln \left[\frac{(k + \omega_-)(k - \omega_+)}{(k - \omega_-)(k + \omega_+)} \right] \right) \\
\text{Re}H(\omega, q) &= \frac{3}{\pi^2 T^2} \int_0^\infty dk f(k) \left(2k - \frac{4k^2 + \omega^2 - q^2}{4q} \ln \left[\frac{(k + \omega_-)(k - \omega_+)}{(k - \omega_-)(k + \omega_+)} \right] \right. \\
&\quad \left. - \frac{2k\omega}{q} \ln \frac{\omega_+}{\omega_-} - \frac{k\omega}{q} \ln \left[\frac{(k + \omega_-)(k - \omega_+)}{(k - \omega_-)(k + \omega_+)} \right] \right) \\
\text{Im}G(\omega, q) &= \frac{3}{\pi^2 T^2} \int_0^\infty dk f(k) \frac{q^2 - \omega^2}{2q} [\Theta(k + \omega_+) \Theta(-k - \omega_-) - \Theta(-k + \omega_+) \Theta(k - \omega_-)] \\
\text{Im}H(\omega, q) &= \frac{3}{\pi^2 T^2} \int_0^\infty dk f(k) \left[-\frac{(2k + \omega)^2 - q^2}{4q} \Theta(k + \omega_+) \Theta(-k - \omega_-) \right. \\
&\quad \left. + \frac{(2k - \omega)^2 - q^2}{4q} \Theta(k - \omega_-) \Theta(-k + \omega_+) + \frac{2k\omega}{q} \Theta(\omega_+) \Theta(-\omega_-) \right] \tag{6}
\end{aligned}$$

In the hard thermal loop, which means taking $\omega \ll T, q \ll T$ and extracting the nonvanishing part, the functions $H(\omega, q)$ and $G(\omega, q)$ are simply:

$$H_{HTL}(\omega/q) = 1 - \frac{\omega}{2q} \ln \frac{\omega_+}{\omega_-} + i \frac{\pi\omega}{2q} \Theta(\omega_+) \Theta(-\omega_-) \tag{7}$$

$$G_{HTL}(\omega/q) = 1 \tag{8}$$

General expressions for $H(\omega, q)$ and $G(\omega, q)$ can be found in [111], along with a more detailed discussion of vacuum and thermal contributions in different energy limits.

To better study the HTL expansion's reliability at high densities, we present here a leading order calculation of collision integrals directly compared with full self-energies. In figure 1, one can see the ratio between collision integrals for $s^2 + u^2/t^2$ calculated by taking the HTL limit and performing the integrals for the thermal part of the self-energy, both using a one function ansatz. These calculations strongly depend on the choice of screening mass; as one goes to the high-density region, the increase in the number of quarks will increase screening effects in that region. Therefore, we take $m_D^2 = T^2 + \mu^2/\pi^2$. It is clear from the plot that as the screening effects become larger, the HTL approximation has a better accuracy at leading order, which is a consequence of the fact that now small momentum transfer can be taken to be $q \ll \mu$.

2 Photon emission rate

Here, we derive an expression for the gluon emission rate based on the work from [11, 12], where the author computed the photon emission rate for ultrarelativistic plasmas.

We begin with the differential photon emission rate per unit volume, at leading order in α_{EM} , is given by the relation[11]

$$d\Gamma_\gamma = \frac{d^3\mathbf{k}}{(2\pi)^3 2|\mathbf{k}|} \sum_{a=1,2} \epsilon_{(a)}^\mu(\mathbf{k})^* \epsilon_{(a)}^\nu(\mathbf{k}) W_{\mu\nu}(K), \quad (9)$$

where $K = (k^0, \mathbf{k}) = (|\mathbf{k}|, \mathbf{k})$ denotes the photon 4-momentum, the ϵ represents a basis of transverse polarizations for the photon and $W_{\mu\nu}(K)$ is the Wightman electromagnetic current-current correlator, given by

$$W_{\mu\nu}(K) = \int d^4x e^{-iKx} \langle j_\mu(0) j_\nu(x) \rangle. \quad (10)$$

To obtain the photon emission rate, we must first perform some intermediate steps. Our first task is to rewrite the current correlator (10) in terms of propagation amplitudes of single-particle states in the random background. We will focus on the bremsstrahlung process and comment on the pair annihilation in the end since these processes can be computed analogously. Bremsstrahlung emission corresponds to a contribution to the current correlator (10) of the form

$$W_{\mu\nu}^{brem}(K) = \int d^4x e^{-iKx} \int_{\mathbf{p}_i \mathbf{p}_f} f(p_i) [1 \pm f(p_f)] \left\langle\left\langle \langle \mathbf{p}_i | j_\mu(0) | \mathbf{p}_f \rangle \langle \mathbf{p}_f | j_\nu(x) | \mathbf{p}_i \rangle \right\rangle\right\rangle, \quad (11)$$

where $|\mathbf{p}_i\rangle$ and $|\mathbf{p}_f\rangle$ represent one-particle states of the emitting, and n is the equilibrium distribution function, which can be written as $f_b(p)$ or $f_f(p)$. The next step uses a relativistic one-particle Schrödinger equation to describe particles propagating nearly on-shell in a soft background. With this description, one can obtain the contribution from a single carrier type and spin state; this is done using

$$W_{\mu\nu}^{brem}(K) = 2 \text{Re} \left[\int_P f(\mathbf{p}+\mathbf{k}) [1 \pm f(\mathbf{p})] \langle \mathbf{p} | j_\mu(\mathbf{k}) | \mathbf{p}+\mathbf{k} \rangle^* \mathcal{S}_\nu(P; K) \right]. \quad (12)$$

Here, the photon four-momentum K is fixed, but the four-vector P has to be integrated over. However, we will simplify the dependence of $\mathcal{S}_\nu(P; K)$ on P as follows. First, we write the component of \mathbf{p} in the direction \mathbf{k} of the photon as $p_{||}$, and let \mathbf{p}_\perp be the part of \mathbf{p} perpendicular to \mathbf{k} . Finally, $\mathcal{S}_\nu(P; K)$ satisfies the integral equation,

$$\begin{aligned} \mathcal{S}_\nu(P; K) = & \left(\frac{i}{(p^0 + k^0) - E_{\mathbf{p}+\mathbf{k}} + i\Gamma_{\mathbf{p}+\mathbf{k}}} \right)^* \frac{i}{p^0 - E_{\mathbf{p}} + i\Gamma_{\mathbf{p}}} \\ & \times \left[\langle \mathbf{p} | j_\nu(\mathbf{k}) | \mathbf{p}+\mathbf{k} \rangle + g^2 C_R \int_Q \left\langle\left\langle [v_{\mathbf{p}+\mathbf{k}} \cdot A(Q)] [v_{\mathbf{p}} \cdot A(Q)]^* \right\rangle\right\rangle \mathcal{S}_\nu(P-Q; K) \right], \end{aligned} \quad (13)$$

where $E_{\mathbf{p}} = \sqrt{p^2 + m_\infty^2}$, and $m_\infty^2 = 1/4C_R g^2 T^2$, is the thermal mass. In [11], it was observed that the momentum transfer in this process is $O(gT)$, and so the relevant values of \mathbf{p}_\perp are $O(gT)$. Therefore, we can expand the expression in \mathbf{p}_\perp and m_∞ , this leads to,

$$p^0 - E_{\mathbf{p}} + i\Gamma_{\mathbf{p}} \simeq (p^0 - p_{\parallel}) - \frac{p_\perp^2 + m_\infty^2}{2p_{\parallel}} + i\Gamma_{\mathbf{p}}, \quad (14)$$

$$(p^0 + k^0) - E_{\mathbf{p}+\mathbf{k}} + i\Gamma_{\mathbf{p}+\mathbf{k}} \simeq (p^0 - p_{\parallel}) - \frac{p_\perp^2 + m_\infty^2}{2(p_{\parallel} + k)} + i\Gamma_{\mathbf{p}+\mathbf{k}}, \quad (15)$$

in this expression, the photon is on-shell, and $p_{\parallel} > 0$, meaning that the photon travels in the same direction as the emitter.

Now we take advantage of the fact that $S_\nu(P; K)$ is only going to be integrated against functions that are smooth on the scale of $O(g^2 T)$ variations in $p^0 - p_{\parallel}$, and perform the following approximation,

$$\begin{aligned} \left(\frac{i}{(p^0 + k^0) - E_{\mathbf{p}+\mathbf{k}} + i\Gamma_{\mathbf{p}+\mathbf{k}}} \right)^* \frac{i}{p^0 - E_{\mathbf{p}} + i\Gamma_{\mathbf{p}}} &\simeq \frac{2\pi i \delta(p^0 - p_{\parallel}) \theta(p_{\parallel})}{(E_{\mathbf{p}+\mathbf{k}} + i\Gamma_{\mathbf{p}+\mathbf{k}}) - (k^0 + E_{\mathbf{p}} - i\Gamma_{\mathbf{p}})} \\ &\simeq \frac{2\pi \delta(p^0 - p_{\parallel}) \theta(p_{\parallel})}{i \delta E + (\Gamma_{\mathbf{p}+\mathbf{k}} + \Gamma_{\mathbf{p}})}, \end{aligned} \quad (16)$$

where we have used that,

$$\delta E \equiv \frac{k(p_\perp^2 + m_\infty^2)}{2p_{\parallel}(k + p_{\parallel})} \simeq k^0 + E_{\mathbf{p}} - E_{\mathbf{p}+\mathbf{k}}. \quad (17)$$

This is known as the pinching pole approximation. Making this substitution into the integral equation (13), one sees that the resulting solution will have the form

$$S_\nu(P; K) = S_\nu(\mathbf{p}; K) 2\pi \delta(p^0 - p_{\parallel}) \theta(p_{\parallel}). \quad (18)$$

Inserting this form and rewriting

$$\delta(p^0 - p_{\parallel}) \delta[(p^0 - q^0) - (p_{\parallel} - q_{\parallel})] = \delta(p^0 - p_{\parallel}) \delta(q^0 - q_{\parallel}), \quad (19)$$

one finds

$$W_{\mu\nu}^{brem}(K) = 2 \operatorname{Re} \int_{\mathbf{p}} f(\mathbf{p}+\mathbf{k}) [1 \pm f(\mathbf{p})] \langle \mathbf{p} | j_\mu(\mathbf{k}) | \mathbf{p}+\mathbf{k} \rangle^* S_\nu(\mathbf{p}; \mathbf{k}) \theta(p_{\parallel}), \quad (20)$$

where

$$S_\nu(\mathbf{p}; \mathbf{k}) = \frac{1}{i\delta E + (\Gamma_{\mathbf{p}+\mathbf{k}} + \Gamma_{\mathbf{p}})} \left[\langle \mathbf{p} | j_\nu(\mathbf{k}) | \mathbf{p}+\mathbf{k} \rangle + g^2 C_R \int_Q 2\pi \delta(q^0 - q_\parallel) \left\langle \left\langle [v_{\mathbf{p}+\mathbf{k}} \cdot A(Q)] [v_{\mathbf{p}} \cdot A(Q)]^* \right\rangle \right\rangle S_\nu(\mathbf{p}-\mathbf{q}; \mathbf{k}) \right]. \quad (21)$$

In terms of the current matrix elements appearing in the original definition (11), the function $S_\nu(\mathbf{p}; \mathbf{k})$ is given by that portion of the time-evolved off-diagonal matrix element of the current, evaluated in the fluctuating background gauge field[11]. At leading order in g , this is written as,

$$\int d^4x \theta(-x^0) e^{-iKx} \left\langle \left\langle \mathbf{p} | j_\nu(x) | \mathbf{p}+\mathbf{k} \right\rangle \right\rangle = S_\nu(\mathbf{p}; \mathbf{k}) \theta(p_\parallel). \quad (22)$$

Here, time evolution is given implicitly in $j_\nu(x) = j_\nu(x^0, \mathbf{x}) = U(0, x^0) j_\nu(\mathbf{x}) U(x^0, 0)$.

In the interaction term of Eq. (21) one may, at leading order, replace $v_{\mathbf{p}} \cdot A$ by

$$A^+ \equiv A^0 - A_\parallel \quad (23)$$

and rewrite the integral equation in the form

$$\langle \mathbf{p} | j_\nu(\mathbf{k}) | \mathbf{p}+\mathbf{k} \rangle = [i\delta E + (\Gamma_{\mathbf{p}+\mathbf{k}} + \Gamma_{\mathbf{p}})] S_\nu(\mathbf{p}; \mathbf{k}) - g^2 C_R \int_Q 2\pi \delta(q^0 - q_\parallel) \left\langle \left\langle A^+(Q) [A^+(Q)]^* \right\rangle \right\rangle S_\nu(\mathbf{p}-\mathbf{q}; \mathbf{k}). \quad (24)$$

This integral equation mixes different values of p_\parallel and \mathbf{p}_\perp in the argument of $S(\mathbf{p}; \mathbf{k})$. This is a consequence of the $O(gT)$ momentum transfers in the interaction term. The characteristic size of p_\parallel for a hard quasi-particle is $O(T)$. In leading order, no elements in the equation are sensitive to gT variations in p_\parallel . Consequently, we can treat p_\parallel as fixed inside the interaction term, replacing the equation by

$$\langle \mathbf{p} | j_\nu(\mathbf{k}) | \mathbf{p}+\mathbf{k} \rangle = [i\delta E + (\Gamma_{\mathbf{p}+\mathbf{k}} + \Gamma_{\mathbf{p}})] S_\nu(\mathbf{p}_\perp; p_\parallel, \mathbf{k}) - g^2 C_R \int_Q 2\pi \delta(q^0 - q_\parallel) \left\langle \left\langle A^+(Q) [A^+(Q)]^* \right\rangle \right\rangle S_\nu(\mathbf{p}_\perp - \mathbf{q}_\perp; p_\parallel, \mathbf{k}). \quad (25)$$

So far, we have been able to simplify the expressions and obtain a linear integral equation in \mathbf{p}_\perp space, for fixed values of p_\parallel and \mathbf{k} . However, we still haven't addressed the fact that both the width $\Gamma_{\mathbf{p}}$ and the total scattering cross-section has infrared divergences in

these approximations. These infrared divergencies were shown to be proportional to the $Q \rightarrow 0$ divergence of $\int_Q 2\pi\delta(q^0 - q_{\parallel}) \langle\langle A^+(Q)[A^+(Q)]^* \rangle\rangle$ in [11]. Particularly, in the case of $\Gamma_{\mathbf{p}}$, this apparent infrared sensitivity is illusory for our problem. This can be observed by rewriting the width in a form similar to the interaction term in Eq. (25). The width comes from the imaginary parts of self-energy insertions for nearly on-shell particles and, to leading order, is given by[11]

$$\begin{aligned}\Gamma_{\mathbf{p}} &= \text{Im} \left[ig^2 C_R \int_Q \frac{i}{(p^0 - q^0) - E_{\mathbf{p}-\mathbf{q}} + i} \langle\langle A^+(Q) A^+(-Q) \rangle\rangle \right]_{p^0 = E_{\mathbf{p}}} \\ &\simeq g^2 C_R \int_Q \pi\delta(q^0 - q_{\parallel}) \langle\langle A^+(Q) [A^+(Q)]^* \rangle\rangle.\end{aligned}\quad (26)$$

Substituting this into (25), one obtains the infrared-safe equation

$$\begin{aligned}\langle\mathbf{p}|j_{\nu}(\mathbf{k})|\mathbf{p}+\mathbf{k}\rangle &= i\delta E S_{\nu}(\mathbf{p}_{\perp}; p_{\parallel}, \mathbf{k}) + g^2 C_R \int_Q 2\pi\delta(q^0 - q_{\parallel}) \langle\langle A^+(Q) [A^+(Q)]^* \rangle\rangle \\ &\quad \times [S_{\nu}(\mathbf{p}_{\perp}; p_{\parallel}, \mathbf{k}) - S_{\nu}(\mathbf{p}_{\perp} - \mathbf{q}_{\perp}; p_{\parallel}, \mathbf{k})].\end{aligned}\quad (27)$$

We may rewrite the expression for $W_{\mu\nu}$ using that $n(p) \simeq n(p_{\parallel})$, since \mathbf{p}_{\perp} is $O(gT)$. Hence, up to leading order, we have

$$W_{\mu\nu}^{\text{brem}}(K) = 2 \text{Re} \int_{\mathbf{p}} f(p_{\parallel} + k) [1 \pm n(p_{\parallel})] \langle\mathbf{p}|j_{\mu}(\mathbf{k})|\mathbf{p}+\mathbf{k}\rangle^* S_{\nu}(\mathbf{p}_{\perp}; p_{\parallel}, \mathbf{k}) \theta(p_{\parallel}). \quad (28)$$

The current matrix element $\langle\mathbf{p}|j_{\mu}(\mathbf{k})|\mathbf{p}+\mathbf{k}\rangle$ is the only ingredient of these expressions that depends on the nature of the emitter. We now perform another approximation, since \mathbf{p}_{\perp} is parametrically small compared to p_{\parallel} , we will only evaluate these matrix elements in the limit of small transverse momentum. This is justified since we only need the transverse components of j_{μ} . We can use rotational invariance about the \mathbf{k} axis to conclude that these must be proportional to \mathbf{p}_{\perp} . Then in the small \mathbf{p}_{\perp} limit, the transverse current matrix element takes the form

$$\langle\mathbf{p}|j_{\perp}(\mathbf{k})|\mathbf{p}+\mathbf{k}\rangle \simeq 2qe \mathbf{p}_{\perp} \mathcal{J}_{p_{\parallel} \leftarrow p_{\parallel} + k}, \quad (29)$$

where qe denotes the electric charge of the emitting particle. The explicit form of the "splitting function" $\mathcal{J}_{p_{\parallel} \leftarrow p_{\parallel} + k}$, will be given later in the text. For now, we proceed, as in [11], and factor out all dependence on the emitter type by redefining the transverse part of $S_{\nu}(\mathbf{p}_{\perp}; p_{\parallel}, k)$ as

$$\mathbf{S}_{\perp}(\mathbf{p}_{\perp}; p_{\parallel}, \mathbf{k}) = qe \mathcal{J}_{p_{\parallel} \leftarrow p_{\parallel} + k} \mathbf{F}(\mathbf{p}_{\perp}; p_{\parallel}, \mathbf{k}) \quad (30)$$

to obtain

$$\sum_a \epsilon_a^{\mu*} \epsilon_a^\nu W_{\mu\nu}^{\text{brem}}(K) = 2(qe)^2 \text{Re} \int_{\mathbf{p}} f(p_{\parallel}+k) [1 \pm f(p_{\parallel})] |\mathcal{J}_{p_{\parallel} \leftarrow p_{\parallel}+k}|^2 2\mathbf{p}_{\perp} \cdot \mathbf{F}(\mathbf{p}_{\perp}; p_{\parallel}, \mathbf{k}) \theta(p_{\parallel}), \quad (31)$$

where $\mathbf{f}(\mathbf{p}_{\perp}; p_{\parallel}, \mathbf{k})$ is the solution to

$$2\mathbf{p}_{\perp} = i \delta E \mathbf{F}(\mathbf{p}_{\perp}; p_{\parallel}, \mathbf{k}) + g^2 C_R \int_Q 2\pi \delta(q^0 - q_{\parallel}) \left\langle\left\langle A^+(Q) [A^+(Q)]^* \right\rangle\right\rangle \times [\mathbf{F}(\mathbf{p}_{\perp}; p_{\parallel}, \mathbf{k}) - \mathbf{F}(\mathbf{p}_{\perp} - \mathbf{q}_{\perp}; p_{\parallel}, \mathbf{k})]. \quad (32)$$

This gives the result for bremsstrahlung production from a single type, spin, and color of the charged particle. The advantage of this expression is that it isolates the dependence on the type of the particle in the splitting factor $|\mathcal{J}_{p_{\parallel} \leftarrow p_{\parallel}+k}|^2$, and the dependence on the details of the frequency-dependent correlation of the background field in the correlator $\langle\langle AA \rangle\rangle$.

Now, we can explicitly write the "splitting function." For fermions, expression (29) gives the following,

$$|\mathcal{J}_{p_{\parallel} \leftarrow p_{\parallel}+k}|^2 = \begin{cases} 1, & \text{scalars;} \\ \frac{4p_{\parallel} (p_{\parallel}+k)}{p_{\parallel}^2 + (p_{\parallel}+k)^2}, & \text{fermions.} \\ \frac{8p_{\parallel}^2 (p_{\parallel}+k)^2}{8p_{\parallel}^2 (p_{\parallel}+k)^2}, & \end{cases} \quad (33)$$

The same treatment can be used for pair annihilation. We start by writing the analogous form of the contribution to the current-current correlator,

$$W_{\mu\nu}^{\text{pair}}(K) = \left\langle\left\langle \int d^4x e^{-iKx} \int_{\mathbf{p}\bar{\mathbf{p}}} n(p) n(\bar{p}) \langle \mathbf{p}\bar{\mathbf{p}} | j_{\mu}(0) | \text{vac} \rangle \langle \text{vac} | j_{\nu}(x) | \mathbf{p}\bar{\mathbf{p}} \rangle \right\rangle\right\rangle. \quad (34)$$

Performing the same approximations as before, one obtains,

$$\sum_a \epsilon_a^{\mu*} \epsilon_a^\nu W_{\mu\nu}^{\text{pair}}(K) = 2(qe)^2 \text{Re} \int_{\mathbf{p}} f(k-p_{\parallel}) [1 \pm f(p_{\parallel})] |\mathcal{J}_{\text{vac} \leftarrow p_{\parallel}, k-p_{\parallel}}|^2 \times 2\mathbf{p}_{\perp} \cdot \tilde{\mathbf{F}}(\mathbf{p}_{\perp}; p_{\parallel}, \mathbf{k}) \theta(p_{\parallel}) \theta(k-p_{\parallel}), \quad (35)$$

and

$$2\mathbf{p}_{\perp} = i \delta \tilde{E} \tilde{\mathbf{F}}(\mathbf{p}_{\perp}; p_{\parallel}, \mathbf{k}) + g^2 C_R \int_Q 2\pi \delta(q^0 - q_{\parallel}) \left\langle\left\langle A^+(Q) [A^+(Q)]^* \right\rangle\right\rangle \times [\tilde{\mathbf{F}}(\mathbf{p}_{\perp}; p_{\parallel}, \mathbf{k}) - \tilde{\mathbf{F}}(\mathbf{p}_{\perp} - \mathbf{q}_{\perp}; p_{\parallel}, \mathbf{k})], \quad (36)$$

where,

$$\widetilde{\delta E} \equiv - \left[\frac{p_{\perp}^2 + m_{\infty}^2}{2} \right] \left[\frac{k}{p_{\parallel} (k - p_{\parallel})} \right] \simeq k^0 - E_{\mathbf{k}-\mathbf{p}} - E_{\mathbf{p}}. \quad (37)$$

Proceeding analogously, one also obtains the "joining functions" as,

$$|\mathcal{J}_{\text{vac} \leftarrow p_{\parallel}, k-p_{\parallel}}|^2 = \begin{cases} \frac{1}{4p_{\parallel} (k-p_{\parallel})}, & \text{scalars;} \\ \frac{p_{\parallel}^2 + (k-p_{\parallel})^2}{8[p_{\parallel} (k-p_{\parallel})]^2}, & \text{fermions;} \end{cases} \quad (38)$$

which is the same, up to an overall sign, as taking $p_{\parallel} \rightarrow -p_{\parallel}$ in the bremsstrahlung formula (33).

3 Coupling prescription

Here, we describe how to obtain the running coupling used in the calculations for this thesis. The code for the coupling prescription was written by G. Moore and adapted to the calculations performed here. The effective EQCD coupling is given by [96]

$$g_{\text{EQCD}(N_f)}^2(\mu) = g_{\text{QCD}(N_f)}^2(\mu) + \alpha_{\text{E7}}^{(N_f)} \frac{g_{\text{QCD}(N_f)}^4(\mu)}{(4\pi)^2} + \gamma_{\text{E1}}^{(N_f)} \frac{g_{\text{QCD}(N_f)}^6(\mu)}{(4\pi)^4}, \quad (39)$$

where μ represents the renormalization scale, and [78, 88, 96]

$$\begin{aligned} \alpha_{\text{E7}} &= -\beta_0 \ln \left(\frac{\mu e^{\gamma_E}}{4\pi T} \right) + \frac{C_A}{3} - \frac{8}{3} N_f \ln 2, \\ \gamma_{\text{E1}} &= -\beta_1 \ln \left(\frac{\mu e^{\gamma_E}}{4\pi T} \right) + \alpha_{\text{E7}}^2 - \frac{1}{18} \left\{ C_A^2 [-341 + 20\zeta(3)] \right. \\ &\quad \left. + 2C_A N_f [43 + 24 \ln 2 + 5\zeta(3)] + 3C_F N_f [23 + 80 \ln 2 - 14\zeta(3)] \right\}. \end{aligned} \quad (40)$$

Eq. (39) holds for $m_q^{(N_f)} \leq \mu \leq m_q^{(N_f+1)}$. The value of $g_{\text{QCD}(N_f)}^2(\mu)$ was obtained from a numerical two-loop evolution from $\alpha_z(M_z) = 0.1185$, with the MS renormalization scale μ in the range $[\pi T, 4\pi T]$ and with one-loop quark threshold matching at $\mu = m_q$, using

the equation,

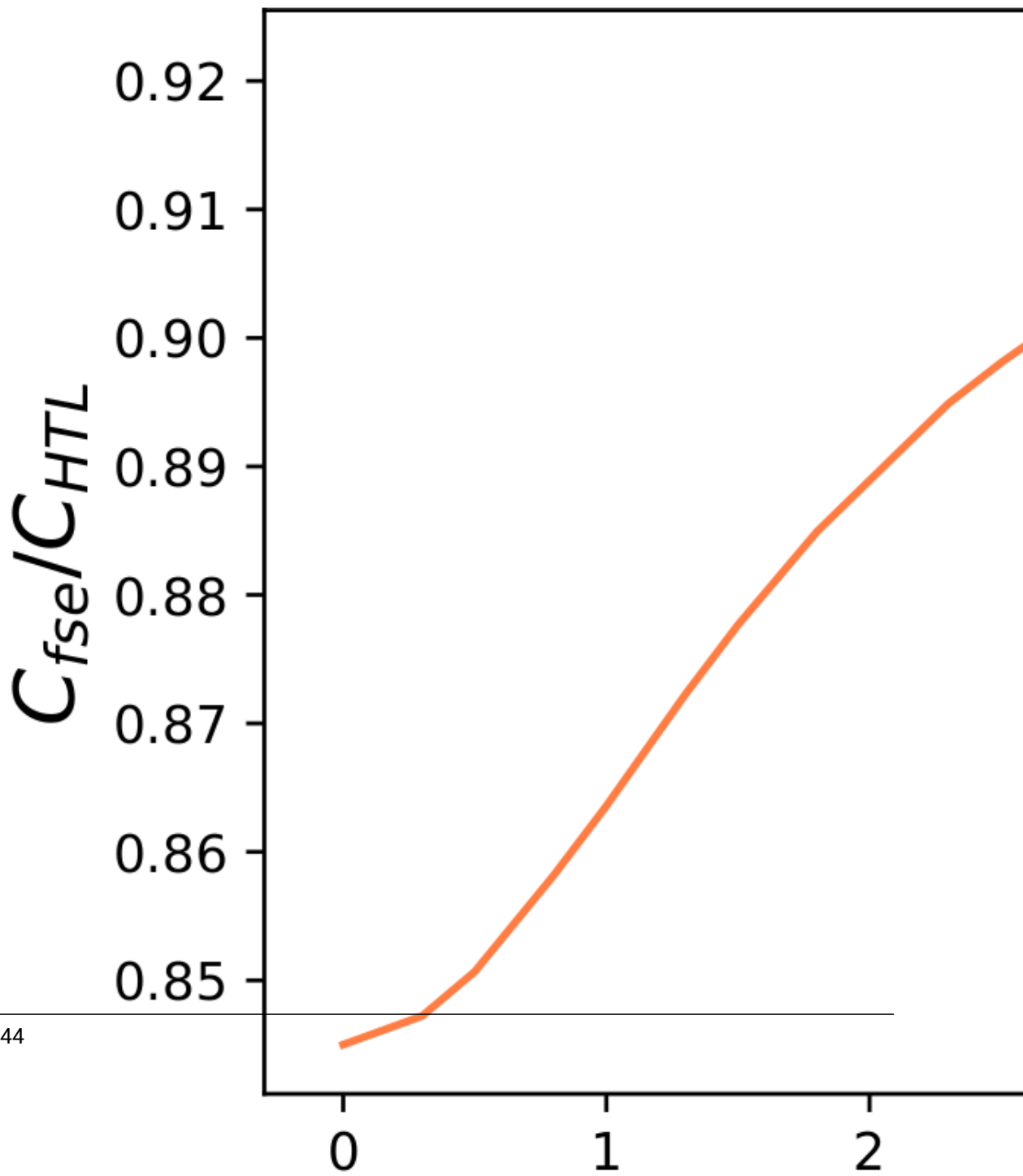
$$\mu \frac{d}{d\mu} g_{\text{QCD}}^2(N_f)(\mu) = \frac{\beta_0^{(N_f)}}{(4\pi)^2} g_{\text{QCD}}^4(N_f)(\mu) + \frac{\beta_1^{(N_f)}}{(4\pi)^4} g_{\text{QCD}}^6(N_f)(\mu), \quad (41)$$

$$m_q^{(N_f)} \leq \mu \leq m_q^{(N_f+1)}, \quad (42)$$

$$g_{\text{QCD}}^2(N_f) \left(m_q^{(N_f+1)} \right) = g_{\text{QCD}}^2(N_f+1) \left(m_q^{(N_f+1)} \right), \quad (43)$$

at the fermion thresholds, we switch to the values of the coefficients in Eq. (40) with $n_f \pm 1$, following the prescription used in [62]. Hence, the EQCD coupling is not continuous at the thresholds. In Fig. 2, we plot the screening mass, m_D , as a function of the temperature for different chemical potential values at $\mu_{\text{EQCD}} = 2.7T$. As one can see, some discontinuities in these curves cause shear viscosity to have a curve less smooth than expected.

We conclude by noting that this prescription was first used for vanishing densities, and there is no indication of which values of μ_{EQCD} should be used for the high-density regime. Therefore, although the results in this thesis are all calculated using $\mu_{\text{EQCD}} = 2.7T$, we highlight that other choices might also be reasonable for high chemical potentials.



144

Figure 1: Collision integral, $(\chi_{ij}, C_{\chi_{ij}})$, calculated using hard thermal loops and using full self energies.

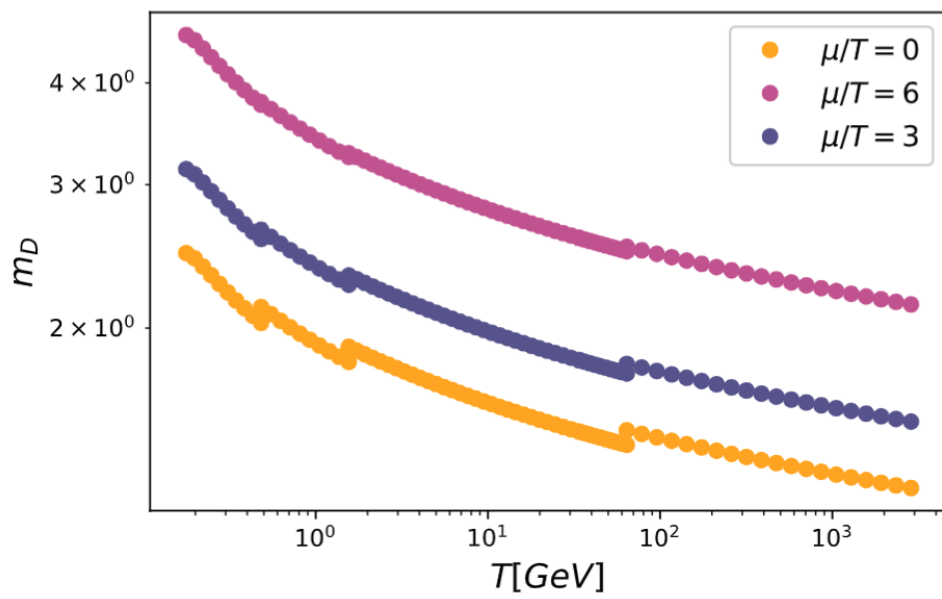


Figure 2: Kinematic shear viscosity as a function of the temperature for $\mu = 0, 3, 6$.

Bibliography

- [1] K Aamodt et al. “Elliptic flow of charged particles in Pb-Pb collisions at 2.76 TeV”. In: *Phys. Rev. Lett.* 105 (2010), p. 252302. doi: 10.1103/PhysRevLett.105.252302. arXiv: 1011.3914 [nucl-ex].
- [2] B. P. Abbott et al. “GW170817: Observation of Gravitational Waves from a Binary Neutron Star Inspiral”. In: *Phys. Rev. Lett.* 119.16 (2017), p. 161101. doi: 10.1103/PhysRevLett.119.161101. arXiv: 1710.05832 [gr-qc].
- [3] Mark C. Abraao York et al. “UV cascade in classical Yang-Mills theory via kinetic theory”. In: *Phys. Rev. D* 89.7 (2014), p. 074036. doi: 10.1103/PhysRevD.89.074036. arXiv: 1401.3751 [hep-ph].
- [4] J. Adamczewski-Musch et al. “Probing dense baryon-rich matter with virtual photons”. In: *Nature Phys.* 15.10 (2019), pp. 1040–1045. doi: 10.1038/s41567-019-0583-8.
- [5] L. Adamczyk et al. “Beam energy dependence of moments of the net-charge multiplicity distributions in Au+Au collisions at RHIC”. In: *Phys. Rev. Lett.* 113 (2014), p. 092301. doi: 10.1103/PhysRevLett.113.092301. arXiv: 1402.1558 [nucl-ex].
- [6] John Adams et al. “Experimental and theoretical challenges in the search for the quark gluon plasma: The STAR Collaboration’s critical assessment of the evidence from RHIC collisions”. In: *Nucl. Phys. A* 757 (2005), pp. 102–183. doi: 10.1016/j.nuclphysa.2005.03.085. arXiv: nucl-ex/0501009.
- [7] K. Adcox et al. “Formation of dense partonic matter in relativistic nucleus-nucleus collisions at RHIC: Experimental evaluation by the PHENIX collaboration”. In: *Nucl. Phys. A* 757 (2005), pp. 184–283. doi: 10.1016/j.nuclphysa.2005.03.086. arXiv: nucl-ex/0410003.
- [8] Dekrayat Almaalol, Travis Dore, and Jacquelyn Noronha-Hostler. “Stability of multi-component relativistic viscous hydrodynamics from Israel-Stewart and reproducing DNMR from maximizing the entropy”. In: (Sept. 2022). arXiv: 2209.11210 [hep-th].

-
-
- [9] Peter Brockway Arnold, Guy D Moore, and Laurence G. Yaffe. “Transport coefficients in high temperature gauge theories. 2. Beyond leading log”. In: *JHEP* 05 (2003), p. 051. DOI: 10.1088/1126-6708/2003/05/051. arXiv: hep-ph/0302165.
- [10] Peter Brockway Arnold, Guy D. Moore, and Laurence G. Yaffe. “Effective kinetic theory for high temperature gauge theories”. In: *JHEP* 01 (2003), p. 030. DOI: 10.1088/1126-6708/2003/01/030. arXiv: hep-ph/0209353.
- [11] Peter Brockway Arnold, Guy D. Moore, and Laurence G. Yaffe. “Photon and gluon emission in relativistic plasmas”. In: *JHEP* 06 (2002), p. 030. DOI: 10.1088/1126-6708/2002/06/030. arXiv: hep-ph/0204343.
- [12] Peter Brockway Arnold, Guy D. Moore, and Laurence G. Yaffe. “Photon emission from ultrarelativistic plasmas”. In: *JHEP* 11 (2001), p. 057. DOI: 10.1088/1126-6708/2001/11/057. arXiv: hep-ph/0109064.
- [13] Peter Brockway Arnold, Guy D. Moore, and Laurence G. Yaffe. “Transport coefficients in high temperature gauge theories. 1. Leading log results”. In: *JHEP* 11 (2000), p. 001. DOI: 10.1088/1126-6708/2000/11/001. arXiv: hep-ph/0010177.
- [14] Peter Brockway Arnold, Dam T. Son, and Laurence G. Yaffe. “Effective dynamics of hot, soft nonAbelian gauge fields. Color conductivity and $\log(1/\alpha)$ effects”. In: *Phys. Rev. D* 59 (1999), p. 105020. DOI: 10.1103/PhysRevD.59.105020. arXiv: hep-ph/9810216.
- [15] Peter Brockway Arnold and Laurence G. Yaffe. “Effective theories for real time correlations in hot plasmas”. In: *Phys. Rev. D* 57 (1998), pp. 1178–1192. DOI: 10.1103/PhysRevD.57.1178. arXiv: hep-ph/9709449.
- [16] P. Aurenche, F. Gelis, and H. Zaraket. “A Simple sum rule for the thermal gluon spectral function and applications”. In: *JHEP* 05 (2002), p. 043. DOI: 10.1088/1126-6708/2002/05/043. arXiv: hep-ph/0204146.
- [17] P. Aurenche et al. “Bremsstrahlung and photon production in thermal QCD”. In: *Phys. Rev. D* 58 (1998), p. 085003. DOI: 10.1103/PhysRevD.58.085003. arXiv: hep-ph/9804224.
- [18] R. Baier et al. “Bottom up’ thermalization in heavy ion collisions”. In: *Phys. Lett. B* 502 (2001), pp. 51–58. DOI: 10.1016/S0370-2693(01)00191-5. arXiv: hep-ph/0009237.

-
- [19] R. Baier et al. “Production rate of hard thermal photons and screening of quark mass singularity”. In: *Z. Phys. C* 53 (1992), pp. 433–438. DOI: 10.1007/BF01625902.
- [20] Rudolf Baier et al. “Relativistic viscous hydrodynamics, conformal invariance, and holography”. In: *JHEP* 04 (2008), p. 100. DOI: 10.1088/1126-6708/2008/04/100. arXiv: 0712.2451 [hep-th].
- [21] G. Baym et al. “Transverse interactions and transport in quark gluon and QED plasmas”. In: *Nucl. Phys. A* 525 (1991). Ed. by J. P. Blaizot et al., pp. 415C–418C. DOI: 10.1016/0375-9474(91)90355-A.
- [22] Gordon Baym et al. “Transverse interactions and transport in relativistic quark-gluon and electromagnetic plasmas”. In: *Phys. Rev. Lett.* 64 (16 Apr. 1990), pp. 1867–1870. DOI: 10.1103/PhysRevLett.64.1867. URL: <https://link.aps.org/doi/10.1103/PhysRevLett.64.1867>.
- [23] A. Bazavov et al. “Chiral crossover in QCD at zero and non-zero chemical potentials”. In: *Phys. Lett. B* 795 (2019), pp. 15–21. DOI: 10.1016/j.physletb.2019.05.013. arXiv: 1812.08235 [hep-lat].
- [24] Michel Le Bellac. *Thermal Field Theory*. Cambridge Monographs on Mathematical Physics. Cambridge University Press, Mar. 2011. ISBN: 978-0-521-65477-7. DOI: 10.1017/CB09780511721700.
- [25] R. Bellwied et al. “The QCD phase diagram from analytic continuation”. In: *Phys. Lett. B* 751 (2015), pp. 559–564. DOI: 10.1016/j.physletb.2015.11.011. arXiv: 1507.07510 [hep-lat].
- [26] Fábio S. Bemfica et al. “Nonlinear Constraints on Relativistic Fluids Far from Equilibrium”. In: *Phys. Rev. Lett.* 126.22 (2021), p. 222301. DOI: 10.1103/PhysRevLett.126.222301. arXiv: 2005.11632 [hep-th].
- [27] Stefan Bernhard et al. “Relativistic hydrodynamics for heavy ion collisions: Freeze-out and particle spectra”. In: *Nucl. Phys. A* 605 (1996), pp. 566–582. DOI: 10.1016/0375-9474(96)00165-0. arXiv: nucl-th/9602011.
- [28] Jonah E. Bernhard, J. Scott Moreland, and Steffen A. Bass. “Bayesian estimation of the specific shear and bulk viscosity of quark-gluon plasma”. In: *Nature Phys.* 15.11 (2019), pp. 1113–1117. DOI: 10.1038/s41567-019-0611-8.
- [29] Sayantani Bhattacharyya et al. “Nonlinear Fluid Dynamics from Gravity”. In: *JHEP* 02 (2008), p. 045. DOI: 10.1088/1126-6708/2008/02/045. arXiv: 0712.2456 [hep-th].

-
-
- [30] Szabolcs Borsanyi et al. “QCD Crossover at Finite Chemical Potential from Lattice Simulations”. In: *Phys. Rev. Lett.* 125.5 (2020), p. 052001. DOI: 10.1103/PhysRevLett.125.052001. arXiv: 2002.02821 [hep-lat].
- [31] Szabolcs Borsanyi et al. “Transition temperature and the equation of state from lattice QCD, Wuppertal-Budapest results”. In: *J. Phys. Conf. Ser.* 316 (2011). Ed. by Rene Bellwied and Claude Pruneau, p. 012020. DOI: 10.1088/1742-6596/316/1/012020. arXiv: 1109.5032 [hep-lat].
- [32] Eric Braaten. “Solution to the perturbative infrared catastrophe of hot gauge theories”. In: *Phys. Rev. Lett.* 74 (1995), pp. 2164–2167. DOI: 10.1103/PhysRevLett.74.2164. arXiv: hep-ph/9409434.
- [33] Eric Braaten and Agustin Nieto. “Effective field theory approach to high temperature thermodynamics”. In: *Phys. Rev. D* 51 (1995), pp. 6990–7006. DOI: 10.1103/PhysRevD.51.6990. arXiv: hep-ph/9501375.
- [34] Eric Braaten and Agustin Nieto. “Free energy of QCD at high temperature”. In: *Phys. Rev. D* 53 (1996), pp. 3421–3437. DOI: 10.1103/PhysRevD.53.3421. arXiv: hep-ph/9510408.
- [35] Eric Braaten and Robert D. Pisarski. “Simple effective Lagrangian for hard thermal loops”. In: *Phys. Rev. D* 45.6 (1992), R1827. DOI: 10.1103/PhysRevD.45.R1827.
- [36] Eric Braaten and Robert D. Pisarski. “Soft Amplitudes in Hot Gauge Theories: A General Analysis”. In: *Nucl. Phys. B* 337 (1990), pp. 569–634. DOI: 10.1016/0550-3213(90)90508-B.
- [37] Wit Busza, Krishna Rajagopal, and Wilke van der Schee. “Heavy Ion Collisions: The Big Picture, and the Big Questions”. In: *Ann. Rev. Nucl. Part. Sci.* 68 (2018), pp. 339–376. DOI: 10.1146/annurev-nucl-101917-020852. arXiv: 1802.04801 [hep-ph].
- [38] Simon Caron-Huot. “O(g) plasma effects in jet quenching”. In: *Phys. Rev. D* 79 (2009), p. 065039. DOI: 10.1103/PhysRevD.79.065039. arXiv: 0811.1603 [hep-ph].
- [39] Isabella Danhoni, Jordi Salinas San Martin, and Jacquelyn Noronha-Hostler. “Shear viscosity from perturbative Quantum Chromodynamics to the hadron resonance gas at finite baryon, strangeness, and electric charge densities”. In: (June 2024). arXiv: 2406.04968 [hep-ph].
- [40] Isabella Danhoni and Guy D. Moore. “Hot and Dense QCD Shear Viscosity at (almost) NLO”. In: (Aug. 2024). arXiv: 2408.00524 [hep-ph].

-
- [41] Isabella Danhoni and Guy D. Moore. “Hot and dense QCD shear viscosity at leading log”. In: *JHEP* 02 (2023), p. 124. DOI: 10.1007/JHEP02(2023)124. arXiv: 2212.02325 [hep-ph].
- [42] S. R. De Groot. *Relativistic Kinetic Theory. Principles and Applications*. Ed. by W. A. Van Leeuwen and C. G. Van Weert. 1980.
- [43] G Denicol and D H Rischke. *Microscopic Foundations of Relativistic Fluid Dynamics*. Springer, 2021.
- [44] G. S. Denicol, S. Jeon, and C. Gale. “Transport Coefficients of Bulk Viscous Pressure in the 14-moment approximation”. In: *Phys. Rev. C* 90.2 (2014), p. 024912. DOI: 10.1103/PhysRevC.90.024912. arXiv: 1403.0962 [nucl-th].
- [45] G. S. Denicol et al. “Derivation of transient relativistic fluid dynamics from the Boltzmann equation”. In: *Phys. Rev. D* 85 (2012). [Erratum: *Phys.Rev.D* 91, 039902 (2015)], p. 114047. DOI: 10.1103/PhysRevD.85.114047. arXiv: 1202.4551 [nucl-th].
- [46] Gabriel S. Denicol and Jorge Noronha. “Spectrum of the Boltzmann collision operator for $\lambda\phi^4$ theory in the classical regime”. In: *Phys. Lett. B* 850 (2024), p. 138487. DOI: 10.1016/j.physletb.2024.138487. arXiv: 2209.10370 [nucl-th].
- [47] Gabriel S. Denicol et al. “Origin of the Relaxation Time in Dissipative Fluid Dynamics”. In: *Phys. Rev. D* 83 (2011), p. 074019. DOI: 10.1103/PhysRevD.83.074019. arXiv: 1102.4780 [hep-th].
- [48] H. -T. Ding et al. “Curvature of the chiral phase transition line from the magnetic equation of state of (2+1)-flavor QCD”. In: (Mar. 2024). arXiv: 2403.09390 [hep-lat].
- [49] *NIST Digital Library of Mathematical Functions*. <http://dlmf.nist.gov/>, Release 1.1.3 of 2021-09-15. F. W. J. Olver, A. B. Olde Daalhuis, D. W. Lozier, B. I. Schneider, R. F. Boisvert, C. W. Clark, B. R. Miller, B. V. Saunders, H. S. Cohl, and M. A. McClain, eds. URL: <http://dlmf.nist.gov/>.
- [50] Lipei Du, Agnieszka Sorensen, and Mikhail Stephanov. “The QCD phase diagram and Beam Energy Scan physics: a theory overview”. In: Feb. 2024. arXiv: 2402.10183 [nucl-th].
- [51] K. Dusling and D. Teaney. “Simulating elliptic flow with viscous hydrodynamics”. In: *Phys. Rev. C* 77 (2008), p. 034905. DOI: 10.1103/PhysRevC.77.034905. arXiv: 0710.5932 [nucl-th].

-
- [52] D. Everett et al. “Multisystem Bayesian constraints on the transport coefficients of QCD matter”. In: *Phys. Rev. C* 103.5 (2021), p. 054904. doi: 10.1103/PhysRevC.103.054904. arXiv: 2011.01430 [hep-ph].
- [53] K. Farakos et al. “3-D physics and the electroweak phase transition: Perturbation theory”. In: *Nucl. Phys. B* 425 (1994), pp. 67–109. doi: 10.1016/0550-3213(94)90173-2. arXiv: hep-ph/9404201.
- [54] J. Frenkel and J. C. Taylor. “High Temperature Limit of Thermal QCD”. In: *Nucl. Phys. B* 334 (1990), pp. 199–216. doi: 10.1016/0550-3213(90)90661-V.
- [55] V. Friese. “The CBM experiment at GSI/FAIR”. In: *Nucl. Phys. A* 774 (2006). Ed. by T. Csorgo et al., pp. 377–386. doi: 10.1016/j.nuclphysa.2006.06.018.
- [56] Wei-jie Fu, Jan M. Pawłowski, and Fabian Rennecke. “Strangeness neutrality and baryon-strangeness correlations”. In: *Phys. Rev. D* 100.11 (2019), p. 111501. doi: 10.1103/PhysRevD.100.111501. arXiv: 1809.01594 [hep-ph].
- [57] Charles Gale, Sangyong Jeon, and Bjoern Schenke. “Hydrodynamic Modeling of Heavy-Ion Collisions”. In: *Int. J. Mod. Phys. A* 28 (2013), p. 1340011. doi: 10.1142/S0217751X13400113. arXiv: 1301.5893 [nucl-th].
- [58] Lorenzo Gavassino. “Infinite Order Hydrodynamics: an Analytical Example”. In: (Feb. 2024). arXiv: 2402.19343 [nucl-th].
- [59] Robert P. Geroch and L. Lindblom. “Dissipative relativistic fluid theories of divergence type”. In: *Phys. Rev. D* 41 (1990), p. 1855. doi: 10.1103/PhysRevD.41.1855.
- [60] Jacopo Ghiglieri and Guy D. Moore. “Low Mass Thermal Dilepton Production at NLO in a Weakly Coupled Quark-Gluon Plasma”. In: *JHEP* 12 (2014), p. 029. doi: 10.1007/JHEP12(2014)029. arXiv: 1410.4203 [hep-ph].
- [61] Jacopo Ghiglieri, Guy D. Moore, and Derek Teaney. “Jet-Medium Interactions at NLO in a Weakly-Coupled Quark-Gluon Plasma”. In: *JHEP* 03 (2016), p. 095. doi: 10.1007/JHEP03(2016)095. arXiv: 1509.07773 [hep-ph].
- [62] Jacopo Ghiglieri, Guy D. Moore, and Derek Teaney. “QCD Shear Viscosity at (almost) NLO”. In: *JHEP* 03 (2018), p. 179. doi: 10.1007/JHEP03(2018)179. arXiv: 1802.09535 [hep-ph].
- [63] Jacopo Ghiglieri and Derek Teaney. “Parton energy loss and momentum broadening at NLO in high temperature QCD plasmas”. In: *Int. J. Mod. Phys. E* 24.11 (2015). Ed. by Xin-Nian Wang, p. 1530013. doi: 10.1142/S0218301315300131. arXiv: 1502.03730 [hep-ph].

-
- [64] Jacopo Ghiglieri et al. “Next-to-leading order thermal photon production in a weakly coupled quark-gluon plasma”. In: *JHEP* 05 (2013), p. 010. DOI: 10.1007/JHEP05(2013)010. arXiv: 1302.5970 [hep-ph].
- [65] I. Ghisoiu and M. Laine. “Interpolation of hard and soft dilepton rates”. In: *JHEP* 10 (2014), p. 083. DOI: 10.1007/JHEP10(2014)083. arXiv: 1407.7955 [hep-ph].
- [66] M. I. Gorenstein, M. Hauer, and O. N. Moroz. “Viscosity in the excluded volume hadron gas model”. In: *Phys. Rev. C* 77 (2008). Ed. by Bernd Aschenbach et al., p. 024911. DOI: 10.1103/PhysRevC.77.024911. arXiv: 0708.0137 [nucl-th].
- [67] V. A. Goy et al. “Sign problem in finite density lattice QCD”. In: *PTEP* 2017.3 (2017), p. 031D01. DOI: 10.1093/ptep/ptx018. arXiv: 1611.08093 [hep-lat].
- [68] Izrail Solomonovich Gradshteyn and Iosif Moiseevich Ryzhik. *Table of integrals, series, and products*. Academic press, 2014.
- [69] Joaquin Grefa et al. “Transport coefficients of the quark-gluon plasma at the critical point and across the first-order line”. In: *Phys. Rev. D* 106.3 (2022), p. 034024. DOI: 10.1103/PhysRevD.106.034024. arXiv: 2203.00139 [nucl-th].
- [70] Felix M. Haehl, R. Loganayagam, and Mukund Rangamani. “Schwinger-Keldysh formalism. Part I: BRST symmetries and superspace”. In: *JHEP* 06 (2017), p. 069. DOI: 10.1007/JHEP06(2017)069. arXiv: 1610.01940 [hep-th].
- [71] R. Hagedorn and Johann Rafelski. “Hot Hadronic Matter and Nuclear Collisions”. In: *Phys. Lett. B* 97 (1980), p. 136. DOI: 10.1016/0370-2693(80)90566-3.
- [72] F. Halzen and H. C. Liu. “Experimental signatures of phase transition to quark matter in high-energy collisions of nuclei”. In: *Phys. Rev. D* 25 (7 Apr. 1982), pp. 1842–1846. DOI: 10.1103/PhysRevD.25.1842. URL: <https://link.aps.org/doi/10.1103/PhysRevD.25.1842>.
- [73] Jan Hammelmann, Jan Staudenmaier, and Hannah Elfner. “Collision term dependence of the hadronic shear viscosity and diffusion coefficients”. In: (July 2023). arXiv: 2307.15606 [nucl-th].
- [74] Najmul Haque et al. “Three-loop HTLpt thermodynamics at finite temperature and chemical potential”. In: *JHEP* 05 (2014), p. 027. DOI: 10.1007/JHEP05(2014)027. arXiv: 1402.6907 [hep-ph].

-
- [75] Ulrich Heinz and Raimond Snellings. “Collective flow and viscosity in relativistic heavy-ion collisions”. In: *Ann. Rev. Nucl. Part. Sci.* 63 (2013), pp. 123–151. DOI: 10.1146/annurev-nucl-102212-170540. arXiv: 1301.2826 [nucl-th].
- [76] Ulrich W. Heinz and S. M. H. Wong. “Elliptic flow from a transversally thermalized fireball”. In: *Phys. Rev. C* 66 (2002), p. 014907. DOI: 10.1103/PhysRevC.66.014907. arXiv: hep-ph/0205058.
- [77] Juhee Hong and Derek Teaney. “Spectral densities for hot QCD plasmas in a leading log approximation”. In: *Phys. Rev. C* 82 (2010), p. 044908. DOI: 10.1103/PhysRevC.82.044908. arXiv: 1003.0699 [nucl-th].
- [78] Su-zhou Huang and Marcello Lissia. “The Relevant scale parameter in the high temperature phase of QCD”. In: *Nucl. Phys. B* 438 (1995), pp. 54–66. DOI: 10.1016/0550-3213(95)00007-F. arXiv: hep-ph/9411293.
- [79] R. C. Hwa and K. Kajantie. “Diagnosing Quark Matter by Measuring the Total Entropy and the Photon Or Dilepton Emission Rates”. In: *Phys. Rev. D* 32 (1985), p. 1109. DOI: 10.1103/PhysRevD.32.1109.
- [80] W. Israel. “Nonstationary irreversible thermodynamics: A Causal relativistic theory”. In: *Annals Phys.* 100 (1976), pp. 310–331. DOI: 10.1016/0003-4916(76)90064-6.
- [81] W. Israel and J. M. Stewart. “Transient relativistic thermodynamics and kinetic theory”. In: *Annals Phys.* 118 (1979), pp. 341–372. DOI: 10.1016/0003-4916(79)90130-1.
- [82] Kazunori Itakura, Osamu Morimatsu, and Hiroshi Otomo. “Shear viscosity of a hadronic gas mixture”. In: *Phys. Rev. D* 77 (2008), p. 014014. DOI: 10.1103/PhysRevD.77.014014. arXiv: 0711.1034 [hep-ph].
- [83] Amaresh Jaiswal. “Formulation of relativistic dissipative fluid dynamics and its applications in heavy-ion collisions”. Other thesis. Aug. 2014. arXiv: 1408.0867 [nucl-th].
- [84] Amaresh Jaiswal and Victor Roy. “Relativistic hydrodynamics in heavy-ion collisions: general aspects and recent developments”. In: *Adv. High Energy Phys.* 2016 (2016), p. 9623034. DOI: 10.1155/2016/9623034. arXiv: 1605.08694 [nucl-th].
- [85] K. Kajantie and H. I. Miettinen. “Temperature Measurement of Quark-Gluon Plasma Formed in High-Energy Nucleus-Nucleus Collisions”. In: *Z. Phys. C* 9 (1981), p. 341. DOI: 10.1007/BF01548770.

-
- [86] K. Kajantie and P. V. Ruuskanen. “Shielding of Quark Mass Singularities in Photon Emission From Hot Quark - Gluon Plasma”. In: *Phys. Lett. B* 121 (1983), pp. 352–354. DOI: 10.1016/0370-2693(83)91385-0.
- [87] K. Kajantie et al. “3-D SU(N) + adjoint Higgs theory and finite temperature QCD”. In: *Nucl. Phys. B* 503 (1997), pp. 357–384. DOI: 10.1016/S0550-3213(97)00425-2. arXiv: hep-ph/9704416.
- [88] K. Kajantie et al. “Generic rules for high temperature dimensional reduction and their application to the standard model”. In: *Nucl. Phys. B* 458 (1996), pp. 90–136. DOI: 10.1016/0550-3213(95)00549-8. arXiv: hep-ph/9508379.
- [89] O. K. Kalashnikov and V. V. Klimov. “Polarization Tensor in QCD for Finite Temperature and Density”. In: *Sov. J. Nucl. Phys.* 31 (1980), p. 699.
- [90] Joseph I. Kapusta, P. Lichard, and D. Seibert. “High-energy photons from quark - gluon plasma versus hot hadronic gas”. In: *Phys. Rev. D* 44 (1991). [Erratum: *Phys.Rev.D* 47, 4171 (1993)], pp. 2774–2788. DOI: 10.1103/PhysRevD.47.4171.
- [91] Joseph I. Kapusta and Keith A. Olive. “Thermodynamics of Hadrons: Delimiting the Temperature”. In: *Nucl. Phys. A* 408 (1983), pp. 478–494. DOI: 10.1016/0375-9474(83)90241-5.
- [92] P. F. Kolb et al. “Centrality dependence of multiplicity, transverse energy, and elliptic flow from hydrodynamics”. In: *Nucl. Phys. A* 696 (2001), pp. 197–215. DOI: 10.1016/S0375-9474(01)01114-9. arXiv: hep-ph/0103234.
- [93] Peter F. Kolb, Josef Sollfrank, and Ulrich W. Heinz. “Anisotropic transverse flow and the quark hadron phase transition”. In: *Phys. Rev. C* 62 (2000), p. 054909. DOI: 10.1103/PhysRevC.62.054909. arXiv: hep-ph/0006129.
- [94] P. Kovtun, Dan T. Son, and Andrei O. Starinets. “Viscosity in strongly interacting quantum field theories from black hole physics”. In: *Phys. Rev. Lett.* 94 (2005), p. 111601. DOI: 10.1103/PhysRevLett.94.111601. arXiv: hep-th/0405231.
- [95] Alekski Kurkela and Aleksas Mazeliauskas. “Chemical equilibration in weakly coupled QCD”. In: *Phys. Rev. D* 99.5 (2019), p. 054018. DOI: 10.1103/PhysRevD.99.054018. arXiv: 1811.03068 [hep-ph].
- [96] M. Laine and Y. Schroder. “Two-loop QCD gauge coupling at high temperatures”. In: *JHEP* 03 (2005), p. 067. DOI: 10.1088/1126-6708/2005/03/067. arXiv: hep-ph/0503061.

-
- [97] L. D. Landau and I. Pomeranchuk. “Electron cascade process at very high-energies”. In: *Dokl. Akad. Nauk Ser. Fiz.* 92 (1953), pp. 735–738.
- [98] L. D. Landau and I. Pomeranchuk. “Limits of applicability of the theory of bremsstrahlung electrons and pair production at high-energies”. In: *Dokl. Akad. Nauk Ser. Fiz.* 92 (1953), pp. 535–536.
- [99] L.D. Landau and EM Lifshitz. “Fluid Mechanics”. In: *Course of Theoretical Physics, Pergamon Press, London* 6 (1959).
- [100] R. van Leeuwen et al. *Introduction to the Keldysh Formalism*. Ed. by Miguel A.L. Marques et al. Berlin, Heidelberg: Springer Berlin Heidelberg, 2006, pp. 33–59. ISBN: 978-3-540-35426-0. DOI: 10.1007/3-540-35426-3_3. URL: https://doi.org/10.1007/3-540-35426-3_3.
- [101] E.M. LIFSHITZ and L.P. PITAEVSKI. *CHAPTER I - KINETIC THEORY OF GASES (paragraph 10)*. Ed. by E.M. LIFSHITZ and L.P. PITAEVSKI. Vol. 10. Course of Theoretical Physics. Amsterdam: Pergamon, 1981, pp. 1–88. ISBN: 978-0-08-026480-6. DOI: <https://doi.org/10.1016/B978-0-08-026480-6.50006-0>. URL: <https://www.sciencedirect.com/science/article/pii/B9780080264806500060>.
- [102] Matthew Luzum and Hannah Petersen. “Initial State Fluctuations and Final State Correlations in Relativistic Heavy-Ion Collisions”. In: *J. Phys. G* 41 (2014), p. 063102. DOI: 10.1088/0954-3899/41/6/063102. arXiv: 1312.5503 [nucl-th].
- [103] Matthew Luzum and Paul Romatschke. “Conformal Relativistic Viscous Hydrodynamics: Applications to RHIC results at $s(\text{NN})^{1/2} = 200\text{-GeV}$ ”. In: *Phys. Rev. C* 78 (2008). [Erratum: *Phys.Rev.C* 79, 039903 (2009)], p. 034915. DOI: 10.1103/PhysRevC.78.034915. arXiv: 0804.4015 [nucl-th].
- [104] Emma McLaughlin et al. “Building a testable shear viscosity across the QCD phase diagram”. In: *Phys. Rev. C* 105.2 (2022), p. 024903. DOI: 10.1103/PhysRevC.105.024903. arXiv: 2103.02090 [nucl-th].
- [105] A. B. Migdal. “Bremsstrahlung and pair production in condensed media at high-energies”. In: *Phys. Rev.* 103 (1956), pp. 1811–1820. DOI: 10.1103/PhysRev.103.1811.
- [106] Sukanya Mitra and Vinod Chandra. “Transport coefficients of a hot QCD medium and their relative significance in heavy-ion collisions”. In: *Phys. Rev. D* 96.9 (2017), p. 094003. DOI: 10.1103/PhysRevD.96.094003. arXiv: 1702.05728 [nucl-th].

-
-
- [107] Sylvain Mogliacci et al. “Equation of State of hot and dense QCD: Resummed perturbation theory confronts lattice data”. In: *JHEP* 12 (2013), p. 055. DOI: 10.1007/JHEP12(2013)055. arXiv: 1307.8098 [hep-ph].
- [108] E. Molnár et al. “Relative importance of second-order terms in relativistic dissipative fluid dynamics”. In: *Phys. Rev. D* 89.7 (2014), p. 074010. DOI: 10.1103/PhysRevD.89.074010. arXiv: 1308.0785 [nucl-th].
- [109] Guy D. Moore. “Shear viscosity in QCD and why it’s hard to calculate”. In: *Criticality in QCD and the Hadron Resonance Gas*. Oct. 2020. arXiv: 2010.15704 [hep-ph].
- [110] Guy D. Moore. “Stress-stress correlator in ϕ^4 theory: poles or a cut?” In: *JHEP* 05 (2018), p. 084. DOI: 10.1007/JHEP05(2018)084. arXiv: 1803.00736 [hep-ph].
- [111] Guy D. Moore. “Transport coefficients in large N(f) gauge theory: Testing hard thermal loops”. In: *JHEP* 05 (2001), p. 039. DOI: 10.1088/1126-6708/2001/05/039. arXiv: hep-ph/0104121.
- [112] Guy D. Moore and Kiyomars A. Sohrabi. “Kubo Formulae for Second-Order Hydrodynamic Coefficients”. In: *Phys. Rev. Lett.* 106 (2011), p. 122302. DOI: 10.1103/PhysRevLett.106.122302. arXiv: 1007.5333 [hep-ph].
- [113] Govert Nijs et al. “Bayesian analysis of heavy ion collisions with the heavy ion computational framework Trajectum”. In: *Phys. Rev. C* 103.5 (2021), p. 054909. DOI: 10.1103/PhysRevC.103.054909. arXiv: 2010.15134 [nucl-th].
- [114] Jorge Noronha et al. “Progress and Challenges in Small Systems”. In: Jan. 2024. arXiv: 2401.09208 [nucl-th].
- [115] Jacquelyn Noronha-Hostler, Jorge Noronha, and Carsten Greiner. “Hadron Mass Spectrum and the Shear Viscosity to Entropy Density Ratio of Hot Hadronic Matter”. In: *Phys. Rev. C* 86 (2012), p. 024913. DOI: 10.1103/PhysRevC.86.024913. arXiv: 1206.5138 [nucl-th].
- [116] Jacquelyn Noronha-Hostler, Jorge Noronha, and Carsten Greiner. “Transport Coefficients of Hadronic Matter near T(c)”. In: *Phys. Rev. Lett.* 103 (2009), p. 172302. DOI: 10.1103/PhysRevLett.103.172302. arXiv: 0811.1571 [nucl-th].
- [117] Stephan Ochsensfeld and Sören Schlichting. “Hydrodynamic and non-hydrodynamic excitations in kinetic theory — a numerical analysis in scalar field theory”. In: *JHEP* 09 (2023), p. 186. DOI: 10.1007/JHEP09(2023)186. arXiv: 2308.04491 [hep-th].

-
- [118] Jean-François Paquet. “Applications of emulation and Bayesian methods in heavy-ion physics”. In: (Oct. 2023). arXiv: 2310.17618 [nucl-th].
- [119] Jean-François Paquet et al. “Production of photons in relativistic heavy-ion collisions”. In: *Phys. Rev. C* 93.4 (2016), p. 044906. DOI: 10.1103/PhysRevC.93.044906. arXiv: 1509.06738 [hep-ph].
- [120] J. E. Parkkila, A. Onnerstad, and D. J. Kim. “Bayesian estimation of the specific shear and bulk viscosity of the quark-gluon plasma with additional flow harmonic observables”. In: *Phys. Rev. C* 104.5 (2021), p. 054904. DOI: 10.1103/PhysRevC.104.054904. arXiv: 2106.05019 [hep-ph].
- [121] Michael E. Peskin and Daniel V. Schroeder. *An Introduction to quantum field theory*. Reading, USA: Addison-Wesley, 1995. ISBN: 978-0-201-50397-5.
- [122] G. Policastro, Dan T. Son, and Andrei O. Starinets. “The Shear viscosity of strongly coupled N=4 supersymmetric Yang-Mills plasma”. In: *Phys. Rev. Lett.* 87 (2001), p. 081601. DOI: 10.1103/PhysRevLett.87.081601. arXiv: hep-th/0104066.
- [123] Dirk H. Rischke, Stefan Bernard, and Joachim A. Maruhn. “Relativistic hydrodynamics for heavy ion collisions. 1. General aspects and expansion into vacuum”. In: *Nucl. Phys. A* 595 (1995), pp. 346–382. DOI: 10.1016/0375-9474(95)00355-1. arXiv: nucl-th/9504018.
- [124] Dirk H. Rischke et al. “Excluded volume effect for the nuclear matter equation of state”. In: *Z. Phys. C* 51 (1991), pp. 485–490. DOI: 10.1007/BF01548574.
- [125] Gabriel S. Rocha et al. “Branch-cut in the shear-stress response function of massless $\lambda\phi^4$ with Boltzmann statistics”. In: (Apr. 2024). arXiv: 2404.04679 [nucl-th].
- [126] Gabriel S. Rocha et al. “Theories of Relativistic Dissipative Fluid Dynamics”. In: *Entropy* 26.3 (2024), p. 189. DOI: 10.3390/e26030189. arXiv: 2311.15063 [nucl-th].
- [127] Paul Romatschke. “New Developments in Relativistic Viscous Hydrodynamics”. In: *Int. J. Mod. Phys. E* 19 (2010), pp. 1–53. DOI: 10.1142/S0218301310014613. arXiv: 0902.3663 [hep-ph].
- [128] Paul Romatschke and Ulrike Romatschke. *Relativistic Fluid Dynamics In and Out of Equilibrium*. Cambridge Monographs on Mathematical Physics. Cambridge University Press, May 2019. ISBN: 978-1-108-75002-8. DOI: 10.1017/9781108651998. arXiv: 1712.05815 [nucl-th].

-
- [129] S. Ryu et al. “Importance of the Bulk Viscosity of QCD in Ultrarelativistic Heavy-Ion Collisions”. In: *Phys. Rev. Lett.* 115.13 (2015), p. 132301. DOI: 10.1103/PhysRevLett.115.132301. arXiv: 1502.01675 [nucl-th].
- [130] Sangwook Ryu et al. “Effects of bulk viscosity and hadronic rescattering in heavy ion collisions at energies available at the BNL Relativistic Heavy Ion Collider and at the CERN Large Hadron Collider”. In: *Phys. Rev. C* 97.3 (2018), p. 034910. DOI: 10.1103/PhysRevC.97.034910. arXiv: 1704.04216 [nucl-th].
- [131] Jordi Salinas San Martin et al. “Thermodynamics of an updated hadronic resonance list and influence on hadronic transport”. In: (Sept. 2023). arXiv: 2309.01737 [nucl-th].
- [132] Thomas Schäfer and Derek Teaney. “Nearly Perfect Fluidity: From Cold Atomic Gases to Hot Quark Gluon Plasmas”. In: *Rept. Prog. Phys.* 72 (2009), p. 126001. DOI: 10.1088/0034-4885/72/12/126001. arXiv: 0904.3107 [hep-ph].
- [133] Bjoern Schenke, Sangyong Jeon, and Charles Gale. “(3+1)D hydrodynamic simulation of relativistic heavy-ion collisions”. In: *Phys. Rev. C* 82 (2010), p. 014903. DOI: 10.1103/PhysRevC.82.014903. arXiv: 1004.1408 [hep-ph].
- [134] Chun Shen and Li Yan. “Recent development of hydrodynamic modeling in heavy-ion collisions”. In: *Nucl. Sci. Tech.* 31.12 (Oct. 2020), p. 122. DOI: 10.1007/s41365-020-00829-z. arXiv: 2010.12377 [nucl-th].
- [135] Chun Shen et al. “The iEBE-VISHNU code package for relativistic heavy-ion collisions”. In: *Comput. Phys. Commun.* 199 (2016), pp. 61–85. DOI: 10.1016/j.cpc.2015.08.039. arXiv: 1409.8164 [nucl-th].
- [136] Edward V. Shuryak. “Quark-Gluon Plasma and Hadronic Production of Leptons, Photons and Psions”. In: *Phys. Lett. B* 78 (1978), p. 150. DOI: 10.1016/0370-2693(78)90370-2.
- [137] G. Staadt, W. Greiner, and Johann Rafelski. “Photons From Strange Quark Annihilation in Quark - Gluon Plasma”. In: *Phys. Rev. D* 33 (1986), p. 66. DOI: 10.1103/PhysRevD.33.66.
- [138] Nan Su. “A brief overview of hard-thermal-loop perturbation theory”. In: *Commun. Theor. Phys.* 57 (2012), p. 409. DOI: 10.1088/0253-6102/57/3/12. arXiv: 1204.0260 [hep-ph].
- [139] D. Teaney and Edward V. Shuryak. “An Unusual space-time evolution for heavy ion collisions at high-energies due to the QCD phase transition”. In: *Phys. Rev. Lett.* 83 (1999), pp. 4951–4954. DOI: 10.1103/PhysRevLett.83.4951. arXiv: nucl-th/9904006.

-
- [140] Derek Teaney. “The Effects of viscosity on spectra, elliptic flow, and HBT radii”. In: *Phys. Rev. C* 68 (2003), p. 034913. DOI: 10.1103/PhysRevC.68.034913. arXiv: nucl-th/0301099.
- [141] Derek A. Teaney. “Viscous Hydrodynamics and the Quark Gluon Plasma”. In: *Quark-gluon plasma 4*. Ed. by Rudolph C. Hwa and Xin-Nian Wang. 2010, pp. 207–266. DOI: 10.1142/9789814293297_0004. arXiv: 0905.2433 [nucl-th].
- [142] R. Venugopalan and M. Prakash. “Thermal properties of interacting hadrons”. In: *Nucl. Phys. A* 546 (1992), pp. 718–760. DOI: 10.1016/0375-9474(92)90005-5.
- [143] Ramona Vogt. *Ultrarelativistic heavy-ion collisions*. Amsterdam: Elsevier, 2007. ISBN: 978-0-444-52196-5.
- [144] David Wagner and Lorenzo Gavassino. “Regime of applicability of Israel-Stewart hydrodynamics”. In: *Phys. Rev. D* 109.1 (2024), p. 016019. DOI: 10.1103/PhysRevD.109.016019. arXiv: 2309.14828 [nucl-th].
- [145] H. A. Weldon. “Reformulation of finite temperature dilepton production”. In: *Phys. Rev. D* 42 (1990), pp. 2384–2387. DOI: 10.1103/PhysRevD.42.2384.
- [146] H. Arthur Weldon. “Covariant Calculations at Finite Temperature: The Relativistic Plasma”. In: *Phys. Rev. D* 26 (1982), p. 1394. DOI: 10.1103/PhysRevD.26.1394.
- [147] Anton Wiranata, Madappa Prakash, and Purnendu Chakraborty. “Comparison of Viscosities from the Chapman-Enskog and Relaxation Time Methods”. In: *Central Eur. J. Phys.* 10 (2012), pp. 1349–1351. DOI: 10.2478/s11534-012-0082-3. arXiv: 1201.3104 [nucl-th].
- [148] Mark Abraao York and Guy D. Moore. “Second order hydrodynamic coefficients from kinetic theory”. In: *Phys. Rev. D* 79 (2009), p. 054011. DOI: 10.1103/PhysRevD.79.054011. arXiv: 0811.0729 [hep-ph].

Acknowledgments

I would like to first thank my family for their unconditional love and support throughout my life. My parents for working so hard to give me the education they never had, even though physics was not really their first choice of career, and my sister for being my number-one supporter since I can remember.

I would not have made it this far without the support of all my friends here in Germany. Special thanks to Chiara, Theo, Renan, Oscar, Travis, Caio, Gabriel, Marina, Camila, Nina, Hanna and Lars for being my family here in Germany. Not only for the fun moments we had in these years but also for the support during the stressful and difficult moments. I would also like to thank my friends in Illinois, who have made my stay there the best it could have been and have been kind enough to support me during application season. To my friends in Brazil, who have always been present in my life, even with the distance, thank you for all.

I'm also thankful to my colleagues in Darmstadt for all the physics discussions, interesting group meetings, and fun lunches at the Italian place. Special thanks to those who agreed to split the pizza with me because we all know I need some help there. I also thank Simon for correcting my German translation. I couldn't forget to also mention my CRC young scientist colleagues for the good moments at the CRC colloquiums and retreats and the interesting physics discussions we all had.

I also have to acknowledge the Equal Opportunity Committee of the CRC for giving me the opportunity to go to the US for a mentoring trip. This trip allowed me to collaborate with different people and see a different work environment.

Finally, I will be forever grateful to my supervisor, Prof. Guy Moore. Not only for being a great supervisor but also for always doing his best to make his students feel at home in Germany. His group has been a healthy and fun environment to discuss physics and career perspectives, providing us with a safe space to ask all the stupid questions we had.

Curriculum Vitae

Personal Information

Name: Isabella Danhoni
Address: Darmstadt, Germany
Email: idanhoni@theorie.ikp.physik.tu-darmstadt.de

Education

2021-present Ph.D. in Physics, Technische Universitat Darmstadt, Darmstadt, Deutschland
Ph.D. Dissertation: *"Shear Viscosity for QCD at High Chemical Potentials"*, under supervision of Prof. Dr. Guy D. Moore.
Sept-Dec 2023 - Visiting Ph.D. student at the University of Illinois working with Dr. Jorge Noronha and Dr. Jacquelyn Noronha-Hostler.

2019-2021 M.Sc. in Physics, University of Sao Paulo, Sao Paulo, Brasil
M.Sc. Thesis: *"Magnetic transitions and pion production in ultraperipheral heavy-ion collisions"*, under supervision of Prof. Dr. Fernando Silveira Navarra.

2015-2019 B.Sc. in Physics, University of Sao Paulo, Sao Paulo, Brasil

Grants

2023 Giersch-Excellence-Grant, awarded for outstanding work or progress in the thesis project in the past year, under the supervision of Dr. Guy D. Moore

2019-2021 Coordenacao de Aperfeicoamento de Pessoal de Nivel Superior (CAPES), Master's fellowship, under the supervision of Dr. Fernando Silveira Navarra

2017-2018 Conselho Nacional de Desenvolvimento Cientifico e Tecnologico (CNPq), Undergraduate research, under the supervision of Dr. Joao Evangelista Steiner

Publications

- I. Danhoni, J. S. S. Martin and J. Noronha-Hostler, **"Shear viscosity from perturbative Quantum Chromodynamics to the hadron resonance gas at finite baryon, strangeness, and electric charge densities"**, 2024 [arXiv:2406.04968 [hep-ph]]
- G. S. Rocha, I. Danhoni, K. Ingles, G. S. Denicol and J. Noronha, **"Branch-cut in the shear-stress response function of massless $\lambda\varphi^4$ with Boltzmann statistics"**, 2024 [arXiv:2404.04679 [nucl-th]]
- Danhoni, I. and Moore G. D., **"Hot and Dense QCD Shear Viscosity at Leading Log"**, JHEP 124, 2023
- Danhoni, I. ; Navarra, F.S., **"Magnetic field in relativistic heavy-ion collisions: testing the classical approximation"**, Phys. Rev. C, 2021
- Danhoni, I. ; Navarra, F.S., **"Magnetic excitation in relativistic heavy-ion collisions"**, PHYSICS LETTERS B, 2020

Participation in Events

- | | |
|------|---|
| 2023 | XXXth International Conference on Ultra-relativistic Nucleus-Nucleus Collisions (Quark Matter)
<i>Poster Presentation: Shear Viscosity at High Chemical Potentials</i> |
| 2023 | QCD Master Class, Summer School |
| 2022 | 18th International Conference on QCD in Extreme Conditions (XQCD 2022)
<i>Oral Presentation: Extending AMY Shear Viscosity Calculations to Finite Baryon Chemical Potentials</i> |
| 2022 | 2022 XQCD PhD school, Summer School |
| 2022 | ELEMENTS Annual Conference 2022
<i>Poster: Leading-Log Shear Viscosity at High Chemical Potentials</i> |
| 2022 | Strong and Electro-Weak Matter 2022
<i>Oral Presentation: Magnetic field in relativistic heavy ion collisions: how good is the classical approximation?</i> |

Programming

Experience with: C, Python, Mathematica

Teaching Experiences

- 2022/23** Teaching Assistant, Advanced Quantum Mechanics, Technische Universität Darmstadt
- 2019** Teaching Assistant, Oscillations and Waves, University of São Paulo

Languages

- English:** Fluent - Toefl: 101 (2021)
Portuguese: Native speaker
Spanish: Good command

References

Dr. Guy D. Moore
guy.moore@physik.tu-darmstadt.de
Institut für Kernphysik
Technische Universität Darmstadt
Darmstadt, Germany

Dr. Dirk H. Rischke
drischke@itp.uni-frankfurt.de
Institut für Theoretische Physik
Johann Wolfgang Goethe-Universität
Frankfurt am Main, Germany